Fall 2015

POROUS MEDIUM CONVECTION AT LARGE RAYLEIGH NUMBER: STUDIES OF COHERENT STRUCTURE, TRANSPORT, AND REDUCED DYNAMICS

Baole Wen
University of New Hampshire, Durham

POROUS MEDIUM CONVECTION AT LARGE RAYLEIGH NUMBER: STUDIES OF COHERENT STRUCTURE, TRANSPORT, AND REDUCED DYNAMICS

BY

BAOLE WEN

Baccalaureate Degree, Beijing University of Aeronautics and Astronautics, 2007

Master's Degree, Beijing University of Aeronautics and Astronautics, 2010

DISSERTATION

Submitted to the University of New Hampshire

in Partial Fulfillment of

the Requirements for the Degree of

Doctor of Philosophy

in

Applied Mathematics

September, 2015

The dissertation has been examined and approved in partial fulfillment of the requirements for the degree of Doctor of Philosophy in Applied Mathematics by:

Dissertation Director, Gregory P. Chini
Associate Professor of Mechanical Engineering

John P. McHugh
Associate Professor of Mechanical Engineering

Christopher M. White
Associate Professor of Mechanical Engineering

Nivedita Gupta
Associate Professor of Chemical Engineering

John F. Gibson
Assistant Professor of Mathematics & Statistics

On July 14th 2015

Original approval signatures are on file with the University of New Hampshire Graduate School.

DEDICATION

To my lovely wife, Ke Shao, and our parents ...

ACKNOWLEDGEMENTS

I would like to express my gratitude to many people without whom I would not have been able to complete my doctoral study and to have written this dissertation. First and foremost, I would like to give my deepest appreciation to my advisor Dr. Greg Chini for his continuous and patient support for my PhD study, research and life. His encouragement and guidance helped me in all the time of research and writing of this dissertation. Working with him on such an interesting project is one of the best choices I have made for the past few years.

Besides my advisor, I would like to thank my collaborators, Dr. Charlie Doering in University of Michigan, Dr. John Gibson in Department of Mathematics & Statistics, and Dr. Rich Kerswell in University of Bristol for their valuable advice and discussions; and I would also like to acknowledge my committee members, Dr. John McHugh, Dr. Christopher White and Dr. Nivedita Gupta for their helpful comments and suggestions on my dissertation.

Next, I would like to thank my good friend Zhexuan Zhang who is always willing to help and give his best suggestions for my research and life. Many thanks to other good friends in the IAM lab: Evan Brand, John McClain, Ali Nassiri, Ziemowit Malecha and Mimi Szeto, and to my previous roommates (also good friends): Xiongzhuo Gao and Zhengang Hong. The assistance from the administrators April Flore and Tracey Harvey and the technical support from Gerry Pregent and Gina Desmarais are also gratefully acknowledged.

Most importantly, I would like to thank my family: my wife Ke Shao, and our parents Junting Wen & Xianqin Liu and Guoliang Shao & Fang Liu. Without their support, quiet patience, encouragement and unwavering love, I would be lost. Finally, financial support from NSF Award DMS-0928098, CEPS Fellowship, UNH Summer TA Fellowship, and UNH Dissertation Year Fellowship for this research is greatly appreciated.

TABLE OF CONTENTS

LIST OF TABLES

LIST OF FIGURES

ABSTRACT

POROUS MEDIUM CONVECTION AT LARGE RAYLEIGH NUMBER: STUDIES OF COHERENT STRUCTURE, TRANSPORT, AND REDUCED DYNAMICS

by

Baole Wen

University of New Hampshire, September, 2015

Buoyancy-driven convection in fluid-saturated porous media is a key environmental and technological process, with applications ranging from carbon dioxide storage in terrestrial aquifers to the design of compact heat exchangers. Porous medium convection is also a paradigm for forced-dissipative infinite-dimensional dynamical systems, exhibiting spatiotemporally chaotic dynamics if not "true" turbulence. The objective of this dissertation research is to quantitatively characterize the dynamics and heat transport in two-dimensional horizontal and inclined porous medium convection between isothermal plane parallel boundaries at asymptotically large values of the Rayleigh number Ra by investigating the emergent, quasi-coherent flow. This investigation employs a complement of direct numerical simulations (DNS), secondary stability and dynamical systems theory, and variational analysis.

The DNS confirm the remarkable tendency for the interior flow to self-organize into closely-spaced columnar plumes at sufficiently large Ra (up to $Ra \simeq 10^5$), with more complex spatiotemporal features being confined to boundary layers near the heated and cooled walls. The relatively simple form of the interior flow motivates investigation of unstable steady and

time-periodic convective states at large Ra as a function of the domain aspect ratio L. To gain insight into the development of spatiotemporally chaotic convection, the (secondary) stability of these fully nonlinear states to small-amplitude disturbances is investigated using a spatial Floquet analysis. The results indicate that there exist two distinct modes of instability at large Ra: a bulk instability mode and a wall instability mode. The former usually is excited by long-wavelength disturbances and is generally much weaker than the latter. DNS, strategically initialized to investigate the fully nonlinear evolution of the most dangerous secondary instability modes, suggest that the (long time) mean inter-plume spacing in statistically-steady porous medium convection results from an interplay between the competing effects of these two types of instability.

Upper bound analysis is then employed to investigate the dependence of the heat transport enhancement factor, i.e. the Nusselt number Nu, on Ra and L. To solve the optimization problems arising from the "background field" upper-bound variational analysis, a novel two-step algorithm in which time is introduced into the formulation is developed. The new algorithm obviates the need for numerical continuation, thereby enabling the best available bounds to be computed up to $Ra \approx 2.65 \times 10^4$. A mathematical proof is given to demonstrate that the only steady state to which this numerical algorithm can converge is the required global optimal of the variational problem. Using this algorithm, the dependence of the bounds on $L(Ra)$ is explored, and a "minimal flow unit" is identified. Finally, the upper bound variational methodology is also shown to yield quantitatively useful predictions of Nu and to furnish a functional basis that is naturally adapted to the boundary layer dynamics at large Ra.

CHAPTER 1

INTRODUCTION

1.1 Background

Porous medium convection is a key environmental process that has been extensively studied since the 1940s (Horton and Rogers, 1945; Lapwood, 1948) owing to its numerous geoscientific applications including oil recovery, groundwater flow, and geothermal energy extraction (Nield and Bejan, 2006; Phillips, 1991, 2009). More fundamentally, as a paradigm for forced-dissipative infinite-dimensional nonlinear dynamical systems, buoyancy-driven convection in a fluid-saturated porous layer retains much of the rich dynamics of Rayleigh–Bénard convection in a pure fluid layer yet provides a simpler physical and mathematical setting for studying instabilities, bifurcations, pattern formation, and spatiotemporally chaotic dynamics. Recently, this system has again become the subject of intense scrutiny owing to applications in carbon dioxide (CO_2) sequestration in terrestrial aquifers, one promising means of reducing the emission of greenhouse gases into the atmosphere (Metz et al., 2005).

When CO_2 is injected into a deep aquifer, it forms an immiscible CO_2-rich vapor phase (Riaz et al., 2006), as shown in Figure 1-1. The uncontrolled upward movement of the

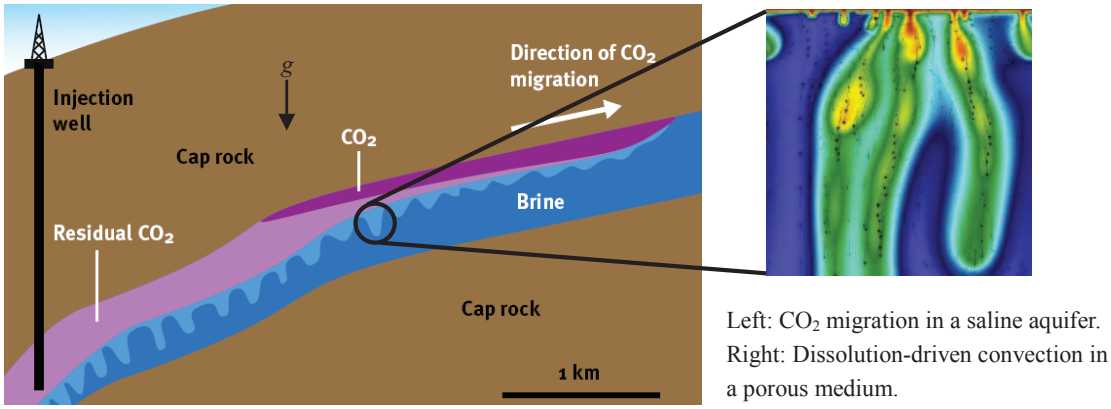

Left: CO_2 migration in a saline aquifer. Right: Dissolution-driven convection in a porous medium.

Figure 1-1: Schematic of the CO_2 sequestration process (Blunt, 2010; Pau et al., 2010).

buoyant vapor is largely inhibited by low-permeability cap rock (Blunt, 2010), but secure long-term storage is not guaranteed since fractures in the cap rock can lead to undesired leakage (Neufeld et al., 2011). Fortunately, as the CO_2 vapor spreads, it dissolves into the liquid brine that fills the porous rock layer comprising the aquifer. The brine becomes top-heavy and, under the influence of gravity, sinks in plumes of comparatively heavy CO_2-rich fluid (Pau et al. (2010), see Figure 1-1). This phenomenon, known as *porous medium convection*, greatly increases the rate of CO_2 dissolution and modifies the spread of the overlying CO_2 vapor.

Although carbon sequestration is already being pursued at various sites around the globe (Metz et al., 2005), there is a pressing need for improved mathematical and computational models to facilitate evaluation of injection scenarios, estimation of reservoir storage capacities, and assessment of leakage risks. To develop quantitatively reliable yet computationally efficient models for use in studies of carbon sequestration, a thorough understanding of the underlying flow and transport mechanisms governing this spatiotemporally-chaotic system is required. This need motivates the dissertation studies of coherent structure, transport, and reduced

dynamics in porous medium convection. The long-term objective of this dissertation research is to contribute to the development of efficient models of CO_2 sequestration, while a more fundamental aim is to further the general understanding of spatiotemporally chaotic nonlinear systems.

In pursuit of these goals, a *canonical configuration* for studying the essential features of porous medium convection – namely, Rayleigh–Bénard convection in a fluid-saturated porous medium – is employed (Nield and Bejan, 2006). In Rayleigh–Bénard convection, fluid is heated from below and cooled from above. Since warmer fluid is less dense than colder fluid, convection sets in when the imposed temperature difference across the porous layer, encapsulated in a parameter termed the Rayleigh number Ra, is large enough. Note that, here, the fluid temperature is strictly analogous to the concentration of CO_2 in carbon sequestration; similarly, the enhancement in heat transport across the layer, quantified by the so-called Nusselt number Nu, is directly proportional to the increased CO_2 dissolution rate.

1.2 Rayleigh–Bénard Convection in a Fluid-Saturated Porous Medium

The flow in a horizontal porous layer uniformly heated from below undergoes a sequence of bifurcations as the Rayleigh number Ra, the normalized temperature drop across the layer, is increased (see Figure 1-2). When $Ra > 4\pi^2$, the simple conduction solution becomes linearly unstable (Nield and Bejan, 2006) and steady $O(1)$ aspect-ratio large-scale convective rolls emerge. In a two-dimensional (2D) domain, the steady rolls strengthen but remain stable as

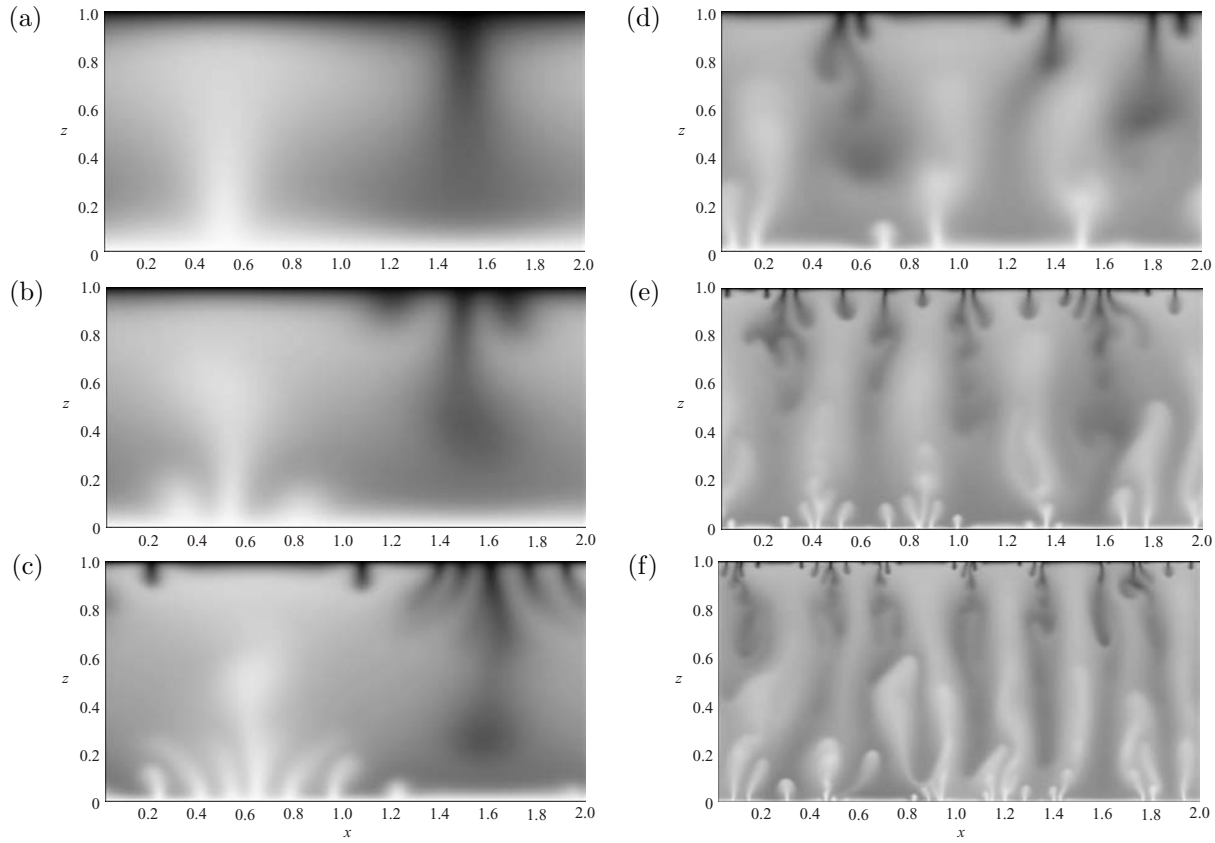

Figure 1-2: Snapshots of temperature field from DNS (Otero et al., 2004) for (a) $Ra = 315$, (b) $Ra = 500$, (c) $Ra = 1255$, (d) $Ra = 1581$, (e) $Ra = 5000$, (f) $Ra = 7924$. Colorbar: the hot roll/plume is in white color; the cold roll/plume is in dark color.

Ra is increased up to $Ra \approx 400$ (Schubert and Straus, 1982). For Ra slightly greater than 400, instabilities within the upper and lower thermal boundary layers generate small-scale features that are advected around the cell by the large-scale convective rolls. In this moderate Ra parameter regime, $400 < Ra < 1300$, the resulting flow exhibits a series of transitions between periodic and quasi-periodic convective roll motions, as discussed in considerable detail by Kimura et al. (1986, 1987) and Graham and Steen (1992, 1994). However, the background convective rolls are not completely broken down until $Ra > 1300$. The overall dynamics are then better characterized as spatiotemporally chaotic plume shedding from the

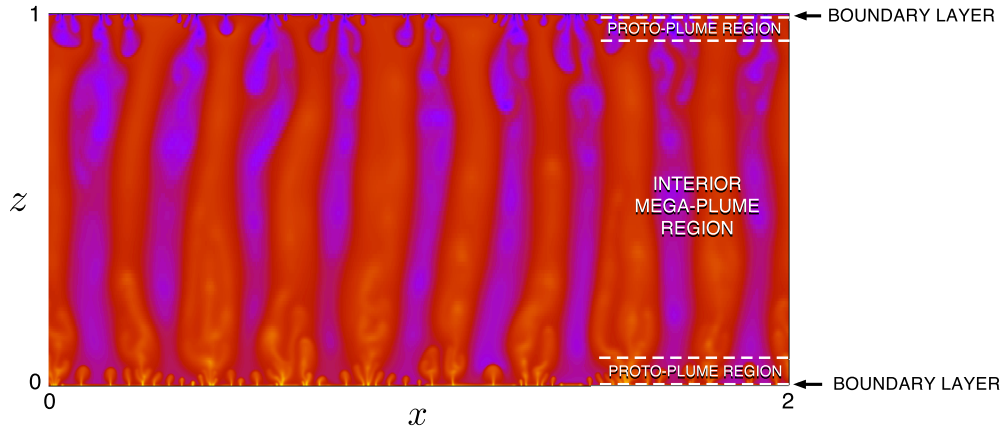

Figure 1-3: Snapshot of the temperature field from DNS at $Ra = 20000$ (Hewitt et al., 2012). Colorbar: the hot plume is in red color; the cold plume is in blue color. At large Ra, the time-mean inter-plume spacing measured from DNS is $L_m = (2\pi/0.47)Ra^{-0.4}$.

boundaries rather than quasi-coherent cellular flow (Otero et al., 2004; Hewitt et al., 2012). This marks the transition to the "turbulent" high-Ra regime.

The direct numerical simulations (DNS) of Hewitt et al. (2012) reveal that at large Ra porous medium convection exhibits a three-region asymptotic structure (see Figure 1-3): adjacent to the upper and lower walls are extremely thin thermal boundary layers, with a thickness that scales as $O(Ra^{-1})$; the interior region is dominated by a nearly vertical columnar exchange flow ("mega-plumes") spanning the height of the domain; and the transition zone between these regions, where a series of small "proto-plumes" grow from the boundaries and merge with the interior mega-plumes. Remarkably, as Ra is increased, the interior vertical columnar exchange flow becomes increasingly well organized. Hewitt et al. (2012) model this interior flow analytically using a single horizontal Fourier-mode "heat-exchanger" solution, and extract a $Ra^{-0.4}$ scaling for the time-mean inter-plume spacing L_m from their simulation data. Actually, this heat-exchanger solution is identical to the asymptotic core solution, obtained by Corson (2011) based on certain assumptions. To explore the mechanisms for

this nonlinear scale selection, in a subsequent investigation, Hewitt et al. (2013) show that the vertical columnar exchange flow is unstable for horizontal wavenumbers k greater than $k \sim Ra^{5/14}$ as $Ra \to \infty$ in evident agreement with their DNS results.

1.3 Challenges and Objectives

Although many investigations have been conducted to study the physics of porous medium convection as discussed above, there still exist many challenges in understanding the flow mechanisms and dynamics at large Ra. First, the relevance of the stability analysis in Hewitt et al. (2013) remains an open question, since it employs the analytical heat-exchanger model – in which the upper and lower boundaries are ignored – as the pertinent base flow on the grounds that k is not controlled directly by the small-scale dynamics of proto-plumes near the boundary, since these have a lateral scale of Ra^{-1}. The view of the present study is that to elucidate the mechanisms for the high-Ra lateral scale selection, it is preferable to analyze the stability of (numerically) exact solutions of the complete dynamical system (i.e. in which the base flow exactly satisfies the governing equations and all boundary conditions) that also exhibit certain flow structures observed in DNS.[1] As described above, at large Ra porous medium convection exhibits spatiotemporally chaotic dynamics. DNS show that the instantaneous flow self-organizes into recurring quasi-coherent structures, suggesting that basic physics of high-Ra porous medium convection can be understood in terms of these "building blocks" and the patterns they form. Consequently, one specific aim of this dissertation research is to quantify the periods, stability, and heat-transport properties of

[1]The term "exact" shown in "numerically exact solutions" or "numerically exact coherent states" here and throughout means the errors between the numerical and the analytical solutions are so small (e.g. of the order of machine epsilon) that the numerical solutions can be treated as the exact solutions.

the coherent structures exhibited in this spatiotemporally chaotic dynamical system. To avoid arbitrary definitions involving averages or thresholds, these structures are identified with simple *exact coherent states* (e.g. steady and time-periodic solutions) of the governing equations. Moreover, as shown in Figure 1-1, the underground saline aquifers are generally inclined at an angle to the horizontal. Nevertheless, the effects of the inclination of the layer on the flow structure and transport properties for high-Ra porous medium convection have largely been unexplored. Hence, another aim of this dissertation is to explore pattern formation in the inclined porous medium convection at large Ra and to investigate the physical mechanisms resulting in these patterns.

Secondly, a primary quantity of interest in convection is the Nusselt number Nu, the ratio of the heat transport in the presence of convective motion to the conductive heat transport in the absence of fluid motion. An open question important for reduced modeling is: *is there a smallest domain aspect ratio $L(Ra)$ above which the Nusselt number Nu becomes independent of L?* This question is loosely analogous to that of determining the "minimal flow unit" in wall-bounded shear flow turbulence, the smallest physical domain with horizontally periodic boundary conditions in which (low-dimensional) turbulence can sustain itself. In this dissertation, this question is addressed by studying the optimal upper bounds on $Nu(Ra, L)$ obtained from the rigorous "background" (sometimes called Constantin–Doering–Hopf) variational formalism (Doering and Constantin, 1998). These bounds are then compared with the DNS results provided by Dianati (2013) as a function of Ra and L.

Finally, at large values of the Rayleigh number, DNS of porous medium convection is computationally expensive. Computer simulations that resolve all dynamical flow features in kilometer-wide geological formations into which CO_2 is sequestered would require years to perform! Consequently, efficient and reliable reduced dynamical models that resolve only a

subset of the dynamics are needed. Motivated by this need, another aim of this dissertation research is to develop a reduced dynamical model of high-Ra porous medium convection.

It should be noted that the investigations of porous medium convection considered in this dissertation are restricted to 2D configurations. However, recent DNS of Rayleigh–Bénard convection in a three-dimensional (3D) porous layer at large Rayleigh number clearly exhibit the emergence of a three-region asymptotic structure, with an interior flow that is increasingly well described by an extension of the heat-exchanger model and comprised by mega-plumes whose spacing decreases approximately as $Ra^{-0.5}$ (Hewitt et al., 2014). Thus, the results of the 2D investigations in the present study may be reasonably expected to provide at least partial insight into 3D porous medium convection. In short, this dissertation research comprises investigations of three aspects of 2D porous medium convection: coherent structure, transport, and reduced dynamics.

1.4 Problem Formulation

Before performing systematic studies of porous medium convection, it is instructive to thoroughly understand the basic laws that control the dynamics of this system. In this section, the derivation of the equations governing porous medium convection is summarized, as adapted from Nield and Bejan (2006) and Bejan (2013). The limitations of and the assumptions underlying the resulting models of porous medium convection are also discussed.

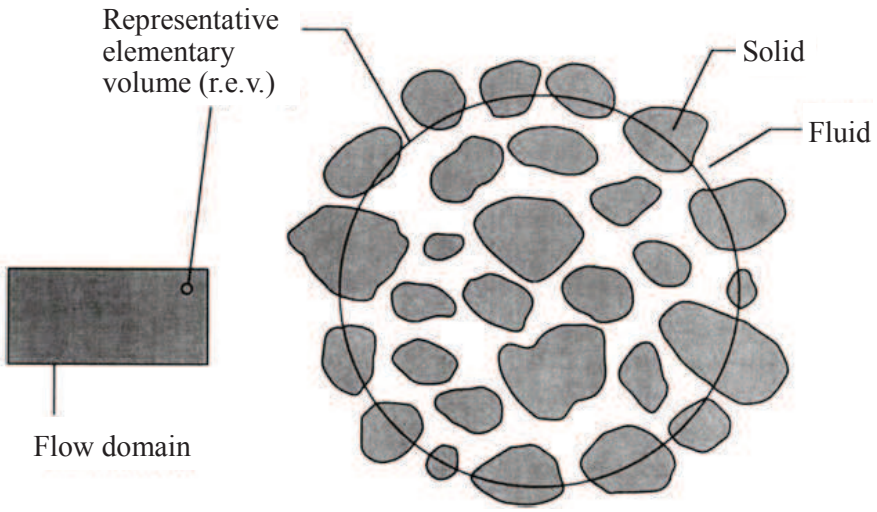

Figure 1-4: Schematic identifying the scale of a r.e.v. relative to the scales of the flow domain and the pores (Nield and Bejan, 2006).

1.4.1 Dimensional Equations

Consider thermal convection in a fluid-saturated porous medium which consists of a solid matrix with an interconnected void. Instead of studying the motions of the microscopic fluid particles, engineers and scientists generally are more interested in variations of coarse-grained properties of the porous medium. Therefore, to derive the laws governing these macroscopic variables, a spatial average is taken over a sufficiently large "representative elementary volume" (r.e.v.) which contains many pores. As shown in Figure 1-4, the r.e.v. is much larger than the pore, but considerably smaller than the entire domain; in other words, the appropriate mean quantities over each r.e.v. are studied.

Following Nield and Bejan (2006) and Bejan (2013), the conservation of mass can be expressed by the continuity equation

$$\varphi \frac{\partial \rho_f}{\partial t} + \nabla \cdot (\rho_f \mathbf{u}) = 0, \tag{1.1}$$

where $\varphi = V_f/V_m$ is the ratio of the volume V_f consisting of fluid only and the volume V_m of the medium (including both solid and fluid material) in the r.e.v., e.g. $\varphi = 1$ for pure fluid; ρ_f is the fluid density; $\mathbf{u} = u\mathbf{e}_x + v\mathbf{e}_y + w\mathbf{e}_z$ is the average of the fluid velocity over V_m ($\mathbf{e}_x$, $\mathbf{e}_y$ and $\mathbf{e}_z$ are unit vectors in the x, y and z directions, respectively); and $\nabla = \mathbf{e}_x \frac{\partial}{\partial x} + \mathbf{e}_y \frac{\partial}{\partial y} + \mathbf{e}_z \frac{\partial}{\partial z}$ is a differential operator. If the flow is incompressible, then

$$\nabla \cdot \mathbf{u} = 0. \tag{1.2}$$

The movement of fluid through a porous medium can be modeled by Darcy's law

$$\frac{\mu}{K}\mathbf{u} = -\nabla p, \tag{1.3}$$

where μ the dynamic viscosity of the fluid, K is the medium permeability with dimension $(length)^2$ ($K^{1/2}$ is a length-scale representative of the effective pore diameter), and the left-hand side term of (1.3) denotes the resistance force acting on the fluid while the right-hand side term denotes the driving force. If gravity (a body force) is considered, then (1.3) becomes

$$\frac{\mu}{K}\mathbf{u} = -\nabla p + \rho_f \mathbf{g}, \tag{1.4}$$

where $\mathbf{g} = (g_x, g_y, g_z)$ is the acceleration of gravity, and $\rho_f \mathbf{g}$ actually is a buoyancy force, as shown later. For the unsteady case, (1.4) becomes

$$\rho_f c_a \frac{\partial \mathbf{u}}{\partial t} = -\frac{\mu}{K}\mathbf{u} - \nabla p + \rho_f \mathbf{g}, \tag{1.5}$$

where c_a is a constant tensor that depends on the geometry of the porous medium. The exclusion of the inertial term $\mathbf{u}\cdot\nabla\mathbf{u}$ in (1.5) (as would appear in the Navier–Stokes equations)

is partly because for the steady case, i.e. $\frac{\partial \mathbf{u}}{\partial t} = 0$, the inclusion of the inertial term in (1.5) will make the momentum equation contradict (1.4) unless $\mathbf{u}\cdot\nabla\mathbf{u} \equiv 0$. More detailed explanations about why this term can be omitted can be found in Nield and Bejan (2006). Actually, (1.5) can be further simplified by using the Oberbeck–Boussinesq approximation:

$$\rho_0 c_a \frac{\partial \mathbf{u}}{\partial t} = -\frac{\mu}{K}\mathbf{u} - \nabla p + \rho_f \mathbf{g}, \tag{1.6}$$

$$\rho_f = \rho_0[1 - \alpha(T - T_0)], \tag{1.7}$$

where ρ_f only depends on the temperature T, ρ_0 is the density of fluid at T_0, and α is the coefficient of thermal expansion.

Assume the medium is homogeneous and isotropic, and the radiative effects, viscous dissipation, and the work done by pressure changes are negligible. Then, from the first law of thermodynamics, the energy equations for the solid and fluid phases can be expressed as

$$(1-\varphi)(\rho c)_s \frac{\partial T_s}{\partial t} = (1-\varphi)\nabla\cdot(\mathcal{K}_s \nabla T_s) + (1-\varphi)q_s''' + \mathcal{H}(T_f - T_s), \tag{1.8}$$

$$\varphi(\rho c_p)_f \frac{\partial T_f}{\partial t} + (\rho c_p)_f \mathbf{u}\cdot\nabla T_f = \varphi\nabla\cdot(\mathcal{K}_f \nabla T_f) + \varphi q_f''' + \mathcal{H}(T_s - T_f), \tag{1.9}$$

where the subscripts s and f refer to the solid and fluid phases, respectively, c is the specific heat of the solid, c_p the specific heat at constant pressure of fluid, $\mathcal{K}$ the thermal conductivity, q''' the heat production per unit volume, and $\mathcal{H}$ the heat transfer coefficient. If there is no heat production, and the solid matrix and fluid are in *local thermal equilibrium* so that $T_s = T_f = T$, then adding (1.8) and (1.9) yields

$$(\rho c)_m \frac{\partial T}{\partial t} + (\rho c_p)_f \mathbf{u}\cdot\nabla T = \nabla\cdot(\mathcal{K}_m \nabla T), \tag{1.10}$$

where

$$(\rho c)_m = (1-\varphi)(\rho c)_s + \varphi(\rho c_p)_f, \tag{1.11}$$

$$\mathcal{K}_m = (1-\varphi)\mathcal{K}_s + \varphi\mathcal{K}_f. \tag{1.12}$$

Strictly, the assumption of local thermal equilibrium is only valid when there is no exchange of heat between the fluid and solid matrix or when the heat capacity per unit volume of the fluid and solid are equal. However, these equations are formally identical to the appropriate equations governing *solutal* convection (where the temperature T is replaced with the concentration C of a solute), which is, of course, the more relevant interpretation for convective and diffusive transport of carbon dioxide in the context of sequestration and for which no-flux of solute between the fluid and solid is an appropriate idealization. Moreover, this assumption can be shown to be a reasonable approximation in many applications for which rapid thermal adjustment of the solid matrix may be expected, as is often the case for small-pore media such as fibrous insulation (Nield and Bejan, 2006; Bejan, 2013).

Since $(\rho c)_s$, $(\rho c_p)_f$, $\mathcal{K}_s$ and $\mathcal{K}_s$ are constant for homogeneous and isotropic medium, (1.10) can also be rewritten as

$$\alpha_m \frac{\partial T}{\partial t} + \mathbf{u}\cdot\nabla T = \kappa\nabla^2 T, \tag{1.13}$$

where

$$\alpha_m = \frac{(\rho c)_m}{(\rho c_p)_f}, \tag{1.14}$$

$$\kappa = \frac{\mathcal{K}_m}{(\rho c_p)_f}, \tag{1.15}$$

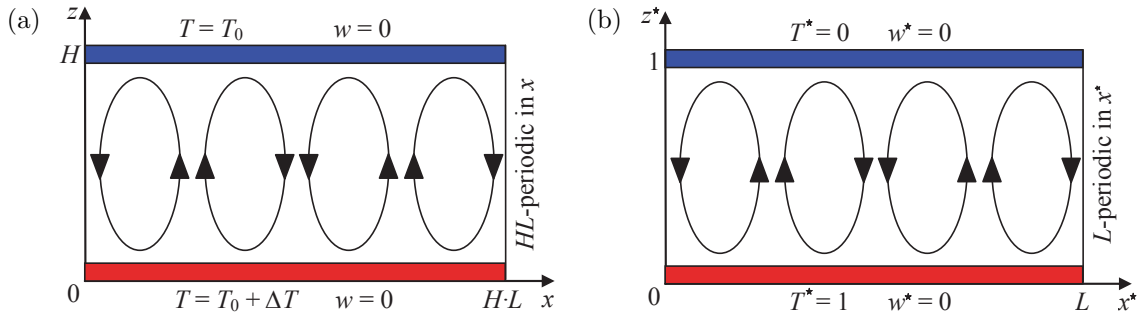

Figure 1-5: Geometry for horizontal 2D porous medium convection: (a) dimensional and (b) dimensionless porous Rayleigh–Bénard cells.

are the heat capacity ratio and the thermal diffusivity with dimension $(length^2/time)$, respectively, and ∇^2 is the Laplacian operator. In short, the equations (1.2), (1.6) and (1.13) are the so-called Darcy–Oberbeck–Boussinesq equations governing the evolution of the temperature field $T(\mathbf{x}, t)$ in porous medium convection.

1.4.2 Dimensionless Equations

In this dissertation, the classical Horton–Rogers–Lapwood problem (Nield and Bejan, 2006) is studied in a 2D porous Rayleigh–Bénard cell, as shown in Figure 1-5. Consider a fluid-saturated porous layer with layer thickness H heated from below at $z = 0$ $(T = T_0 + \triangle T)$ and cooled from above at $z = H$ $(T = T_0)$ (see Figure 1-5a). For this system, there exist two types of nondimensionalizations depending on which time scale, diffusion or convection, is chosen. In both approaches, H, $\triangle T$, $\mathcal{T}$, U and P are chosen as scales for horizontal/vertical length, temperature, time, velocity and pressure, respectively, where $\mathcal{T}$, U and P are to be determined.

First, dimensional analysis of the energy equation (1.13), namely,

$$\alpha_m \frac{\triangle T}{\mathcal{T}} \quad \sim \quad U \frac{\triangle T}{H} \quad \sim \quad \kappa \frac{\triangle T}{H^2}, \tag{1.16}$$

yields a diffusion time $\mathcal{T}_d = \alpha_m H^2/\kappa$ and a diffusion velocity $U_d = \kappa/H$. Then, the scale for pressure would be $P = \mu\kappa/K$ from dimensional analysis of the momentum equation (1.6). Therefore, the dimensional variables can be normalized as

$$\mathbf{x}^\star = \frac{\mathbf{x}}{H}, \quad T^\star = \frac{T - T_0}{\triangle T}, \quad t^\star = \frac{t}{\mathcal{T}_d}, \quad \mathbf{u}^\star = \frac{\mathbf{u}}{U_d}, \quad p^\star = \frac{p}{P}. \tag{1.17}$$

Thus, the dimensionless equations can be written as

$$\nabla^\star \cdot \mathbf{u}^\star = 0, \tag{1.18}$$

$$\gamma_a \frac{\partial \mathbf{u}^\star}{\partial t^\star} = -\mathbf{u}^\star - \nabla^\star \tilde{p}^\star + Ra T^\star \mathbf{e}_{z^\star}, \tag{1.19}$$

$$\frac{\partial T^\star}{\partial t^\star} + \mathbf{u}^\star \cdot \nabla^\star T^\star = \nabla^{\star 2} T^\star, \tag{1.20}$$

where

$$\gamma_a = \frac{c_a D_a}{\alpha_m Pr}, \quad D_a = \frac{K}{H^2}, \quad Pr = \frac{\nu}{\kappa}, \quad Ra = \frac{g\alpha K H \triangle T}{\nu\kappa} \tag{1.21}$$

are the inverse Prandtl–Darcy number, Darcy number, Prandtl number and Rayleigh number, respectively, $\nu = \mu/\rho_0$ is the kinematic viscosity of the fluid and $\tilde{p}^\star = p^\star + gKHz^\star/(\nu\kappa)$. Generally, the pore scale $K \ll H^2$, namely, $Da \ll 1$. Moreover, in many cases, $Pr \gg 1$, e.g. $Pr \sim 10^{23}$ for the Earth's mantle. Hence, the inverse Prandtl–Darcy number γ_a is exceedingly small in most applications. Finally, the dimensionless Darcy–Oberbeck–Boussinesq

equations in the infinite Prandtl–Darcy number limit can be expressed as

$$\nabla \cdot \mathbf{u} = 0, \tag{1.22}$$

$$\mathbf{u} + \nabla p = RaT\mathbf{e}_z, \tag{1.23}$$

$$\frac{\partial T}{\partial t} + \mathbf{u} \cdot \nabla T = \nabla^2 T, \tag{1.24}$$

where the tilde and stars have been dropped for brevity of notation. The dimensionless variables in the porous Rayleigh–Bénard cell satisfy the boundary conditions

$$T(x,0,t) = 1, \quad T(x,1,t) = 0, \quad w(x,0,t) = 0, \quad w(x,1,t) = 0 \tag{1.25}$$

and L-periodicity of all fields in x, as shown in Figure 1-5(b). It should be emphasized here that the Darcy's equation (1.23) requires (1) the smallest length scale of the flow is much larger than the length scale of the pore; (2) the Reynolds number Re_p of the flow, based on the length scale of the pore, is of order unity or smaller. However, given that the pore scale is small, the second requirement, $Re_p \sim O(1)$, is not in contradiction to $Ra \gg 1$. Although both (1) and (2) indicate that Darcy's equation will be invalid when Ra is sufficiently large (e.g. $Ra = \infty$), according to the analysis in Hewitt (2014), the above requirements can be satisfied at least for $Ra \lesssim 10^6$.

The second approach to nondimensionalizing the governing equations is to choose the convective time scale, as shown in Hewitt (2014). Dimensional analysis of the right-hand side terms of the momentum equation (1.6), namely,

$$\frac{\mu}{K}U \quad \sim \quad \frac{P}{H} \quad \sim \quad \rho_0 \alpha \triangle T g, \tag{1.26}$$

yields the convective velocity $U_c = K\rho_0\alpha\triangle T g/\mu$ and pressure $P = \rho_0\alpha\triangle T g H$. Then, the convective time $\mathcal{T}_c = \alpha_m H/U_c$ can be obtained from the dimensional analysis of the energy equation (1.13). Therefore, the dimensional variables can be normalized as

$$\mathbf{x}^\star = \frac{\mathbf{x}}{H}, \quad T^\star = \frac{T - T_0}{\triangle T}, \quad t^\star = \frac{t}{\mathcal{T}_c}, \quad \mathbf{u}^\star = \frac{\mathbf{u}}{U_c}, \quad p^\star = \frac{p}{P}. \tag{1.27}$$

Finally, the dimensionless continuity equation retains the same form as in (1.22); however, in the infinite Prandtl–Darcy number limit, the dimensionless momentum and energy equations are changed to

$$\mathbf{u} + \nabla p = T\mathbf{e}_z, \tag{1.28}$$

$$\frac{\partial T}{\partial t} + \mathbf{u}\cdot\nabla T = \frac{1}{Ra}\nabla^2 T, \tag{1.29}$$

respectively. Note that Ra can be also written in the form of the ratio of the diffusion to convection time scales, namely $Ra = \mathcal{T}_d/\mathcal{T}_c$.

One of the key quantities of interest in convection is the Nusselt number Nu, the ratio of the heat transport in the presence of convective motion to the conductive heat transport when $\mathbf{u} = \mathbf{0}$ in the horizontal porous layer:

$$Nu = 1 + \frac{1}{L}\left\langle \int wT dx dz \right\rangle, \tag{1.30}$$

where the angle brackets denote a long-time average; i.e. for some function f

$$\langle f \rangle = \lim_{\tilde{t}\to\infty} \frac{1}{\tilde{t}} \int_0^{\tilde{t}} f dt. \tag{1.31}$$

From the equations of motion an alternative but equivalent expression for the Nusselt number can be derived,

$$Nu = -\frac{1}{L}\left\langle \int_{z=0} \partial_z T dx \right\rangle \equiv -\langle \partial_z \overline{T}|_{z=0} \rangle = \frac{1}{L}\langle ||\nabla T||^2 \rangle, \tag{1.32}$$

where $\overline{f} = \frac{1}{L}\int_0^L f dx$ and $||f|| = (\int |f|^2 dxdz)^{1/2}$.

1.5 Layout

The reminder of this dissertation is organized as follows. To characterize the asymptotic structure of flow in 2D porous medium convection at $Ra \gg 1$, new DNS are performed up to $Ra = O(10^5)$ for long times and in wide domains (large aspect ratios) in chapter 2. The DNS confirm the remarkable tendency for the interior flow to self-organize into narrow columnar plumes at sufficiently large Ra, with more complex spatiotemporal features being confined to boundary layers near the heated and cooled walls. However, the new data indicates that the mean inter-plume spacing L_m deviates from the $Ra^{-0.4}$ scaling for $Ra > 10^4$. In particular, the interior flow can be statistically steady for a band of wavelengths at sufficiently large Ra. Moreover, the first systematic study of high-Ra inclined porous medium convection is also presented in this chapter. The DNS results reveal that when the inclination angle of the porous layer ϕ is between 0° and 25°, the flow exhibits a similar three-region structure as is manifest in the horizontal case, except that as ϕ is increased the time-mean spacing between neighboring interior mega-plumes is also substantially increased. Nevertheless, for $0^\circ \leq \phi \lesssim 20^\circ$, the Nusselt number Nu is almost unchanged. However, when $\phi > \phi_c$, where $30^\circ < \phi_c < 32^\circ$, the columnar flow structure is completely broken down: the flow transitions

to a large-scale traveling-wave convective roll state, and the heat transport is significantly reduced.

In chapter 3, the structure and stability of equilibrium solutions of the Darcy–Oberbeck–Boussinesq equations as functions of both Ra and domain aspect ratio L are investigated. These solutions take the form of steady convective states that share certain attributes of the columnar flows seen in the DNS. At large Ra, the steady flows can be broadly categorized into two distinct forms: for small L (close to the linear stability threshold) the flow in the interior can be well predicted using a heat-exchanger model given by Hewitt et al. (2012); for larger L, the convective state changes form, exhibiting a stably stratified core. Quantitative comparisons with the time-mean columnar core flow obtained from DNS show that the latter is neither an equilibrium heat-exchanger nor a stably-stratified core solution but, rather, an admixture of these steady convective states. The equilibrium solutions transport less heat than does the statistically steady turbulent flow at the same parameter values. Specifically, the Nusselt number $Nu \sim Ra$ for turbulent porous medium convection, while $Nu \sim Ra^{0.6}$ for the maximum heat-transporting steady solutions; like the unsteady flow, however, the plume spacing for these maximum heat-transporting steady states decreases as the thermal forcing is increased, approximately as $L \sim Ra^{-0.52}$ for $10^3 < Ra < 10^4$ (see also Corson (2011)). To gain insight into the development of spatiotemporally chaotic convection, the (secondary) stability of the fully nonlinear steady states to small-amplitude disturbances is investigated using a spatial Floquet analysis. At large Ra, two distinct modes of instability are found. For sufficiently small L, the fastest-growing secondary instability mode has a wall-normal structure that spans the layer. Interestingly, for larger L, secondary instability modes associated with a continuous band of horizontal scales are equally amplified. Unlike the bulk modes manifested at smaller L, these modes are strongly localized near the hot

and cold boundaries. DNS strategically initialized with a superposition of the nonlinear equilibrium solutions and small-amplitude contributions from the fastest-growing secondary instability modes suggest that the mean inter-plume spacing observed at large Ra results from an interplay between these two types of instability.

In chapter 4, the physics of pattern formation in inclined porous medium convection is elucidated using linear stability and secondary stability analyses of different steady states (the background linear basic state and the fully nonlinear convective state). Theoretical analysis indicates the inclination of the porous layer will induce a basic unicellular flow which strengthens as the inclination angle ϕ is increased from 0° to 90°. The neutral stability analysis of this base flow by Rees and Bassom (2000) predicted a critical value of the angle 31.30° above which the base unicellular flow is linearly stable in an infinitely wide 2D domain at large Ra. This critical value appears very close to the transitional angle with a value between 30° and 32° around which the convective flow in DNS exhibits distinct patterns, implying that the linear stability analysis could provide at least partial insight into the pattern formation of the flow at large Ra. Therefore, in this section, the linear stability analysis is revisited to study the distribution of the eigenspectrum for various disturbances with different wavelengthes from the onset of convection up to $Ra = 50000$. Since DNS generally exhibits a convective flow pattern with boundary layers near the upper and lower walls, the structure and stability of steady, fully nonlinear convective states are investigated at moderate and large Rayleigh number. At moderate Ra, these steady states take the form of large-scale, counter-rotating convective rolls. The results indicate that small inclination of the layer will strengthen and stabilize the counterclockwise-rotating rolls, while suppressing and destabilizing the clockwise rolls and thereby making them detach from the upper and lower walls at large angles. At high Ra, depending on the value of the aspect ratio, the steady

convective state is distorted in a different direction (either clockwise or counterclockwise), in contrast with the vertically straight steady flow in the horizontal case. Secondary stability analysis of these steady solutions indicates that there still exist two types of instability when $\phi \neq 0°$: a bulk instability and a wall instability, consistent with the previous findings for $\phi = 0°$. However, the background flow induced by the inclination of the layer intensifies the bulk instability during its subsequent nonlinear evolution, thereby favoring increased spacing between the interior plumes relative to the horizontal scenario.

Although the steady convective states contain many features of the columnar flows seen in the DNS, there are evident differences, too. For example, unlike the unsteady flow observed in DNS, the proto-plumes are absent in these steady solutions. Moreover, DNS also suggest that both the bulk instability and the wall instability are operative in the turbulent flow. Hence, it is more desirable to analyze the structure and stability of some (numerically) exact coherent solutions which contain the three-region structure including proto-plumes, as exhibited in the turbulent flow. Consequently, the structure and stability of time-periodic solutions of high-Ra porous medium convection are computed and assessed in chapter 5. By classifying the eigenfunctions emerging from a stability analysis of the steady convective states, four types of periodic-orbit solutions with different symmetries have been found. The results indicate that both the instantaneous and time-averaged mean flows of these time-periodic solutions retain the critical characteristics of the turbulent columnar flow observed in DNS. Compared with the steady states, these time-periodic states are closer to the real flow, not only in flow structure but also in terms of heat transport. Moreover, the stability analysis of these time-periodic solutions reveals that the wall and bulk instabilities coexist for an unsteady columnar flow.

One of the central challenges in porous medium convection is to determine the heat transport

enhancement factor Nu as a function of the Rayleigh number Ra and domain aspect ratio L. In chapter 6, upper bound theory is used to investigate the dependence of the Nusselt number Nu on the domain aspect ratio L at large values of the Rayleigh number Ra. A novel *two-step* algorithm in which time is introduced into the variational formulation is utilized to solve the optimization problems arising from the upper bound analysis, *without* requiring numerical continuation, enabling the best available bounds to be computed up to $Ra \approx 2.65 \times 10^4$. Mathematical analysis indicates that the only steady state to which this numerical algorithm can converge is the required global optimal of the variational problem. Moreover, using this new upper bound algorithm, the dependence of the bounds on $L(Ra)$ is explored and a minimal flow unit is identified.

As noted above, DNS show that buoyancy-driven convection in a fluid-saturated porous layer self-organizes into narrow columnar plumes at large Ra. According to the specific well-organized structure of high-Ra columnar flow, two strategies are presented in chapter 7 to reduce the degrees of freedom in numerical simulations of porous medium convection in the minimal flow unit. In the first approach, the domain is decomposed into three regions: one interior region and two near-wall regions. It will be shown that in the interior region, the high-wavenumber Fourier modes basically do not affect the flow features and heat transport. Nevertheless, to resolve chaotic small-scale convective motions within the upper and lower boundary layers, exceedingly many Chebyshev or Fourier modes are needed. In the second approach, an alternative, fully *a priori* spectral basis composed of eigenfunctions from upper bound theory is employed for reduced dynamical modeling of porous medium convection. These upper bound eigenfunctions, extracted directly from the governing equations, contain many characteristics observed in the real flow. In this dissertation research, the previous model reduction strategy developed by Chini et al. (2011) has been extended to large Ra to

efficiently represent the small-scale rolls within the thin thermal boundary layers.

Conclusions are given in chapter 8.

CHAPTER 2

DIRECT NUMERICAL SIMULATIONS

2.1 Introduction

As noted in chapter 1, DNS have been carried out by Otero et al. (2004) and Hewitt et al. (2012) to study the flow structure and transport properties of horizontal porous medium convection at large Ra (up to $Ra = 4 \times 10^4$); in particular, Hewitt et al. (2012) extract a $Ra^{-0.4}$ scaling for the mean inter-plume spacing from their DNS data. However, these DNS are generally conducted in domains with $L = 2$. In this chapter, new DNS is performed for $1900 < Ra < 10^5$ in wide domains and for long times containing more than 15 pairs of plumes for hundreds to thousands of convective time units. To characterize the structure of flow in 2D porous medium convection at large Ra, the new DNS data is analyzed statistically and compared with the previous results.

Moreover, as shown in Figure 1-1, porous medium convection in carbon sequestration generally occurs in inclined aquifers. Therefore, another primary aim of this chapter is to study the flow and transport mechanisms in inclined porous medium convection using DNS. Early experimental investigations by Bories and collaborators (Bories et al., 1972; Bories and

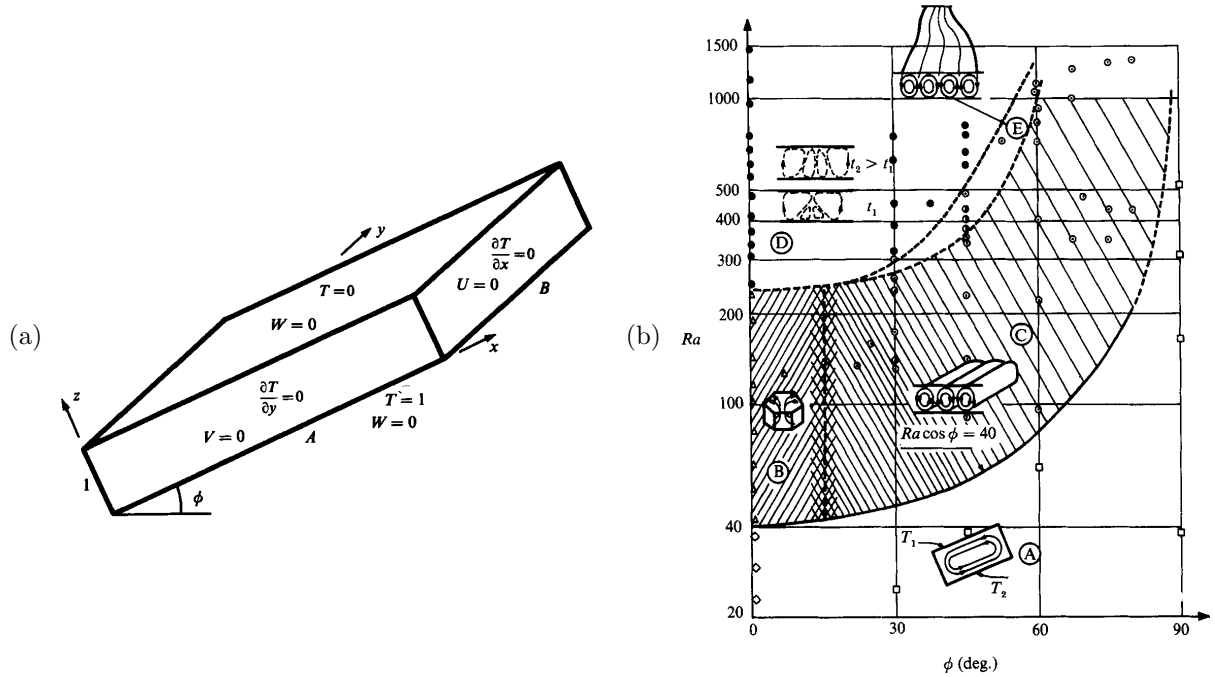

Figure 2-1: (a) Geometry and boundary conditions for a tilted porous cavity with an inclination angle ϕ, where the x axis is taken in the longitudinal direction, and the y axis in the transverse direction; (b) Different configurations of convective motion experimentally observed in a tilted porous cavity (Bories et al., 1972). Symbols in (b): Ⓐ unicellular flow; Ⓑ polyhedral cells; Ⓒ longitudinal stable coils; Ⓓ fluctuating regime; Ⓔ oscillating longitudinal coils.

Monferran, 1972; Bories and Combarnous, 1973) revealed three types of flows near the onset of convection in a sloping 3D porous layer with an inclination angle ϕ above the horizontal (see Figure 2-1a): the basic unicellular flow with an upward current near the lower (heated) wall at $z = 0$ and a downward current near the upper (cooled) wall at $z = 1$; the polyhedral cells with a vertical axis; and the longitudinal helicoidal cells resulting from the longitudinal rolls (with axes parallel to the sloping walls) superposed on the basic flow, as shown in Figure 2-1(b). Their experiments indicated that for $Ra\cos\phi \leq 4\pi^2$, only the basic unicellular flow remains; when $Ra\cos\phi$ is slightly greater than $4\pi^2$, convection appears in the form of polyhedral cells for small inclination angles ($\phi \lesssim 15°$) and longitudinal helicoidal

rolls for larger ϕ. If the influence of the side walls is ignored or in an infinitely extended layer, the unicellular flow is x- and y-independent (i.e. $k_x = 0$ and $k_y = 0$ where k_x and k_y are Fourier wavenumbers in x and y, respectively); and the longitudinal helicoidal cells are x-independent (i.e. $k_x = 0$); however, for polyhedral cells, both k_x and k_y are nonzero. In addition to these three flow configurations, there also exists another type of convective motion: y-independent transverse rolls (i.e. $k_y = 0$) observed in experiments by Caltagirone et al. (1971), Kaneko (1972) and Kaneko et al. (1974), and in numerical simulations by Caltagirone and Bories (1985).

In order to investigate the transition conditions between these different flows, a series of subsequent studies were carried out. Using linear stability analysis, Caltagirone and Bories (1985) demonstrated that in an infinitely long and wide porous layer, the basic unicellular flow is indeed stable for $Ra\cos\phi \leq 4\pi^2$, as shown in region I in Figure 2-2. Moreover, from linear stability analysis, Caltagirone and Bories (1985) also obtained a transition criteria from region II ($k_x \neq 0$, corresponding to the polyhedric cells or transverse rolls) to region III ($k_x = 0$, $k_y \neq 0$, corresponding to the helicoidal cells), namely the dash-dot line in Figure 2-2, and their analysis yielded a transition angle $\phi_t \simeq 31.8^\circ$ from II to III. Although these theoretical predictions by Caltagirone and Bories (1985) are consistent with the experimental results, their analysis did not lead to a small enough transition angle $\phi_{exp} \simeq 15^\circ$ which characterizes the change from polyhedric cells to longitudinal coils in the experiments. The preference of the polyhedral cells observed for $\phi \lesssim 15^\circ$ in experiments may result from many factors, e.g. nonlinear effects such as the variation of the viscosity and thermal diffusivity with temperature (Weber, 1975), or spatial restrictions imposed by having a finite layer in experiments (Rees and Bassom, 2000). Furthermore, in 3D numerical simulations, Caltagirone and Bories (1985) and Voss et al. (2010) confirmed the existence of transverse rolls in

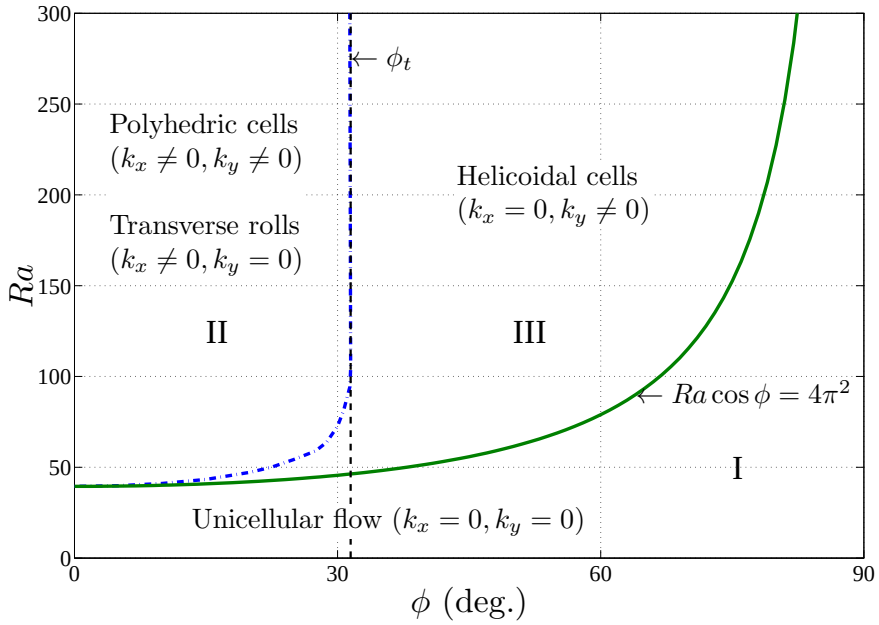

Figure 2-2: Transition criteria, predicted theoretically by Caltagirone and Bories (1985) using linear stability analysis, between different flow configurations in an infinitely extended inclined porous layer. The label for region II, "Polyhedric cells, $k_x \neq 0$ and $k_y \neq 0$", is misleading, as pointed out by Nield (2011). Since the dash-dot line in this plot is actually a criterion for the change from $k_x = 0$ to $k_x \neq 0$, and the analysis in Caltagirone and Bories (1985) does not predict whether $k_y = 0$ or not when $k_x \neq 0$, hence the transverse rolls are also possible in region II. ϕ_t is a transition angle corresponding to the change from region II to region III. At large Ra, Caltagirone and Bories (1985) showed $\phi_t \simeq 31.8°$, while the precise value is $\phi_t \simeq 31.30°$ reported by Rees and Bassom (2000).

region II and helicoidal cells in region III, although Voss et al. (2010) indicated the helicoidal cells can also exist in region II. However, it should be noted that neither Caltagirone and Bories (1985) nor Voss et al. (2010) found hexagonal cells in the inclined porous layer. In short, the mechanisms leading to the transitions between the different flow regimes have not been fully understood.

More recently, a full numerical investigation of the marginal stability of the unicellular flow was performed by Rees and Bassom (2000) in a 2D inclined porous layer. Since the transverse

(y) direction is removed, the polyhedric cells and helicoidal rolls do not exist in the 2D layer, and the basic unicellular flow will be linearly stable in both region I and region III. Hence, as shown in Rees and Bassom (2000), at *large* Ra the 2D instability can only arise when $\phi \leq 31.30°$, while the maximum inclination below which this instability may be possible is the slightly greater value of 31.49° *corresponding to* a critical Rayleigh number of 104.30. Furthermore, the onset of convective instability has also been explored extensively in inclined porous layers with an anisotropic medium (Ormond and Genthon, 1993; Trew and McKibbin, 1994; Storesletten and Tveitereid, 1999; Rees and Postelnicu, 2001; Rees et al., 2006) and different boundary conditions, e.g. constant-flux heating problems (Alex and Patil, 2000; Park et al., 2006; Barletta and Storesletten, 2011; Rees and Barletta, 2011).

As Ra is increased, the flow becomes unsteady: when $Ra\cos\phi$ exceeds about 250, for small ϕ there exists a transition to a fluctuating regime with continuous creation and disappearance of convective cells; while for large ϕ the transition is to an oscillating flow characterized by longitudinal rolls oscillating along their axis, in accord with observations by Bories and Combarnous (1973) and as shown in Figure 2-1(b). Moreover, depending on the Rayleigh number Ra, inclination angle ϕ and domain aspect ratio, multiple steady-state solutions which appear in the form of single/multiple cell convection, or "natural"/"antinatural" unicellular convection with counterclockwise/clockwise circulation, were found at small Ra in a 2D inclined porous layer (Walch and Dulieu, 1982; Caltagirone and Bories, 1985; Moya et al., 1987; Sen et al., 1987), and a numerical bifurcation study was conducted by Riley and Winters (1990) to investigate the bifurcation structure of different branches of solutions.

Although numerous studies of inclined porous medium convection have been performed, they generally focus on the onset of convection and flow patterns and transport properties at small and moderate Ra so that the dynamics in the high-Ra regime has largely been unexplored.

Therefore, in this chapter, two questions are addressed for the inclined problem: (1) *what flow structures are exhibited at large Ra and different inclination angles?* (2) *how does Nu change as a function of Ra and tilt angle ϕ?* To address these questions, the first systematic numerical study of 2D porous medium convection in an inclined porous layer is performed from $Ra = 100$ up to $Ra \simeq 10^5$. Although convection in porous media is generally 3D, under certain conditions approximately 2D flows exist both in practice and in the laboratory. Hence, the results of the 2D investigation could provide at least partial insight into the fully 3D problem. Moreover, in previous investigations, a sloping square porous cavity with two opposing isothermal walls held at different temperatures and thermally insulated lateral walls was utilized as the physical/numerical domain. In contrast, the focus of this dissertation is on infinite-Pr convection in an inclined porous layer with *L-periodic* boundary conditions in x (see Figure 2-3), as for the horizontal case in this study (see Figure 1-5*b*). It should be noted that in a 2D infinitely wide layer, for which the aspect ratio of the domain is infinite, these two systems (with thermally insulated and L-periodic boundary conditions in x, respectively) should be equivalent.

The remainder of the chapter is organized as follows. In section 2.2, the derivation of equations governing inclined porous medium convection is summarized following Nield and Bejan (2006) and the computational methodology is outlined. In section 2.3, the statistical results of horizontal porous medium convection, for which $\phi = 0°$, are presented and compared with the previous DNS. In section 2.4, the flow structure and transport properties in a 2D tilted porous layer at different Rayleigh numbers and inclination angles are analyzed. Finally, the results are summarized and discussed in section 2.5.

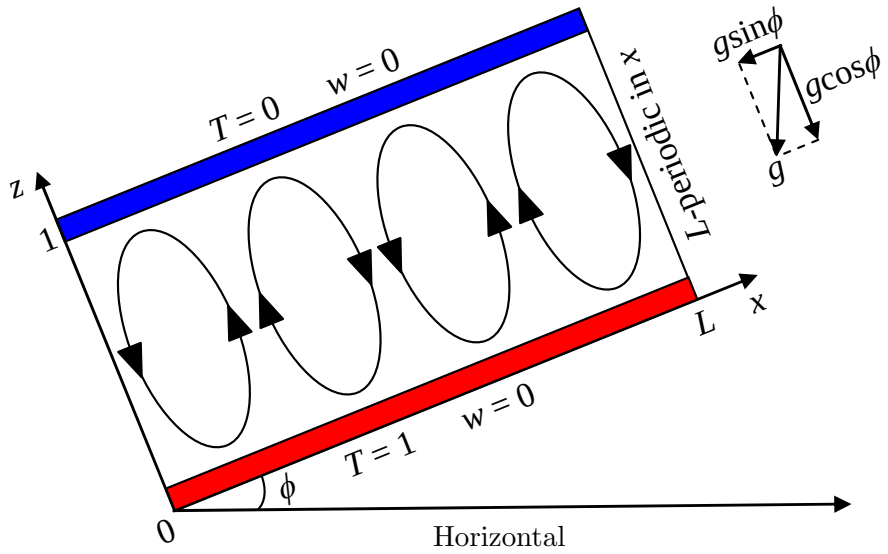

Figure 2-3: Geometry for 2D convection in the inclined dimensionless porous Rayleigh–Bénard cell.

2.2 Streamfunction/Vorticity Formulation and Computational Methodology

Consider a 2D tilted porous layer with an angle of inclination ϕ above the horizontal, as shown in Figure 2-3. For this problem, the acceleration of gravity $\mathbf{g} = -g\sin\phi\mathbf{e}_x - g\cos\phi\mathbf{e}_z$, where $g \approx 9.8m/s^2$. Then the dimensional momentum equation (1.6) becomes

$$\rho_0 c_a \frac{\partial \mathbf{u}}{\partial t} = -\frac{\mu}{K}\mathbf{u} - \nabla p - \rho_f g(\sin\phi\mathbf{e}_x + \cos\phi\mathbf{e}_z). \tag{2.1}$$

Following the first type of nondimensionalization (utilizing the diffusion time $\mathcal{T}_d = \alpha_m H^2/\kappa$) in chapter 1.4.2, one can obtain the dimensionless momentum equation for the inclined case

$$\gamma_a \frac{\partial \mathbf{u}^\star}{\partial t^\star} = -\mathbf{u}^\star - \nabla^\star \tilde{p}^\star + RaT^\star(\sin\phi\mathbf{e}_x^\star + \cos\phi\mathbf{e}_z^\star), \tag{2.2}$$

where $\tilde{p}^\star = p^\star + gKH/(\nu\kappa)(\sin\phi x^\star + \cos\phi z^\star)$. In infinite Prandtl–Darcy number limit,

$$\mathbf{u} + \nabla p = RaT(\sin\phi \mathbf{e}_x + \cos\phi \mathbf{e}_z), \tag{2.3}$$

where the tilde and stars have been dropped for brevity of notation. It can be seen that (2.3) is exactly equivalent to (1.23) when $\phi = 0°$. The continuity equation (1.22) and energy equation (1.24) are unchanged for the inclined convection problem.

By taking the curl of (2.3), one can obtain the vorticity equation

$$\Omega = -Ra(\partial_z T \sin\phi - \partial_x T \cos\phi), \tag{2.4}$$

where the scalar vorticity $\Omega = \partial_x w - \partial_z u$. To solve these governing equations numerically, it is convenient to first introduce a stream function ψ to describe the fluid velocity, so that $(u, w) = (\partial_z\psi, -\partial_x\psi)$. Then the dimensionless equations (2.4) and (1.24) can be written as

$$\nabla^2\psi = Ra(\partial_z T \sin\phi - \partial_x T \cos\phi), \tag{2.5}$$

$$\partial_t\theta + \partial_z\psi\partial_x\theta - \partial_x\psi\partial_z\theta = -\partial_x\psi + \nabla^2\theta, \tag{2.6}$$

where $\theta(x, z, t) = T(x, z, t) - (1 - z)$, and θ and ψ satisfy L-periodic boundary conditions in x and homogeneous Dirichlet boundary conditions in z. Actually, there exists a basic unidirectional (wall-parallel) shear flow solution for this system: $T = 1-z$, $\mathbf{u} = Ra\sin\phi(\frac{1}{2}-z)\mathbf{e}_x$ (or $\psi = Ra\sin\phi(z - z^2)/2$) and $p = \frac{1}{2}Ra\sin\phi x + Ra\cos\phi(z - \frac{1}{2}z^2)$, which is consistent with the conduction state for horizontal porous medium convection when $\phi = 0°$: $T = 1 - z$, $\mathbf{u} = 0$ (or $\psi = 0$) and $p = Ra(z - \frac{1}{2}z^2)$. Note that this base flow corresponds to the infinite aspect-ratio limit of the steady unicellular base state that exists in inclined porous medium

convection in a finite domain.

For the horizontal and inclined cases, the unsteady system (2.5)–(2.6) is solved numerically using a Fourier–Chebyshev-tau pseudospectral algorithm. For temporal discretization, a two-step second-order-accurate semi-implicit Adams–Bashforth/Crank–Nicolson (AB/CN) scheme is employed for the horizontal case; while, for the inclined case, a third-order-accurate semi-implicit Runge–Kutta (RK3) scheme is utilized for computations of the first three steps, and then a four-step fourth-order-accurate semi-implicit Adams–Bashforth/Backward–Differentiation (AB/BDI4) scheme is used for computation of the remaining steps. Further details regarding the numerical algorithms can be found in appendix A.

2.3 Convection in a Horizontal Porous Layer

As Ra is increased, the previous DNS by Otero et al. (2004) and Hewitt et al. (2012) indicate that the interior flow becomes *more* organized and is dominated by persistent vertical columnar flow across the domain, driven by the chaotic mixing of small proto-plumes at the upper and lower boundaries. This interior flow is modeled by Hewitt et al. (2012) using the analytical heat-exchanger solution

$$T(x,z) = \hat{T}\cos(kx) - \tfrac{k^2}{Ra}z + \left(\tfrac{k^2}{2Ra} + \tfrac{1}{2}\right), \tag{2.7}$$

$$w(x) = Ra\,\hat{T}\cos(kx), \tag{2.8}$$

$$u = 0, \tag{2.9}$$

in which the vertical advection of a linearly-varying (interior) mean temperature field $\overline{T}$ balances horizontal diffusion of temperature anomalies (with Fourier amplitude $\hat{T}$, which must

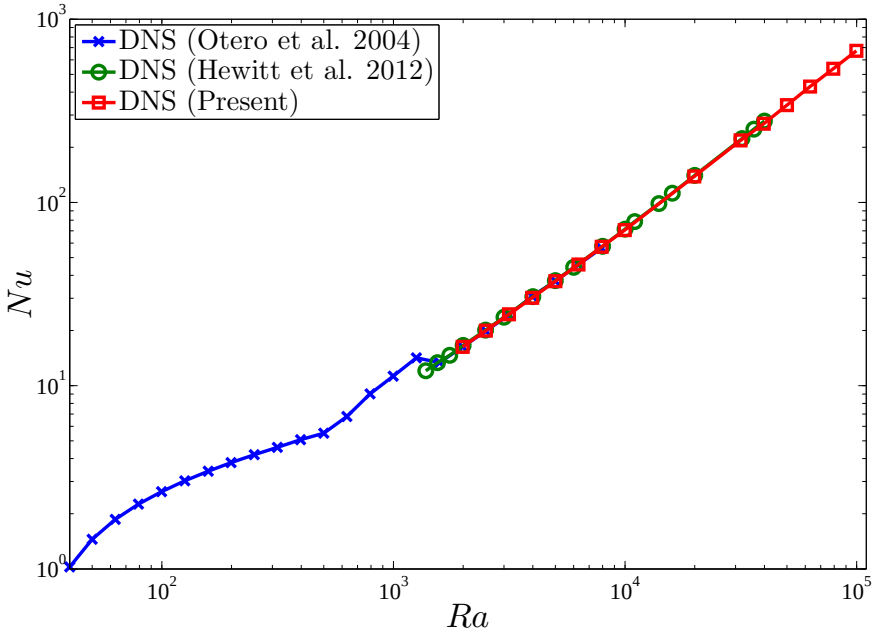

Figure 2-4: Nu vs. Ra for horizontal porous medium convection. Both the present and previous DNS predict $Nu \sim 0.0068Ra$ in the high-Ra regime.

be determined) between neighbouring mega-plumes. Although the analytical heat-exchanger solution exactly satisfies the governing equations and horizontal boundary conditions, it does *not* satisfy the vertical boundary conditions. In this section, the time-averaged asymptotic structure of the columnar flow is investigated at larger Ra – *via* new DNS – up to $O(10^5)$. The solver was thoroughly validated and gives Nu values quantitatively matching those of previous DNS, as shown in Figure 2-4.

Figure 2-5 shows the structure of the time-averaged flow observed in DNS at $Ra = 50000$. Clearly, at the given parameter values, there exist 17 very well organized columnar flows, each consisting of a single rising and descending mega-plume. Near the heated and cooled walls, the thermal boundary layers are extremely thin; in the interior, the mean temperature profile is roughly linear in z and *seems* to be well approximated by the heat-exchanger model

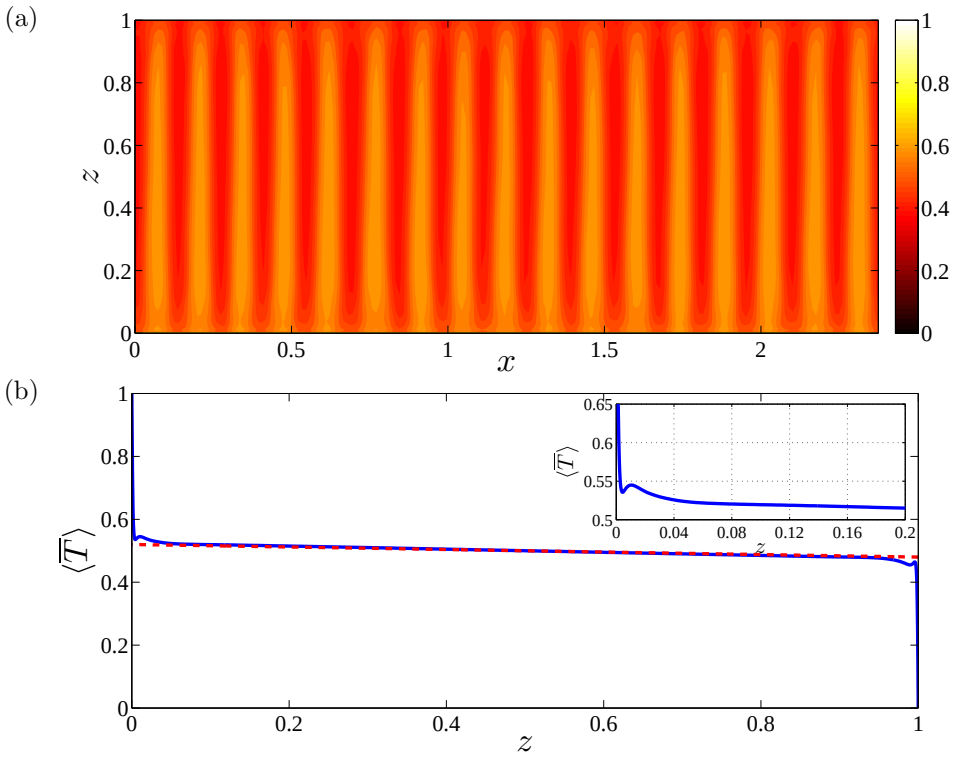

Figure 2-5: Time average of (a) T and (b) $\overline{T}$ for $Ra = 50000$ and $L = 2.39$. The averaging is taken over 200 convective time units. In (a), there exist 17 vertical columnar flows. In (b), the inset shows a magnification of the region near the lower wall and the dashed line denotes the horizontal mean temperature of the corresponding heat-exchanger solution with $k = 2\pi/(2.39/17) \approx 44.7$.

(see Figure 2-5*b*). Figure 2-6 shows snapshots of the temperature fields and corresponding long-time-averaged magnitudes of the (complex) Fourier amplitudes of the temperature fluctuations (i.e. deviations from the horizontal mean) as functions of z from the DNS at $Ra = 50000$ conducted in two different domains. As evident in Figure 2-6(a), 17 pairs of turbulent columnar plumes with three-region structure are well organized. The time-averaged amplitudes of the temperature fluctuations, $\langle|\hat{\theta}_n|\rangle$, in Figure 2-6($c$) reveal that the interior flow is a composite of a few low-wavenumber Fourier modes but dominated by one mode. Furthermore, at high wavenumber, the Fourier amplitudes $\hat{\theta}_n$ are strongly localized near the

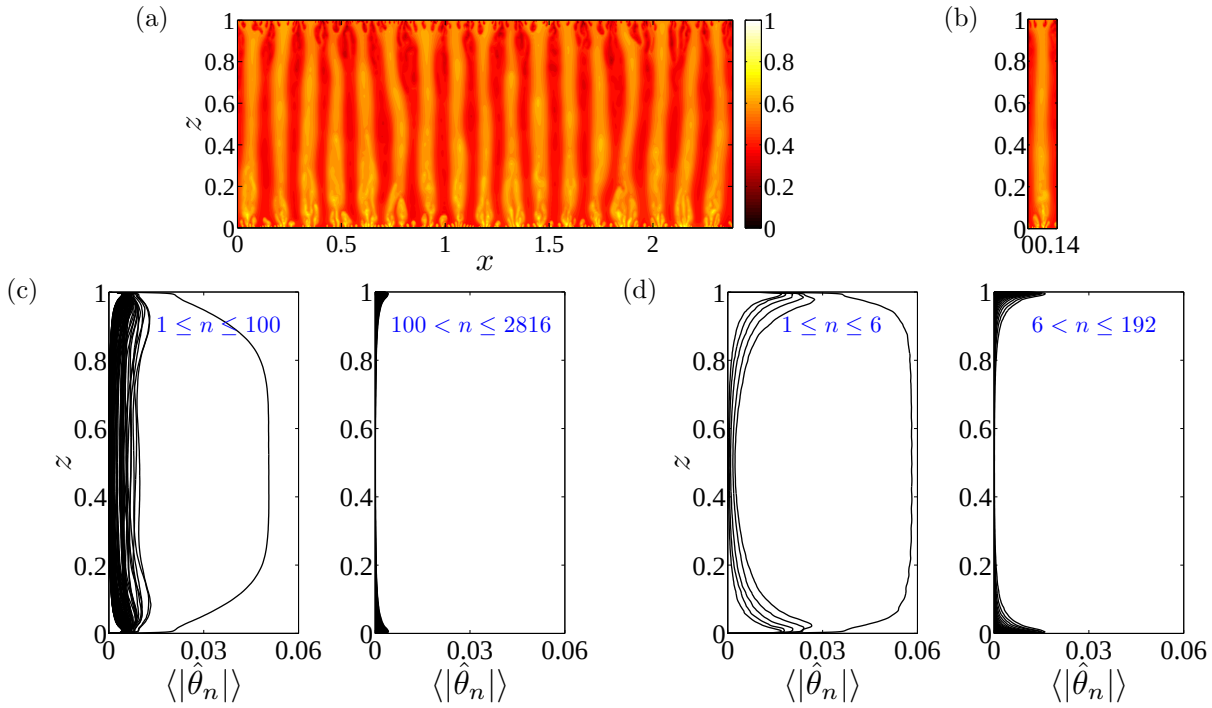

Figure 2-6: Snapshots of the temperature fields (a,b) and corresponding time-averaged Fourier amplitudes (c,d) of the temperature fluctuations (i.e. deviations from the horizontal mean) from DNS at $Ra = 50000$. In (a,c) $L = 2.39$, while in (b,d) $L = 2.39/17$.

upper and lower walls, where they superpose to comprise the small rolls and proto-plumes within the thermal and vorticity boundary layers. Figure 2-6(b) and (d) show corresponding results for DNS performed in a narrower domain, confirming that the flow has a structure similar to that in the larger domain. In particular, the time-averaged interior flow is well represented by only 6 Fourier modes.

As shown above in Figure 2-5(b), at large Ra, the slopes of interior mean temperature profiles measured from DNS and predicted by the heat-exchanger model are very small and seem to agree very well. However, Figure 2-7(a) shows that, upon closer inspection, there are clear discrepancies. Although both the DNS and the heat-exchanger model indicate that

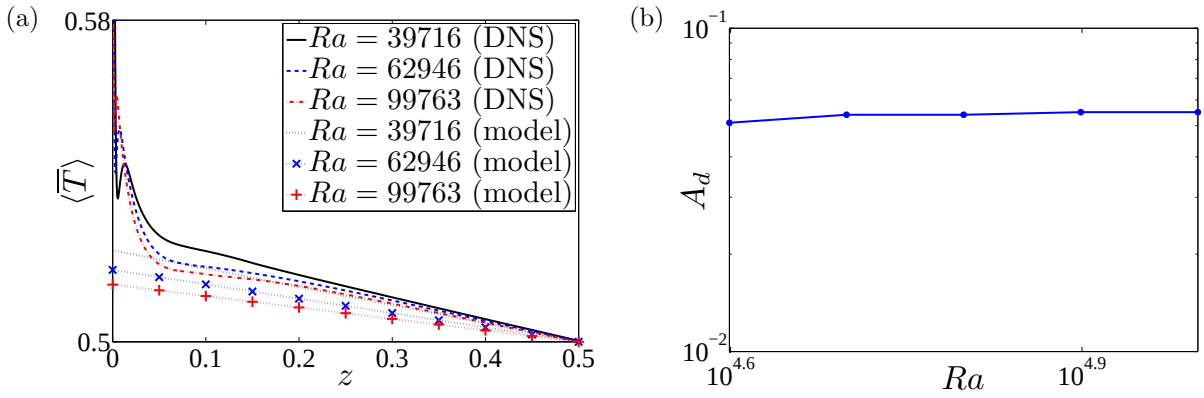

Figure 2-7: Statistical structure of turbulent convection obtained from DNS. (*a*) Comparison of the long time- and horizontally-averaged temperature profile $\langle\overline{T}\rangle$ from DNS with $\overline{T}$ from the analytical heat-exchanger model. (*b*) Time-averaged amplitude A_d of the dominant Fourier mode (after subtraction of the horizontal mean) at $z = 0.5$. For each Ra, DNS were performed in a domain with $L = 10L_f$ so that 17 columnar flows were captured, where L_f is wavelength of the fastest growing linear mode as defined in chapter 3. In (a), only half of the mean temperature profile (i.e. for $0 \leq z \leq 0.5$) is plotted owing to statistical anti-symmetry about the mid-plane.

the interior slope of the time- and horizontal-mean temperature field is negative, implying the core is unstably stratified (colder fluid overlies hotter fluid in the interior), the interior slope of $\langle\overline{T}\rangle$ is not well predicted by the heat-exchanger solution: compared with the slope of $\overline{T}$ for the heat-exchanger solution, the mean temperature gradient from the DNS is more negative. On the other hand, Figure 2-7 does suggest that the mean temperature gradient approaches zero as Ra is increased and that the mean amplitude of the dominant Fourier mode in the interior is almost independent of Ra at large Ra (Figure 2-7*b*), consistent with the measurements in Hewitt et al. (2012) and the form of the heat-exchanger solution. In short, the statistical structure of the turbulent columnar flow at large Ra resembles the heat-exchanger solution in the interior, but with a modified mean temperature gradient and more than one Fourier mode to adequately represent the fluctuations.

The mean inter-plume spacing L_m measured from the present DNS up to $Ra \approx 10^5$ in wide

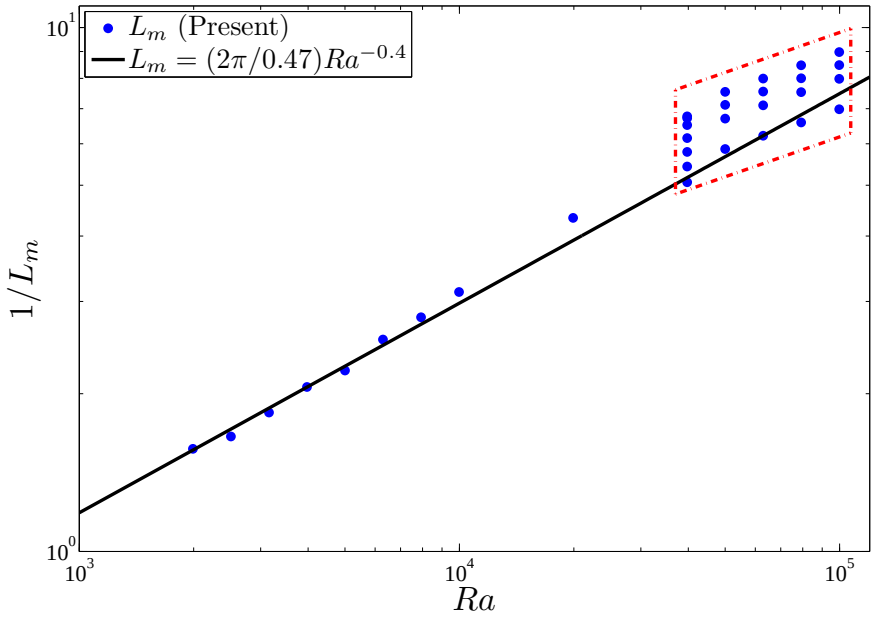

Figure 2-8: Variation of mean inter-plume spacing with Ra. The points have been computed from the DNS reported here; the solid line marks the fitted mean inter-plume spacing measured from the DNS of Hewitt et al. (2012). The DNS performed in this study were carried out in a domain with aspect ratio $L = 10L_f$ for $39716 \leq Ra \leq 99763$; a domain with $L = 11L_f$ was also used for $Ra = 39716$. For $Ra \leq 19905$, the dominant interior horizontal mode varies (in time) within a small range so that L_m can be determined by taking a long-time average of the inter-plume spacing. However, for $Ra \geq 39716$, the interior flow becomes very well-organized and (apparently) can be statistically steady for a band of wavelengths (the dashed-dot box).

domains and with long averaging times is plotted in Figure 2-8. It is seen that the new data agree very well with the previous results only for $Ra < 10000$. Interestingly, for $Ra \geq 39716$, the interior flow becomes very well organized and appears to be metastable within a band of wavelengths. For instance, at $Ra = 50000$, given different initial conditions, there can exist 14, 16, 17 or 18 plumes in a domain with $L = 10L_f$ (see the definition of L_f in chapter 3). These numerical experiments suggest that extremely long averaging times and very wide domains are required to firmly establish the nonlinear scale selection manifested in turbulent

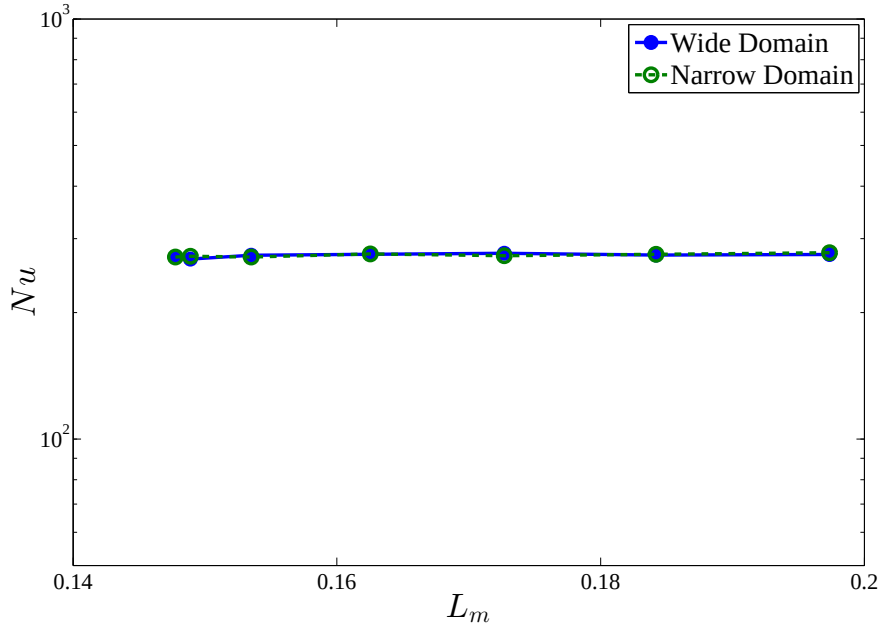

Figure 2-9: Variation of Nusselt number Nu for flows with different L_m at $Ra = 39716$. In wide domains, the same L as in Figure 2-8 is utilized in DNS; in narrow domains, there exists only one pair of turbulent columnar plumes, namely $L = L_m$. It should be noted that in wide domains, the heat transport is nearly independent of L_m; in narrow domains, the same amount of heat is transported as in wide domains and the Nusselt number is almost independent of the domain aspect ratio when L is large enough.

porous medium convection.[1] In particular, the new data arguably could be fit by scaling relations of the form $L_m \sim Ra^{\alpha}$ with $\alpha \neq -0.4$, the exponent proposed by Hewitt et al. (2012). Although L_m is not unique at sufficiently large Ra, DNS reveal that the variation of the mean inter-plume spacing in wide domains almost does not affect the value of Nusselt number Nu, as shown in Figure 2-9. Moreover, it is also shown that in narrow domains, where there exists only one pair of columnar plumes, the turbulent flow transports nearly the same amount of heat, as is manifest in the wide domains, which is independent of the

[1]From the stability analysis of the steady convective states in chapter 3, there exists a small-growth-rate and long-wavelength bulk instability mode which requires the simulations to be performed for long times and in wide domains.

aspect ratio as long as L is large enough.

2.4 Convection in an Inclined Porous Layer

In order to study the flow structure and transport for convection in an inclined porous layer, DNS are performed in this section from the onset of convection up to $Ra \approx 10^5$ for different angles of inclination ($\phi = 1$, 5, 10, 25, 30, and 35 degrees). At each Ra, the final state from a simulation at a smaller ϕ is utilized as an initial condition for a simulation at a larger one. As described above, there exists a simple solution for inclined porous medium convection: $T = 1 - z$, $\mathbf{u} = Ra \sin\phi(\frac{1}{2} - z)\mathbf{e}_x$ and $p = \frac{1}{2}Ra \sin\phi x + Ra\cos\phi(z - \frac{1}{2}z^2)$. In a 2D domain and as shown in Figure 2-2, this solution is indeed stable in region I ($Ra\cos\phi \leq 4\pi^2$) and linearly stable in region III. From III to II, this basic solution becomes linearly unstable and the system undergoes a bifurcation along the boundary between III and II, namely the dash-dot line in Figure 2-2.

At small Ra (just above the onset of convection), the flow exhibits steady stable $O(1)$ aspect-ratio large-scale convective rolls when the layer is inclined. As shown in Figures 2-10 and 2-11, for $Ra = 100$ and $L = 2$ there exist two steady cells corresponding to counter-rotating convective rolls: the counterclockwise circulation with positive ψ and the clockwise circulation with negative ψ, hereafter referred to as natural and antinatural convective rolls, respectively. For the horizontal case ($\phi = 0°$), the steady flow has a centro-reflection symmetry (see Figure 2-10*a*). However, the reflection symmetry in x no longer exists for the inclined case ($0° < \phi < 90°$), although the centrosymmetry is retained (see Figure 2-10*b*-*f*). Note that the inclination of the layer modifies the boundary layer thickness of the velocity field for the natural and antinatural rolls: the former becomes thinner while the latter becomes

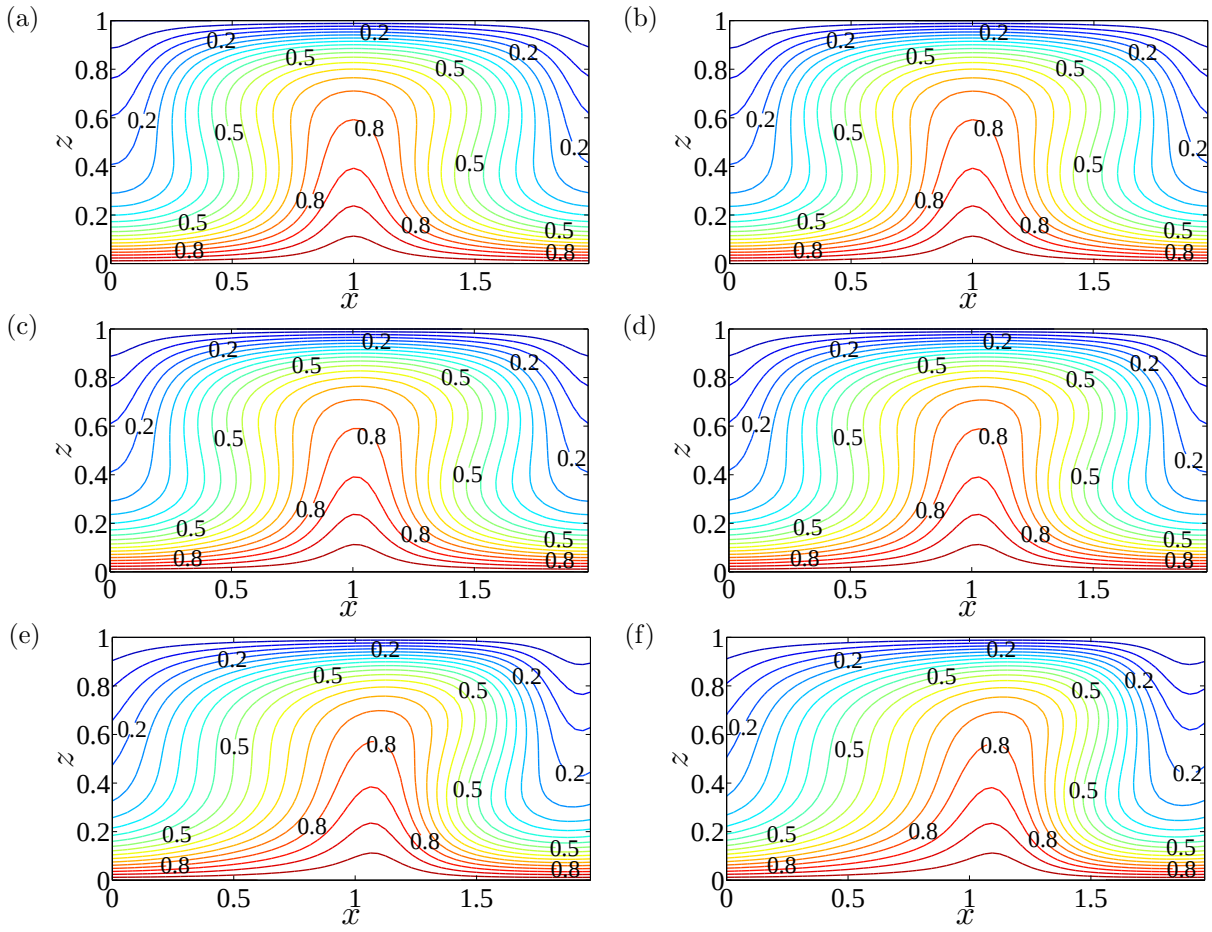

Figure 2-10: Snapshots of isotherms from DNS at $Ra = 100$ and $L = 2$. $\phi = 0$ (a), 1 (b), 5 (c), 10 (d), 25 (e), and 30 (f) degrees. The flow takes the form of stable and steady convective rolls at different ϕ.

thicker (see Figure 2-11). Furthermore, it is seen from Table 2-1 that the ψ extremum value of the natural roll becomes larger as ϕ is increased, in contrast to that of the antinatural roll, implying that compared with antinatural convective motion, the natural convective motion becomes more vigorous when the layer is inclined. This may be understood in following way: since the basic counterclockwise unicellular flow arises when $0° < \phi < 90°$, it enhances fluid motions with the same sense of rotation and suppresses motions rotating in the opposite sense.

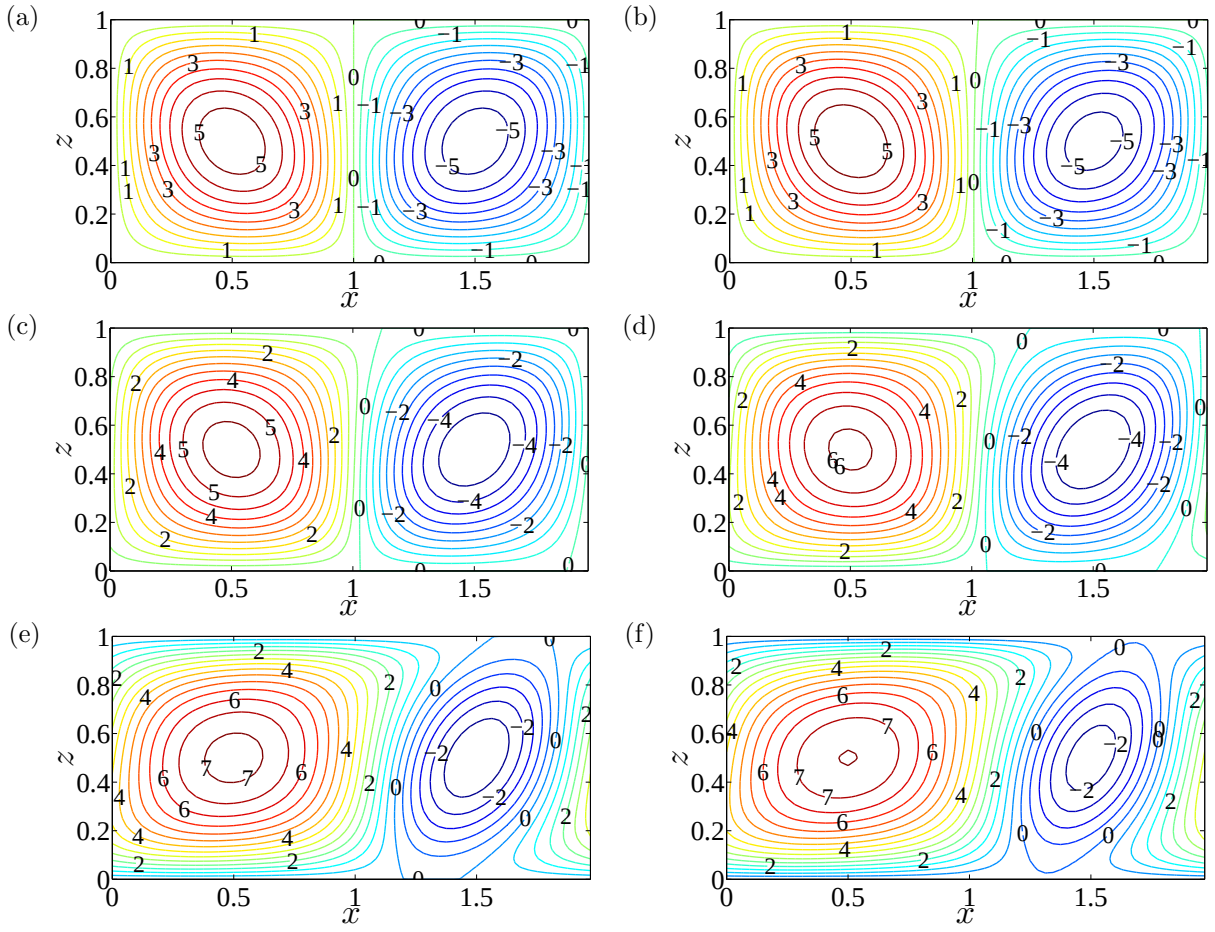

Figure 2-11: Snapshots of streamlines from DNS at $Ra = 100$ and $L = 2$. $\phi = 0$ (a), 1 (b), 5 (c), 10 (d), 25 (e), and 30 (f) degrees. These streamlines correspond to the flows in Figure 2-10. Positive ψ stands for counterclockwise circulation (natural roll) and negative ψ for clockwise circulation (antinatural roll).

Cell \ ϕ	0°	1°	5°	10°	25°	30°
Natural	5.37	5.45	5.76	6.14	7.19	7.52
Antinatural	5.37	5.28	4.96	4.52	2.98	2.31

Table 2-1: Magnitude of the ψ extremum values for natural and antinatural rolls at $Ra = 100$ for different ϕ. These ψ extremum values correspond to the flows in Figures 2-10 and 2-11.

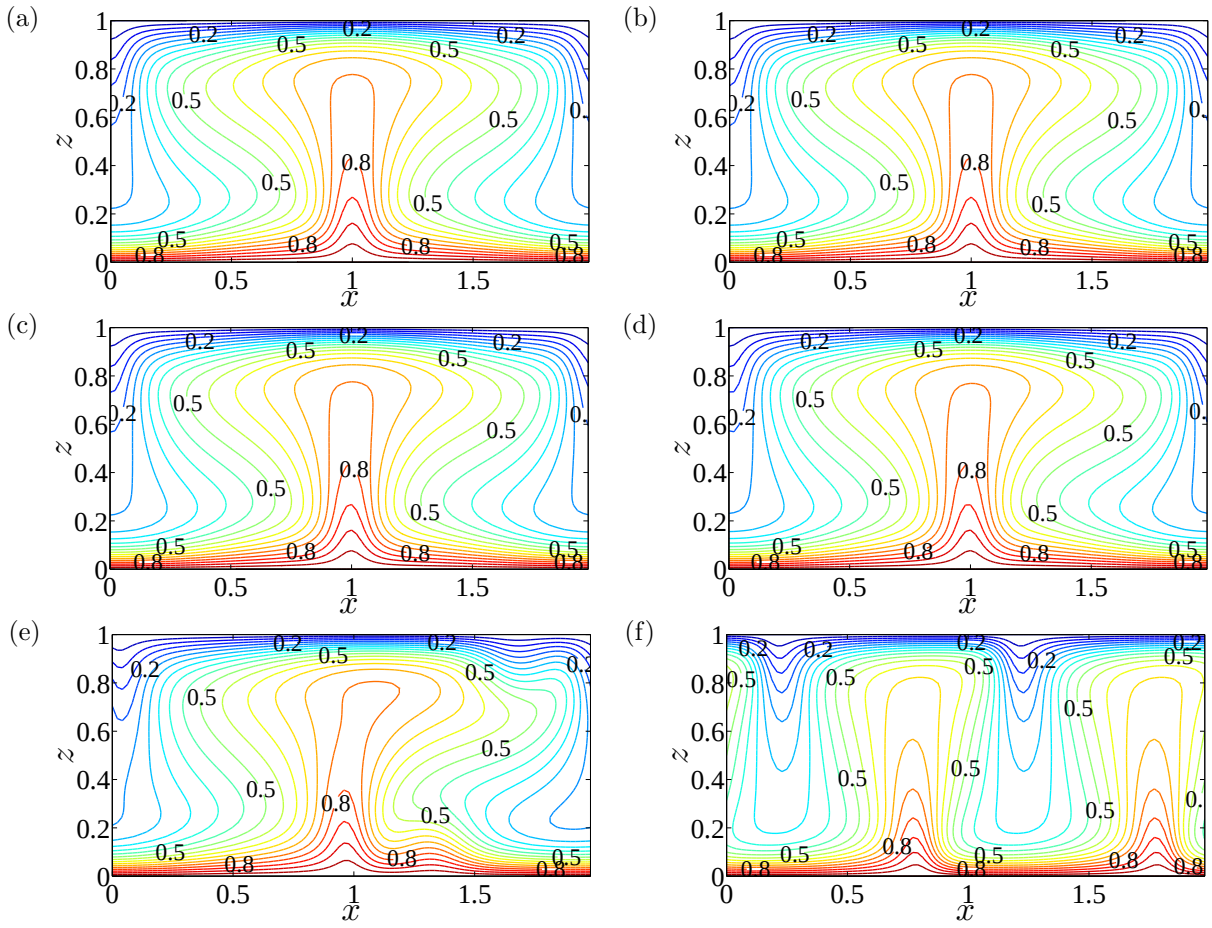

Figure 2-12: Snapshots of isotherms from DNS at $Ra = 300$ and $L = 2$. $\phi = 0$ (a), 1 (b), 5 (c), 10 (d), 17.5 (e), and 25 (f) degrees. In this case, the flows in (a)–(c) and (f) are steady; in (d) and (e), the boundary layers of the antinatural rolls become unstable.

As for horizontal convection, the steady rolls strengthen but remain stable as Ra is increased up to 200. At $Ra = 300$, however, the antinatural roll becomes unstable first for $\phi \gtrsim 10°$ (while the natural roll remains stable) and some small-scale proto-plumes are generated from the upper and lower thermal boundary layers and advected around the cell by the background roll (see Figures 2-12e and 2-13e). Moreover, this boundary layer instability becomes much stronger as the inclination angle is increased so that the two-cell unsteady convective rolls

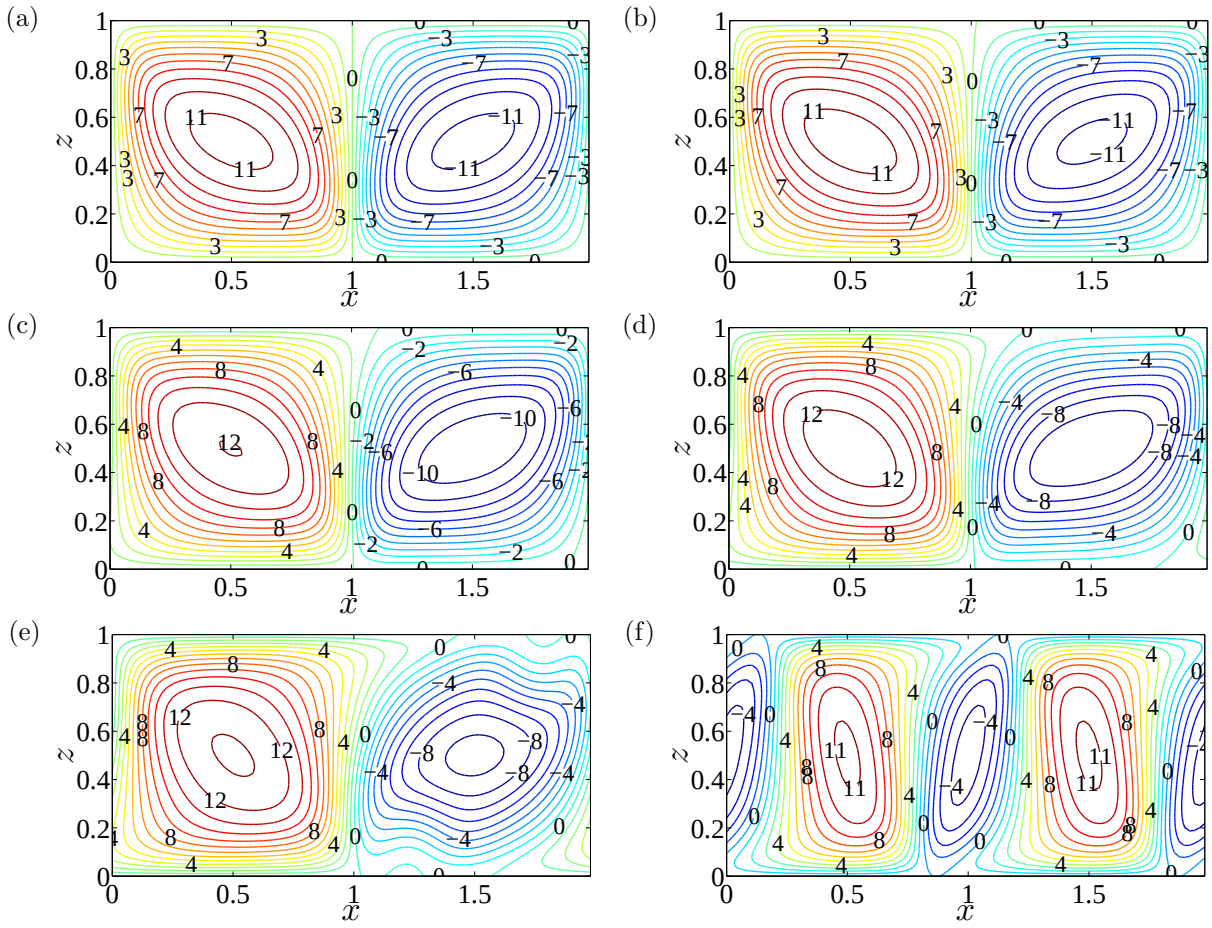

Figure 2-13: Snapshots of streamlines from DNS at $Ra = 300$ and $L = 2$. $\phi = 0$ (a), 1 (b), 5 (c), 10 (d), 17.5 (e), and 25 (f) degrees. These streamlines correspond to the flows in Figure 2-12.

are split into four-cell stable steady convective rolls at $\phi = 25°$, as shown in Figures 2-12(f) and 2-13(f).

For $Ra \gtrsim 400$, the steady convective rolls become unstable even at small ϕ, and the resulting flow exhibits a series of transitions between periodic and quasi-periodic roll motions (see Figure 2-14), as observed in the horizontal case. However, one significant difference between inclined and horizontal porous medium convection is that the inclination of the layer changes the symmetry of the flow, namely, it intensifies the near-wall instability of the antinatural

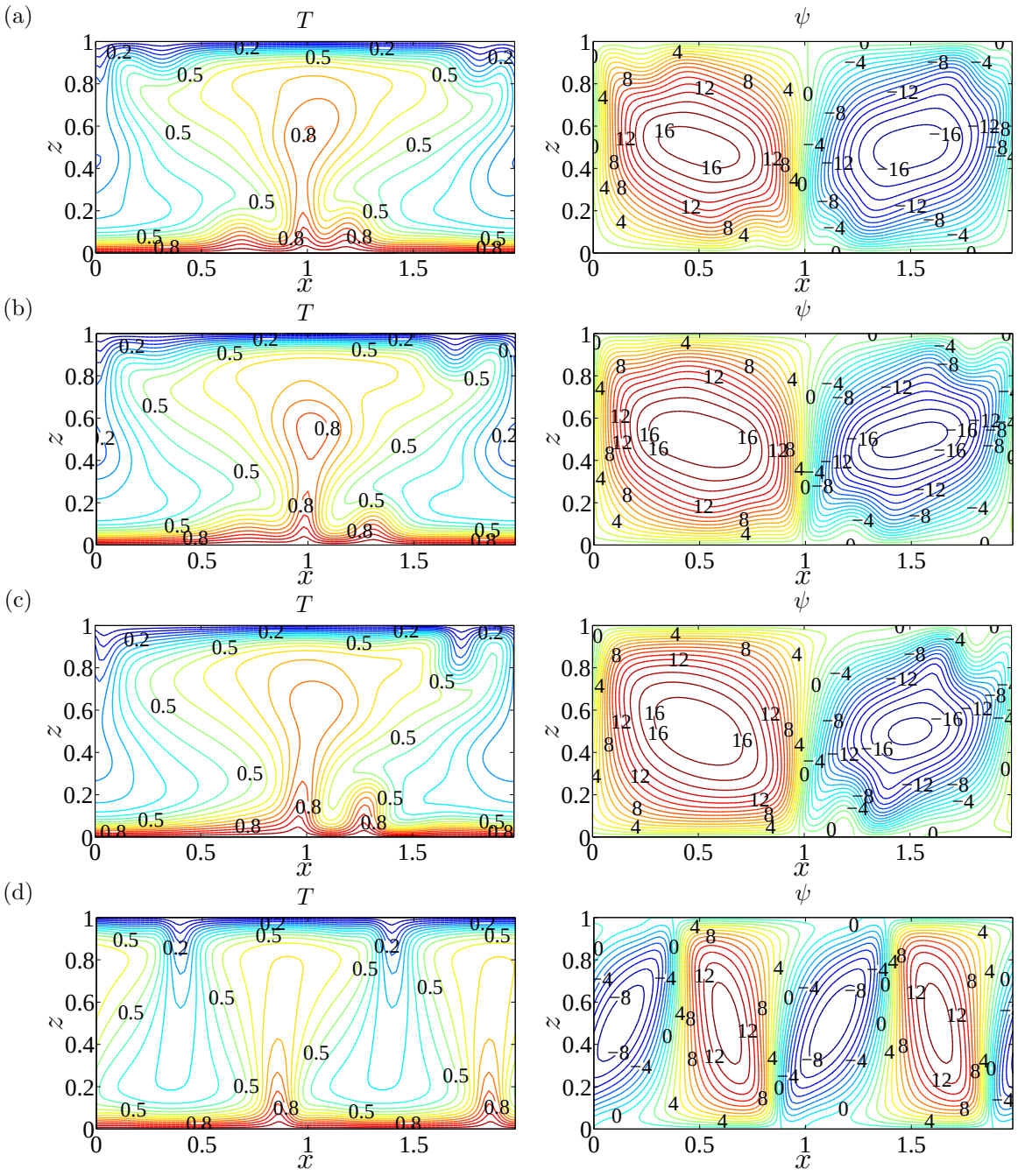

Figure 2-14: Snapshots of isotherms (left) and corresponding streamlines (right) from DNS at $Ra = 500$ and $L = 2$. $\phi = 0$ (a), 5 (b), 10 (c), and 15 (d) degrees.

Ra	300	500	792	998
ϕ	25°	15°	10°	5°

Table 2-2: Approximate angle ϕ at which flow transitions from two-cell convection to four-cell convection in DNS at moderate Ra.

roll by increasing its velocity boundary-layer thickness while stabilizing the natural roll by decreasing its velocity boundary-layer thickness. And as ϕ is increased, the boundary-layer instability of the antinatural roll becomes more vigorous so that the plumes generated from the thermal boundary layers split the original two-cell (one natural and one antinatural) convection into multiple-cell convection, as shown in Figure 2-14. It should be noted that as Ra is increased, the value of ϕ at which the flow transitions from two-cell convection to four-cell convection decreases, as shown in Table 2-2.

In Caltagirone and Bories (1985) and Moya et al. (1987), the 2D numerical simulations revealed that the system exhibits the basic unicellular flow at large ϕ in wide domains (e.g. $L = 10$). Certainly, this base flow is linearly stable for $\phi > \phi_t$ with $\phi_t \approx 31.30°$ (Rees and Bassom, 2000). However, it may become unstable when the amplitude of disturbance is large enough since the base flow may not be energy stable. Figure 2-15 shows the snapshots of isotherms from DNS at $\phi = 35°$ and $L = 10$ for different Rayleigh number. Interestingly, given different initial conditions, the convective flow can take different forms. For instance, at $Ra = 100$, the flow can exhibit a stable localized two-cell convective structure (see Figure 2-15*a*); however, it can also exist as 5 replicas of a stable two-cell convective state obtained from $L = 2$ (see Figure 2-15*b*). In this study, the flow structure for $\phi > \phi_t$ at small and moderate Ra will not be discussed in detail.

When $Ra > 1300$, the convection exhibits spatiotemporally chaotic dynamics in a horizontal

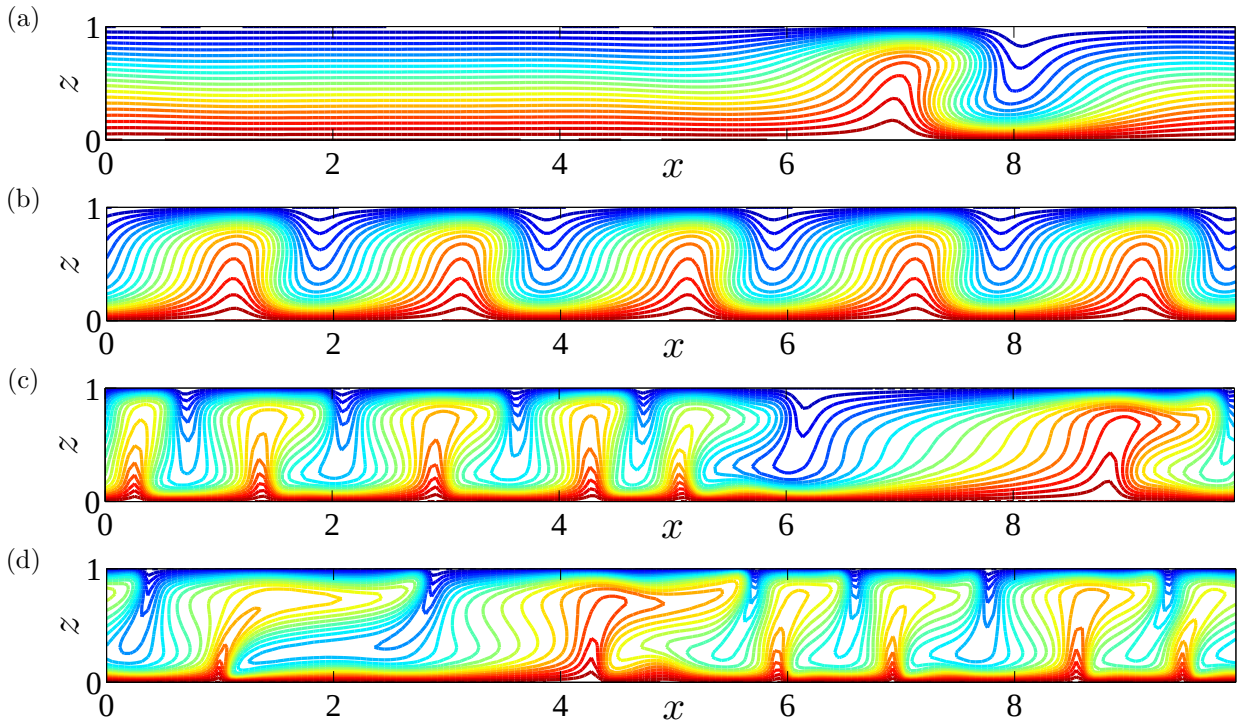

Figure 2-15: Snapshots of isotherms from DNS at $\phi = 35°$ and $L = 10$. $Ra =$ 100 (a) and (b), 300 (c), and 500 (d). (a) and (b) are obtained using different initial conditions. Although the basic unicellular flow is linearly stable for $\phi > \phi_t$ in 2D, other types of convection are still possible by initializing with sufficiently large-amplitude disturbances.

porous layer. In the following sections, the flow structure and transport properties at large Ra in an inclined porous layer will be discussed. Figure 2-16 shows snapshots of the temperature fields at $Ra = 1991$ for different inclination angles. For $0° < \phi \lesssim 25°$, the flow still retains the three-region columnar structure as is manifest in the horizontal case: spatiotemporally chaotic plumes generated from the boundary layers are continually swept into and thus merge with the mega-plumes. For $\phi \gtrsim 25°$, however, the thermal plumes and, hence, the overall flow begin to have a clear inclination toward the direction of buoyancy or the opposite direction of gravity. Moreover, since the counterclockwise circulation of the background base flow, which becomes more vigorous as ϕ is increased, intensifies the motions of the natural

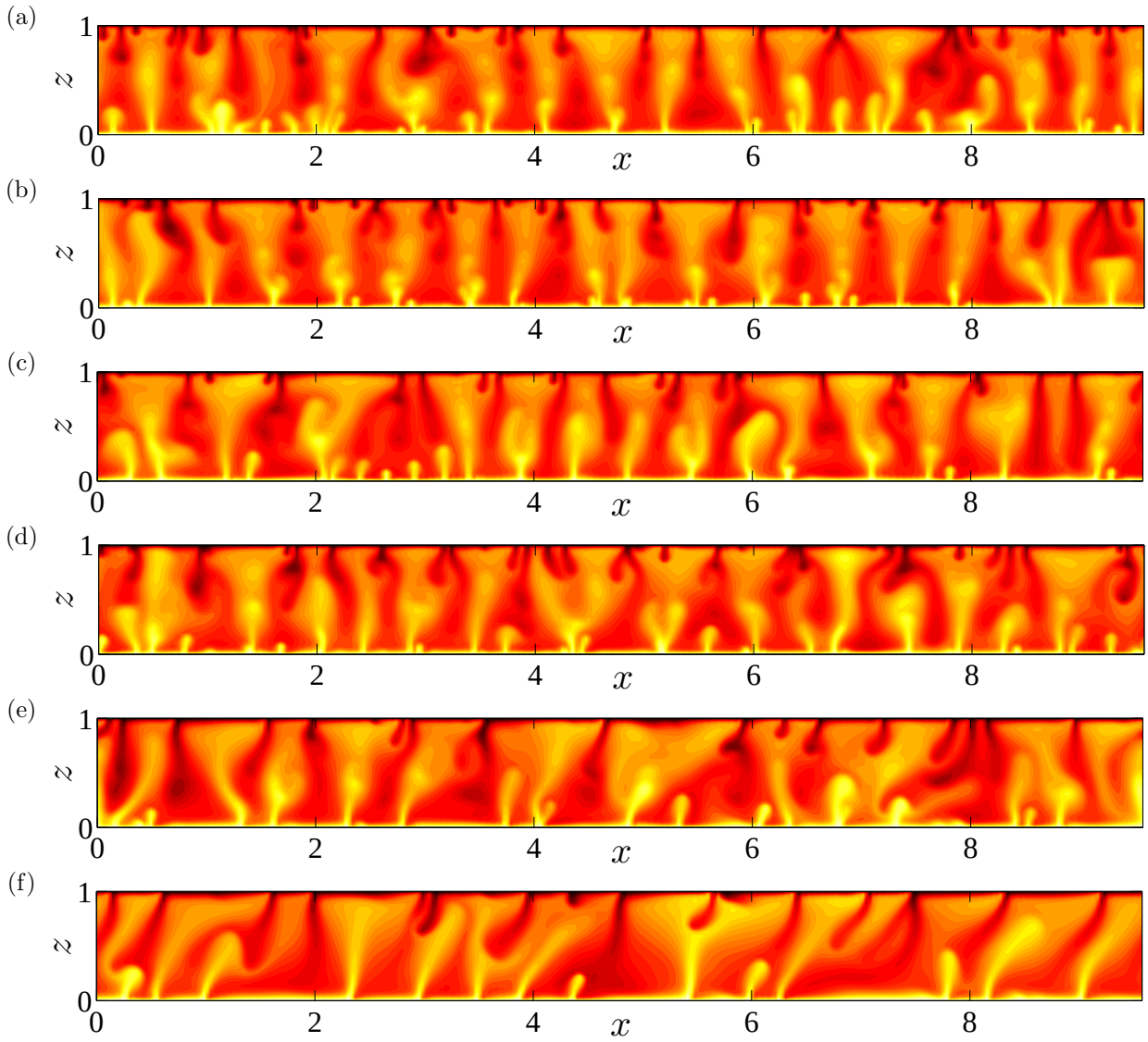

Figure 2-16: Snapshots of temperature fields from DNS at $Ra = 1991$ and $L = 9.6$. $\phi = 0$ (a), 1 (b), 5 (c), 10 (d), 25 (e), and 30 (f) degrees.

rolls and suppresses those of the antinatural rolls (as will be shown in chapter 4), the latter (antinatural rolls) begin to detach from the upper and lower walls (see Figure 2-17) at large ϕ. As evident in Figure 2-17, the contact area between the antinatural rolls and two walls is decreased as ϕ is increased; on the contrary, the natural rolls are attached to the walls

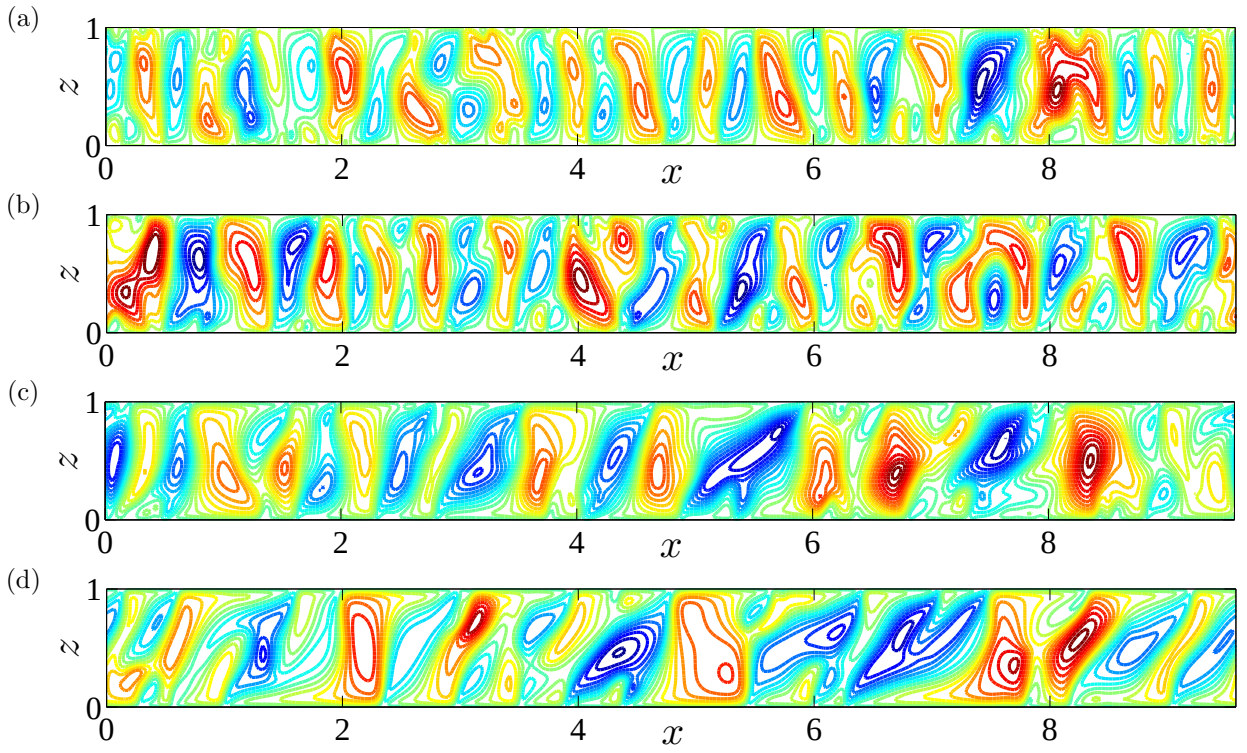

Figure 2-17: Snapshots of streamlines from DNS at $Ra = 1991$ and $L = 9.6$. $\phi =$ 0 (a), 10 (b), 25 (c), and 30 (d) degrees. These streamlines correspond to the flows in Figure 2-16. The natural rolls are in red color and antinatural rolls in blue color.

more tightly. Finally, the flow pattern is completely changed at $\phi = 35°$: the convection transitions to a large-scale-roll motion with the antinatural rolls connected with the heated and cooled walls only at certain localized points (see Figures 2-18 and 2-19).

However, unlike the quasi-coherent cellular flows at moderate Ra in the horizontal case, the resulting large-scale convective flow at $Ra = 1991$, $L = 9.6$ and $\phi = 35°$ appears as one of two types of relative periodic orbits (i.e. time-periodic orbits traveling at constant velocity in $\pm x$ in one period) which are no longer *centro-symmetric*, hereafter referred to as pattern I and II. For each pattern, there exist four large-scale (two natural and two antinatural) rolls in $L = 9.6$, and the natural rolls are tightly attached to either the upper wall (see Figure 2-18)

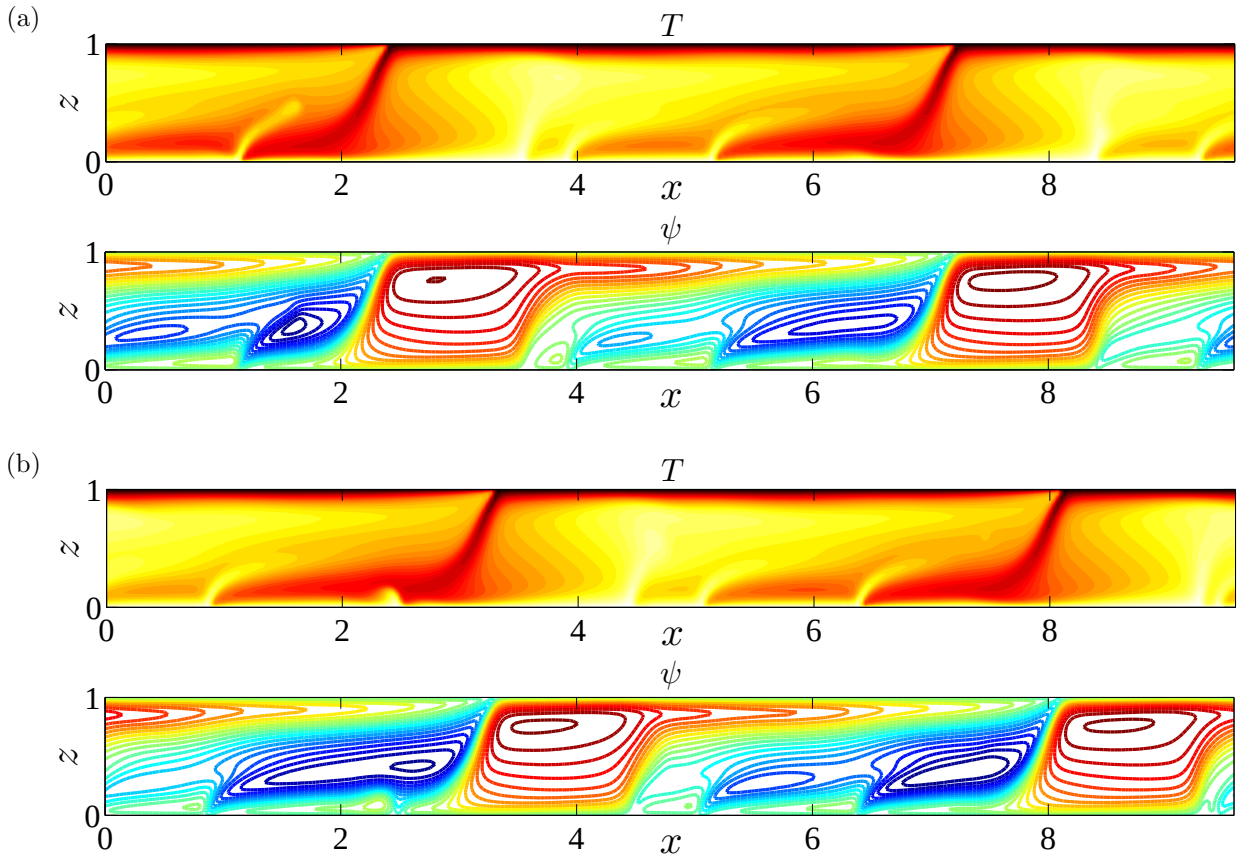

Figure 2-18: Snapshots of temperature fields and corresponding streamlines for pattern I from DNS at $Ra = 1991$, $L = 9.6$ and $\phi = 35°$. Time evolves from (a) to (b). For pattern I, there exist four large-scale cells in the domain: two natural rolls (red ψ) and two antinatural rolls (blue ψ). The lower boundary layers of the antinatural rolls are unstable: small plumes generated from the heated wall owing to the boundary-layer instability are continually swept to the left $(-x)$ and merge with the large-scale hot plumes. However, the natural rolls are tightly attached to the cooled wall, the upper boundary layer is stable, and as time evolves the entire flow pattern moves to the right $(+x)$.

or the lower wall (see Figure 2-19), with a stable upper or lower boundary layer, respectively. Nevertheless, near the opposite walls (the lower for pattern I and upper for pattern II), small-scale proto-plumes periodically grow from the *unstable* boundary layers, and are continually swept into and thus merge with the large-scale plumes in the interior. Interestingly, for both

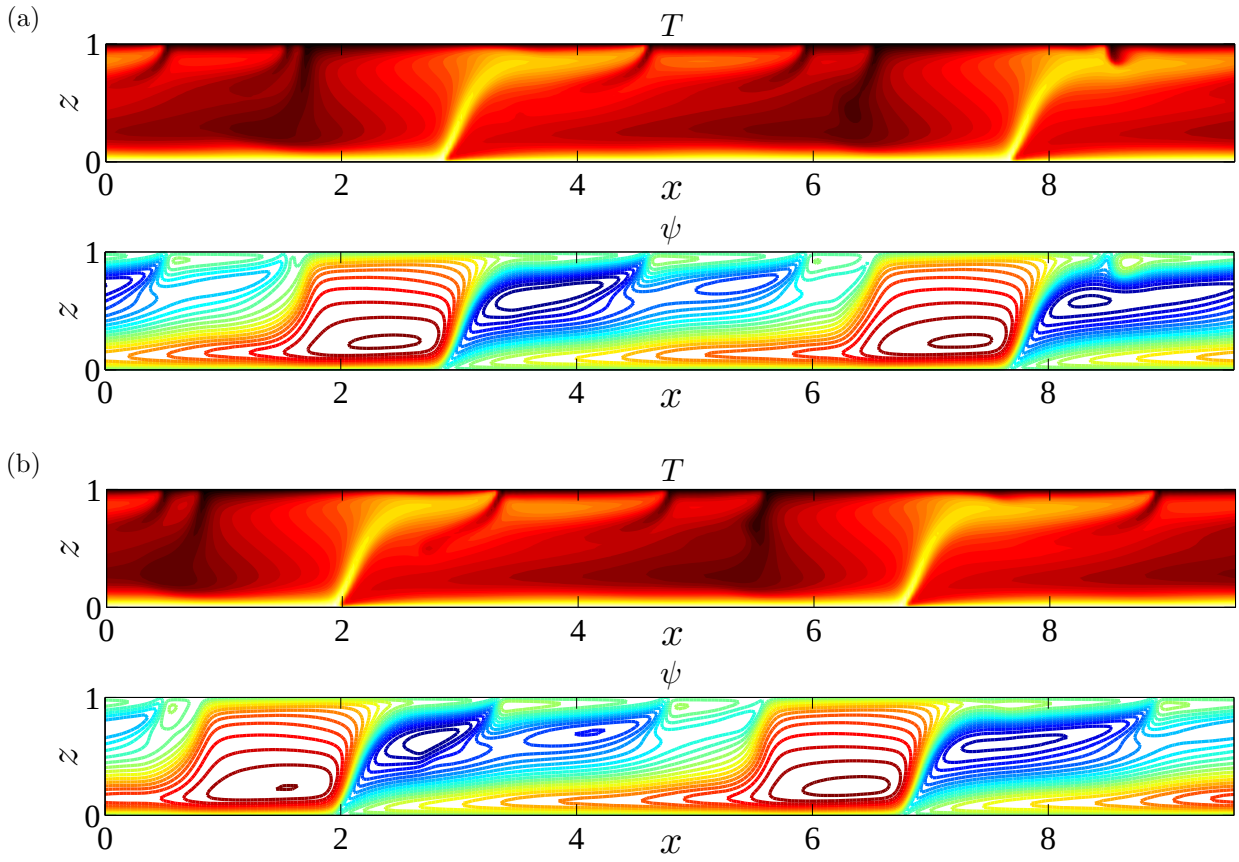

Figure 2-19: Snapshots of temperature fields and corresponding streamlines for pattern II from DNS at $Ra = 1991$, $L = 9.6$ and $\phi = 35°$. Time evolves from (a) to (b). For pattern II, there also exist four large-scale cells in the domain: two natural rolls (red ψ) and two antinatural rolls (blue ψ). However, unlike pattern I, the upper boundary layers of the antinatural rolls are unstable: small plumes generated from the cooled wall owing to the boundary-layer instability, are continually swept to the right $(+x)$ and merge with the large-scale cold plumes. Nevertheless, the natural rolls are tightly attached to the heated wall, the lower boundary layer is stable, and as time evolves the entire flow pattern moves to the left $(-x)$.

pattern I and II, the large-scale background flow travels in the direction opposite that of the proto-plumes.

Figure 2-20 shows the time series of the *instantaneous* Nusselt number $nu(t) = -\partial_z \overline{T}|_{z=0}$ and the time- and horizontal-mean temperature profile $\langle \overline{T} \rangle$ for these two patterns at $\phi = 35°$.

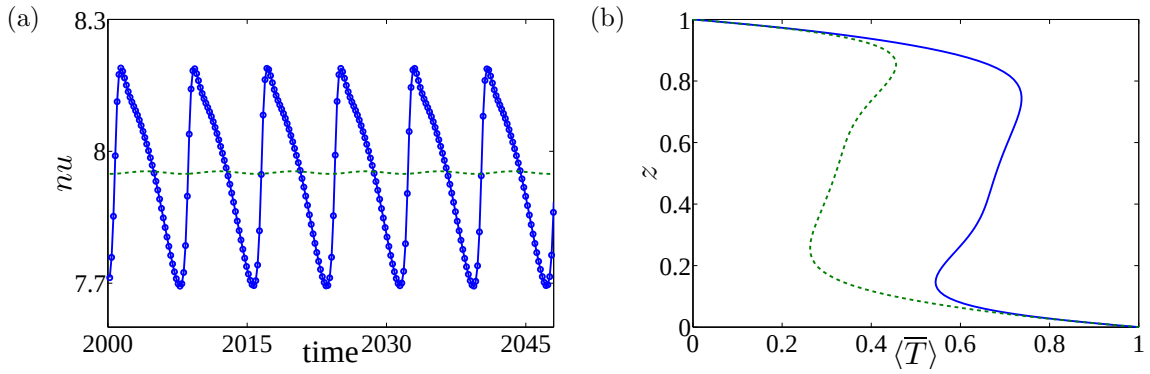

Figure 2-20: Time series of instantaneous Nusselt number nu (a) and time- and horizontal-mean temperature profile $\langle\overline{T}\rangle$ (b) from DNS at $Ra = 1991$, $L = 9.6$ and $\phi = 35°$. (a) nu varies periodically with time for both I (solid line with circles) and II (dashed line). (b) Neither of the mean temperature profiles for I (solid line) and II (dashed line) is antisymmetric about the mid-plane. Nevertheless, $Nu = 7.95$ for both I and II.

Clearly, nu varies periodically for both I and II, and the mean temperature profiles for I and II are no longer antisymmetric about the mid-plane ($z = 0.5$). For pattern I, the hot plume occupies a majority of the area of the interior domain so that the magnitude of $\langle\overline{T}\rangle$ is generally greater than 0.5 in the core; on the contrary, for pattern II, the cold plume dominates the interior so that the magnitude of $\langle\overline{T}\rangle$ is generally less than 0.5 in the core. However, these two patterns transport the same amount of heat, as shown in Figure 2-20. It should be noted that for $\phi = 35°$, these two types of patterns exist up to $Ra = 3972$ where the only change is that the four-cell convective flow changes to a two-cell convective flow.

As Ra is increased, the columnar flow at small inclination becomes more well-organized (see Figure 2-21a-d). However, the convection at $\phi = 35°$ changes form at $Ra \geq 5000$. Rather than the two types of flow patterns entirely traveling in one direction ($+x$ or $-x$) at $Ra \lesssim 3972$ (see Figures 2-18 and 2-19), the flow at $Ra = 5000$ exhibits a large-scale two-cell convective pattern with the cells traveling in opposite directions. As shown in Figures 2-22 and 2-23, the hot and cold plumes are stretched under the effect of buoyancy. During the

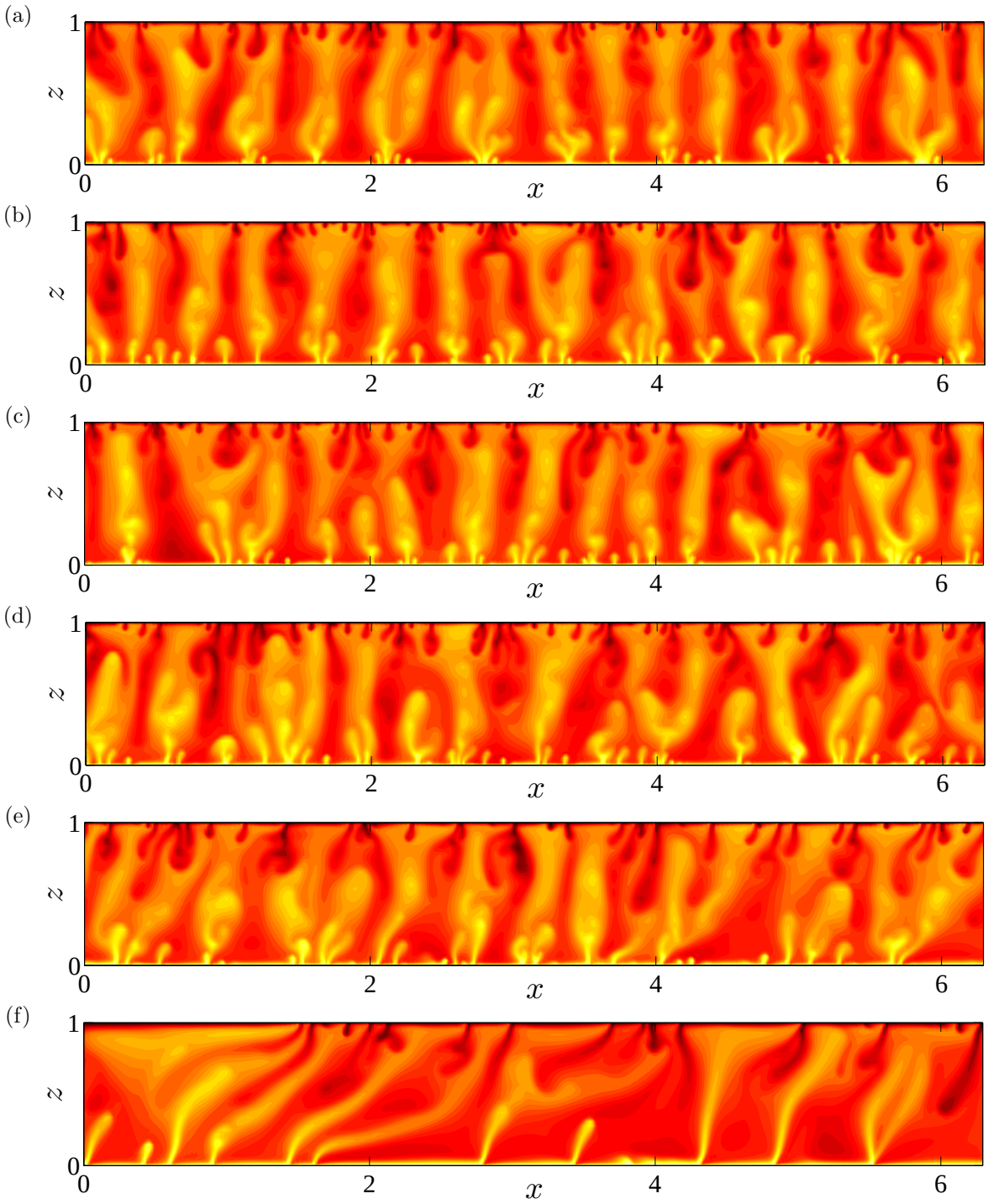

Figure 2-21: Snapshots of temperature fields from DNS at $Ra = 5000$ and $L = 6.3$. $\phi = 0$ (a), 1 (b), 5 (c), 10 (d), 25 (e), and 30 (f) degrees. As Ra is increased, the three-region columnar flow becomes more well-organized at small inclination. For $\phi \gtrsim 25°$, the flow pattern begins to exhibits a clear inclination in the direction opposite to gravity, as observed for $Ra = 1991$.

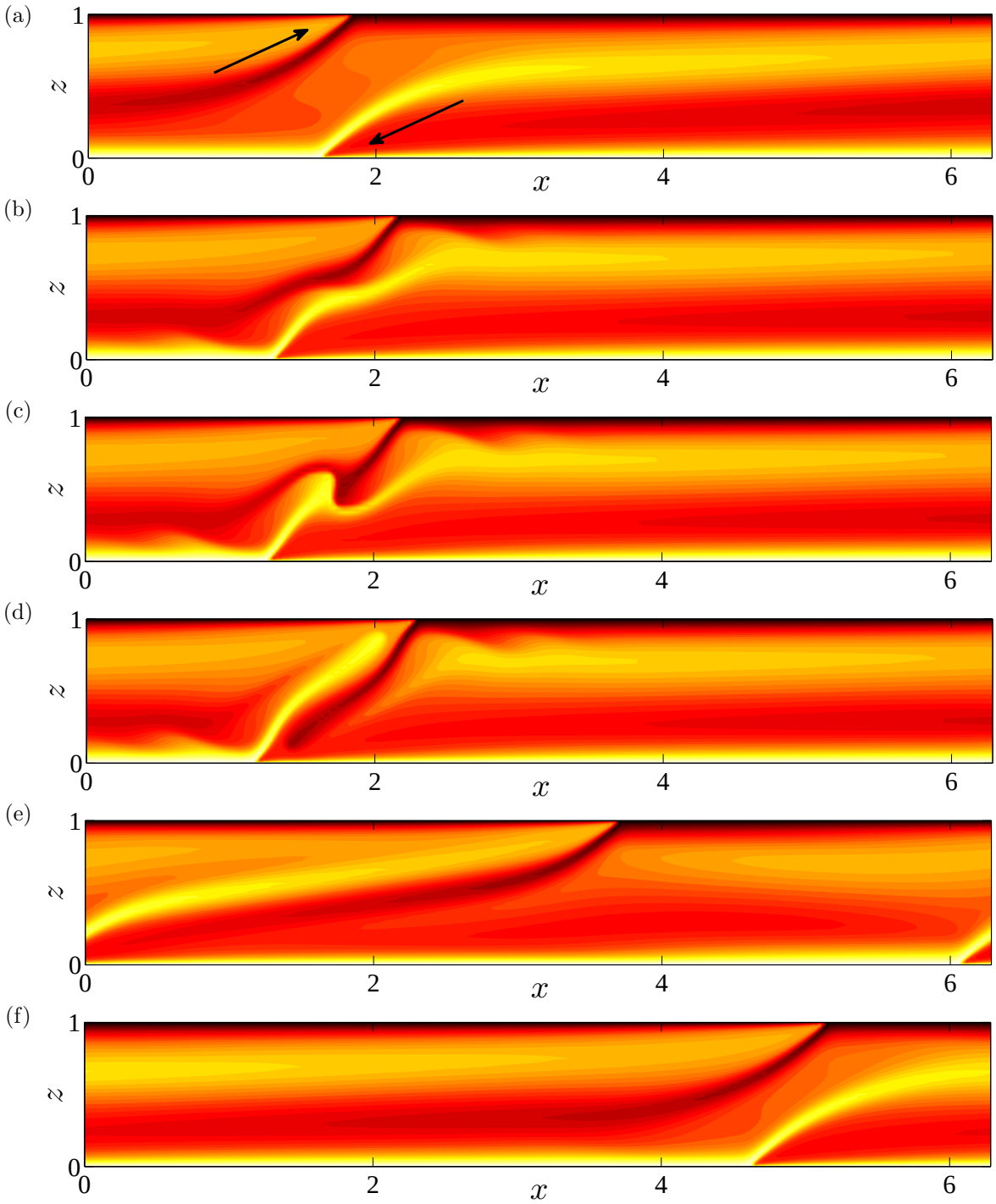

Figure 2-22: Snapshots of temperature fields from DNS at $Ra = 5000$, $L = 6.3$ and $\phi = 35°$. Time evolves from (a) to (f). The arrows in (a) represent the direction of motion of the roots of the hot and cold plumes.

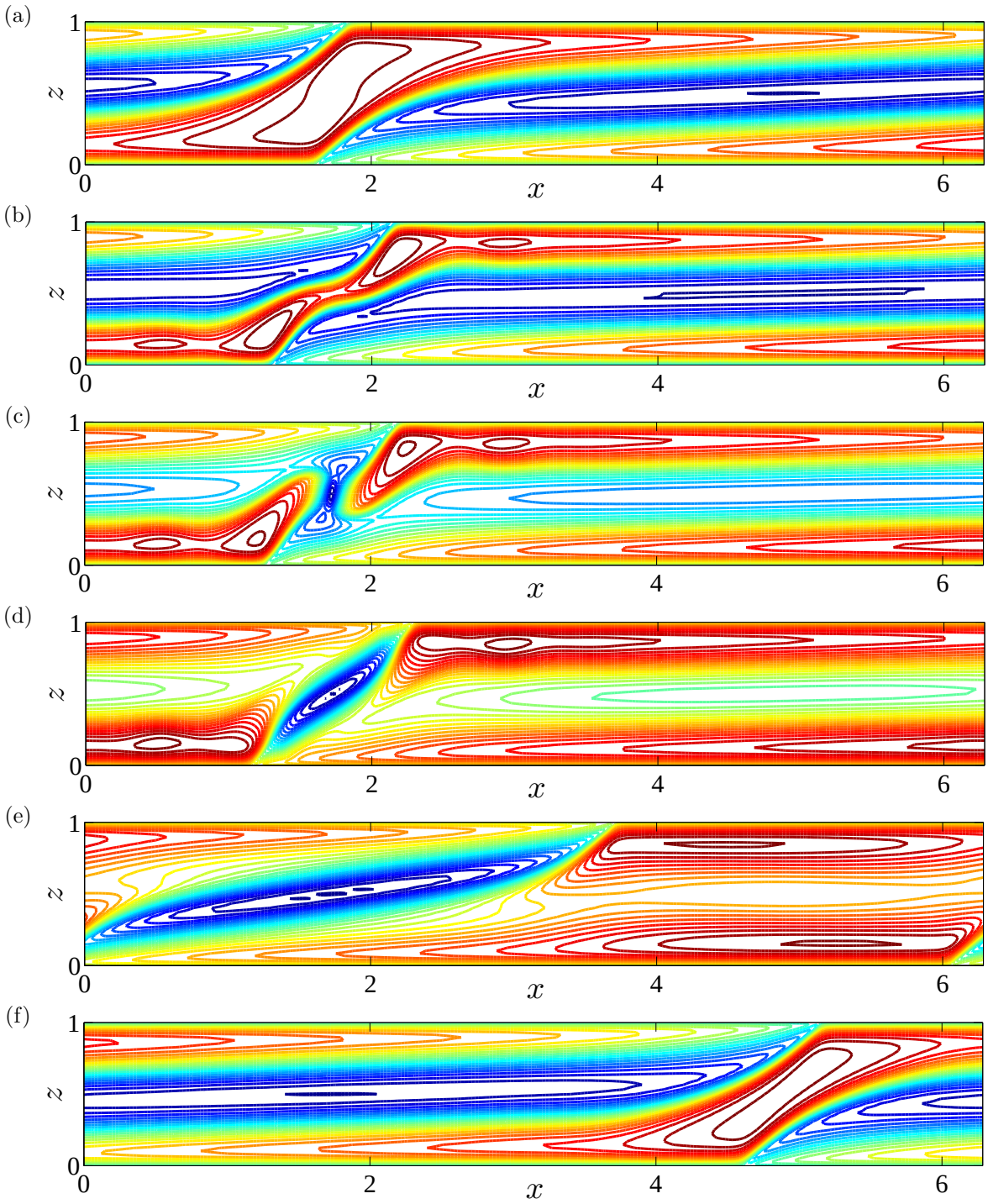

Figure 2-23: Snapshots of streamlines from DNS at $Ra = 5000$, $L = 6.3$ and $\phi = 35°$. These streamlines correspond to the flows in Figure 2-22. The natural roll is in red color and the antinatural roll in blue color.

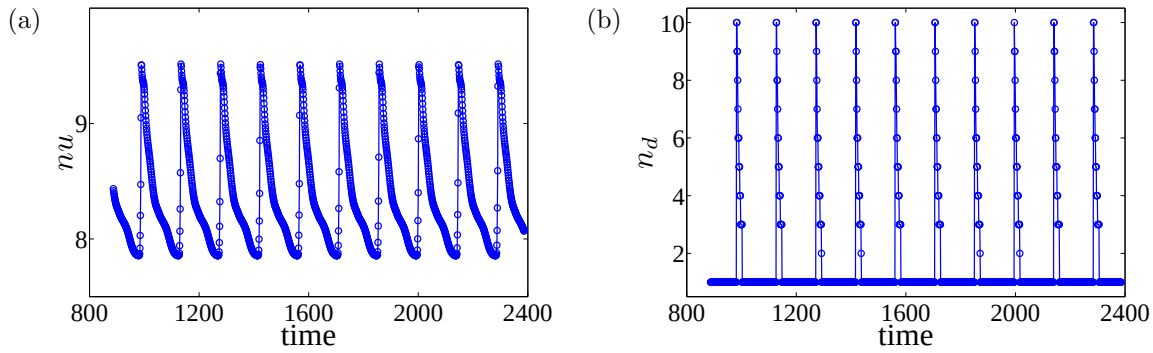

Figure 2-24: Time series of instantaneous (a): Nusselt number nu and (b): dominant horizontal mode number n_d in the core ($z = 0.5$) at $Ra = 5000$, $L = 6.3$ and $\phi = 35°$. nu and n_d vary periodically with convective time in these plots. In the interior, the flow consists of several Fourier modes but is dominated by the first mode ($n_d = 1$) except when the two plumes collide.

stretching process, the root of the cold/hot plume is pushed by the hot/cold plume toward the $+x/-x$ direction (see Figure 2-22a). The two plumes meet at some point, then collide and thus switch their positions (see Figure 2-22b-e). In a L-periodic domain, this process occurs time-periodically for $5000 \leq Ra \leq 9976$ (see Figure 2-24). Moreover, Figure 2-23 also indicates that the natural roll is tightly attached to the heated and cooled walls with stable (lower and upper) boundary layers, while the antinatural roll is detached from the walls and is only connected to the walls at two points (one at the lower wall and the other at the upper wall). In short, both the DNS results from $Ra = 1991$ and $Ra = 5000$ reveal that for $0° < \phi \lesssim 25°$, the flow at large Ra exhibits a similar three-region columnar structure as is manifest in the horizontal case. Nevertheless, when the inclination angle ϕ exceeds some critical value ϕ_t that is independent of Ra, the columnar flow structure is completely broken down and the flow then transitions to a large-scale traveling-wave convective roll state (see Figures 2-18, 2-19, 2-22 and 2-23). In this dissertation study, DNS performed at other, large values of Ra also confirm this trend. Specifically, the DNS results at $Ra = 9976$ indicate that the transition angle is $30° < \phi_t < 32°$, namely, for $\phi \leq 30°$, the convection appears in form

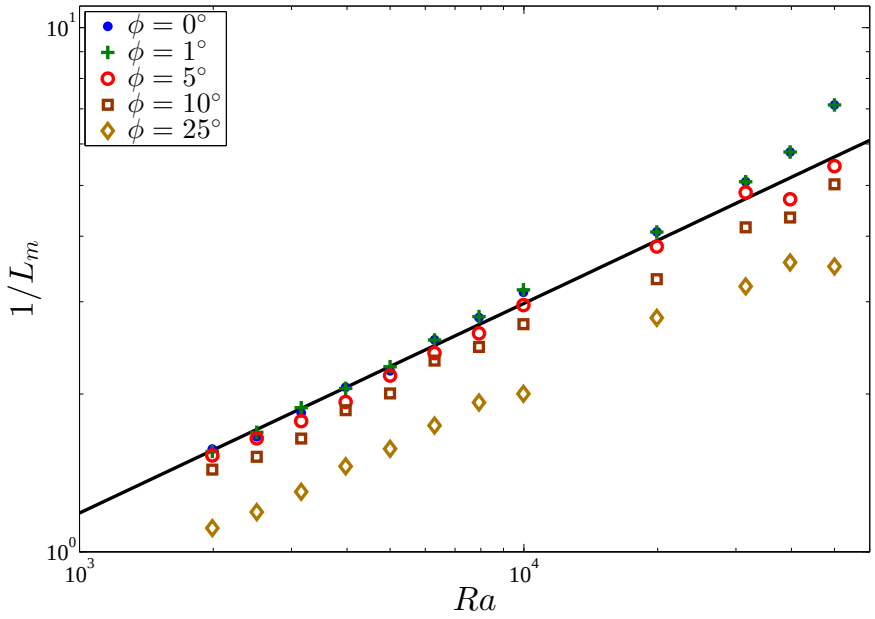

Figure 2-25: Variation of mean inter-plume spacing with Ra and ϕ. The solid line marks the fitted mean inter-plume spacing $L_m = (2\pi/0.47)Ra^{-0.4}$ measured from the DNS of Hewitt et al. (2012) at $\phi = 0°$; the symbols are measured from the DNS in present study for different ϕ. The same aspect ratio L as in Figure 2-8 is used here and for each Ra the results from smaller ϕ are utilized as the initial conditions for simulations at larger ϕ. At sufficiently large Ra (e.g. $Ra \gtrsim 19905$), although the final inter-plume spacing is not unique but may itself fall within some small band in the horizontal case (see Figure 2-8), the results for only one L_m are chosen as the initial conditions for the inclined case. It can be seen that as ϕ is increased the time-mean inter-plume spacing is also substantially increased for each Ra.

of three-region turbulent flow, while for $\phi \geq 32°$, the convection transitions to the large-scale traveling-wave convective flow. Interestingly, as discussed in section 2.1, the linear stability analysis in Rees and Bassom (2000) also predicts a transition angle $\phi_t = 31.30°$ above which the basic state is linearly stable at large Ra in the 2D domain. Although it is still unclear whether these two transition angles are exactly equivalent, there are indications that they are at least very close.

As described above, the flow continues to exhibit a three-region columnar structure for

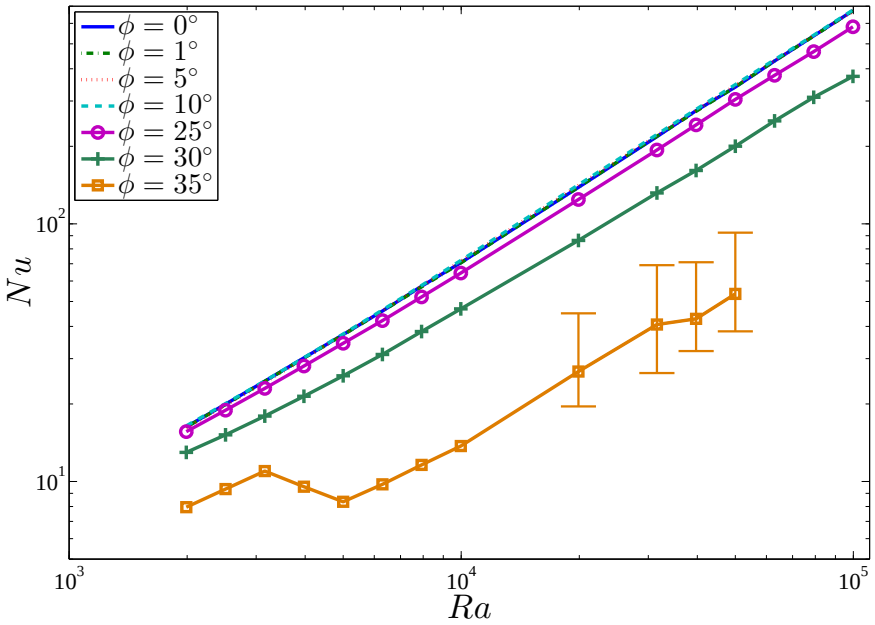

Figure 2-26: Variation of Nu with Ra and ϕ. For $Ra \leq 50000$, the same aspect ratio L as in Figure 2-8 (more than 15 pairs of plumes exist at $\phi = 0°$) is used to perform the DNS; however, for $50000 < Ra \leq 99763$, the DNS are conducted in narrower domains with $L = 1.76L_f$ (3 pairs of plumes exist at $\phi = 0°$). It is seen that at large Ra, the heat transport is nearly unaffected by the inclination of the layer until $\phi \geq 25°$. The sharp changes of Nu at $\phi = 35°$ for $3155 \leq Ra \leq 5000$ are due to the transitions of the flow from a four-cell pattern at $Ra = 3155$, as in Figures 2-18 and 2-19, to a similar two-cell pattern at $Ra = 3972$, and then to another two-cell pattern as in Figures 2-22 and 2-23 for $Ra \geq 5000$. It should be noted that for $Ra \geq 19905$ and at $\phi = 35°$, the slow large-scale convective motions require extremely long computing times to obtain accurate values of Nu, so error bars are included to show the range of variation of the instantaneous Nusselt number in the present computations (where the averaging times are not sufficiently long).

$\phi \lesssim 25°$ at large Ra. A natural question concerns the variation of the mean inter-plume spacing L_m with Ra and ϕ in the high-Ra regime. From Figure 2-25, it can be concluded that for fixed ϕ, the mean inter-plume spacing still shrinks as the Rayleigh number is increased. Moreover, when the inclination is small enough, e.g. $\phi = 1°$, L_m is basically unchanged. However, for each fixed Ra, as ϕ is increased the time-mean spacing between neighboring interior mega-plumes is also substantially increased. The physics leading to this increasing

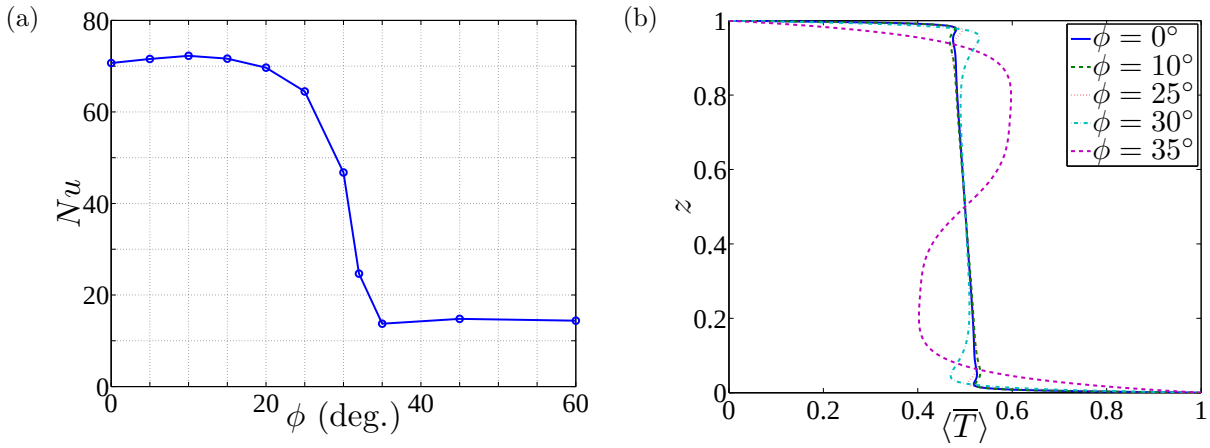

Figure 2-27: Variations of Nu (a) and $\langle\overline{T}\rangle$ (b) with ϕ at $Ra = 9976$ and $L = 5.01$. (a): Nu is almost unchanged for $\phi \lesssim 20°$, although it is slightly increased up to a maximum around $\phi = 10°$. For $\phi \geq 25°$, the columnar flow structure begins to be destroyed and Nu decreases rapidly as ϕ is increased. (b): The main features of mean temperature profiles are retained for $\phi \leq 30°$.

trend of L_m with increased ϕ at large Ra will be discussed in detail in chapter 4.

Figure 2-26 shows the variation of Nu with Ra and ϕ at large Rayleigh number. For $\phi \leq 10°$ (actually $\phi \lesssim 20°$ as shown in Figure 2-27a), Nu is almost unchanged since the flow still exhibits a similar three-region structure as is manifest in the horizontal case. However, for $\phi > 25°$, the antinatural rolls begin to detach from the upper and lower walls, so that the organized columnar flow structure is destroyed and less heat is transported. Moreover, when $\phi > \phi_t$, where $30° < \phi_t < 32°$, the columnar flow structure is completely broken down: the flow transitions to the large-scale traveling-wave convective roll state, and the heat transport is significantly reduced. Figure 2-27 shows the detailed variations of Nu and $\langle\overline{T}\rangle$ with ϕ at $Ra = 9976$. It should be noted that the variation of Nu with ϕ at large Rayleigh number (see Figure 2-27a) exhibits a very similar trend with that at $Ra = 100$ in Caltagirone and Bories (1985) except that the flow patterns reported here are quite different. For instance, as ϕ is increased, the flow at large Ra is changed from turbulent columnar flow to large-scale

traveling-wave states, while in Caltagirone and Bories (1985) the flow at $Ra = 100$ is changed from multi-cellular steady states to the basic unicellular state. Furthermore, Figure 2-27(b) indicates that the main characteristics of the mean temperature profiles are unchanged for $\phi \leq 30^\circ$, e.g. thin thermal boundary layers and an unstably stratified core. Nevertheless, the core becomes stably stratified at $\phi = 35^\circ$.

2.5 Summary

In this chapter, a series of DNS are performed to investigate the high-Ra flow structure for both horizontal and inclined porous medium convection. In order to obtain reliable estimates of the statistical flow characteristics, these DNS are conducted in wide domains and for long computational times. For the horizontal case, the new DNS up to $Ra \approx 10^5$ confirm the remarkable tendency for the interior flow to self-organize into narrow columnar plumes at sufficiently large Ra, with more complex spatiotemporal features being confined to boundary layers near the heated and cooled walls. However, one key finding is that the interior columnar exchange flow becomes very well-organized for $Ra \geq 39716$ and that the final inter-plume spacing is not unique but may itself fall within some small band. Although more simulations are required to determine the boundaries of this band, it is clear that the precise high-Ra scaling of the mean interior inter-plume spacing in statistically-steady porous medium convection remains to be firmly established and will require extremely long simulations in very wide computational domains.

For inclined porous medium convection, the first systematic studies of pattern formation and

heat transport at different inclination angels ϕ and large Ra have been carried out using high-resolution DNS. The results indicate that for $0^\circ < \phi \lesssim 25^\circ$, the flow still exhibits the three-region columnar structure as in the horizontal case, except that as ϕ is increased the time-mean inter-plume spacing is also substantially increased. Nevertheless, for $0^\circ < \phi \lesssim 20^\circ$, the Nusselt number is almost unchanged. However, when $\phi > \phi_t$, where $30^\circ < \phi_t < 32^\circ$, the columnar flow structure is completely broken down: the flow transitions to a large-scale traveling-wave convective roll state, and the heat transport is significantly reduced.

Based on these characteristics of the flow observed in DNS, some natural questions arise concerning the physics responsible for the quasi-coherent flow patterns at large Ra: (1) *what physical mechanisms control lateral scale selection in horizontal convection?* (2) *why does the inclination of the porous layer increase the mean inter-plume spacing?* Given these questions, a primary objective of this dissertation is to elucidate the flow and transport mechanisms governing these recurring quasi-coherent motions by studying the corresponding exact coherent states manifest in this spatiotemporally-chaotic system. Hence, in following three chapters, the structure of steady and/or time-periodic convective solutions at large Ra in horizontal and inclined porous medium convection will be characterized, and their stability and nonlinear evolution will be analyzed numerically using spatial Floquet theory and strategically initialized DNS.

CHAPTER 3

STRUCTURE AND STABILITY OF STEADY CONVECTION IN A HORIZONTAL POROUS LAYER AT LARGE RAYLEIGH NUMBER

3.1 Introduction

At large Ra, porous medium convection exhibits spatiotemporally chaotic (turbulent) dynamics. DNS indicate that the instantaneous flow self-organizes into recurrent quasi-coherent structures (i.e. three-region columnar flows), suggesting that the basic physics of high-Ra porous medium convection can be understood by studying the corresponding *exact coherent states*. Exact coherent states must satisfy the following conditions: (1) they must be (numerically) exact invariant of the dynamical system with simple (or no) time dependence, e.g. a steady solution, periodic orbit, relative periodic orbit, traveling wave, etc.; (2) these solutions must contain certain features of the turbulent flow, e.g. thermal boundary layers near the heated and cooled walls or columnar structure in the interior.

Actually, in order to explore the physics of turbulence, studies of exact coherent solutions have been performed in various types of turbulent shear flows, e.g. pipe flow, plane Couette flow and plane Poiseuille flow. The first pair of nontrivial steady solutions and the first traveling wave in 3D plane Couette flow were found by Nagata (1990, 1997). Subsequently, a series of investigations have been carried out to find more equilibria, traveling-wave solutions, periodic orbits and relative periodic orbits in different shear flow turbulence configurations (Clever and Busse, 1992; Waleffe, 1998, 2001, 2003; Itano and Toh, 2001; Kawahara and Kida, 2001; Faisst and Eckhardt, 2003; Wedin and Kerswell, 2004; Kerswell and Tutty, 2007; Viswanath, 2007; Gibson et al., 2008, 2009; Cvitanović and Gibson, 2010; Gibson and Brand, 2014; Brand and Gibson, 2014). The over-riding conclusion from these studies is that these exact solutions are remarkably similar to the coherent structures observed in DNS and experiments. Moreover, they can also capture the main statistical features of turbulent flows, e.g. the dissipation rate, and the mean and RMS (root mean square) velocity profiles. Some visualizations of the geometry of the state space (Gibson et al., 2008) imply that exact coherent solutions constrain turbulent trajectories to wander from one solution to another along specific intersecting manifolds. Therefore, studies of exact coherent states may be expected to provide at least partial insight into the underlying physics of the real turbulent flow.

In this dissertation study, one of the central aims is to quantify the structure, stability and heat-transport properties of exact solutions of the Darcy–Oberbeck–Boussinesq equations as functions of both Ra and domain aspect ratio L. In horizontal porous medium convection, these solutions generally take the form of steady and time-periodic convective states, as will be shown in chapters 3 and 5; in the inclined case, the structure and stability analysis of the steady, fully nonlinear convective states will be performed (see chapter 4).

In horizontal porous medium convection, the structure and stability of steady 2D porous medium convection at small to moderate Rayleigh number has been discussed in detail in many previous studies (Elder, 1967; Palm et al., 1972; Horne and OSullivan, 1974; Schubert and Straus, 1982; Aidun and Steen, 1987; Kimura et al., 1987; Graham and Steen, 1992, 1994). The study of high-Rayleigh-number steady solutions, however, has been rather limited, in part because these solutions are unstable and exhibit fine-scale spatial structure. Corson (2011) focuses on the asymptotic structure of the steady solution maximizing the heat flux at large Ra: guided by numerical results, the steady governing equations are reduced into different forms for different regions of the flow, e.g. the interior region, and the momentum and thermal boundary-layer regions. Following the work of Corson (2011), this study solves the steady governing equations numerically using a Newton–Kantorovich iteration scheme (Boyd, 2000) and investigates the dependence of the steady solutions on the domain aspect ratio L. A key finding is that there exist two qualitatively distinct types of steady convective states at large Ra: for small L, the flow has the heat-exchanger structure in the interior identified by Hewitt et al. (2012); however, as L is increased, the steady convection develops a *stably* stratified core with a horizontal structure involving multiple Fourier modes. Comparing the steady solutions with the long-time averaged columnar flow observed in the DNS reveals that the latter is neither a heat-exchanger nor a stably stratified core solution but instead combines certain attributes of both types of steady solutions.

After these steady convective states are characterized as a function of Ra and L, their stability to small-amplitude disturbances is assessed using Floquet theory. The Floquet technique was introduced as a tool for secondary stability analysis in fluid dynamics by Kelly (1967), who applied this method to inviscid shear flows. Since then, Floquet analysis has been applied to numerous other shear and convective flows, including thermal convection (Busse,

1967, 1972; Clever and Busse, 1974), viscous shear flows (Orszag and Patera, 1983; Herbert, 1983, 1988) and Langmuir circulation (Tandon and Leibovich, 1995; Chini et al., 2009). This study follows Chini et al. (2009) by employing a Fourier–Chebyshev spectral method to discretize the differential eigenvalue problem derived from linearizing the governing equations of porous medium convection about the fully nonlinear steady states. The analysis in this chapter reveals the existence of two types of instability for different L at large Ra: a bulk instability in which the most unstable disturbance spans the convective layer, and a wall instability in which the most unstable disturbance is strongly localized near the hot and cold boundaries.

The nonlinear evolution of these secondary instabilities is explored here using high-resolution DNS. Both the bulk and wall instability modes are shown to influence the mean inter-plume spacing at large Ra. To obtain a reliable estimate of this mean spacing the aspect ratio of the computational domain must be sufficiently large to capture long-wavelength secondary instabilities. Moreover, the simulations indicate that the mean inter-plume spacing observed at large Ra results from an interplay between these two types of instability so that the interior columnar exchange flow is statistically steady.

The reminder of this chapter is organized as follows. In next section, the key results of linear stability theory for porous medium convection are recalled. In chapter 3.3, the numerical method used to find (generally unstable) steady high-Ra solutions is outlined, the structure of these solutions for different aspect ratios is described, the variation of heat transport with aspect ratio is documented, and the steady flows that maximize the heat transport as a function of both Ra and L are identified. In chapter 3.4, the (secondary) stability of these steady convective states is analyzed using Floquet theory. In chapter 3.5, DNS strategically initialized with a superposition of the steady solutions and a small-amplitude contribution of

the most unstable secondary instability eigenfunction are performed to investigate how these steady states evolve into the statistically-steady but spatiotemporally chaotic (turbulent) convective flow. A summary is given in chapter 3.6.

3.2 Linear Stability Analysis

One elementary solution of this system is the conduction state: $T = 1 - z$, $\mathbf{u} = 0$ and $p = Ra(z - \frac{1}{2}z^2)$. A linear stability analysis can be performed by setting $T = (1 - z) + \theta^*(x, z, t)$ and $\mathbf{u} = u^*\mathbf{e}_x + w^*\mathbf{e}_z$, where θ^*, u^* and w^* are small perturbations, and linearizing (1.22)–(1.24) about the conduction solution. As first shown by Horton and Rogers (1945) and Lapwood (1948), the resulting (normalized) eigenfunctions are

$$\theta^* = \cos(kx)\sin(m\pi z)e^{\lambda^* t}, \quad w^* = \frac{Rak^2}{m^2\pi^2 + k^2}\cos(kx)\sin(m\pi z)e^{\lambda^* t}, \tag{3.1}$$

with the corresponding eigenvalue

$$\lambda^* = \frac{Rak^2}{m^2\pi^2 + k^2} - (m^2\pi^2 + k^2) \tag{3.2}$$

representing the growth rate of the given eigenmode. The eigenvalues for different Ra, vertical mode number $m \geq 1$ and (continuous) horizontal wavenumber k (in an infinitely wide domain) are strictly real, implying the onset of convection is to steady cells, and the largest growth rates occur for $m = 1$. By setting $\lambda^* = 0$ with $m = 1$, an expression for the marginal stability boundary of the conduction state can be obtained: $Ra = (\pi^2 + k^2)^2/k^2$.

The *high*-wavenumber branch of marginal modes is denoted by

$$k_c = \frac{\sqrt{Ra} + \sqrt{Ra - 4\pi^2}}{2} \tag{3.3}$$

and $L_c = 2\pi/k_c$ is defined as the corresponding wavelength of these marginal modes. At a given $Ra > 4\pi^2$, the conduction solution will become linearly unstable for aspect ratios $L > L_c$. Alternatively, by setting $\frac{\partial \lambda^*}{\partial k} = 0$, one can find that the wavenumber k_f of the fastest growing linear mode is given by

$$k_f = \sqrt{\sqrt{Ra}\pi - \pi^2}. \tag{3.4}$$

$L_f = 2\pi/k_f$ is defined as the corresponding wavelength of this fastest growing linear mode. In the limit $Ra \to \infty$, $k_f \sim \sqrt{\pi} Ra^{1/4}$ while $k_c \sim Ra^{1/2}$.

3.3 Steady Convective States

3.3.1 Newton–Kantorovich Method

Following Corson (2011), the steady version of the governing equations (1.22)–(1.24) is solved numerically using a Newton–Kantorovich (NK) iterative scheme (Boyd, 2000). The time-independent dimensionless equations in stream function form can be written as

$$\nabla^2 \psi = -Ra \partial_x \theta, \tag{3.5}$$

$$\partial_z \psi \partial_x \theta - \partial_x \psi \partial_z \theta = -\partial_x \psi + \nabla^2 \theta, \tag{3.6}$$

where $\theta(x,z) = T(x,z) - (1-z)$, and θ and ψ satisfy L_s-periodic boundary conditions in x and homogeneous Dirichlet boundary conditions in z. To avoid ambiguity, L_s is used here and throughout to denote the domain width associated with a given steady state. The solution of (3.5) and (3.6) can be expressed as

$$\begin{bmatrix} \theta \\ \psi \end{bmatrix} = \sum_{n=-N/2}^{N/2} \begin{bmatrix} \hat{\theta}_n(z) \\ \hat{\psi}_n(z) \end{bmatrix} e^{ink_s x} = \sum_{n=-N/2}^{N/2} \sum_{m=0}^{M} \begin{bmatrix} a_{mn} \\ b_{mn} \end{bmatrix} \mathrm{T}_m(z)\, e^{ink_s x}, \tag{3.7}$$

where $k_s = 2\pi/L_s$ is the fundamental wavenumber of the spatially-periodic steady solution, M is the vertical truncation mode number, N is the horizontal truncation mode number, and $\mathrm{T}_m(z)$ is the m-th Chebyshev polynomial. In each $L_s \times 1$ computational domain steady solutions are sought with reflection symmetry about $x = L_s/2$ and centrosymmetry within each of the two $L_s/2 \times 1$ sub-domains which contain a single convection cell. These symmetry constraints require

$$a_{mn} \text{ is real; } b_{mn} \text{ is imaginary; } a_{mn} = b_{mn} = 0 \text{ if } (m+n) \text{ is even.} \tag{3.8}$$

To employ the NK algorithm, (3.5)–(3.6) are rearranged into the following form:

$$\nabla^2 \psi = F^{\psi}(\theta_x), \tag{3.9}$$

$$\nabla^2 \theta = F^{\theta}(\psi_x, \psi_z, \theta_x, \theta_z), \tag{3.10}$$

where a subscript denotes a partial derivative with respect to the given variable. Suppose the i^{th} iterates $\theta^i(x,z)$ and $\psi^i(x,z)$ in the NK scheme are good approximations to the true solution $\theta(x,z)$ and $\psi(x,z)$. Taylor expanding the functionals F^{ψ} and F^{θ} in (3.9)–(3.10)

about these iterates yields

$$\nabla^2\psi = (F^\psi)^i + (F^\psi_{\theta_x})^i[\theta_x - \theta^i_x] + O([\theta_x - \theta^i_x]^2), \tag{3.11}$$

$$\begin{aligned}\nabla^2\theta = (F^\theta)^i + (F^\theta_{\psi_x})^i[\psi_x - \psi^i_x] + (F^\theta_{\psi_z})^i[\psi_z - \psi^i_z] + (F^\theta_{\theta_x})^i[\theta_x - \theta^i_x] \\ +(F^\theta_{\theta_z})^i[\theta_z - \theta^i_z] + O([\psi_x - \psi^i_x]^2,\, [\psi_z - \psi^i_z]^2,\, [\theta_x - \theta^i_x]^2,\, [\theta_z - \theta^i_z]^2),\end{aligned} \tag{3.12}$$

where, for example, $F^\theta_{\psi_x}$ denotes the Frechet derivative of the function $F^\theta(\psi_x, \psi_z, \theta_x, \theta_z)$ with respect to ψ_x. After defining the correction terms

$$\triangle^\psi = \psi^{i+1} - \psi^i, \quad \triangle^\theta = \theta^{i+1} - \theta^i, \tag{3.13}$$

and evaluating the Frechet derivatives, the linear differential equations for the corrections can be expressed as

$$\nabla^2\triangle^\psi + RaD_x\triangle^\theta = -Ra\theta^i_x - \nabla^2\psi^i, \tag{3.14}$$

$$\begin{aligned}[-D_x + \theta^i_z D_x - \theta^i_x D_z]\triangle^\psi + [\nabla^2 - \psi^i_z D_x + \psi^i_x D_z]\triangle^\theta = \;& \psi^i_z\theta^i_x - \psi^i_x\theta^i_z + \psi^i_x \\ & -\nabla^2\theta^i,\end{aligned} \tag{3.15}$$

where D_x and D_z denote the first partial derivative operators with respect to x and z. According to the symmetry constraints (3.8), the solution (3.7) has the following form

$$\theta = \hat{\theta}_0(z) + 2\sum_{n=1}^{N/2}\hat{\theta}_n(z)\cos(nk_s x), \quad \psi = 2\sum_{n=1}^{N/2} -\hat{\phi}_n(z)\sin(nk_s x) \tag{3.16}$$

where $\hat{\phi}_n \equiv \mathrm{Im}\{\hat{\psi}_n\}$ is real. Then, for a given horizontal wavenumber nk_s, (3.14)–(3.15) become

$$-[D_{zz} - (nk_s)^2]\triangle^{\hat{\phi}_n} - nk_s Ra \triangle^{\hat{\theta}_n} = nk_s Ra \hat{\theta}_n^i + [D_{zz} - (nk_s)^2]\hat{\phi}_n^i, \tag{3.17}$$

$$[nk_s + g_n^i]\triangle^{\hat{\phi}_n} + [D_{zz} - (nk_s)^2 + h_n^i]\triangle^{\hat{\theta}_n} = \hat{f}_n^i, \tag{3.18}$$

where

$$\triangle^{\hat{\phi}_n} = \hat{\phi}_n^{i+1} - \hat{\phi}_n^i, \quad \triangle^{\hat{\theta}_n} = \hat{\theta}_n^{i+1} - \hat{\theta}_n^i, \tag{3.19}$$

D_{zz} is the second partial derivative operator with respect to z, g_n^i and h_n^i can be obtained by calculating the convolution of the non-constant coefficient terms on left-hand side of (3.15) for each iterate, and $\hat{f}_n^i$ represents the coefficients of the right-hand side of (3.15) in Fourier space at the i^{th} iterate. (3.17)–(3.18) are solved numerically using a Chebyshev spectral collocation method.

Although the NK method is only locally convergent (good initial conditions are required to converge to the right state), the basin of attraction (in the space of initial iterates) can be expanded by updating the variables for each iterate using

$$\begin{bmatrix} \hat{\phi}_n \\ \hat{\theta}_n \end{bmatrix}^{i+1} = \begin{bmatrix} \hat{\phi}_n \\ \hat{\theta}_n \end{bmatrix}^{i} + a \begin{bmatrix} \triangle^{\hat{\phi}_n} \\ \triangle^{\hat{\theta}_n} \end{bmatrix}, \tag{3.20}$$

where $0 \leq a \leq 1$. The step-length coefficient a is reduced whenever $F_{res}^{i+1} > bF_{res}^i$, where F_{res}^i is the norm of the residual of the steady governing equations at the i^{th} iterate and $b \approx 1$ is an adjustable parameter. The iteration is continued until $F_{res}^{i+1} < 10^{-7}$, and then the spatial

resolution is increased until the relative error in Nu is less than 10^{-5}.

Computations are performed for a discrete set of $Ra = 50 \cdot 10^{(\hat{\jmath}-1)/10}$ from $Ra = 50$ to $Ra = 31548$ and $L_s = 0.01 \cdot 10^{(\hat{k}-1)/10}$ (for integer $\hat{\jmath}$ and $\hat{k}$). For each Ra, the steady governing equations are first solved for a small aspect ratio L_s that is slightly greater than L_c, and then that solution is used as the initial guess for a case with larger L_s.

3.3.2 Solution Structure

The structure of steady convection at large Ra depends on L_s. When $L_s < L_c$, the only steady solution is the conduction state. As L_s is increased, the conduction solution becomes linearly unstable, and two thin thermal boundary layers arise near the upper and lower walls (Figure 3-1). Unlike the unsteady flow observed in DNS, the proto-plumes are absent in the steady solution. Near the walls there exists a boundary layer in the temperature field and a thicker boundary layer in the stream function field. Away from these nested boundary layers, the interior structure for small L_s is quite simple: the temperature deviation from the horizontal mean $\theta' = T - \overline{T}$ and the stream function ψ are almost independent of z so their z-derivatives are small (see Figures 3-1a,b and 3-2a,b), and there exists only a single non-zero horizontal Fourier mode (Figure 3-2a,b). Indeed, this type of steady interior flow is well-approximated using the analytical heat-exchanger solution (2.7)–(2.9) given by Hewitt et al. (2012). By comparing $\overline{T}$ (Figure 3-2a,b), the analytical heat-exchanger and the steady-state numerical solutions are seen to agree closely. One significant difference, of course, is that the analytical heat-exchanger solutions do not satisfy the vertical boundary conditions. Therefore, the numerically computed steady states at large Ra and small L_s, which not

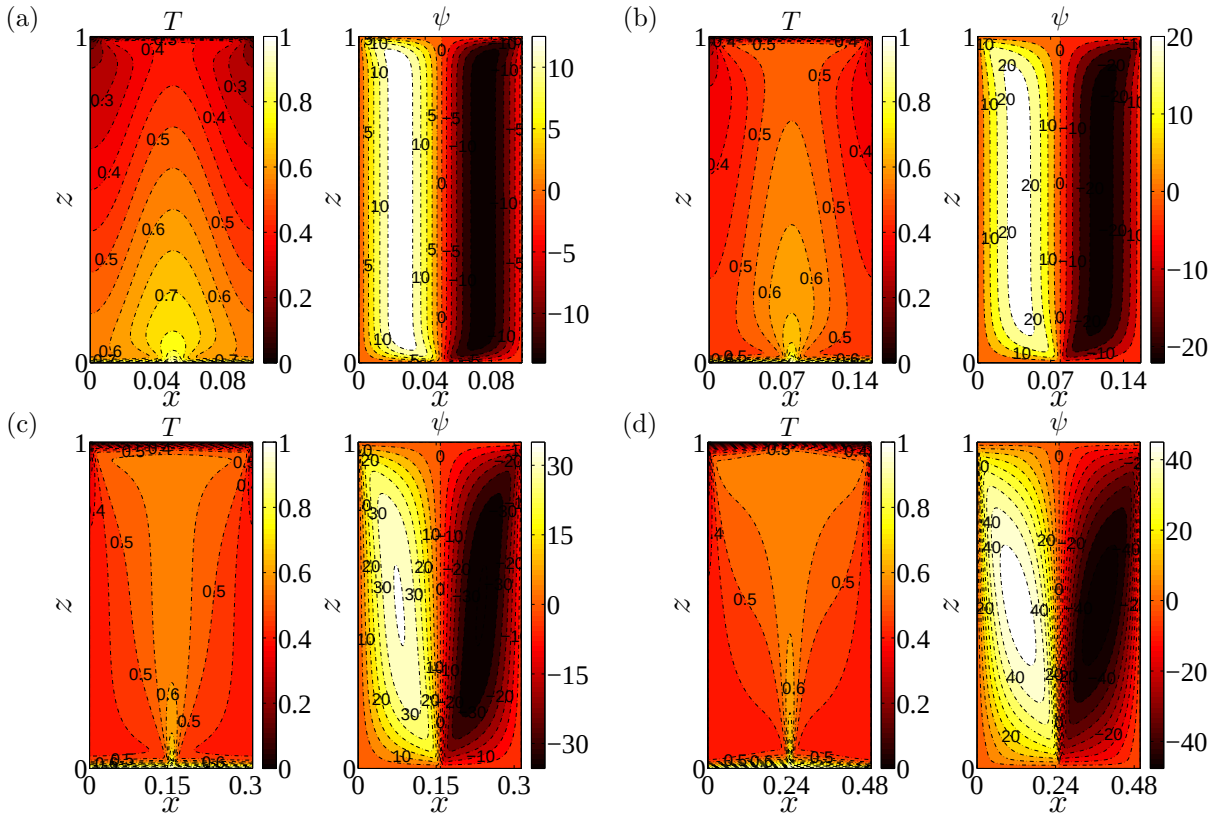

Figure 3-1: Temperature and stream function fields at $Ra = 9976$ ($L_c = 0.063$): (a) $L_s = 0.1$; (b) $L_s = 0.1585$; (c) $L_s = 0.3162$; (d) $L_s = 0.5012$. The aspect ratio in (c) is close to the mean inter-plume spacing $L_m = 0.319$ from DNS performed in a domain with $L = 5.01$. At small L_s (a,b) the interior streamlines are independent of z. However, as L_s is increased (c,d) the interior streamlines become z-dependent. The ψ extremum values ψ_m for (a)–(d) are 14.0, 22.1, 35.4 and 47.7, respectively.

only exhibit the heat-exchanger structure in the interior but also satisfy the steady governing equations and all boundary conditions, will be denoted as numerical heat-exchanger solutions.

Perhaps not surprisingly, as L_s is increased the steady large-Ra numerical solutions do not retain the heat-exchanger structure in the interior. Instead, the streamlines deviate from the vertical (Figure 3-1c,d), and multiple horizontal Fourier modes are excited, although the fundamental mode still dominates the flow (Figure 3-2c,d). Moreover, when L_s is sufficiently

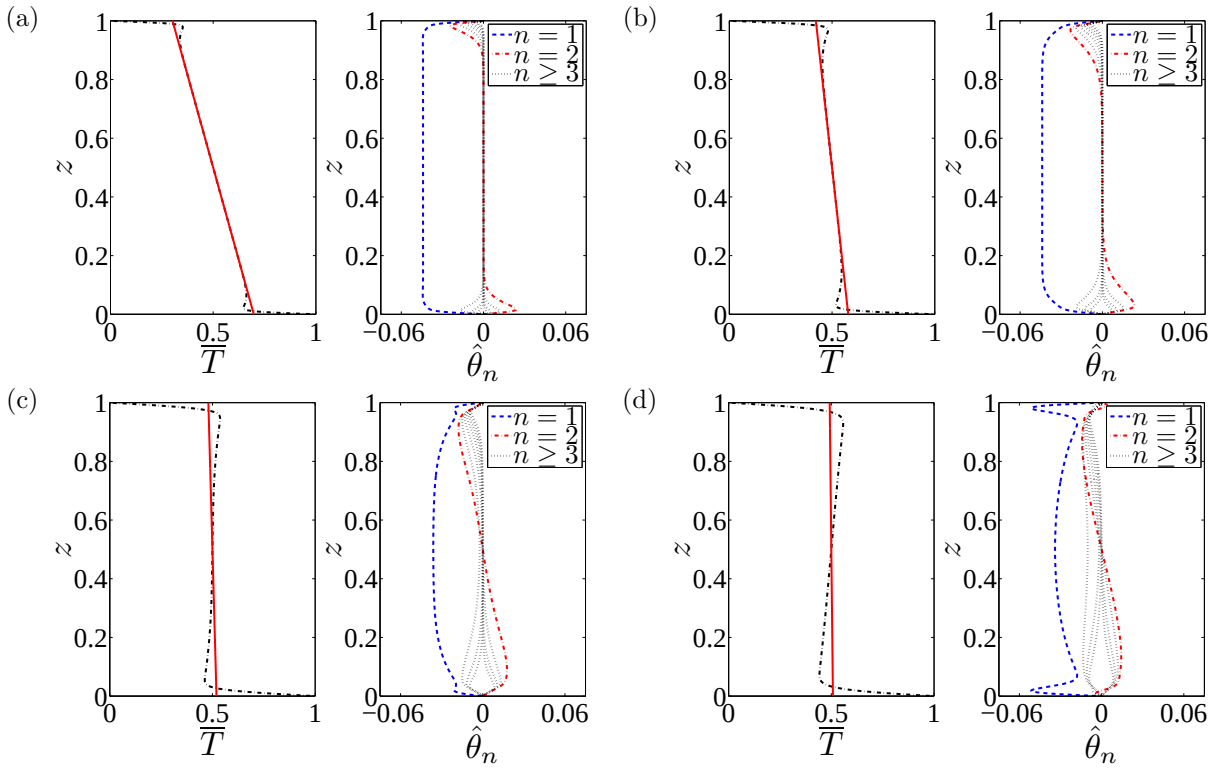

Figure 3-2: z-dependent Fourier components of the temperature field for steady convective states at $Ra = 9976$: (a) $L_s = 0.1$; (b) $L_s = 0.1585$; (c) $L_s = 0.3162$; (d) $L_s = 0.5012$. In the plots of $\overline{T}$, the dashed-dot line is the numerical result and the solid line is the analytical result. At small L_s (a,b) the horizontal mean temperature in the interior agrees closely with the analytical heat-exchanger solution; in the core, only a single (non-mean) Fourier mode is active and the temperature fluctuations are nearly independent of z. However, as L_s is increased (c,d) more Fourier modes arise and the structure of the steady solutions departs from that of the analytical heat-exchanger solution even in the interior.

large, the numerically-computed $\overline{T}$ clearly deviates from that predicted by the heat-exchanger solution. In fact, the slope of $\overline{T}$ at the mid-plane $z = 0.5$ becomes positive, implying hotter fluid overlies colder fluid in the interior. Therefore, this class of numerically-computed steady states will be referred to as stably stratified core solutions.

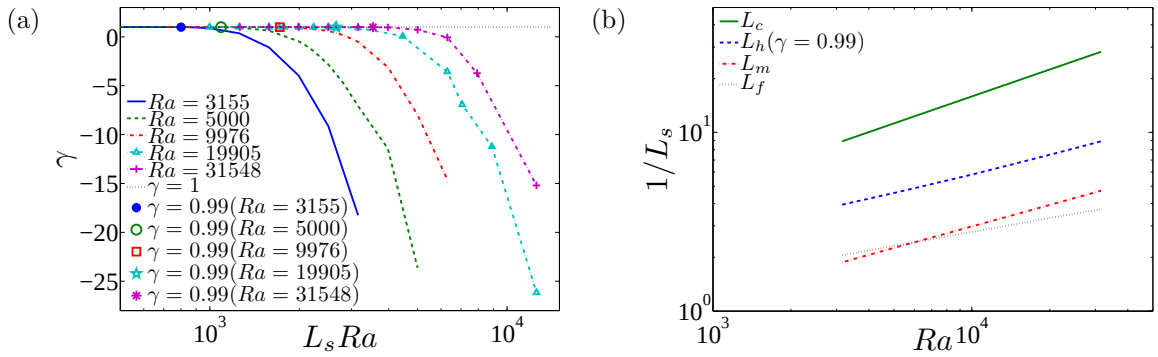

Figure 3-3: (a) Proximity of numerical solutions to the heat-exchanger solution: $\gamma = -(Ra/k_s^2)\partial_z\overline{T}|_{z=0.5}$ versus L_sRa. As L_s is increased, γ eventually departs from unity and the interior structure of the numerical solution changes from that of the heat-exchanger solution to that of the stably-stratified core solution. (b) Variation with Ra of L_h, the wavelength of steady solutions with $\gamma = 0.99$ (i.e. numerical heat-exchanger solutions). Also plotted for comparison are $L_c \sim 2\pi Ra^{-0.5}$, the wavelength of the marginal stability boundary; $L_m \approx (2\pi/0.47)Ra^{-0.4}$, the mean inter-plume spacing measured from the DNS of Hewitt et al. (2012); and $L_f \sim 2\sqrt{\pi}Ra^{-0.25}$, the wavelength of the fastest growing linear mode. Interestingly, at large Ra, $L_m \approx 2L_h$.

To quantify the proximity of a given numerically-computed steady solution to the analytical heat-exchanger solution in the interior, the parameter

$$\gamma = -\frac{Ra}{k_s^2}\partial_z\overline{T}|_{z=0.5} \tag{3.21}$$

measuring the ratio of the numerically-computed mean temperature gradient at the mid-plane to the analytically-predicted (constant) vertical temperature gradient is introduced. The solutions are identical when $\gamma = 1$, and so the steady convective state can be quantitatively (but arbitrarily) defined as a numerical heat-exchanger solution when $0.99 \leq \gamma \leq 1$.

Figure 3-3 shows how the structure of the steady solution changes as Ra and L_s are varied. For small $L_s > L_c$, one can observe that $0.99 \leq \gamma \leq 1$, so these solutions belong to the class of numerical heat-exchanger solutions. However, γ decreases appreciably as L_s increases, and

the steady solutions assume a transitional form for $0 \leq \gamma < 0.99$. When L_s is sufficiently large, γ changes sign, yielding a family of stably stratified core solutions. Note that the wavelength L_h of solutions with $\gamma = 0.99$ (see Figure 3-3b), which separates the heat-exchanger and non-heat-exchanger solutions, is approximately half the mean inter-plume spacing (L_m in Figure 3-3b) measured from the DNS of Hewitt et al. (2012).

As described above, the spatial structure of steady convection varies appreciably with L_s. A natural question concerns the difference between the structure of the steady convective states and that of the time-averaged flow observed in DNS. As Ra increases, DNS indicate that the interior flow self-organizes into narrow columnar plumes, which have been modelled by Hewitt et al. (2012, 2013) using the heat-exchanger solution (2.7)–(2.9). However, the time-averaged columnar flow (see Figure 2-5a) is not strictly equivalent to the heat-exchanger flow: as shown in Figures 3-1(a, b) and 3-2(a, b), the heat-exchanger solution is well represented by the interior part of steady solutions only for convective states with sufficiently small aspect ratios; of course, the time-averaged columnar flow in DNS need not satisfy the steady governing equations. Moreover, the interior part of the columnar flow is a composite of a few low-wavenumber Fourier modes but is dominated by one mode (see Figure 2-6c), features shared by the strictly steady, stably stratified core solutions. Indeed, recall that steady convective states with $L_s = L_m$, the mean inter-plume spacing observed in DNS, are stably stratified core solutions (see Figures 3-1c, 3-2c and 3-3b). Nevertheless, the columnar flow observed in DNS does share some attributes of the heat-exchanger flow: the interior slopes of the corresponding mean temperature fields are not positive; i.e. the core is not stably stratified. Thus, the time-mean columnar core flow is neither an equilibrium heat-exchanger nor a stably-stratified core solutions but, rather, an admixture of these steady convective states.

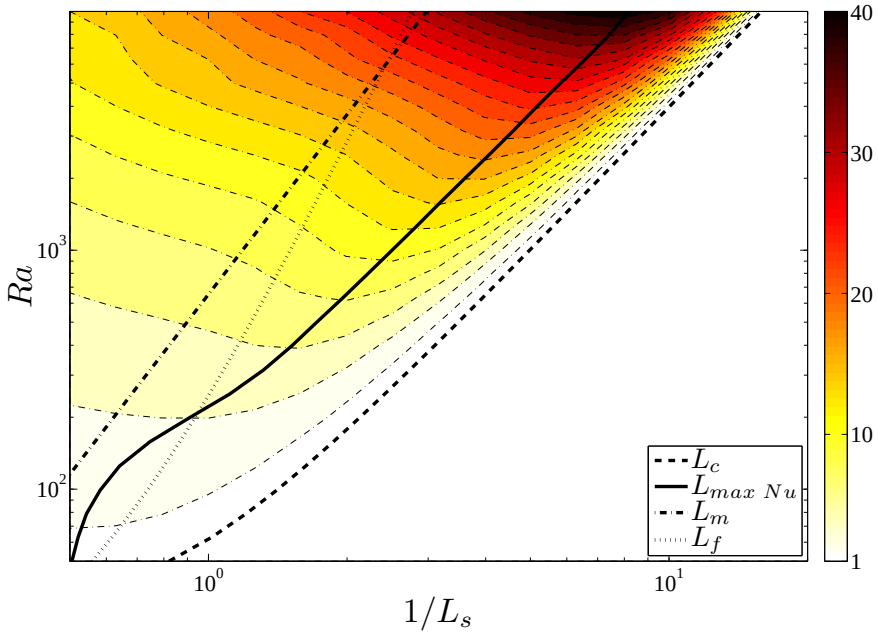

Figure 3-4: Contour plot of Nusselt number in (Ra, L_s) parameter space for steady convective states. The solid line ($L_{max\ Nu}$) marks the path along which Nu is maximized. L_c, L_m and L_f are as in Figure 3-3.

3.3.3 Maximizing Nu

Of particular physical importance is the relationship between the Nusselt number Nu and the two control parameters Ra and L. Figure 3-4 shows the variation of Nu with Ra and L_s for steady convective states (see also Corson (2011)). There is no convection when the domain aspect ratio is smaller than the wavelength L_c of the marginal stability mode, so $Nu = 1$ in this regime. Interestingly, the heat transport in steady convection is maximized along a particular path in (Ra, L_s) parameter space (the solid black curve in Figure 3-4).

To accurately extract the scalings associated with the steady heat-flux-maximizing solutions, greater resolution in parameter space for (Ra, L_s) pairs near the ridge along which Nu is maximized is employed. The computations are also continued to $Ra = 31548$, as shown

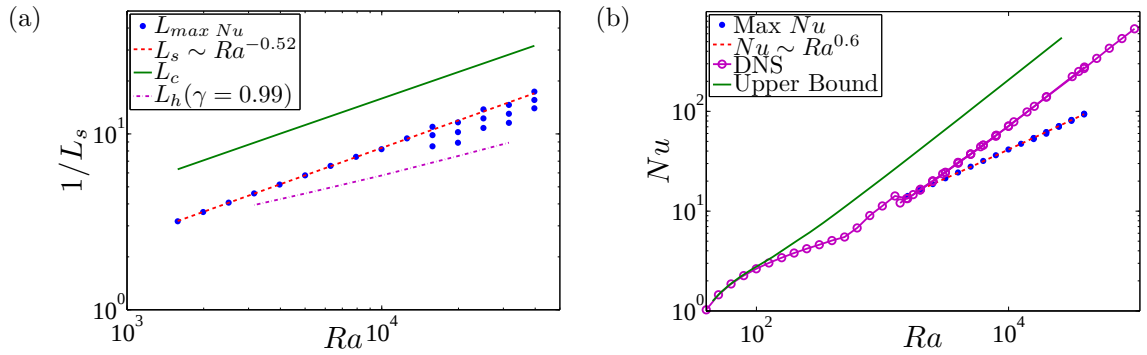

Figure 3-5: (a) Rayleigh-number scaling of the inverse wavelength associated with heat-flux-maximizing steady convective states (dots). Note that at sufficiently large Ra multiple states yield nearly the same (maximum) heat flux. The dashed line is the best fit curve $1/L_s = 0.070Ra^{0.52}$ for $Ra \leq 12559$. For reference, $1/L_h$ and $1/L_c$ are also plotted as functions of Ra. (b) Rayleigh-number scaling of the Nusselt number for steady convective solutions (dots). The dashed line is the best fit curve $Nu = 0.155Ra^{0.60} + 1.213$. For reference, data from various DNS and upper bound analysis is also shown. The DNS results ($Nu \sim 0.0068Ra$) are from Otero et al. (2004), Hewitt et al. (2012) and chapter 2; the upper bound results ($Nu \sim 0.0207Ra$) are from chapter 6.

in Figures 3-4 and 3-5. When Nu is maximum and Ra is less than roughly 100, L_s scales as $Ra^{-1/4}$, the scaling for the wavelength L_f of the fastest-growing linear mode. As Ra is increased, the ridge of maximum Nu shifts to the right and for $10^3 < Ra < 10^4$ $L_s \sim Ra^{-0.52}$. As evident in Figure 3-5(a), the heat-flux-maximizing solutions at large Ra are, in fact, numerical heat-exchanger states. Figure 3-5(b) shows the variation of Nu with Ra for high-Ra steady solutions on the ridge (Corson, 2011), along with results from upper bound analysis and DNS. Both the upper bound calculation and the DNS predict $Nu \sim Ra$ for the unsteady flow. Steady convection at large Ra is thus seen to transport less heat than the realized turbulent flow, with $Nu \sim Ra^{0.6}$ for the equilibrium states (Corson, 2011). However, the heat transported by the steady heat-flux-maximizing solutions increases substantially as the inter-plume spacing (i.e. L_s) decreases from $O(1)$ to asymptotically small values.

3.4 Secondary Stability Analysis

3.4.1 Floquet Theory

To investigate the stability properties of the steady convective states described in the previous section, a secondary stability analysis is performed using spatial Floquet theory. First, all fields are expressed as the sum of the steady nonlinear base flow (denoted with a subscript "s") and a time-varying perturbation,

$$T(x,z,t) = T_s(x,z) + \widetilde{\theta}(x,z,t), \tag{3.22}$$

$$\psi(x,z,t) = \psi_s(x,z) + \widetilde{\psi}(x,z,t), \tag{3.23}$$

where $T_s = (1-z) + \theta_s$. Then the equations governing the evolution of the presumed small-amplitude disturbances can be expressed as

$$\nabla^2\widetilde{\psi} = -Ra\partial_x\widetilde{\theta}, \tag{3.24}$$

$$\partial_t\widetilde{\theta} = \nabla^2\widetilde{\theta} - \partial_x\theta_s\partial_z\widetilde{\psi} + \partial_z\theta_s\partial_x\widetilde{\psi} + \partial_x\psi_s\partial_z\widetilde{\theta} - \partial_z\psi_s\partial_x\widetilde{\theta} - \partial_x\widetilde{\psi}, \tag{3.25}$$

where the perturbation fields also satisfy the boundary conditions

$$\widetilde{\theta}(x,0,t) = 0, \quad \widetilde{\theta}(x,1,t) = 0, \quad \widetilde{\psi}(x,0,t) = 0, \quad \widetilde{\psi}(x,1,t) = 0 \tag{3.26}$$

and L-periodicity (*not* generally L_s-periodicity) in x. Floquet theory implies that the solutions may be sought having the following form:

$$\begin{bmatrix} \widetilde{\theta} \\ \widetilde{\psi} \end{bmatrix} = e^{i\beta k_s x} \left\{ \sum_{n=-\infty}^{\infty} \begin{bmatrix} \hat{\widetilde{\theta}}_n(z) \\ \hat{\widetilde{\psi}}_n(z) \end{bmatrix} e^{ink_s x} \right\} e^{\lambda t} + c.c., \tag{3.27}$$

where λ is the temporal growth rate, $i\beta k_s$ is the Floquet exponent, with the real Floquet parameter β providing the freedom to modify the fundamental horizontal wavenumber of the perturbation (i.e. for $\beta \neq 0$, βk_s is the wavenumber of the largest horizontal scale), and *c.c.* denotes complex conjugate. Since (3.27) is invariant under integer shifts in β and under reflections $\beta \to -\beta$, one can restrict $0 \leq \beta \leq 0.5$ without loss of generality. Substituting (3.27) into (3.24)–(3.25) yields

$$i(n+\beta)kRa\hat{\widetilde{\theta}}_n + \left[D_{zz} - (n+\beta)^2k^2\right]\hat{\widetilde{\psi}}_n = 0, \tag{3.28}$$

$$\left[D_{zz} - (n+\beta)^2k^2 + \widetilde{h}_n\right]\hat{\widetilde{\theta}}_n + \left[-i(n+\beta)k + \widetilde{g}_n\right]\hat{\widetilde{\psi}}_n = \lambda\hat{\widetilde{\theta}}_n \tag{3.29}$$

for each n, where $\widetilde{h}_n$ and $\widetilde{g}_n$ can be determined by calculating the convolution of the non-constant-coefficient terms in (3.25). After setting $\hat{\widetilde{\psi}}_n = i\hat{\widetilde{\phi}}_n$, (3.28)–(3.29) can be written in the form

$$A\mathbf{V} = \lambda B\mathbf{V}, \tag{3.30}$$

where A and B are real matrixes owing to the symmetries (3.8) of the base flow, and the vector $\mathbf{V} = (\cdots\hat{\widetilde{\theta}}_{n-1}, \hat{\widetilde{\theta}}_n, \hat{\widetilde{\theta}}_{n+1}\cdots\hat{\widetilde{\phi}}_{n-1}, \hat{\widetilde{\phi}}_n, \hat{\widetilde{\phi}}_{n+1}\cdots)^T$. The eigenvalue λ and the corresponding eigenvector $\mathbf{V}$ can be obtained by numerically solving this differential eigenvalue problem. Note that in the following sections, the convective rather than diffusive time, $\tau \equiv tRa$, will

be utilized, so that the corresponding convective growth rate $\sigma \equiv \lambda/Ra$.

3.4.2 Secondary Stability Results

The eigensystem (3.30) is discretized using a Chebyshev collocation method and the infinite-dimensional system is truncated to $0 \leq m \leq M$ vertically and $-N/2 \leq n \leq N/2$ horizontally. Arnoldi iteration is used to solve the resulting algebraic eigenvalue problem to obtain the leading eigenvalues and eigenfunctions. The numerical resolution is increased until the relative error in the eigenvalue with the largest real part, σ_m, is less than 10^{-4}.

Figure 3-6 shows the contours of maximum growth rate, $\mathrm{Re}\{\sigma_m\}$, as a function of β and L_s for various Ra. At a given Ra, the steady solution at small L_s (specifically, $L_c < L_s < L_b$, where L_b is a stability boundary defined in Figures 3-8 and 3-9) is marginally stable for $\beta = 0$ – corresponding to disturbances that simply translate the steady base flow in x – although there is insufficient resolution around $\beta = 0$ to observe this clearly in the contour plots. However, the solution is unstable for a range of long-wavelength perturbations ($0 < \beta \leq 0.5$, see Figure 3-6). The Floquet parameter β of the fastest-growing perturbation is approximately 0.2–0.3, implying that the most unstable disturbance has a wavelength 3–5 times the wavelength of the base flow. At $Ra = 1581$ and 3155, the growth rate of the most unstable mode decreases as L_s is increased and, in fact, the steady solution becomes linearly stable for a finite range of L_s. However, as L_s is further increased, the steady state becomes unstable, exhibiting a growth rate that is essentially *independent* of β. Similar phenomena are observed at larger Ra except that the linearly stable region shrinks nearly to a point at $Ra = 5000$ and vanishes completely at larger Ra.

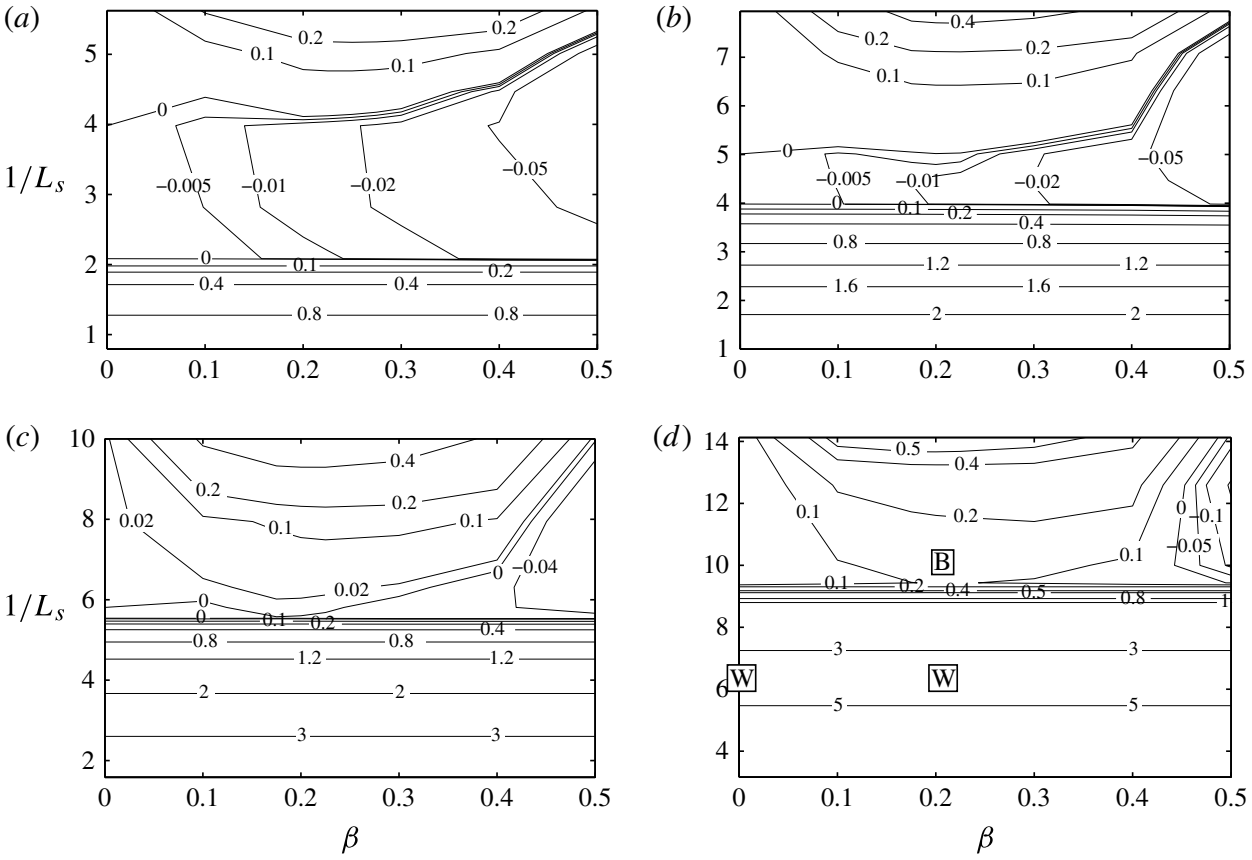

Figure 3-6: Contours of the maximum growth rate $\mathrm{Re}\{\sigma_m\}$ as a function of β and L_s for various Ra: (a) $Ra = 1581$; (b) $Ra = 3155$; (c) $Ra = 5000$; (d) $Ra = 9976$. At small L_s ($L_c < L_s < L_b$), the base state is stable within small domains of size $L_s \times 1$ (since $L = L_s$ for $\beta = 0$), but unstable to certain long-wavelength perturbations ($0 < \beta \leq 0.5$); at large L_s, the base state is unstable even for $\beta = 0$, and has the same growth rate for different β. Note that contour plot in (d) has been annotated to indicate the parameters corresponding the bulk ("B") and wall ("W") mode eigenfunctions displayed in Figure 3-7.

Figure 3-7 shows, for $Ra = 9976$, the 2D eigenfunctions corresponding to these two families of secondary instabilities. At small L_s, e.g., $L_s = 0.1$, when the growth rate depends on the horizontal wavenumber βk_s, the most unstable perturbation (occurring for $\beta \approx 0.2$) is a bulk mode that spans the layer (Figure 3-7a).[1] However, for larger L_s, e.g., $L_s = 0.1585$, the

[1]The term "bulk mode" is used here and throughout to characterize perturbations with non-uniform spatial structures throughout the entire domain including the near-wall and interior regions.

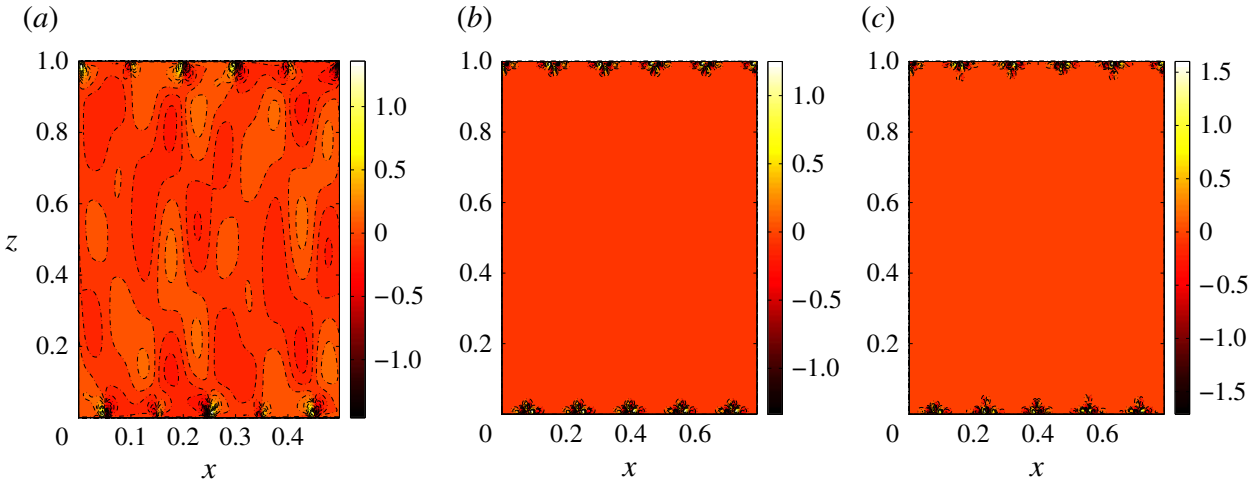

Figure 3-7: Fastest-growing 2D temperature eigenfunctions at $Ra = 9976$ shown in a domain with aspect ratio $L = 5L_s$ (where L_s is the wavelength of the steady base state): (a) $L_s = 0.1$, $\beta = 0.2$; (b) $L_s = 0.1585$, $\beta = 0$; (c) $L_s = 0.1585$, $\beta = 0.2$. At small L_s, a bulk mode controls the instability, and at large L_s, a wall mode dominates. Note that at large L_s the spatial structure of the fastest-growing (wall) mode is nearly independent of β.

most unstable perturbation for each β has nearly the same growth rate and a very similar spatial structure, which is strongly localized near the upper and lower walls (Figure 3-7b,c), and hereafter is referred to as a wall mode. Figure 3-8 shows the eigenspectrum for three different (β,L_s) combinations. Note that the bulk mode, as shown in Figure 3-7(a), occurs for certain long-wavelength (e.g. $\beta = 0.2$) disturbances and exhibits comparably small growth rates ($\sigma_m = O(0.1)$). At small L_s, the bulk modes control the instability. As L_s is increased, however, an increasing number of wall modes becomes unstable. These wall modes, which are born in a Hopf bifurcation associated with the advection of small-scale disturbances within the thermal boundary layers (see Aidun and Steen (1987) and Graham and Steen (1992, 1994)), ultimately dominate the secondary instability with growth rates 10-50 times larger than those associated with the bulk modes. For sufficiently large L_s, the eigenspectra for disturbances with distinct fundamental horizontal wavenumbers are very similar. This

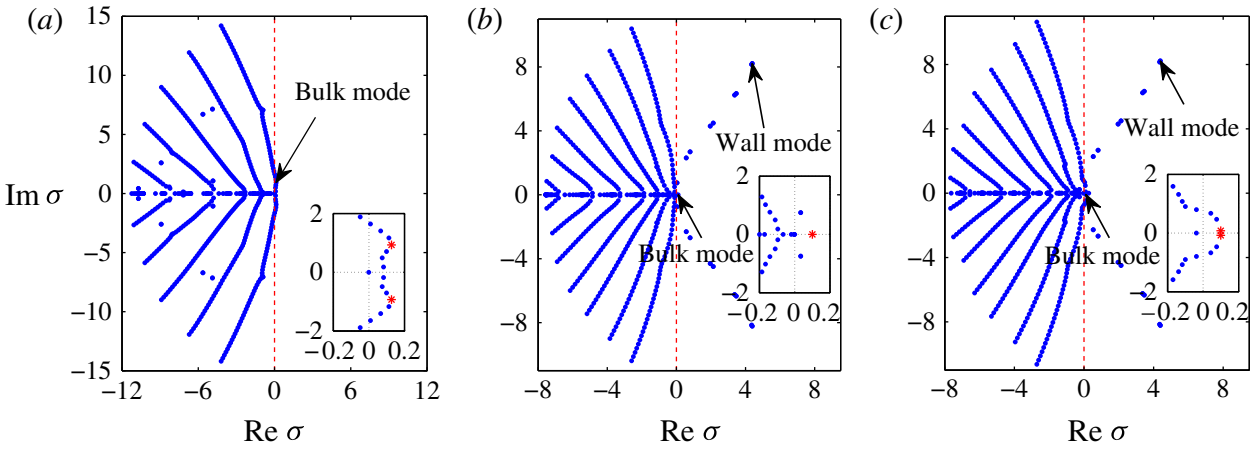

Figure 3-8: Leading eigenvalues at $Ra = 9976$: (a) $L_s = 0.1$, $\beta = 0.2$; (b) $L_s = 0.1585$, $\beta = 0$; (c) $L_s = 0.1585$, $\beta = 0.2$. Re σ (Im σ) is the real (imaginary) part of σ. In each case, the inset shows a magnification of the region near the origin, with the asterisk denoting the most unstable bulk mode(s). L_b is defined such that when $L_s < L_b$ (as in a) only bulk modes exist. As L_s is increased (b,c), an increasing number of wall modes is destabilized. Note the similarity of the eigenspectrum in (b) and (c) for the same (large) L_s.

section can be concluded by contrasting the secondary stability results of this investigation with those of Hewitt et al. (2013). Not only does this study find two modes of instability rather than one, but in the presence of walls the bulk modes are found to have much reduced growth rates: specifically, $O(0.1)$ rather than $O(1)$.

3.5 Nonlinear Evolution of the Instability

In this section strategically initialized, high-resolution DNS in wide domains are used to investigate the nonlinear evolution of the fastest-growing secondary instability mode for various steady convective states distinguished by their wavelength L_s. The aim is to gain insight into the mechanisms by which the base flow, with plume spacing L_s, evolves to the

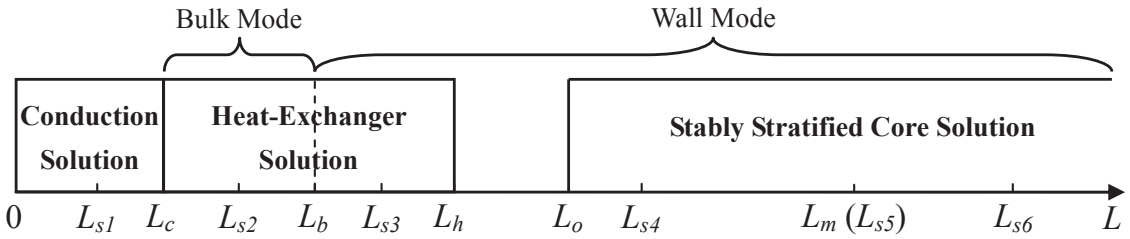

Figure 3-9: Schematic identifying distinct steady states and the associated secondary instability regimes at large Ra. DNS is performed for six steady base states with aspect ratios L_{s1}–L_{s6} to study the fully nonlinear evolution of the fastest-growing instability modes. L_o is the aspect ratio for which the normalized horizontal mean temperature gradient $\gamma = 0$.

final columnar flow, with mean inter-plume spacing L_m (in the bulk). The steady state at a given L_s plus a small-amplitude contribution of the most unstable secondary instability mode is chosen as the initial condition, and then DNS is performed in a large domain with $L = 10L_s$–$20L_s$.

As shown in Figure 3-9, for a specific large $Ra = O(10^4)$, with increasing L, generally $L_c < L_b < L_{max\ Nu} < L_h < L_o < L_m$, where: L_c is the wavelength of the neutral mode on the right-hand marginal stability boundary of the conduction state; L_b is the largest aspect ratio at which only the bulk instability mode exists; $L_{max\ Nu}$ is the wavelength of the steady cellular flow that maximizes the heat transport; L_h is the largest aspect ratio at which the heat exchanger solution is relevant; and L_o is the aspect ratio at which the parameter γ vanishes (implying a steady base flow with zero mean stratification in the centre of the cell). In the following sections, six different steady convective states, five at $Ra = 9976$ and one at $Ra = 50000$, are considered: L_{s1} is less than L_c so that the base state is the conduction solution; L_{s2} is greater than L_c but within the aspect-ratio range for which the bulk mode controls the instability; $L_{s3} > L_b$ but is within the numerical heat-exchanger solution regime; L_{s4} is between L_h and L_m, within the stably stratified core solution regime; L_{s5} is close to the

final mean inter-plume spacing L_m; and L_{s6} is much larger than L_m. Thus, for $Ra = 9976$, for example, $L_c = 0.063$, $L_b = 0.106$, $L_h = 0.172$, $L_m = 0.319$ (measured from DNS in $L = 5.012$), and $L_f = 0.36$.

3.5.1 L_{s2} $(Ra = 9976)$

For $Ra = 9976$, DNS are first performed to investigate the dynamics ensuing from unstable steady states with $L_s = L_{s2}$, which is within the bulk instability parameter regime. The initial condition comprises 20 replicas of the steady convective state at $L_s = 0.1$ plus a small-amplitude contribution of the corresponding fastest growing perturbation at $\beta = 0.2$. Figure 3-10 depicts the nonlinear evolution from this initial state to the final turbulent columnar flow. Initially, the dominant horizontal mode number in the interior $n_d = 20$. In accord with the stability analysis in section 3.4 and as evident in Figure 3-10(b) and (c), the base state is unstable to a bulk mode. As the secondary mode grows in amplitude, the pattern coarsens to an unsteady convective state at $\tau = 87.29$ (Figure 3-10d) with five times the wavelength of the initial steady cellular solution. The resulting mean inter-plume spacing, however, is larger than the final L_m. Subsequently, some plumes growing from the upper and lower boundary layers split the wider plumes into narrower ones (Figure 3-10e). These proto-plumes appear to be generated by a localized instability that closely resembles the wall-mode secondary instability of strictly steady base states having a wavelength greater than L_b (Figure 3-10d). It should be noted that ideally, this dynamical system should retain the $\frac{L}{4}$-periodicity symmetry in x (see Figure 3-10b-e) as time evolves. However, due to the numerical errors (or round-off errors), this lateral symmetry is broken after a long time, and ultimately, the system converges to a statistically steady turbulent state (Figure 3-10f). This "symmetry breaking" is acceptable since small numerical errors generally play the role of

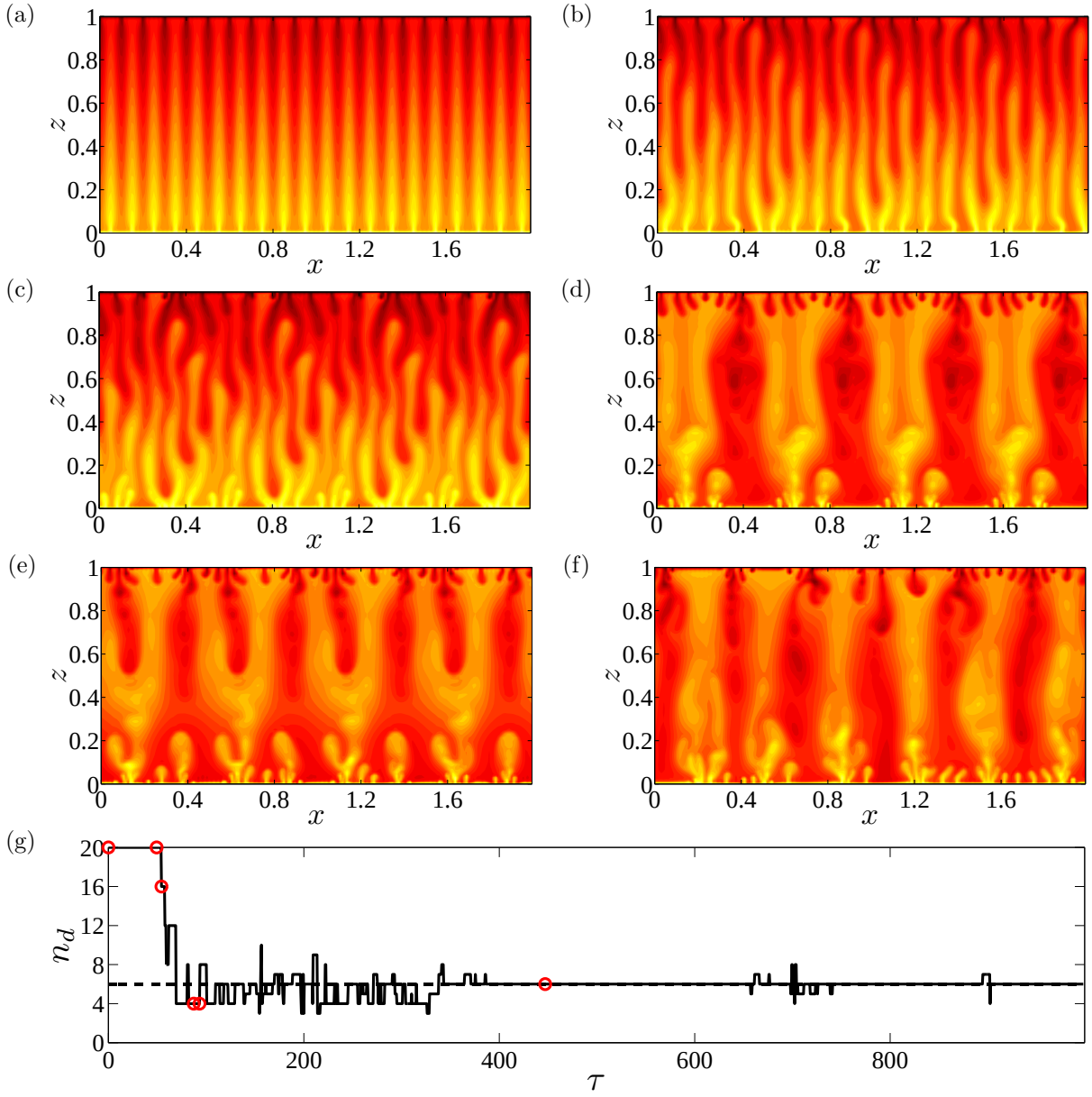

Figure 3-10: Snapshots of the temperature field from DNS showing the nonlinear evolution of the fastest-growing secondary instability mode for $L_{s2} = 0.1$, $L = 20L_{s2}$, $Ra = 9976$. (a) $\tau = 0$; (b) $\tau = 49.38$; (c) $\tau = 54.37$; (d) $\tau = 87.29$; (e) $\tau = 93.28$; (f) $\tau = 446.94$; (g) Time-evolution of the dominant horizontal mode number at $z = 0.5$ (solid line). The dashed line shows the time-average dominant mode number, and the circles correspond to the times highlighted in (a) to (f).

noise in real systems. Thus, there exist two stages of evolution: initially, the bulk instability controls the evolution of the flow so that the background plumes merge forming a convective flow with smaller interior wavenumber; then, as the plume spacing becomes too wide, a variant of the boundary instability intensifies so that small plumes generated from the upper and lower walls are able to split the wider plumes into narrower ones until the flow settles into a statistically-steady state. It should be noted that the first stage of this process is loosely similar to the instability and predicted nonlinear evolution of the analytical heat-exchanger flow described in Hewitt et al. (2013), in which only the bulk instability mode is found.

3.5.2 L_{s3} $(Ra = 9976)$

Next, a wider base flow with $L_s = L_{s3} = 0.1585$, which also is a member of the numerical heat-exchanger family but which is (most) unstable to wall modes, is considered. From the stability analysis, the growth rate and spatial structure of the most unstable perturbation is nearly independent of β (see Figures 3-6*d* and 3-7*b*,*c*). The initial condition for the DNS consists of sixteen copies of this steady state plus a small-amplitude contribution of the most unstable perturbation at $\beta = 0$. Figure 3-11 shows the nonlinear evolution from this initial condition to the final state. By construction, the dominant horizontal mode number in the interior is $n_d = 16$ at $\tau = 0$. At early times ($\tau = 2.49$, Figure 3-11*b*), proto-plumes generated in the upper and lower boundary layers because of the wall instability are continually swept into and thus merge with the mega-plumes in the interior. However, the resulting quasi-time-periodic flow itself evidently is unstable to a variant of the bulk mode (Figure 3-11*c*), causing a coarsening of the convective pattern (Figure 3-11*d*,*e*), in rough correspondence with the first stage of the evolution for the base flow with $L_s = L_{s2}$. The plumes generated from the walls then split the wider plumes before the flow reaches a statistically-steady state (Figure 3-11*f*),

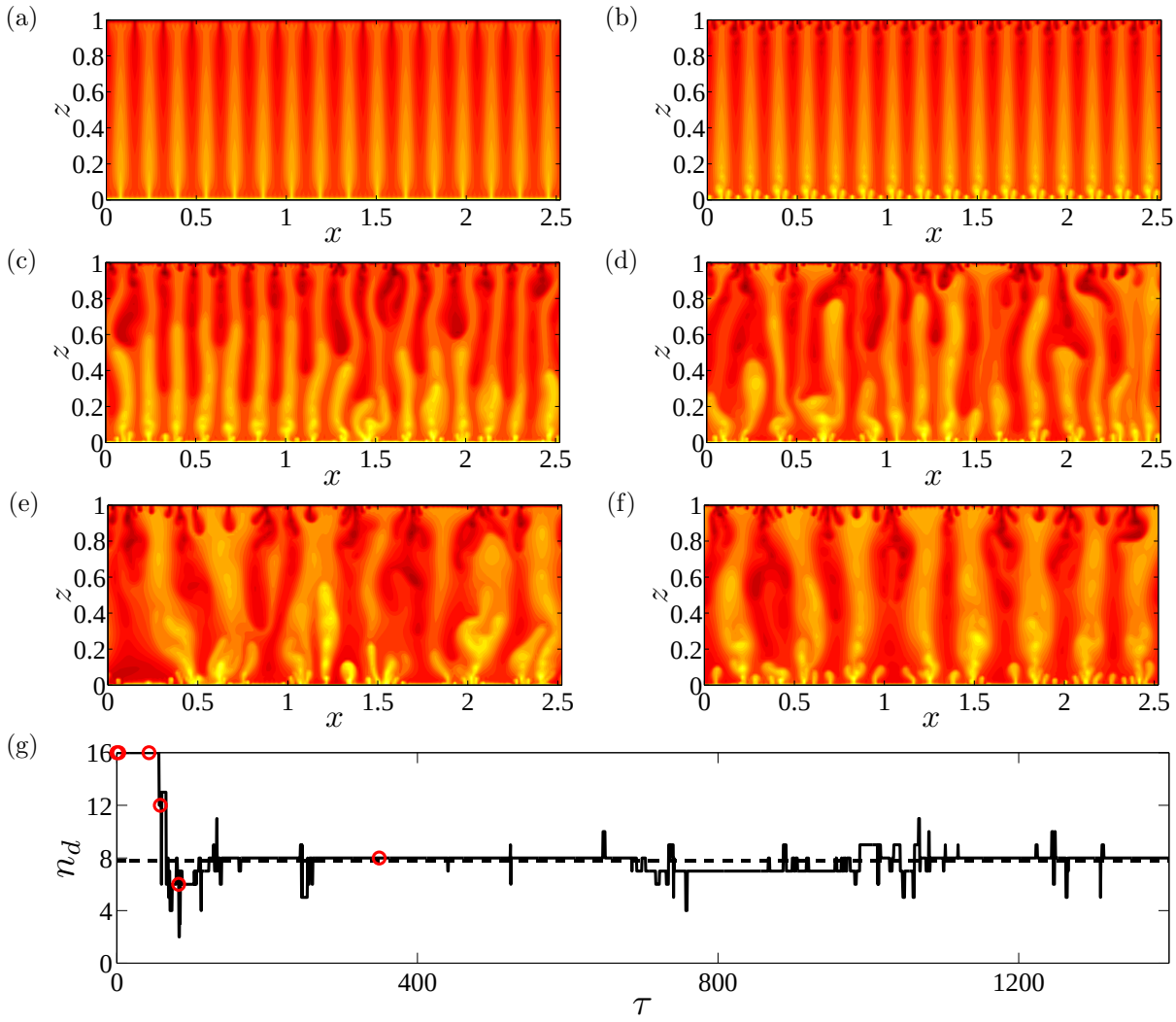

Figure 3-11: Snapshots of the temperature field from DNS showing the nonlinear evolution of the fastest-growing secondary instability mode for $L_{s3} = 0.1585$, $L = 16L_{s3}$, $Ra = 9976$. (a) $\tau = 0$; (b) $\tau = 2.49$; (c) $\tau = 42.90$; (d) $\tau = 57.86$; (e) $\tau = 82.30$; (f) $\tau = 349.17$; (g) Time-evolution of the dominant horizontal mode number at $z = 0.5$ (solid line). The dashed line shows the time-average dominant mode number, and the circles correspond to the times highlighted in (a) to (f).

similar to the second stage of the evolution for the case for which $L_s = L_{s2}$. Interestingly, the final state is not dominated by a unique horizontal wavenumber in the interior. In short, there exist three evolutionary stages for the scenario with $L_s = L_{s3}$. In the linear instability

regime, the wall mode dominates the evolution of the flow so that a series of proto-plumes rising from the walls merge with the background mega-plumes; this process leaves the mean inter-plume spacing unchanged from its initial value L_s. However, the modified, roughly time-periodic flow appears to be susceptible to a bulk instability, causing the merger of some mega-plumes. Finally, as the inter-plume spacing increases, a wall-like mode is again activated and some of the nascent proto-plumes split the wider plumes, yielding the final turbulent convective state. This scenario suggests that a generalization of the bulk instability may occur for unsteady flow, and that this instability intensifies as the inter-plume spacing is reduced.

3.5.3 L_{s4} and L_{s5} $(Ra = 9976)$

Figure 3-12 shows the time-evolution of the dominant horizontal mode number in the interior for cases $L_s = L_{s4}$ and $L_s = L_{s5}$. For $L_s = L_{s4} = 0.224$, the steady state belongs to the family of stably stratified core solutions, but the inter-plume spacing is still less than that of the final state. From Figure 3-12(a), it can be ascertained that the evolution for case L_{s4} is similar to that for case L_{s3}. In Figure 3-12(b), $L_{s5} = 0.316$ is very close to L_m so that the base state evolves directly to the final state, with the dominant interior horizontal wavenumber fluctuating within a small range.

3.5.4 L_{s6} $(Ra = 9976)$

Figure 3-13 shows the evolution for case $L_s = L_{s6} = 0.501$, which is much larger than L_m. As demonstrated using secondary stability analysis, this wide aspect-ratio convective state

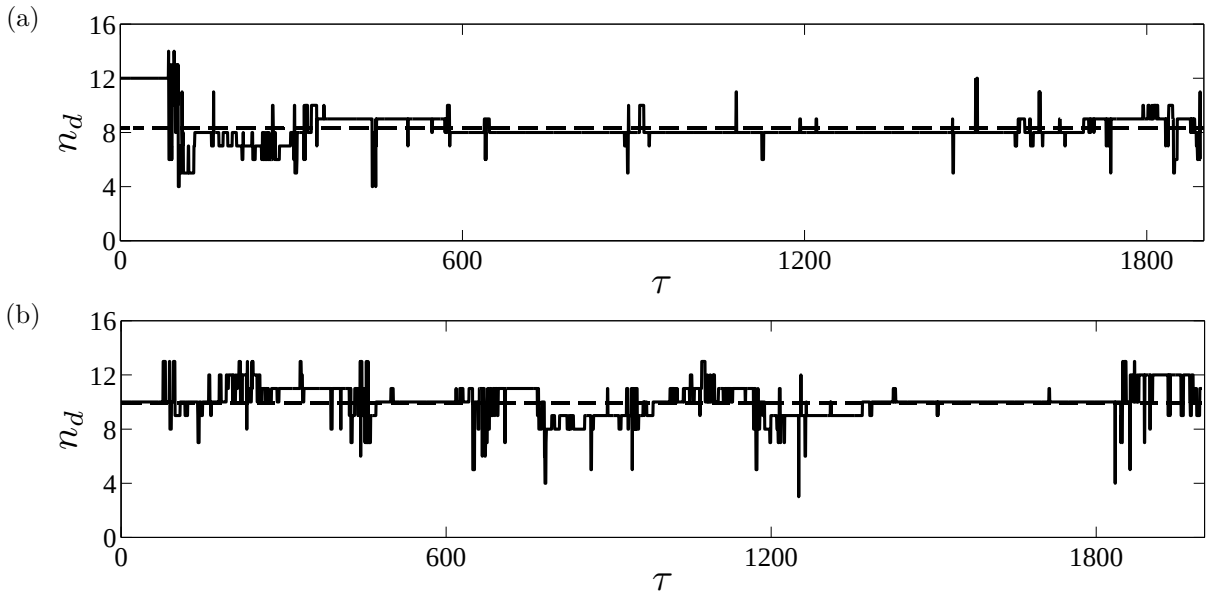

Figure 3-12: Time-evolution of the dominant horizontal mode number at $z = 0.5$ for the temperature field from DNS at $Ra = 9976$ (solid line). The dashed line shows the time-average dominant mode number. (a) $L_{s4} = 0.224$, $L = 12L_{s4}$; (b) $L_{s5} = 0.316$, $L = 10L_{s5}$.

is strongly unstable to a wall mode. At early times, a series of proto-plumes generated from the upper and lower boundary layers continually feed the background mega-plumes (Figure 3-13*b*,*c*), creating a quasi-periodic flow state. Moreover, for a short time, the dominant interior horizontal wavenumber for this unsteady flow remains constant at L_{s6}, hence the inter-plume spacing remains much larger than L_m. However, owing to the strong boundary instability some proto-plumes grow and split the wider mega-plumes into narrower ones. This process continues until the flow converges to the final state. Thus, there is only a single stage of evolution for this case: the strong boundary instability dominates the evolution of both the initial steady state and the ensuing unsteady flow with large L_s, generating boundary plumes that ultimately split the wide aspect-ratio interior mega-plumes. This boundary instability becomes much stronger as L_s increases.

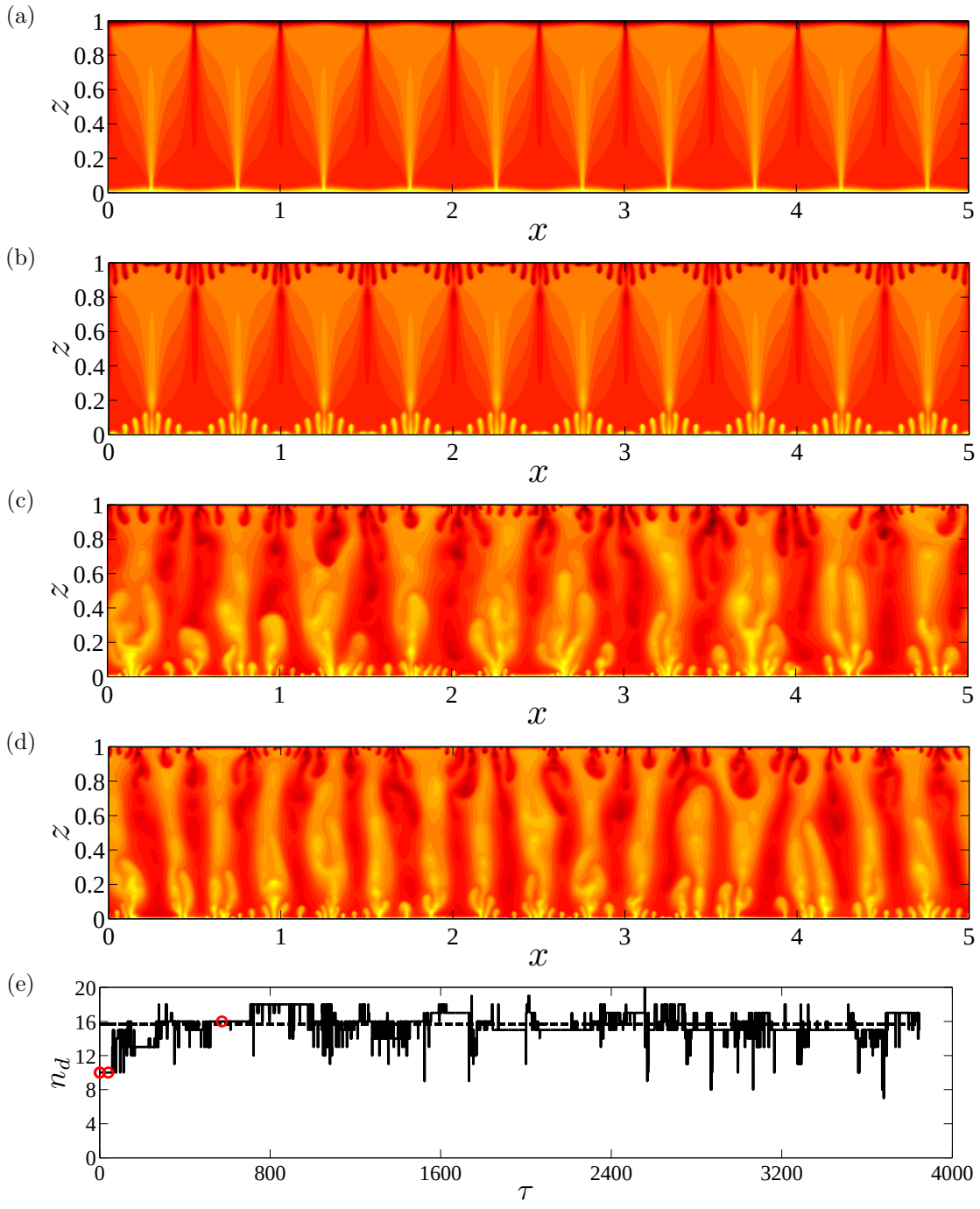

Figure 3-13: Snapshots of the temperature field from DNS showing the nonlinear evolution of the fastest-growing secondary instability mode for $L_{s6} = 0.5012$, $L = 10L_{s6}$, $Ra = 9976$. (a) $\tau = 0$; (b) $\tau = 1.50$; (c) $\tau = 40.40$; (d) $\tau = 573.64$; (e) Time-evolution of the dominant horizontal mode number at $z = 0.5$ (solid line). The dashed line shows the time-average dominant mode number, and the circles correspond to the times highlighted in (a) to (d).

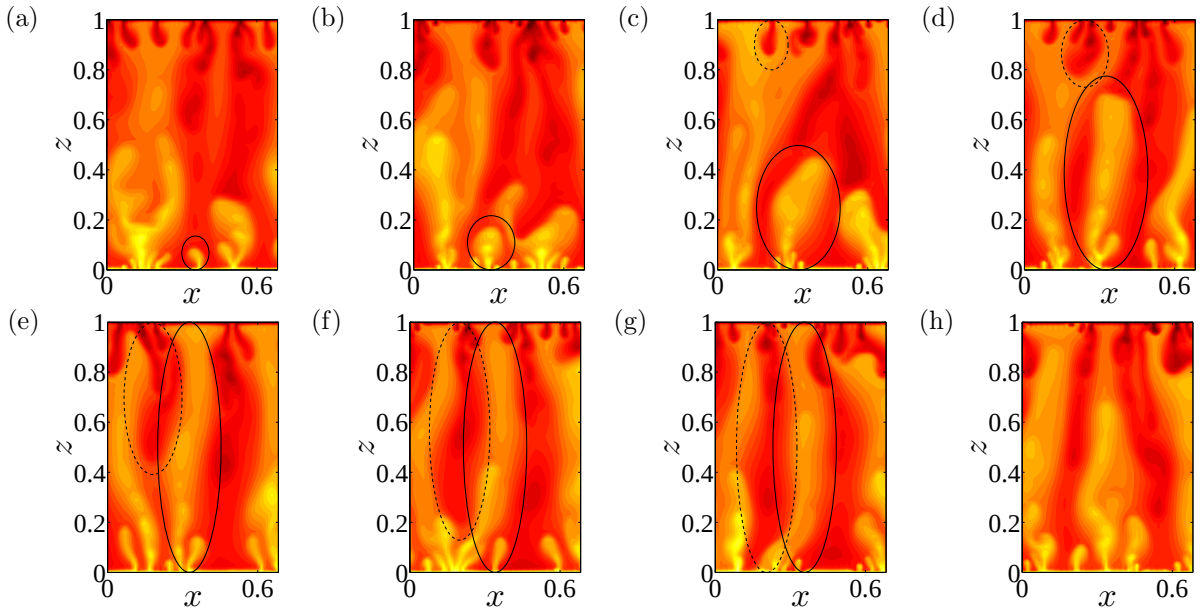

Figure 3-14: Splitting process from a wider plume to a narrower one, $L_{s6} = 0.5012$, $L = 10L_{s6}$, $Ra = 9976$. (a) $\tau = 40.4$; (b) $\tau = 43.4$; (c) $\tau = 47.9$; (d) $\tau = 51.4$; (e) $\tau = 56.4$; (f) $\tau = 59.9$; (g) $\tau = 61.9$; (h) $\tau = 68.8$. Solid ellipse marks the growing process for the hot plume; dashed ellipse marks the growing process for the cold plume. Only the portion of the domain $0 \leq x \leq 0.69$ is shown to highlight the plume splitting process.

As noted above, only a fraction of the growing proto-plumes successfully split the wide mega-plumes. Figure 3-14 shows this plume splitting process. Initially, a small (warm) proto-plume is generated near the lower wall because of the boundary-localized instability (Figure 3-14a). Shortly thereafter, many smaller proto-plumes generated around its root merge with the primary proto-plume, accelerating its growth (Figure 3-14b,c). Meanwhile, another (cold) proto-plume is generated near the upper wall and grows downward (Figure 3-14c,d). The upward growing plume soon reaches the upper wall, forming a mega-plume (Figure 3-14e). Near the bottom wall, this mega-plume begins to merge with its neighboring warm mega-plume; however, the growing cold plume disrupts this merging process by splitting the wider root into two narrower roots (Figure 3-14f). Finally, the cold plume reaches the bottom

wall, forming another downwelling mega-plume (Figure 3-14g). Hence, the wider plume is successfully split into two narrower ones (Figure 3-14h).

3.5.5 L_{s1} $(Ra = 50000)$

As described in section 3.2, the conduction solution is linearly stable in domains of sufficiently small aspect ratio ($L < L_c$). This solution is, of course, linearly unstable at larger L. It should be noted that since the wavenumber of the fastest growing mode $k_f = \pm(\pi\sqrt{Ra} - \pi^2)^{1/2}$, the corresponding wavelength $2\pi/k_f$ is larger than the mean inter-plume spacing measured from DNS at large Ra, e.g., at $Ra = 50000$. To illustrate the nonlinear evolution of a non-convective base flow with very small $L_s = L_{s1} \leq L_c$ in the high-Ra regime, the conduction solution plus its most unstable perturbation at $Ra = 50000$ is used as the initial condition for DNS in a larger domain with $L = 10L_f$. From Figure 3-15, it is seen that at early times the flow evolves in accord with the predictions of linear theory (see (3.1) and Figure 3-15b,c). However, after a short while, thermal boundary layers form near the upper and lower walls, and in the interior the flow develops a stably stratified structure (with hot/lighter fluid above cold/heavier fluid, Figure 3-15d). This structure is similar to that of the steady stably-stratified core solution at large L_s. Since the inter-plume spacing is comparably large, a boundary instability dominates the subsequent evolution, with many small proto-plumes generated near the walls (Figure 3-15e). Unlike the previous cases in which the proto-plumes merge into the background mega-plumes, the strong *stable* stratification in the core prevents the warm and cold plumes from penetrating across the domain. Instead, these proto-plumes impact near the mid-plane (Figure 3-15f). After a series of plume merging and splitting events, the flow evolves to the final state (Figure 3-15g and h). Figure 3-15(i) shows the evolution of the dominant interior mode number for this scenario.

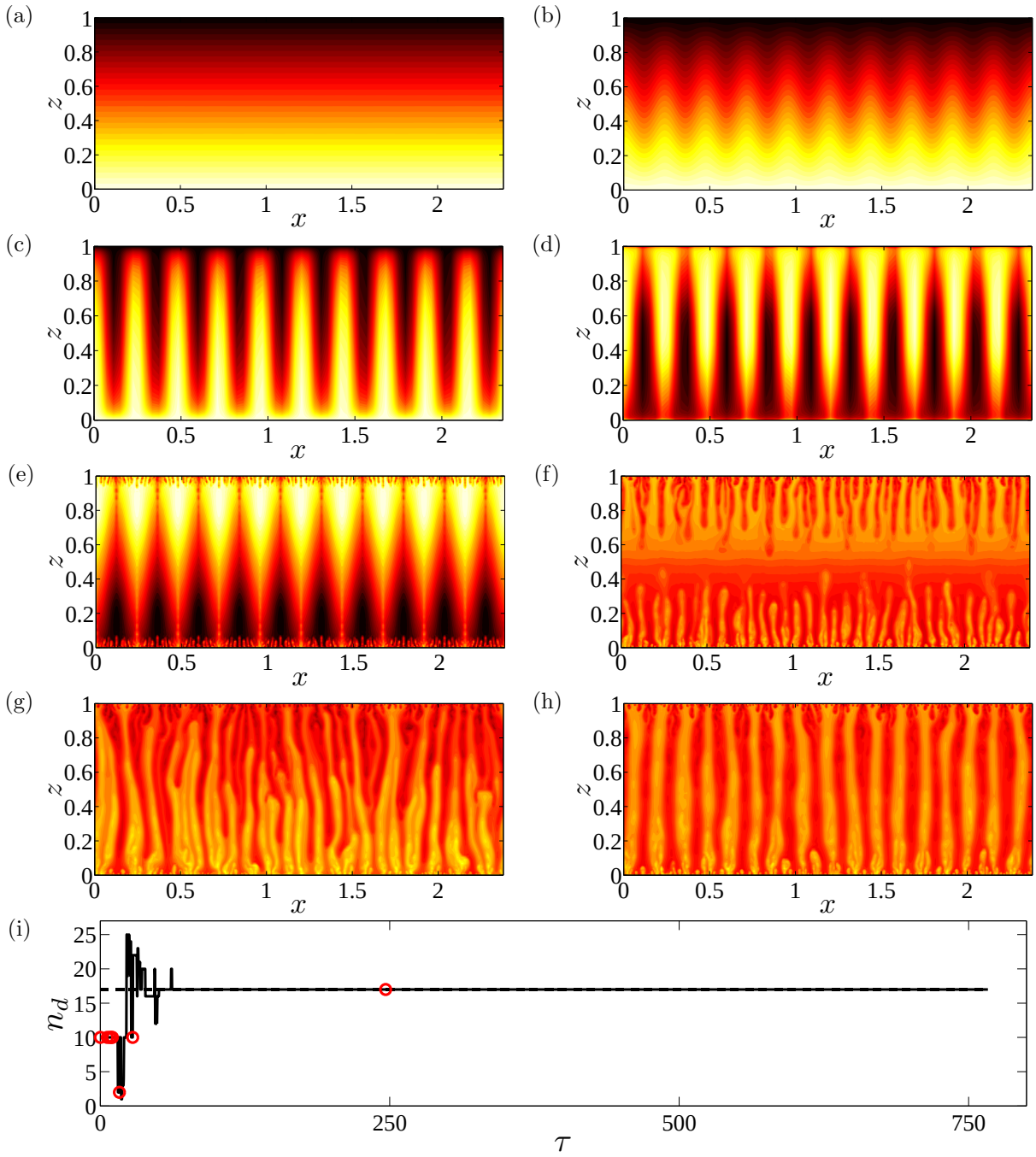

Figure 3-15: Snapshots of the temperature field from DNS showing the nonlinear evolution of the fastest-growing linear instability mode for any $L_{s1} \leq L_c$, $L = 10L_f$ ($L_f = 0.2387$), $Ra = 50000$. (a) $\tau = 0$; (b) $\tau = 6$; (c) $\tau = 8.25$; (d) $\tau = 9.5$; (e) $\tau = 10.5$; (f) $\tau = 16.5$; (g) $\tau = 28$; (h) $\tau = 227$; (i) Time-evolution of the dominant horizontal mode number at $z = 0.5$ (solid line). The circles correspond to the times highlighted in (a) to (h).

From the preceding discussion, it can be concluded that for large Ra the final mean inter-plume spacing is determined by an interplay between (suitably generalized) bulk-mode and wall-mode instabilities. When the inter-plume spacing is small, the bulk mode controls the instability, causing plume merger and coarsening of the convective pattern; when the inter-plume spacing is large, the wall-mode instability dominates, causing small plumes generated from the walls to split the wider plumes into narrower ones. To find the mean inter-plume spacing at which the effects of these two instabilities balance, DNS have been performed up to $Ra = O(10^5)$ in which L_m is measured by taking a long-time average of the inter-plume spacing in wide domains, as shown in Figure 2-8. The results indicate that the scaling relations of $L_m \sim Ra^{-0.4}$ proposed by Hewitt et al. (2012) is only valid for $Ra \leq 10000$, and for $Ra \geq 39716$, the interior flow becomes very well organized and appears to be metastable within a band of wavelengths.

3.6 Summary

In this chapter, the form, stability and nonlinear evolution of initially steady cellular porous medium convection in the high-Ra regime have been examined as a function of the domain aspect ratio. The results show that the steady solutions capture certain features characterizing the turbulent columnar flows observed in DNS. For steady states with small aspect ratio L_s (but for which $L_s > L_c$, the linear stability boundary), the steady flow has a heat-exchanger structure in the interior: the vertical advection of the horizontal mean temperature is precisely balanced by the lateral diffusion of the fluctuation temperature field associated with a *single* horizontal Fourier mode. However, as L_s increases, the interior flow develops a stably stratified core involving many Fourier modes; moreover, the interior fluctuation fields are

not depth-independent, also unlike their heat-exchanger counter-parts. By comparing these equilibrium solutions with the time-averaged columnar flow in DNS, it is found that the interior part of the mean columnar convection is neither a heat-exchanger nor a stably-stratified core flow, but rather blends certain features of these two steady solutions. The results indicate that L_h, the maximum L_s at which the strictly steady heat-exchanger solution exists, is almost half of the mean inter-plume spacing L_m measured from the DNS. Furthermore, heat transport in steady porous medium convection is confirmed to be less efficient than that occurring in turbulent convection. Specifically, steady convection has a ridge of maximum Nu in (Ra,L_s) parameter space along the curve $L_s \sim Ra^{-0.52}$, with $Nu \sim Ra^{0.6}$ along this ridge.

Linear stability analysis of these fully nonlinear steady states indicates that the steady solutions are most unstable at large Ra to one of two types of secondary modes. For small L_s, the most unstable disturbance is a bulk mode having roughly three to five times the wavelength of the steady convective state. The bulk instability intensifies as L_s is reduced. For large L_s, the most unstable disturbance has a growth rate that is essentially independent of horizontal scale and a vertical structure that is strongly localized near the walls. The growth rate of this wall mode increases as L_s increases and is generally an order of magnitude larger than that of the bulk mode. The nonlinear evolution of unstable steady convective states suggests that these two types of secondary instability play a primary role in determining the mean inter-plume spacing realized in turbulent porous medium convection. When the inter-plume spacing is small, the bulk mode drives the instability, causing plume merger and coarsening of the convective pattern; when the inter-plume spacing is large, the wall-mode instability dominates, causing small plumes generated from the walls to split the wider plumes into narrower ones. For generic initial conditions, this to-and-fro process continues until there is

a balance between the effects of these two types of instability. It should be noted that for the particular case in which a conduction solution is established at large Ra and then subjected to a broad spectrum of small-amplitude disturbances, the fastest-growing linear mode will dominate the early evolution. As shown in section 3.5.5, the flow evolves toward a steady convective state that necessarily has a lateral scale $\approx L_f$ (the wavelength of the fastest growing linear mode) that is larger than the final mean inter-plume spacing. In this scenario, too, the dominant secondary instability by which the resulting quasi-steady flow initially approaches the final mean inter-plume spacing L_m observed in statistically steady, but turbulent porous medium convection is the wall mode rather than the bulk mode identified in Hewitt et al. (2013).

CHAPTER 4

STRUCTURE AND STABILITY OF STEADY CONVECTION IN AN INCLINED POROUS LAYER

4.1 Introduction

As noted in chapter 3, the study of exact coherent states may facilitate understanding of the dynamics of porous medium convection. In this chapter, both the linear stability of the basic unicellular state and the secondary stability of the nonlinear convective state are performed to investigate the physics of convection in an inclined porous layer. Although the 2D linear stability analysis has been performed numerically by Rees and Bassom (2000), they mainly focus on the neutral stability of the basic state. In this investigation, the linear stability analysis is revisited to study the distribution of the eigenspectrum for various disturbances with different wavelengths from the onset of convection up to $Ra = 50000$.

In Walch and Dulieu (1982), Caltagirone and Bories (1985), Moya et al. (1987) and Sen et al. (1987), multiple steady convective states have been found in a tilted cavity at small Ra. However, the secondary stability of these steady states has not been fully explored.

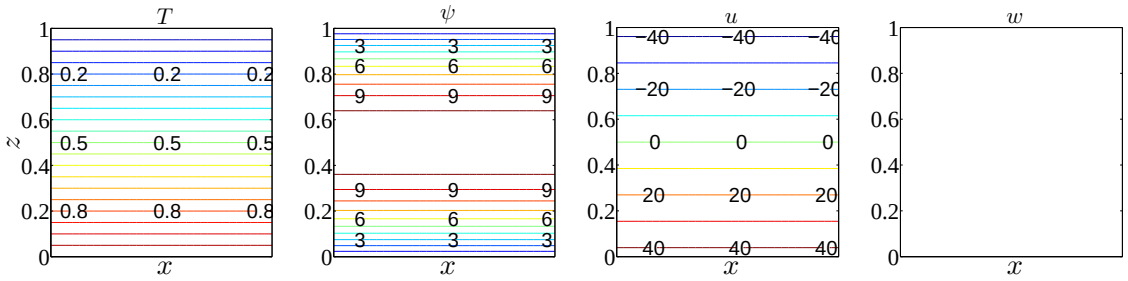

Figure 4-1: Contour plots of temperature, stream function and velocity fields for the basic unicellular solution at $Ra = 500$ and $\phi = 10°$. When $0° < \phi < 90°$, the temperature field of the basic state is still the same as it is in the horizontal case. However, the inclination of the layer will induce a background mean flow which strengthens as ϕ is increased.

Moreover, to the author's knowledge, there have been no investigations of the structure and stability of steady convective states arising in inclined porous medium convection at large Ra. Hence, in this chapter, following the studies of chapter 3, steady convective states composed of one natural roll and one antinatural roll are computed in a sloping porous Rayleigh–Bénard cell at moderate and large Ra, and their stability is then analyzed using Floquet theory.

4.2 Linear Stability Analysis

The basic unicellular solution for this inclined problem is $T = 1 - z$, $\psi = Ra \sin\phi(z - z^2)/2$ or $(u, w) = \big(Ra \sin\phi(\frac{1}{2} - z), 0\big)$, and $p = \frac{1}{2}Ra \sin\phi x + Ra \cos\phi(z - \frac{1}{2}z^2)$ (see Figure 4-1). Although the temperature field of the base state is still the same as that in the horizontal case, the base velocity field is nonzero and the background mean flow (in x) strengthens as the angle of inclination ϕ is increased. A linear stability analysis can be performed by setting $T = (1 - z) + \theta^*(x, z, t)$ and $\psi = Ra \sin\phi(z - z^2)/2 + \psi^*(x, z, t)$, where θ^* and ψ^* are small perturbations satisfying L-periodic boundary conditions in x and homogeneous

Dirichlet boundary conditions in z, and linearizing (2.5)–(2.6) about the basic state:

$$\nabla^2\psi^* = Ra(\theta_z^*\sin\phi - \theta_x^*\cos\phi), \tag{4.1}$$

$$\nabla^2\theta^* = \partial_t\theta^* + \frac{1}{2}Ra\sin\phi(1-2z)\partial_x\theta^* + \partial_x\psi^*. \tag{4.2}$$

The solution of (4.1) and (4.2) can be expressed as

$$\begin{bmatrix} \theta^* \\ \psi^* \end{bmatrix} = \sum_{n=-N/2}^{N/2} \begin{bmatrix} \hat{\theta}_n(z) \\ \hat{\psi}_n(z) \end{bmatrix} e^{inkx}e^{\lambda t} + c.c., \tag{4.3}$$

where λ is the temporal growth rate, nk is the horizontal wavenumber of the perturbation, N is the horizontal truncation mode number, and *c.c.* denotes complex conjugate. Substituting (4.3) into (4.1)–(4.2) yields

$$\begin{bmatrix} D_{zz} - (nk)^2 + inkRa\sin\phi(z-\frac{1}{2}) & -ink \\ Ra(ink\cos\phi - \sin\phi D) & D_{zz} - (nk)^2 \end{bmatrix} \begin{bmatrix} \hat{\theta}_n \\ \hat{\psi}_n \end{bmatrix} = \lambda \begin{bmatrix} I & 0 \\ 0 & 0 \end{bmatrix} \begin{bmatrix} \hat{\theta}_n \\ \hat{\psi}_n \end{bmatrix} \tag{4.4}$$

for each horizontal mode n, where D and D_{zz} denote the first and second partial derivative operator with respect to z, respectively, and I is an identity matrix. After discretization of the z coordinate using a Chebyshev spectral collocation method, this system (4.4) is solved using a global generalized eigenvalue routine subject to the boundary conditions $\hat{\theta}_n = \hat{\psi}_n = 0$ at $z = 0$, 1. In this dissertation, computations are performed for a discrete set of $Ra = 50 \cdot 10^{(\hat{\jmath}-1)/10}$ from $Ra = 50$ to $Ra = 50000$ and different wavelength $L = 2\pi/(nk) = 0.01 \cdot 10^{(\hat{k}-1)/500}$ from $L = 0.01$ to $L = 100$ (for integer $\hat{\jmath}$ and $\hat{k}$).

Figure 4-2 shows the contours of maximum growth rate, $\mathrm{Re}\{\lambda_m\}$ (the real part of maximum λ), as a function of nk and Ra for various ϕ. At $\phi = 0°$, all the eigenvalues are real,

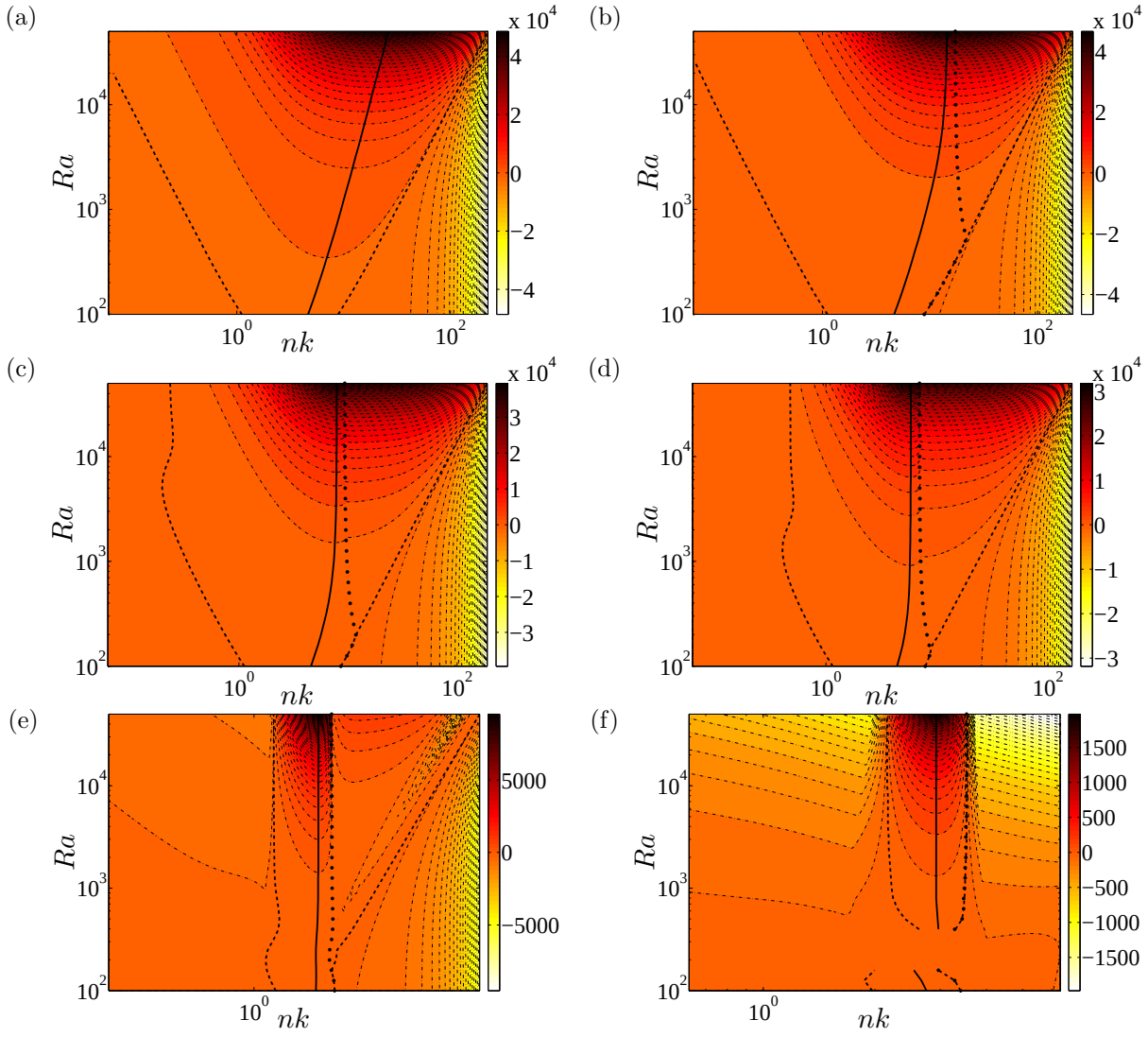

Figure 4-2: Contours of the maximum growth rate $\mathrm{Re}\{\lambda_m\}$ as a function of wavenumber nk and Ra. $\phi = 0$ (a), 1 (b), 5 (c), 10 (d), 25 (e), and 30 (f) degrees. The dashed lines denote the high- and low-wavenumber branches of marginal modes; the solid line corresponds to the fastest growing linear mode; the dotted line marks a boundary between pure real (left) and complex (right) eigenvalues. At $\phi = 25°$ (e), the structure of the contour is more complicated: the modes between the dotted line and the high branch dashed line are not all unstable, e.g. there exists a long narrow band in which the growth rate is negative. At $\phi = 30°$ (f), the discontinuities in these lines arise because the basic state is linearly stable to all small disturbances for $199 \lesssim Ra \lesssim 315$ and the resolution is not sufficient in Ra to generate a smooth curve.

as described in (3.2). Moreover, from the analysis in chapter 3.2 and as also shown in Figure 4-2(a), the high-wavenumber branch of marginal modes has $k_c \sim Ra^{1/2}$, and the wavenumber of the fastest growing linear mode $k_f \sim \sqrt{\pi} Ra^{1/4}$ as $Ra \to \infty$. However, in the inclined case ($0^\circ < \phi < 90^\circ$), the linear operator on the left-hand side of (4.4) is no longer self-adjoint and may yield complex eigenvalues. In Figure 4-2, the unstable eigenvalues (with positive $\mathrm{Re}\{\lambda_m\}$) between the left dashed line (corresponding to the low-wavenumber branch of marginal mode) and the dotted line are real, and become complex between the dotted line and the right dashed line (corresponding to the high-wavenumber branch of marginal modes). For $0^\circ \leq \phi \leq 25^\circ$, the high-wavenumber branch of marginal modes always has k_c growing as $CRa^{1/2}$ in the high-Ra regime, but with a different prefector C for different ϕ. However, the wavenumber of the fastest growing linear mode in inclined porous medium convection asymptotes to a constant at large values of the Rayleigh number. Furthermore, as ϕ is increased, the unstable region (between the two dashed lines in Figure 4-2) shrinks and ultimately disappears when $\phi > \phi_t$ (note that $\phi_t \approx 31.30^\circ$ at large Ra from the linear stability analysis of Rees and Bassom (2000)), implying that the basic unicellular state is linearly stable at sufficiently large inclination angle.

4.3 Steady Convective States

4.3.1 Newton–GMRES Method

The steady version of the governing equations (2.5)–(2.6) is solved numerically using a Newton–GMRES (generalized minimal residuals) iterative scheme. Following the Newton–Kantorovich method in chapter 3.3.1, the linear differential equations for the corrections in

the inclined case can be expressed as

$$\begin{bmatrix} \nabla^2 & Ra(\cos\phi D_x - \sin\phi D_z) \\ -D_x + \theta_z^i D_x - \theta_x^i D_z & \nabla^2 - \psi_z^i D_x + \psi_x^i D_z \end{bmatrix} \begin{bmatrix} \triangle^\psi \\ \triangle^\theta \end{bmatrix} = \begin{bmatrix} -F_{res}^\psi \\ -F_{res}^\theta \end{bmatrix}^i, \tag{4.5}$$

where the correction terms $\triangle^\psi$ and $\triangle^\theta$ are as in (3.13), and

$$\begin{aligned} F_{res}^\psi &= \nabla^2\psi + Ra(\cos\phi\partial_x - \sin\phi\partial_z)\theta + Ra\sin\phi, \\ F_{res}^\theta &= \nabla^2\theta - (\partial_z\psi\partial_x\theta - \partial_x\psi\partial_z\theta + \partial_x\psi), \end{aligned}$$

correspond to the residuals of the steady governing equations, and the superscript i denotes the ith Newton iterate. In the horizontal case, the z-dependent Fourier components $\hat{\theta}_n$ and $\hat{\phi}_n$ of θ and ψ in (3.16) and their correction terms in (3.13) are strictly real due to the centro-reflection symmetry of the solutions, and (3.17) and (3.18) are solved directly using a numerical linear algebra package. However, in the inclined case, $\hat{\theta}_n$ and $\hat{\phi}_n$ are complex (as in (3.7)) since the reflection-symmetry constraint no longer exists, so that the length of the vector $(\cdots\hat{\theta}_{n-1}, \hat{\theta}_n, \hat{\theta}_{n+1}\cdots\hat{\phi}_{n-1}, \hat{\phi}_n, \hat{\phi}_{n+1}\cdots)^T$ is 2 times the length in the horizontal case. Thus, the direct method is not economical numerically since the size of the matrix problem to be solved in the inclined case is 4 times the size in the horizontal case, which requires an excessive amount of memory for the computations. In this section, (4.5) is solved using a Krylov-subspace (GMRES) iterative method. To simplify the iterative scheme, F_{res}^ψ can be set to 0 since for a given $\triangle^\theta$, $\triangle^\psi$ can be obtained by solving

$$\nabla^2\triangle^\psi = Ra(\sin\phi D_z - \cos\phi D_x)\triangle^\theta. \tag{4.6}$$

Thus, (4.5) becomes

$$\begin{bmatrix} -D_x + \theta_z^i D_x - \theta_x^i D_z & \nabla^2 - \psi_z^i D_x + \psi_x^i D_z \end{bmatrix} \begin{bmatrix} \triangle^\psi \\ \triangle^\theta \end{bmatrix} = \begin{bmatrix} -F_{res}^\theta \end{bmatrix}^i, \tag{4.7}$$

and the only unknown is $\triangle^\theta$. For a given horizontal wavenumber nk_s (k_s is the fundamental wavenumber of the spatially-periodic steady solution, as in chapter 3), (4.7) becomes

$$\hat{\mathbb{L}}_n^i(\triangle^\theta) = \hat{f}_n^i, \tag{4.8}$$

where $\hat{\mathbb{L}}_n^i$ and $\hat{f}_n^i$ represent the coefficients of the left- and right-hand sides of (4.7) in Fourier space at the ith Newton iterate, respectively. For each Newton iterate, (4.8) is solved iteratively in the Krylov subspace using the GMRES method (Trefethen and Bau, 1997). Spatial discretization in z is achieved using a Chebyshev spectral collocation method. In order to improve the convergence rate of the GMRES iterations, a preconditioner $\mathbf{M} = \nabla^2$ is chosen for solving (4.8). Hence the actual computational linear algebra problem is

$$\hat{\mathbf{M}}_n^{-1}\hat{\mathbb{L}}_n^i(\triangle^\theta) = \hat{\mathbf{M}}_n^{-1}\hat{f}_n^i, \tag{4.9}$$

where $\hat{\mathbf{M}}_n$ is the matrix of coefficients of $\mathbf{M}$ in Fourier space for the horizontal wavenumber nk_s, namely in this study $\hat{\mathbf{M}}_n = D_{zz} - (nk_s)^2 I$. Although reflection symmetry is not realized for the inclined case, the centrosymmetry still exists and requires

$$a_{mn} \text{ is imaginary if } (m+n) \text{ is even; otherwise, for odd } (m+n),\ a_{mn} \text{ is real.} \tag{4.10}$$

The above centrosymmetry constraint is enforced in the computations. Moreover, the GMRES iteration is stopped once the norm of the residual of (4.9) is less than 10^{-4}, and then $\hat{\theta}_n$ is updated following the same strategy as in (3.20). Finally, the Newton iteration is stopped when the norm of F^{θ}_{res} is less than 10^{-8}.

4.3.2 Solution Structure

As noted in chapter 2.4, steady convective states in an inclined porous layer are stable at small Ra (e.g. $Ra \leq 200$, see Figure 2-10). However, as the Rayleigh number is increased, the boundary layers near the upper and lower walls become unstable and small-scale features are generated and advected around the cell by the large-scale roll, as shown in Figure 2-12(e). In this section, the structure of the (generally unstable) steady convective states will be investigated at moderate and large values of the Rayleigh number for different angles. Figure 4-3 shows the variations in the pattern of isotherms and streamlines with the inclination angle at $Ra = 500$ and $L_s = 2$. It is seen that the increasing inclination of the layer enhances the motion of the background basic mean flow (Figure 4-1), thereby intensifying the natural-roll motion and suppressing the antinatural-roll motion. Consequently, as ϕ is increased, the natural rolls become more vigorous and more tightly attached to the upper and lower walls; on the contrary, the antinatural rolls become much weaker and detached from the walls (see Figures 4-3, 4-4 and 4-5). A similar trend is also found at $Ra = 1991$ and $L_s = 2$ (see Figure 4-6a-b and Table 4-1). Moreover, as shown in Figure 4-6, there exist at least two branches of steady states for different inclinations at $Ra = 1991$. For $\phi \lesssim 15^{\circ}$ (see Figure 4-6a-b), the antinatural roll is gradually detached from the walls as ϕ is increased; however, for $\phi > 15^{\circ}$, the antinatural roll is completely detached from the walls and the flow exhibits a different type of pattern (see Figure 4-6c-d).

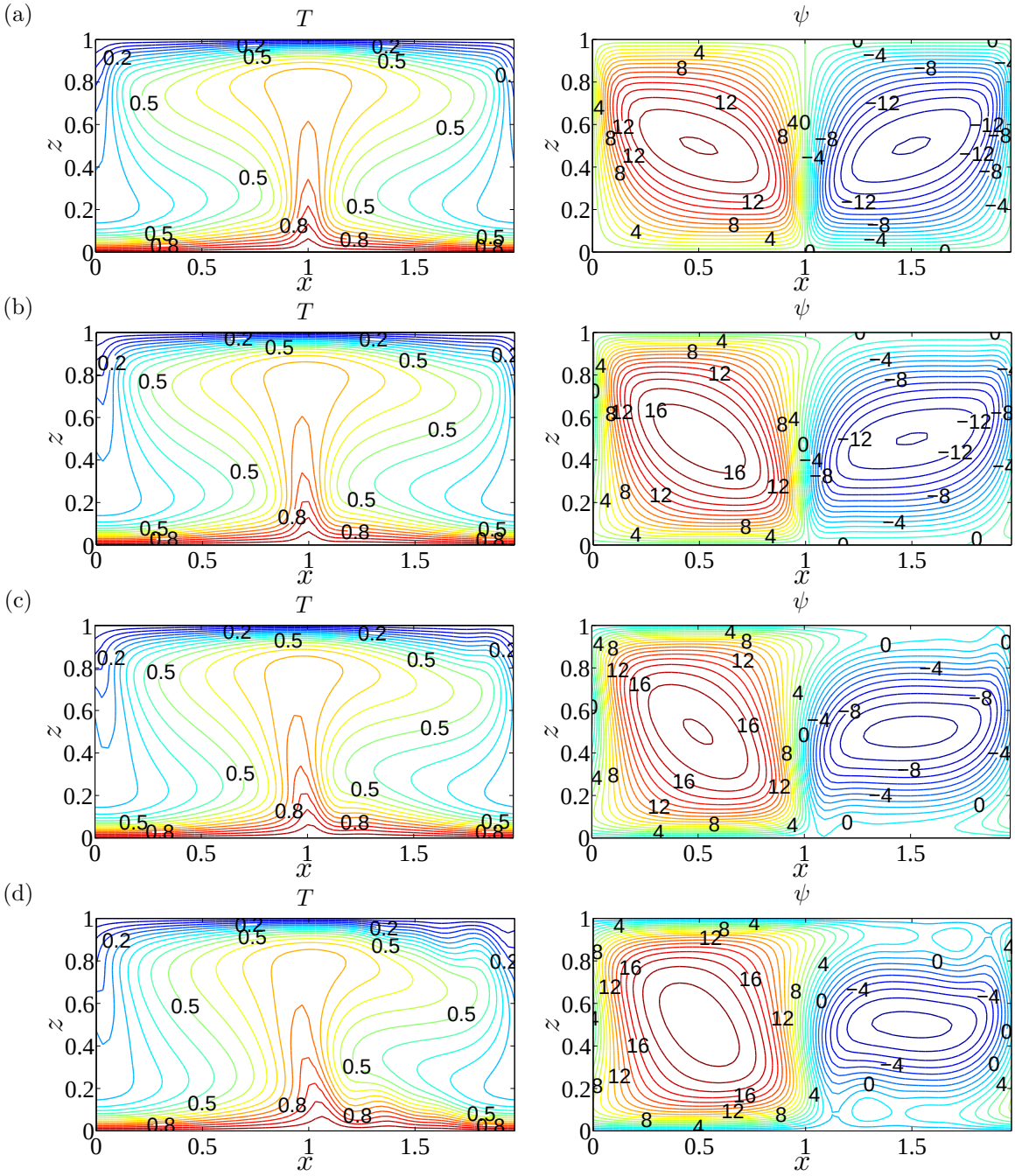

Figure 4-3: Isotherms and streamlines of steady convective states at $Ra = 500$ and $L_s = 2$. $\phi = 0$ (a), 10 (b), 20 (c), and 30 (d) degrees. The steady state at $\phi = 35°$ was not obtained using (d) as an initial guess with the present numerical scheme. As the inclination angle is increased, the natural roll becomes more vigorous and more tightly attached to the walls, while the antinatural roll is suppressed and becomes detached from the walls.

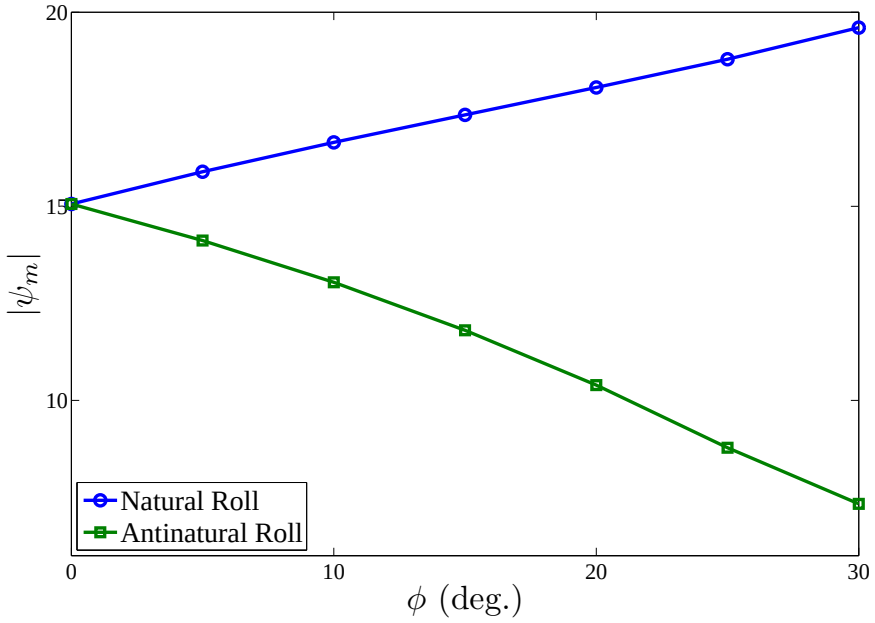

Figure 4-4: Magnitude of ψ_m for steady convective states as a function of ϕ at $Ra = 500$ and $L_s = 2$. ψ_m denotes the ψ extremum value corresponding to the natural roll with $\max(\psi)$ (positive) and antinatural roll with $\min(\psi)$ (negative). As ϕ is increased, the natural-roll motion is intensified, while the antinatural-roll motion is suppressed.

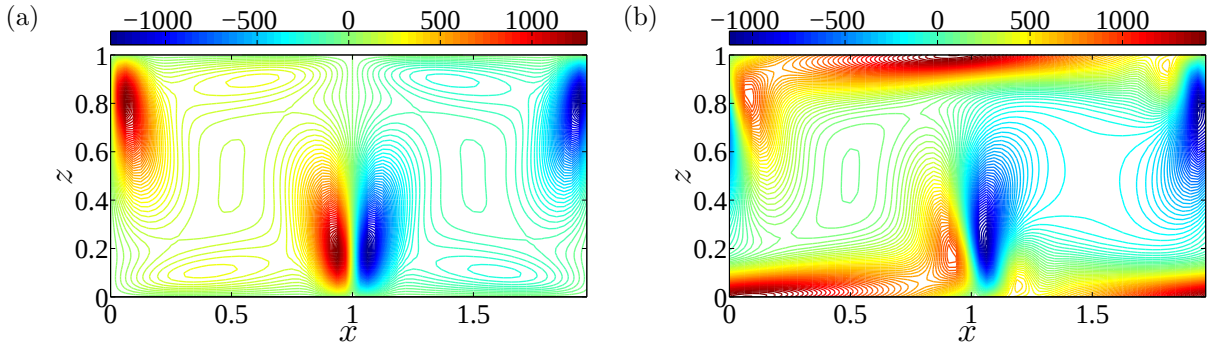

Figure 4-5: Contour plots of vorticity field Ω of steady convective states at $Ra = 500$ and $L_s = 2$. (a): $\phi = 0°$; (b): $\phi = 20°$. For the inclined case, the natural roll is tightly attached to the upper and lower walls, while the antinatural roll is detached from the walls.

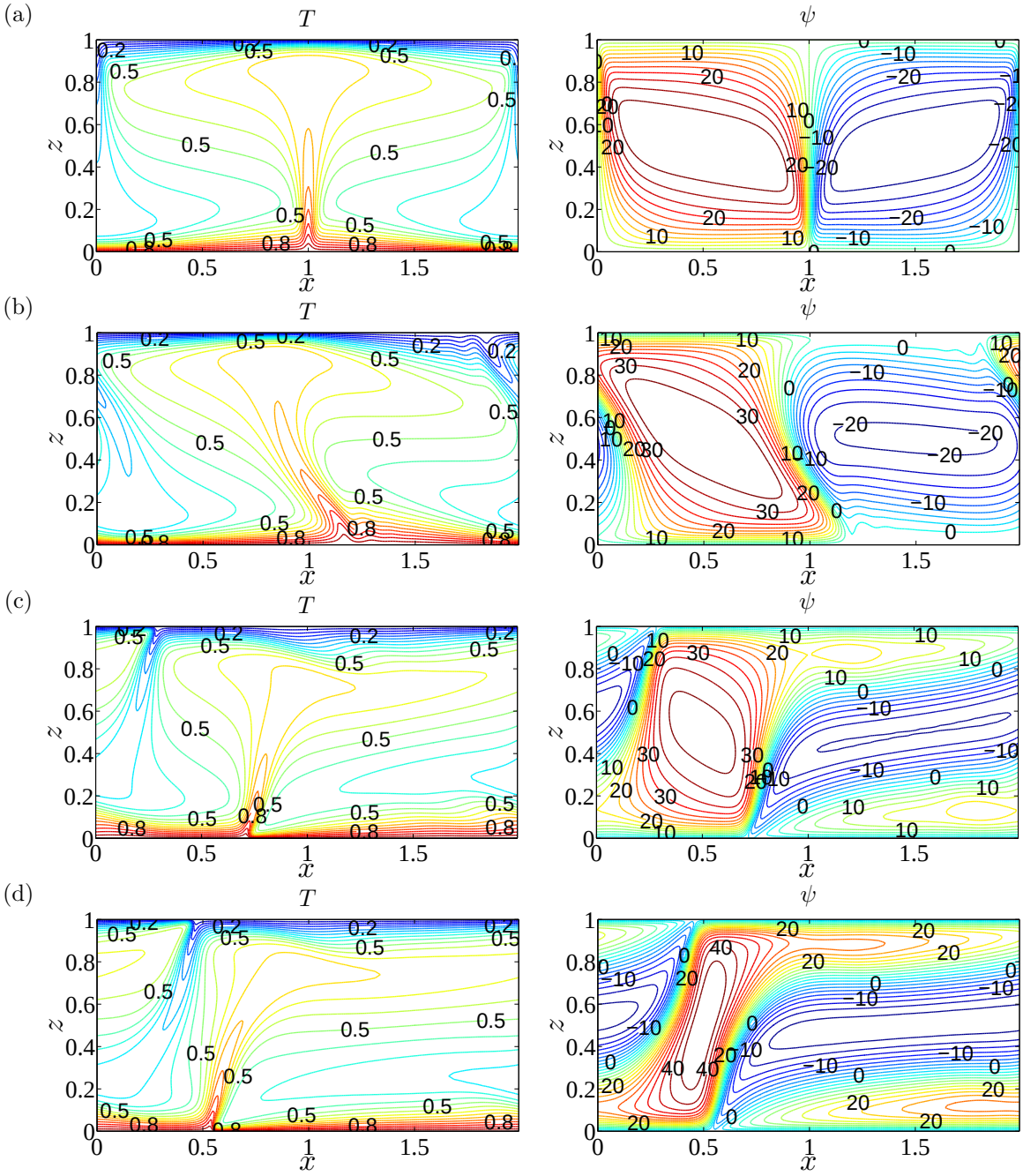

Figure 4-6: Isotherms and streamlines of steady convective states at $Ra = 1991$ and $L_s = 2$. $\phi = 0$ (a), 15 (b), 20 (c), and 35 (d) degrees. The same branch of steady states as in (b) cannot be obtained continuously for $\phi > 15°$ with the present numerical scheme (using the result from a lower ϕ as the initial guess). For $\phi = 35°$ (d), the steady state is stable and can be obtained from DNS. Hence, the same branch of steady states as in (d) can be obtained continuously, using the result from a higher ϕ as the initial guess, until $\phi \approx 17.5°$.

Cell \ ϕ	0°	15°	20°	35°
Natural	30.0	34.9	38.6	43.8
Antinatural	30.0	20.6	17.6	18.2

Table 4-1: Magnitude of the ψ extremum values for natural and antinatural rolls at $Ra = 1991$ for different ϕ. These ψ extremum values correspond to the flows in Figure 4-6. For the inclined case, the natural roll is more vigorous than the antinatural roll.

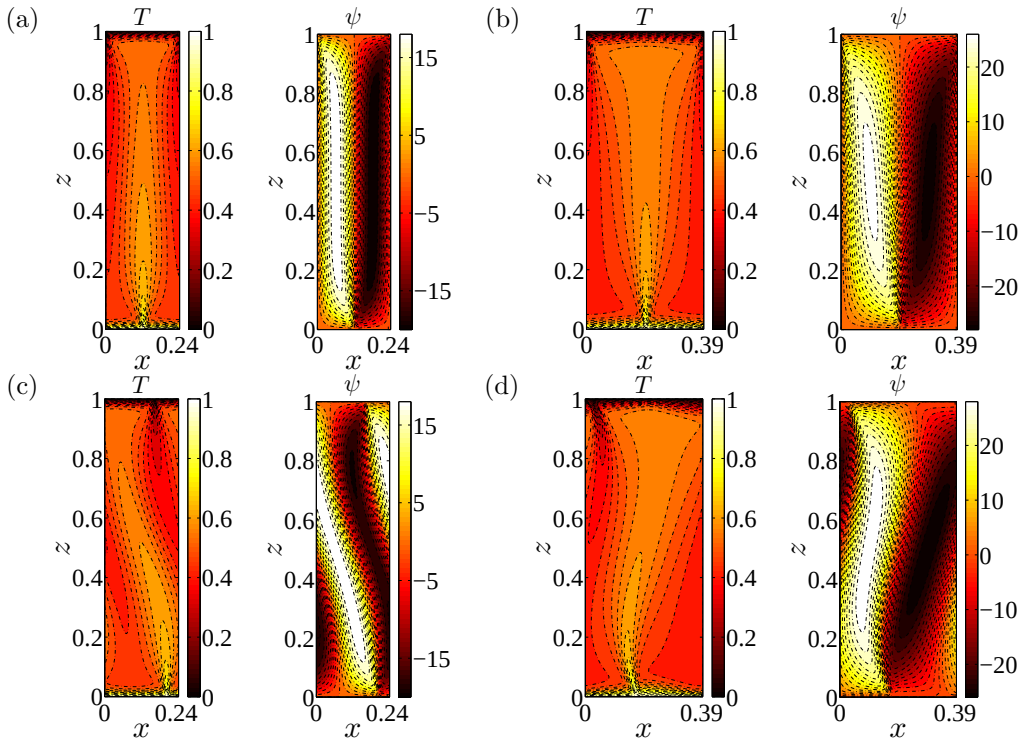

Figure 4-7: Temperature and stream function fields of steady states at $Ra = 5000$. (a): $\phi = 0°$, $L_s = 0.251$; (b): $\phi = 0°$, $L_s = 0.398$; (c): $\phi = 0.96°$, $L_s = 0.251$; (d): $\phi = 6°$, $L_s = 0.398$. $L_s = 0.398$ is close to the mean inter-plume spacing L_m measured from DNS at $\phi = 0°$. Magnitude of the ψ extremum values for natural rolls: (a) 19.7, (b) 27.0, (c) 20.0 and (d) 29.9; for antinatural rolls: (a) 19.7, (b) 27.0, (c) 18.4 and (d) 25.5. For different aspect ratios L_s, the steady state is distorted differently.

As noted in chapter 2.4, DNS reveal that the flow at large Ra and small ϕ still exhibits the three-region narrow columnar structure, as is manifest in the horizontal case. Hence, in this chapter steady convective states are also computed in narrow domains at $Ra = 5000$, as shown in Figure 4-7. It is seen from this figure the steady state is distorted differently, depending on the aspect ratio L_s. For small L_s, the motion of the narrow rolls is too weak to resist the impact of the background base flow. Consequently, both the natural and antinatural rolls are distorted counterclockwise, in the same direction as the flow of the base state. However, as L_s is increased, the motions of rolls become stronger (with higher magnitude of the ψ extremum value, see Figures 3-1 and 4-7) and exhibit a different distorted pattern for $\phi \neq 0°$: the natural roll is more tightly attached to the walls while the antinatural roll begins to be detached from the walls, as also observed at moderate Ra. It should be noted that these two types of patterns can be easily observed in DNS for very narrowly and widely spaced plumes.

4.4 Secondary Stability Analysis

4.4.1 Floquet Theory

As in chapter 3.4.1, spatial Floquet analysis is also performed here to investigate the linear stability of the fully nonlinear steady convective states in an inclined porous layer. The linearized momentum equation (3.24) for the inclined case becomes

$$\nabla^2 \widetilde{\psi} = Ra(\sin\phi\partial_z - \cos\phi\partial_x)\widetilde{\theta}, \tag{4.11}$$

where $\widetilde{\theta}$ and $\widetilde{\psi}$ are small-amplitude disturbances defined as in (3.22) and (3.23), while the linearized energy equation (3.25) is unchanged. Hence, for each n, (3.28) becomes

$$-Ra\left[\sin\phi D_z - i(n+\beta)k_s\cos\phi\right]\hat{\widetilde{\theta}}_n + \left[D_{zz} - (n+\beta)^2 k_s^2\right]\hat{\widetilde{\psi}}_n = 0, \tag{4.12}$$

while (3.29) is unchanged for $\phi \neq 0°$. Since $\hat{\widetilde{\psi}}_n$ is no longer strictly imaginary (the reflection symmetry is not realized), the resulting A and B in (3.30) are complex (not real) matrices.

4.4.2 Secondary Stability Results

The same numerical scheme as in chapter 3.4 is employed here to solve the resulting algebraic eigenvalue problem (3.29) and (4.12) for the inclined case to obtain the leading eigenvalues and eigenfunctions. Figure 4-8 shows the maximum growth rate, $\mathrm{Re}\{\sigma_m\}$, as a function of ϕ at moderate Ra and $L_s = 2$. The inclination of the layer enhances the instability of the steady state, and for each Ra, there exists a peak in $\mathrm{Re}\{\sigma_m\}$. Moreover, the structure of the most unstable eigenfunction in Figure 4-9 and the results in Figure 4-10 confirm that the antinatural rolls are more unstable than the natural rolls at moderate Rayleigh number, as also indicated by DNS in chapter 2.4. Actually, as ϕ is increased, the natural roll of the steady state strengthens and becomes more tightly attached to the walls, and thereby is stabilized; on the contrary, the antinatural roll is suppressed and becomes detached from the walls, and thereby is destabilized. Thus, the increase of the maximum growth rate with ϕ in Figure 4-8 is attributable to the destabilization of the antinatural roll.

At large Ra, the steady state for the inclined case exhibits similar instability properties as for the horizontal case. As shown in Figure 4-11, at small L_s, the steady states for both

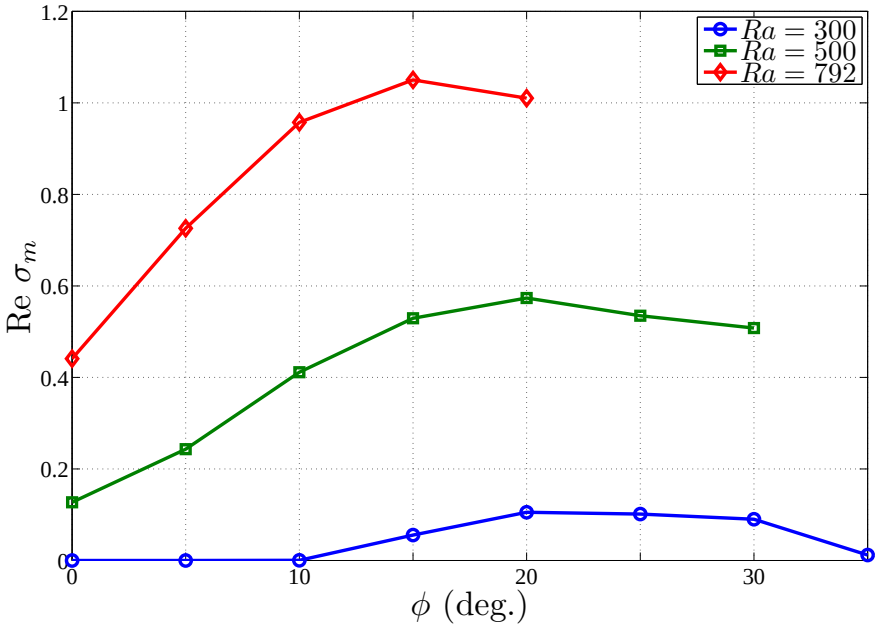

Figure 4-8: Variation of the maximum growth rate, Re$\{\sigma_m\}$, with ϕ at moderate Ra, $L_s = 2$ and $\beta = 0$. Re σ_m is the real part of σ_m. At $Ra = 300$, the steady state is marginally stable for $\phi < 10°$ and becomes weakly unstable at $\phi = 10°$. The same branch of steady states is not obtained at large ϕ for $Ra = 500$ and 792 using the present numerical scheme.

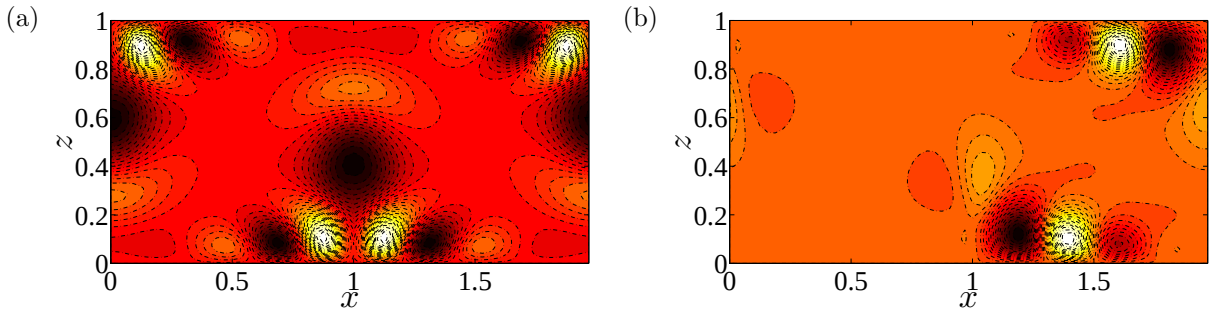

Figure 4-9: The fastest-growing 2D temperature eigenfunctions at $Ra = 500$, $L_s = 2$ and $\beta = 0$. (a): $\phi = 0°$; (b): $\phi = 20°$. For the horizontal case, reflection symmetry is satisfied and both of the natural and antinatural rolls are equally unstable. However, as ϕ is increased, the natural roll is stabilized and the instability of the antinatural roll is intensified.

of the horizontal and inclined porous layers are unstable for a range of long-wavelength perturbations ($0 < \beta \leq 0.5$), and this type of instability is enhanced in the inclined case.

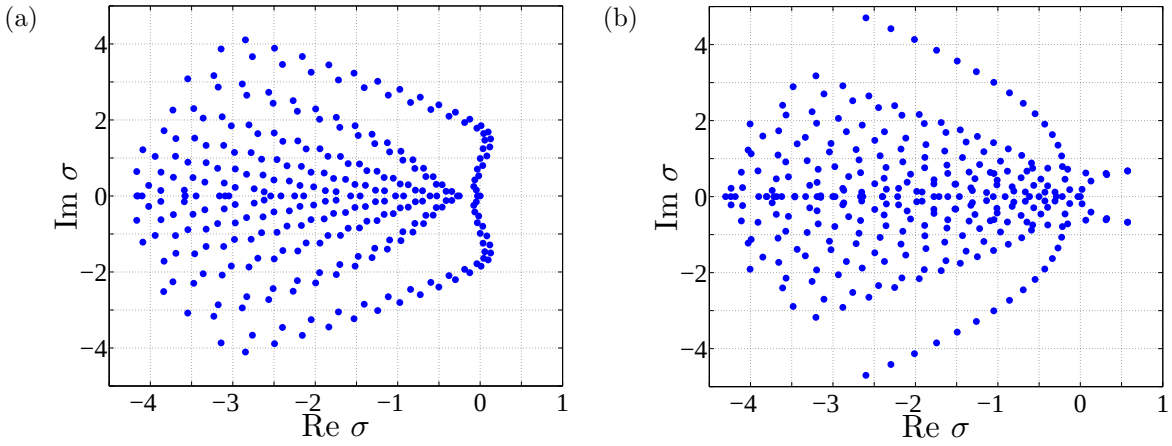

Figure 4-10: The leading eigenvalues at $Ra = 500$, $L_s = 2$ and $\beta = 0$. (a): $\phi = 0°$; (b): $\phi = 20°$. All of the unstable modes for both the horizontal and inclined cases exhibit a similar structure as that of the corresponding fastest-growing mode in Figure 4-9.

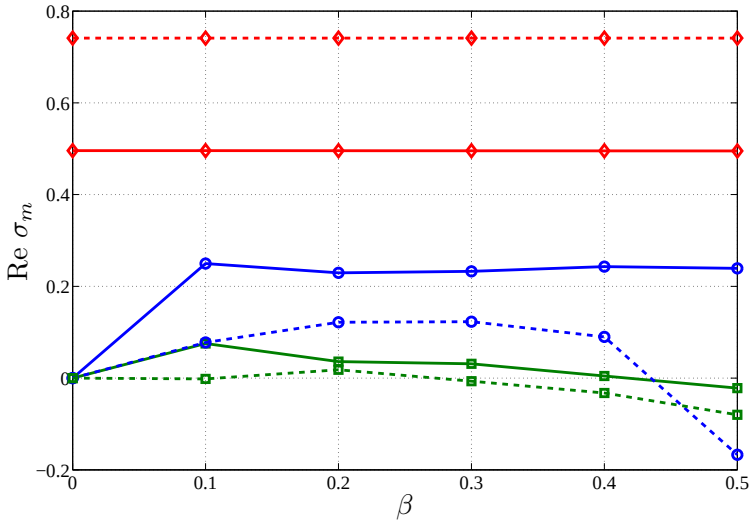

Figure 4-11: Variation of the maximum growth rate, $\mathrm{Re}\{\sigma_m\}$, with β at $Ra = 5000$. Circle: $L_s = 0.1259$; square: $L_s = 0.1667$; diamond: $L_s = 0.1995$. Solid lines: for $L_s = 0.1259$, $\phi = 0.14°$; for $L_s = 0.1667$, $\phi = 0.25°$; for $L_s = 0.1995$, $\phi = 0.4°$. Dashed lines: $\phi = 0°$. At small L_s (e.g. $L_s = 0.1667$), the base state is marginally stable for $\beta = 0$, but unstable to certain long-wavelength perturbations ($0 < \beta \leq 0.5$). The inclination intensifies this long-wavelength instability. At large L_s, the base state is unstable even for $\beta = 0$, and has the same growth rate for different β.

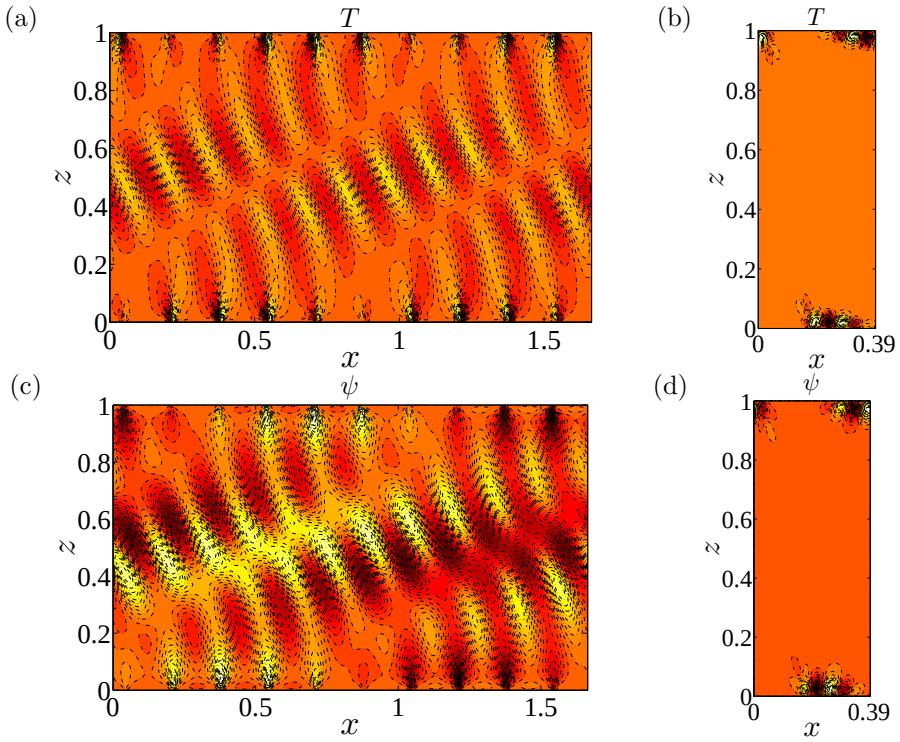

Figure 4-12: The fastest-growing 2D temperature and stream function eigenfunctions at $Ra = 5000$ in inclined porous medium convection. (a) and (c): $L_s = 0.1667$, $\phi = 0.25°$, $\beta = 0.1$; (b) and (d): $L_s = 0.3981$, $\phi = 6°$, $\beta = 0$. The eigenfunctions in (a) and (c) are shown in a domain with aspect ratio $L = 10L_s$. As in the horizontal case, at small L_s (a, c), a bulk mode controls the instability, and at large L_s (b, d), a wall mode dominates.

However, at large L_s, the maximum growth rate $\mathrm{Re}\{\sigma_m\}$ for both the horizontal and inclined cases becomes independent of β. Figure 4-12 shows the 2D eigenfunctions corresponding to these two families of secondary instabilities. As in the horizontal case, at small L_s, e.g. $L_s = 0.1667$, when the growth rate depends on the horizontal wavenumber βk_s, the most unstable perturbation is a bulk mode that spans the layer (Figure 4-12a). However, at large L_s, e.g. $L_s = 0.3981$, when the growth rate is independent of β, the most unstable perturbation for each β is a wall mode that is strongly localized near the upper and lower walls (Figure 4-12b). It should be noted that the wall mode has a very similar spatial

structure for each β, as in the horizontal case, and when ϕ is sufficiently large the fastest growing wall mode only occurs in the antinatural roll (see Figure 4-12*b*), implying that the antinatural roll is more unstable than the natural roll, consistent with the results that have been discussed at moderate Ra.

4.5 Nonlinear Evolution of the Instability

At discussed above, two types of secondary instability are also found in inclined porous medium convection. In this section, strategically initialized DNS are performed to investigate the nonlinear evolution of the fastest-growing secondary instability mode at large Ra. The aim is to gain insight into the mechanisms by which these secondary instabilities influence the mean inter-plume spacing L_m in the inclined case. The steady state at a given L_s plus a small-amplitude contribution of the most unstable secondary instability mode is chosen as the initial condition, and then high-resolution DNS are performed in a wider domain.

Figure 4-13 shows the nonlinear evolution of the most dangerous secondary instability mode for small L_s which is within the bulk instability parameter regime. It is seen that the initial condition comprises 10 replicas of the steady convective state at $L_s = 0.1667$, plus a small-amplitude contribution of the corresponding fastest-growing perturbation at $\beta = 0.1$ (see Figure 4-12*a*). In accord with the stability analysis in chapter 4.4.2 and as is evident in Figure 4-13(*b*,*c*), the base state is unstable to a bulk mode. As the secondary mode grows in amplitude, some narrow plumes are so distorted that the cold (heavy) plumes overlie the hot (light) ones (see Figure 4-13*c*). Then, these strongly distorted plumes are broken and merged into wider plumes, as shown in Figure 4-13(*d*,*e*). However, the resulting wide plumes are strongly unstable to the wall mode. Hence, some plumes growing from the upper and lower

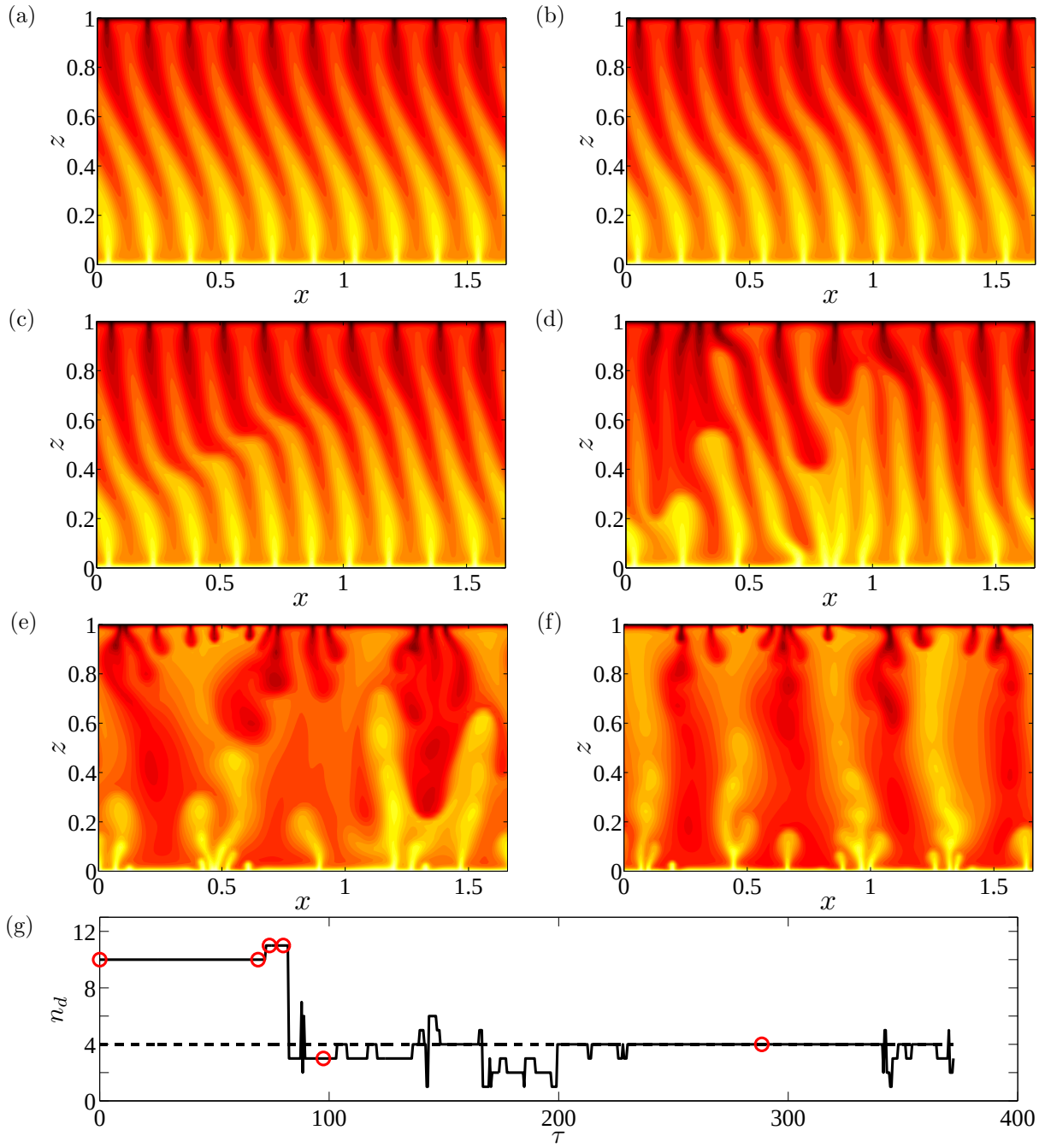

Figure 4-13: Snapshots of the temperature field from DNS showing the nonlinear evolution of the fastest-growing secondary instability mode for $L_s = 0.1667$, $\beta = 0.1$, $L = 10L_s$, $Ra = 5000$, $\phi = 0.25°$: (a) $\tau = 0$; (b) $\tau = 69$; (c) $\tau = 74$; (d) $\tau = 80$; (e) $\tau = 97.5$; (f) $\tau = 288.5$; (g) The time evolution of the dominant horizontal mode number n_d at $z = 0.5$ (solid line). The dashed line shows the time-average dominant mode number and the circles correspond to the times highlighted in (a) to (f).

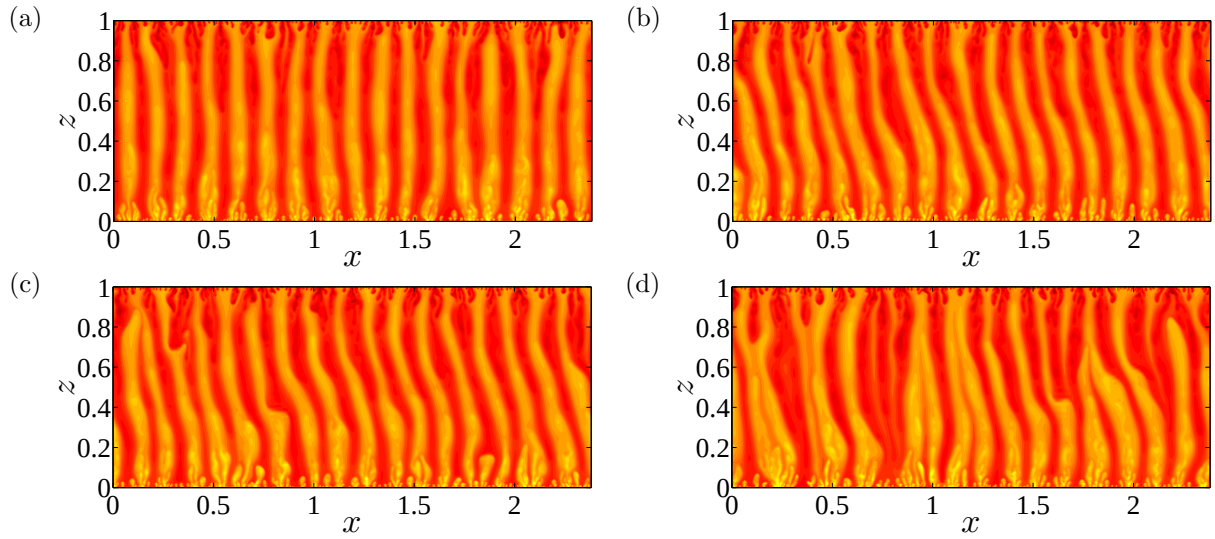

Figure 4-14: Snapshots of the temperature field from DNS showing the bulk instability for narrow columnar flows at $Ra = 50000$ and $\phi = 5°$ in $L = 2.387$: (a) $\tau = 0$; (b) $\tau = 47.4$; (c) $\tau = 51.15$; (d) $\tau = 59.25$. DNS result from the horizontal case at the same Ra and L is utilized as the initial condition. τ is the convective time as in chapter 3. As time evolves, these narrow columnar plumes are distorted by the background mean flow and become unstable to a bulk mode.

boundary layers split the wider plumes into narrower ones (see Figure 4-13e,f). Therefore, in the inclined porous layer, the bulk instability will enhance the distortion of the narrowly spaced plumes, cause plume merger and coarsen the convective pattern.

Since the nonlinear evolution of the bulk mode described above occurs at $\phi = 0.25°$ and $Ra = 5000$, an obvious question is whether this instability still exists at larger inclinations, e.g. $\phi = 5°$ or $10°$. Figure 4-14 shows the snapshots of the temperature field from DNS at $Ra = 50000$ and $\phi = 5°$. In this case, the DNS result from $\phi = 0°$ at the same parameter values is used as the initial condition, so that the narrow columnar flows are generally straight initially (see Figure 4-14a). However, the inclination of the layer will induce a background mean flow which distorts the narrow plumes in a counterclockwise direction (see Figure 4-14b), similarly in the steady case (Figure 4-7c). Then, the resulting distorted

narrow columns become unstable to a bulk mode: as is evident in Figure 4-14(c), some cold plumes overlie hot ones as time evolves, and subsequently these narrow plumes are broken and merged into wider ones (see Figure 4-14d).

4.6 Summary

In this chapter, linear and secondary stability analyses have been employed to study pattern formation in inclined porous medium convection. Theoretical analysis indicates that the inclination of the porous layer will induce a basic unicellular flow which strengthens as ϕ is increased from $\phi = 0^\circ$ to $\phi = 90^\circ$. In an infinitely wide 2D domain, the linear stability analysis of the base state here reveals that for $\phi < 30^\circ$ and at large Ra, the high-wavenumber branch of marginal modes has $k_c \sim CRa^{1/2}$ with a different prefactor C for different inclination angles; however, the wavenumber of the fastest growing linear mode k_f becomes independent of Ra. Moreover, at small and moderate ϕ (e.g. $\phi < 25^\circ$), there exist two distinct unstable regions between the low- and high-wavenumber branches of marginal modes: as the wavenumber k of the disturbance is increased from the low-wavenumber branch to the high-wavenumber branch, the most unstable eigenvalue λ_m for each wavelength changes from a real number to a complex one, implying that the bifurcation near the high-wavenumber branch k_c is not stationary.

In order to better understand the physics of inclined porous medium convection at different ϕ, the structure and stability of steady nonlinear convective states are also investigated at moderate and large values of the Rayleigh number. In the moderate-Ra regime, these steady states appear in the form of large-scale convective rolls: one natural roll rotating in a counterclockwise direction; and one antinatural roll rotating in a clockwise direction.

As the inclination angle is increased, the strengthening background mean flow enhances the motion of the natural roll and makes it more tightly attached to the upper and lower walls, but weakens the motion of the antinatural roll and makes it detached from the walls at sufficiently large ϕ. Moreover, the Floquet analysis of these steady states reveals that before the antinatural roll is completely detached from the walls, the inclination of the layer stabilizes the boundary layers of the natural roll, but intensifies the boundary-layer instability of the antinatural roll.

In the high-Ra regime, DNS indicate that for $0^\circ < \phi \lesssim 25^\circ$, the flow still exhibits a similar three-region structure as is manifest in the horizontal case, except that as ϕ is increased the time-mean spacing between neighboring interior mega-plumes is also substantially increased. To explore the mechanism resulting in such a variation, a spatial Floquet analysis is performed, yielding predictions of the linear stability of numerically-computed, fully nonlinear steady convective states. The results show that there also exist two types of instability when $\phi \neq 0^\circ$: a bulk instability and a wall instability, consistent with the previous findings for $\phi = 0^\circ$. Here, however, the background flow induced by the inclination of the layer intensifies the bulk instability during its subsequent nonlinear evolution, thereby favoring increased spacing between the interior plumes relative to the $\phi = 0^\circ$ scenario.

CHAPTER 5

STRUCTURE AND STABILITY OF TIME-PERIODIC SOLUTIONS IN HORIZONTAL POROUS MEDIUM CONVECTION AT LARGE RAYLEIGH NUMBER

5.1 Introduction

In previous chapters, the structure and stability of steady convective states have been explored as a function of Ra and L in both horizontal and inclined porous medium convection. The results indicate that these states can capture aspects of the structure and dynamics of typical coherent structures observed in turbulent flows at large Ra. However, one obvious difference between the steady flow and the realized turbulent flow at the same parameter values is that the proto-plumes are absent in the former (i.e. steady solution). Specifically, the steady convective flows generally exhibit a two-region structure consisting of thin thermal boundary layers near the walls and a mega-plume region in the interior. Hence, a natural question is raised: *are there any exact coherent solutions that can capture the three-region*

structure of the instantaneous turbulent flow including the proto-plume region, as observed in DNS?

To capture the continually swept proto-plumes, the system must be time-dependent. In this chapter, time-periodic solutions will be investigated numerically in horizontal porous medium convection. As noted in chapter 1.2, the steady convective flow is destabilized by a Hopf bifurcation to a time-periodic oscillatory flow as the Rayleigh number is increased above 400. In the moderate Ra parameter regime, i.e. $400 < Ra < 1300$, the resulting flow exhibits a series of transitions between periodic and quasi-periodic convective roll motions, as discussed in considerable detail by Kimura et al. (1986, 1987), Steen and Aidun (1988), Riley and Winters (1991) and Graham and Steen (1992, 1994). It should be noted that these studies were generally focused on the centro-reflection symmetric time-periodic solutions at moderate Ra. In this study, a primary objective is to explore the (numerically) exact time-periodic states at large Ra (basically in the chaotic convection regime). Moreover, besides the centro-reflection symmetric solution, three other types of periodic orbits with different symmetries are also found by classifying the eigenfunctions emerging from a stability analysis of the steady convective states, The stability of the time-periodic solution with centro-reflection symmetry is then investigated using a spatial Floquet analysis.

The remainder of the chapter is organized as follows. In section 5.2, the computational methodology is outlined, and the symmetry and structure of the time-periodic solutions are described. Then the stability analysis of periodic-orbit solutions with centro-reflection symmetry is performed using Floquet theory in section 5.3. Finally, the results are summarized and discussed in section 5.4.

5.2 Time-Periodic Convective Solutions

5.2.1 Computational Methodology

To seek a time-periodic solution $\theta^\star(x,z,t) = \theta^\star(x,z,t+\tau^\star)$ with period $\tau^\star$, the unsteady energy equation (2.6) can be rewritten as

$$\partial_t\theta = F(\theta) = -\partial_z\psi\partial_x\theta + \partial_x\psi\partial_z\theta - \partial_x\psi + \nabla^2\theta, \tag{5.1}$$

where ψ can be determined through (2.5) with $\phi = 0°$. Define the time-τ forward map of equation (5.1)

$$f^\tau(\theta) = \theta + \int_0^\tau dtF(\theta(t)). \tag{5.2}$$

Then, the exact time-periodic solutions satisfy

$$f^{\tau^\star}(\theta) - \theta = 0, \tag{5.3}$$

with an *unknown* period $\tau^\star$.

Finally, a Newton-hookstep searching algorithm developed by Viswanath (2007) and obtained from "http://channelflow.org/" is utilized to solve (5.3) numerically with the same boundary conditions as described in chapter 2.2. In the computation, the unknown vector consisting of the spectral expansion coefficients of θ and the period $\tau^\star$ is obtained based on Newton search, Krylov subspace methods, and an adaptive hookstep trust-region limitation

to Newton steps. The spatial discretization is achieved using a Fourier–Chebyshev-tau pseudospectral algorithm, and temporal discretization using a semi-implicit RK3 & AB/BDI4 hybrid algorithm (see details in Appendix A), yielding fourth-order accuracy in time. The Newton iteration is continued until the norm of the residual of (5.3) is less than 10^{-12}.

5.2.2 Symmetry

Before investigating the symmetries of the governing equations, it is instructive to analyze the structure of the secondary stability eigenfunctions of the steady convective state, since the unstable eigenfunctions generally represent the directions in which the dynamical system tends to evolve. And within the linear stability regime, the steady state must go through these directions to transition to other states. Figure 5-1 shows the eigenspectra and eigenfunctions for the steady convective state at $Ra = 1991$ having an aspect ratio slightly larger than L_b so that the steady solution becomes weakly unstable to the wall mode. It can be seen from this figure that there exist 4 pairs of unstable conjugate eigenmodes combining different symmetries defined in Table 5-1. As described in chapters 2 and 3, the time-averaged cellular flow and steady convective states generally satisfy a centro-reflection symmetry; however, these unstable eigenfunctions exhibit 4 types of symmetries, as shown in Figure 5-1(c)–(f). In this section, the steady convective state is chosen as a base state. Therefore, the time-periodic solutions can be classified into 4 types of solutions according to the symmetries of the perturbations. For instance, the anticentro-antireflection symmetric periodic orbit means the steady convective base state plus an anticentro-antireflection symmetric perturbation (or oscillation).

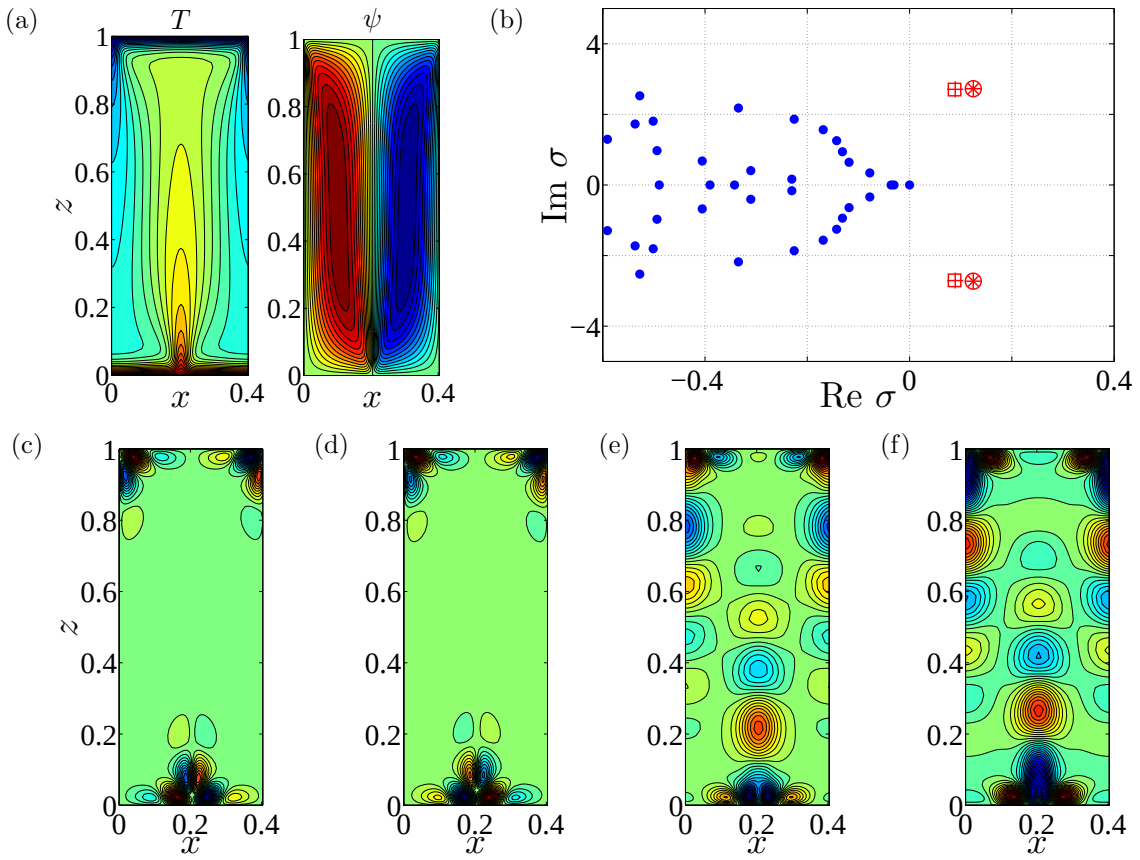

Figure 5-1: Steady convective state and the corresponding leading eigenvalues and temperature eigenfunctions at $Ra = 1991$ and $L = 0.41$: (a) temperature and stream function fields; (b) eigenspectra; (c)–(f) unstable temperature eigenfunctions with anticentro-antireflection symmetry, centro-antireflection symmetry, centro-reflection symmetry, and anticentro-reflection symmetry, respectively. In (b), the asterisk, circle, plus and square denote 4 pairs of unstable conjugate eigenmodes with different symmetries shown in (c)–(f).

At moderate Rayleigh number ($400 < Ra < 1300$), the stable steady convective state undergoes a Hopf bifurcation as Ra is increased for fixed aspect ratio (Steen and Aidun, 1988; Riley and Winters, 1991; Graham and Steen, 1992, 1994). At large Ra, the numerical investigations here indicate that this bifurcation still exists for fixed Ra as L is increased from $L < L_b$ where the steady state is stable within the narrow domain, to $L > L_b$ where the boundary layers begin to become unstable to the wall mode. To more clearly illustrate this bifurcation,

Symmetry	Definition	a_{mn}
Reflection	$\theta(x,z) = \theta(L-x,z)$	real
Antireflection	$\theta(x,z) = -\theta(L-x,z)$	imaginary
Centro	$\theta(x,z) = -\theta(\frac{L}{2}-x,1-z)$	real for odd $(m+n)$; imaginary for even $(m+n)$
Anticentro	$\theta(x,z) = \theta(\frac{L}{2}-x,1-z)$	real for even $(m+n)$; imaginary for odd $(m+n)$

Table 5-1: Symmetries exhibited in horizontal porous medium convection. In each $L_p \times 1$ computational domain, where L_p is used here and throughout to denote the domain width associated with a given periodic orbit, time-periodic solutions are sought with reflection/antireflection symmetry about $x = L_p/2$ and centro/anticentro symmetry within each of the two $L_p/2 \times 1$ subdomains which contain a single convection cell. Recall that $\theta = \sum_{n=-N/2}^{N/2} \sum_{m=0}^{M} a_{mn} \mathrm{T}_m(z)\, e^{inkx}$, as shown in (3.7).

the steady state at $Ra = 1991$ and $L_s = 0.41$ plus a small-amplitude contribution of each unstable secondary instability mode in Figure 5-1 is chosen as the initial condition, and then DNS is performed in the same domain with $L = L_s$. Figure 5-2 shows how the modes $a_{1,0}$ and $a_{0,1}$ grow in amplitude from the steady state and evolve to various time-periodic states with different symmetries. It should be noted that the DNS results in Figure 5-2 do not mean that this system finally *converges* to some stable periodic orbit since it may deviate from the orbit after a long time, but indeed indicate that at least initially, or in a short time, this system (initialized with the steady state plus a certain small perturbation) *approaches* a specific time-periodic state.

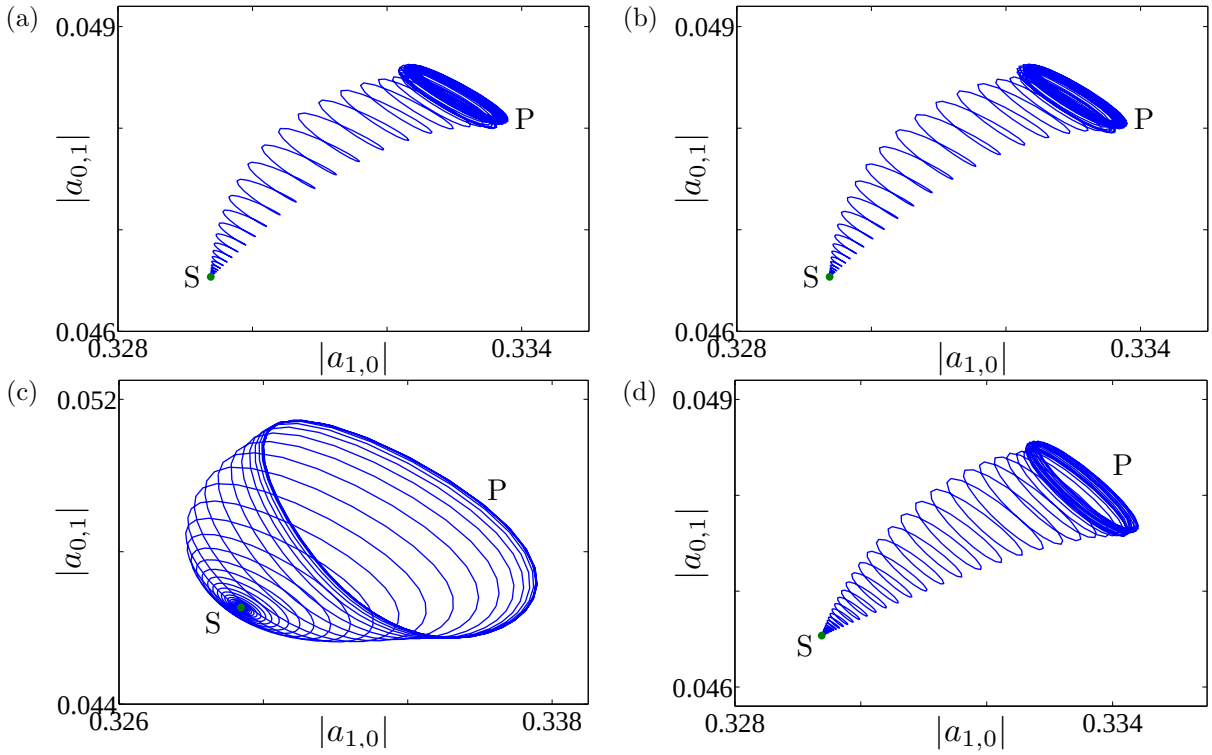

Figure 5-2: Evolution of the magnitudes of modes $a_{1,0}$ and $a_{0,1}$ from DNS showing the Hopf bifurcation from a steady state ("S") to a time-periodic state ("P") at $Ra = 1991$ and $L = 0.41$: (a) anticentro-antireflection symmetry; (b) centro-antireflection symmetry; (c) centro-reflection symmetry; (d) anticentro-reflection symmetry. For each plot, the steady state at the given Ra and L plus a small-amplitude contribution of the unstable secondary instability mode with a certain symmetry is chosen as the initial condition.

5.2.3 Solution Structure

As noted above, four types of time-periodic solutions with different symmetries can be obtained through the Hopf bifurcation of the unstable steady convective state at $Ra = 1991$ and $L_p = 0.41$ (see Figure 5-2, and L_p is defined in the caption of Table 5-1). In this section, numerical continuation is utilized to compute these periodic orbits at the same Rayleigh number but in larger L_p. Figures 5-3–5-6 show snapshots of the temperature field and and time series of the instantaneous Nusselt number nu for the four types of periodic orbits at

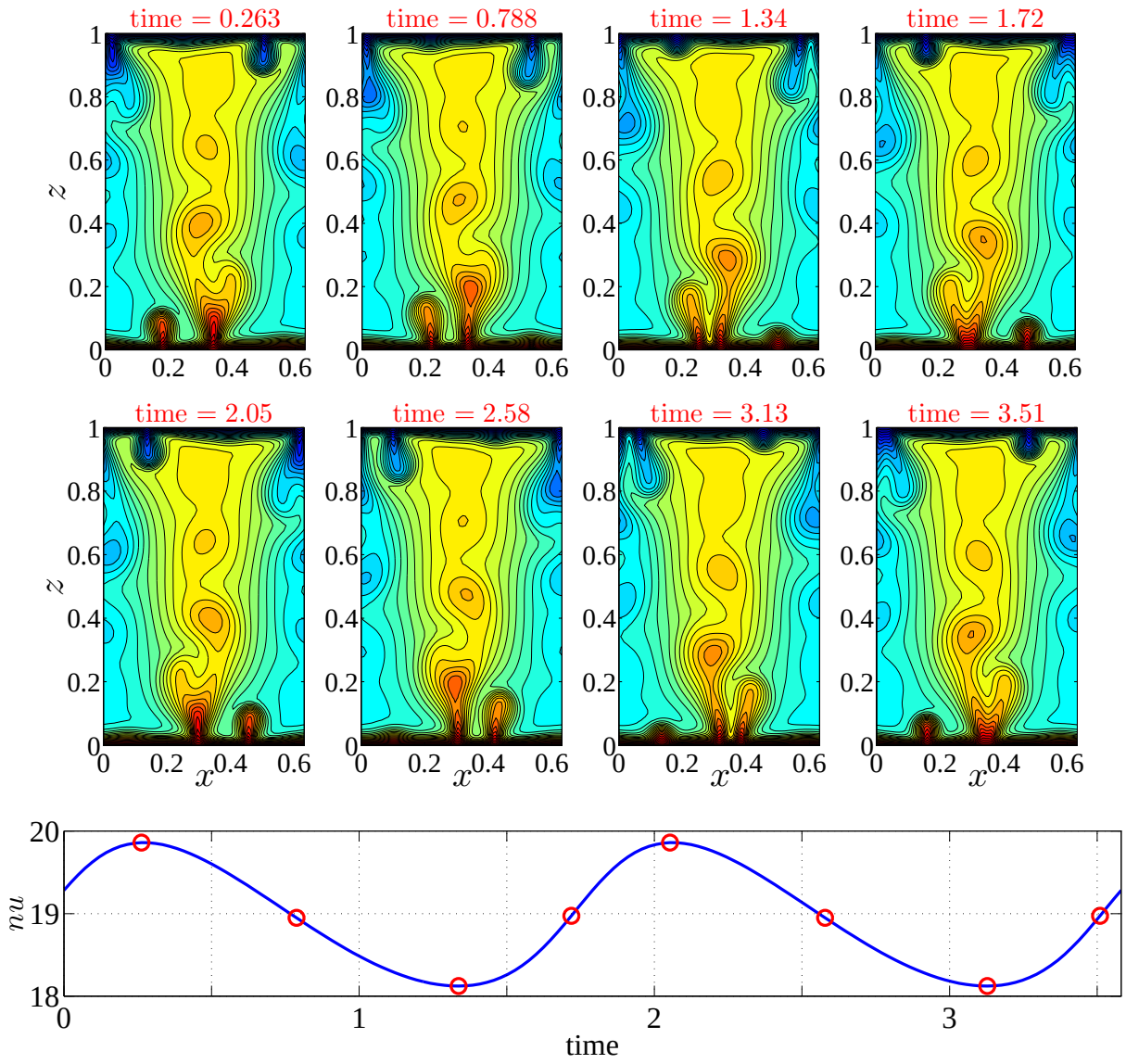

Figure 5-3: Snapshots of the temperature field and time series of the instantaneous Nusselt number for the time-periodic solution with anticentro-antireflection symmetry in one period at $Ra = 1991$ and $L_p = 0.64$. The dots in the bottom plot correspond to the times highlighted in the snapshots. The Nusselt number for this time-periodic solution is $Nu = 18.9$ (DNS: $Nu = 16.3$; steady state: $Nu = 11.3$). It should be noted that the proto-plumes with the centrosymmetry about the point $(x = L_p/2,\ y = 1/2)$ or the reflection symmetry about the plane $x = L_p/2$ always appear with a half-period time delay.

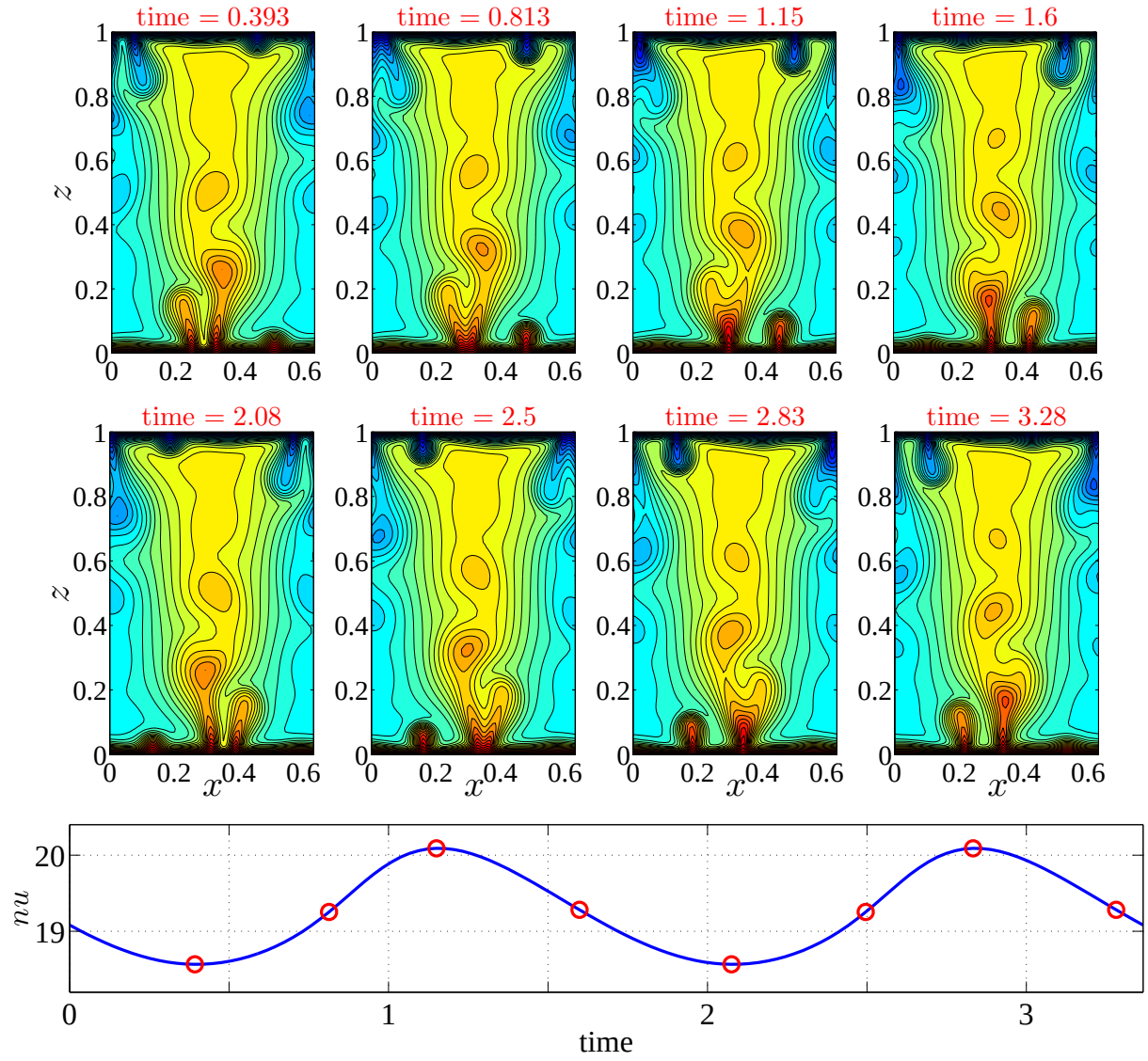

Figure 5-4: Snapshots of the temperature field and time series of the instantaneous Nusselt number for the time-periodic solution with centro-antireflection symmetry in one period at $Ra = 1991$ and $L_p = 0.64$. The dots in the bottom plot correspond to the times highlighted in the snapshots. The Nusselt number for this time-periodic solution is $Nu = 19.3$ (DNS: $Nu = 16.3$; steady state: $Nu = 11.3$). It should be noted that the proto-plumes with the centrosymmetry about the point ($x = L_p/2$, $y = 1/2$) always appear at the same time, while those with reflection symmetry about the plane $x = L_p/2$ always appear with a half-period time delay.

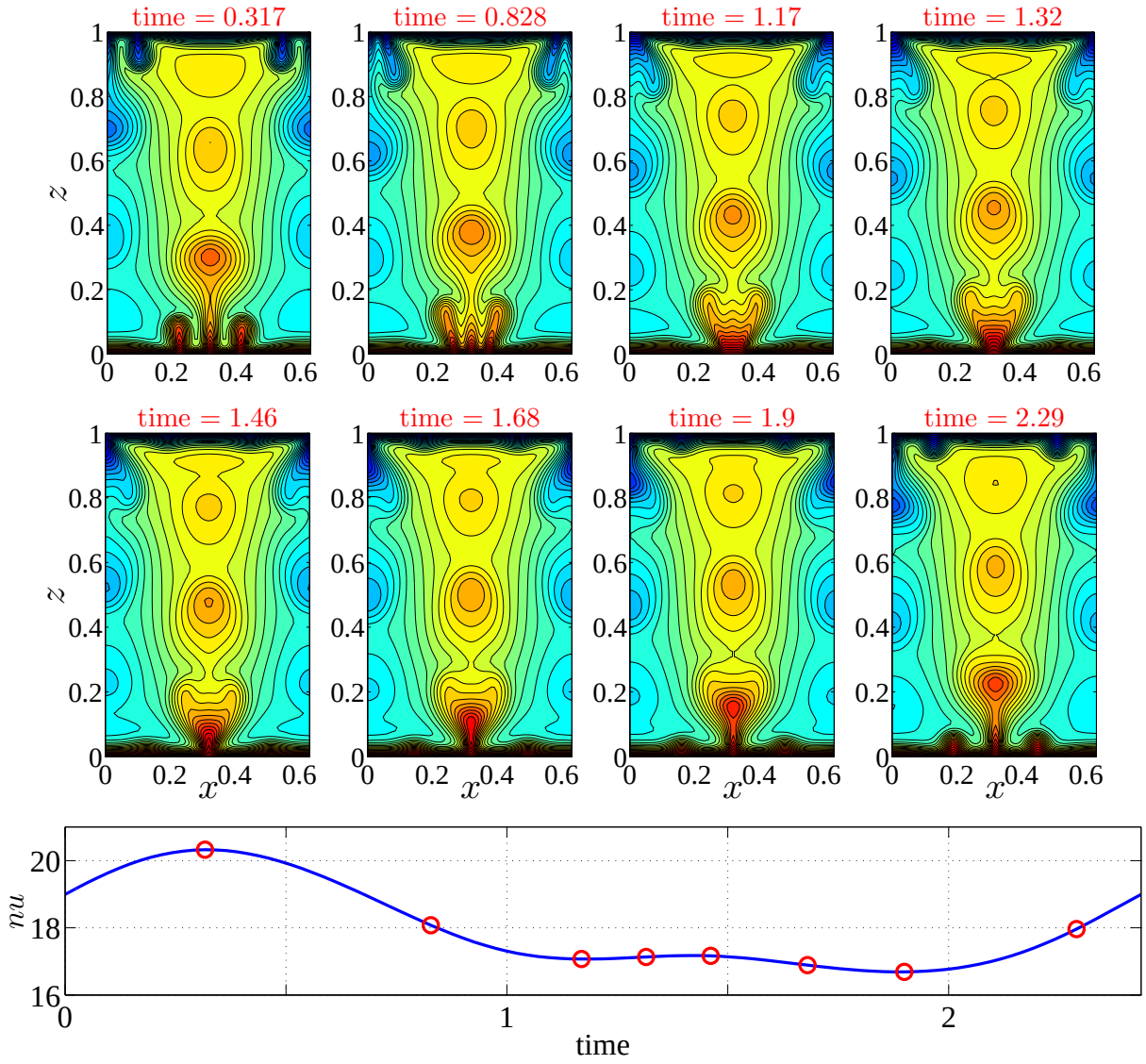

Figure 5-5: Snapshots of the temperature field and time series of the instantaneous Nusselt number for the time-periodic solution with centro-reflection symmetry in one period at $Ra = 1991$ and $L_p = 0.64$. The dots in the bottom plot correspond to the times highlighted in the snapshots. The Nusselt number for this time-periodic solution is $Nu = 18.0$ (DNS: $Nu = 16.3$; steady state: $Nu = 11.3$). It should be noted that the proto-plumes with the centrosymmetry about the point ($x = L_p/2$, $y = 1/2$) or the reflection symmetry about the plane $x = L_p/2$ always appear at the same time.

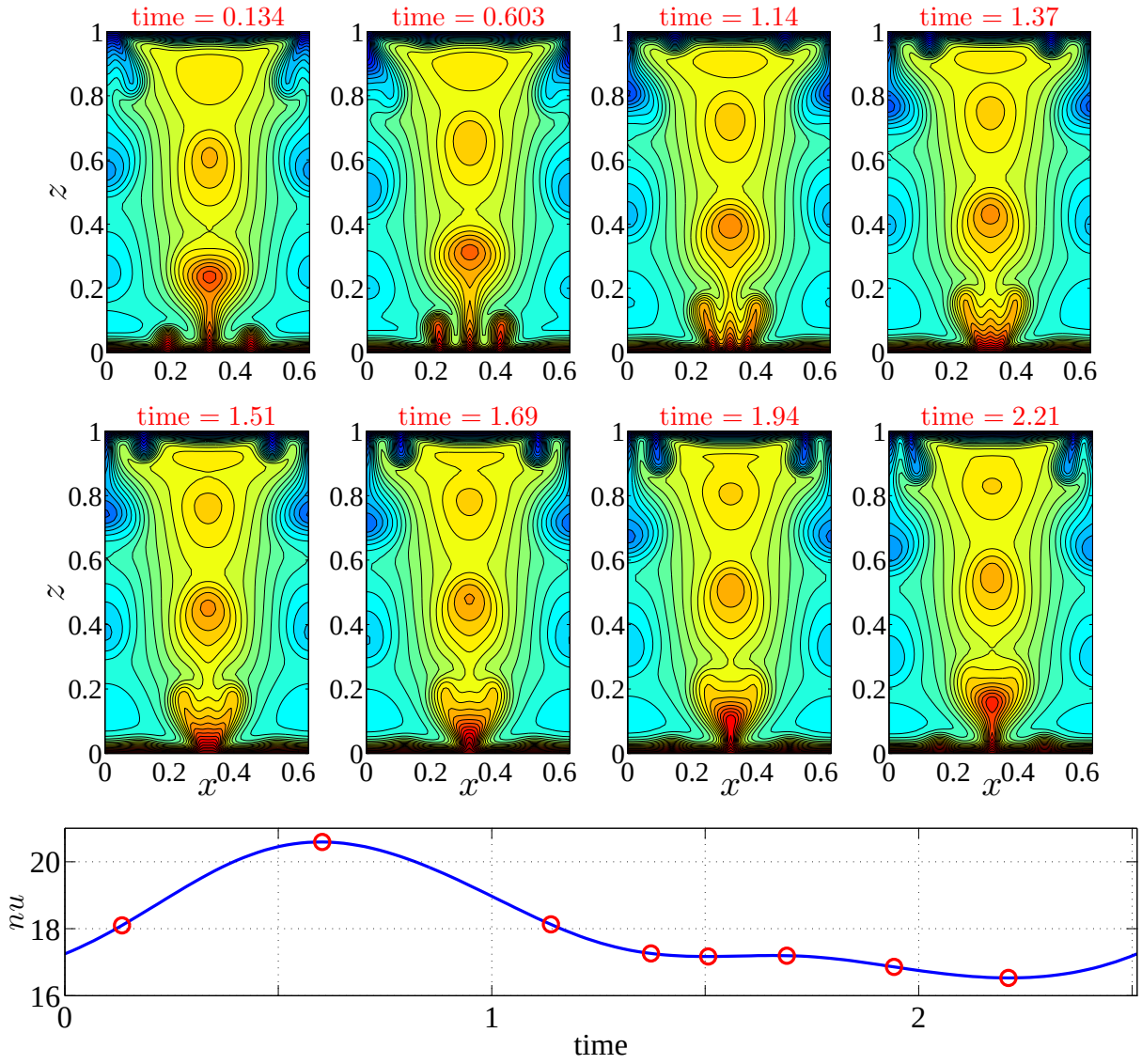

Figure 5-6: Snapshots of the temperature field and time series of the instantaneous Nusselt number for the time-periodic solution with anticentro-reflection symmetry in one period at $Ra = 1991$ and $L_p = 0.64$. The dots in the bottom plot correspond to the times highlighted in the snapshots. The Nusselt number for this time-periodic solution is $Nu = 18.1$ (DNS: $Nu = 16.3$; steady state $Nu = 11.3$). It should be noted that the proto-plumes with the centrosymmetry about the point ($x = L_p/2$, $y = 1/2$) always appear with a half-period time delay, while those with reflection symmetry about the plane $x = L_p/2$ always appear at the same time.

$Ra = 1991$ and $L_p = 0.64$. It should be noted that the domain aspect ratio $L_p = 0.64$ is equal to the mean inter-plume spacing L_m measured from DNS with $L = 9.6$ and all the times appearing in these plots are in convective time units. As shown in these figures, the numerical time-periodic solutions capture the three-region structure of the turbulent columnar flow, including the proto-plume region. In the centro- or reflection-symmetry subspace, the proto-plumes which are symmetrical about the point ($x = L_p/2$, $y = 1/2$) or plane $x = L_p/2$, respectively, always appear and disappear at exactly the same time; on the contrary, in the anticentro- or antireflection-symmetry subspace, the proto-plumes always appear and disappear with a half-period time delay. It should be noted that this phenomenon (appearance of different symmetries) can be easily and frequently observed in the evolution of the statistical turbulent state in DNS, implying that the turbulent state generally wanders among these symmetric subspaces. Moreover, the heat transport accomplished by the time-periodic solutions is (much) closer to that observed in the DNS than is the heat transport achieved by steady convective states without proto-plumes.

The discussion above concerns the instantaneous structure of the periodic-orbit solutions with different symmetries. Next, their time-averaged mean structure will be investigated. If all the variables are decomposed into a time-averaged mean field plus a time-dependent perturbation term, i.e.

$$\psi(x,z,t) = \langle\psi\rangle(x,z) + \psi"(x,z,t), \tag{5.4}$$

$$T(x,z,t) = \langle T\rangle(x,z) + T"(x,z,t), \tag{5.5}$$

then the long time-averaged governing equations are

$$\nabla^2\langle\psi\rangle = -Ra\partial_x\langle T\rangle, \tag{5.6}$$

$$\partial_z\langle\psi\rangle\partial_x\langle T\rangle - \partial_x\langle\psi\rangle\partial_z\langle T\rangle = \nabla^2\langle T\rangle + Q, \tag{5.7}$$

where the effective heat source Q or negative "Reynolds stress divergence" R is given by

$$R = \langle\partial_z\psi"\partial_x T"' - \partial_x\psi"\partial_z T"'\rangle = -Q. \tag{5.8}$$

As shown in Figure 5-7, the time-averaged periodic-orbit flows essentially exhibit a vertical columnar structure in the interior. Moreover, all of the time-averaged flows exhibit a centro-reflection symmetry and the proto-plumes are absent after averaging (see Figure 5-7*a*-*b*), consistent with the steady convective state at these parameters (see Figure 5-7*c*). However, unlike the steady solution, the time-averaged flows become nearly independent of z in the interior, and their mean temperature profile $\langle\overline{T}\rangle$ (dashed lines in Figure 5-7*d*) is (much) closer to that observed in the DNS (solid line in Figure 5-7*d*) than is the mean profile achieved by the steady convective state (dashed-dot line in Figure 5-7*d*). It should be noted that these time-averaged flows cannot be obtained directly from DNS through infinite-time averaging, since chaotic lateral movement of the mega-plumes will yield a horizontally uniform (1D) temperature field in the limit of infinitely long time.

Figure 5-8 shows time-averaged magnitudes of the (complex) Fourier amplitudes of the temperature fluctuations (i.e. deviations from the horizontal mean) as functions of z for the time-periodic solution and turbulent flow in DNS. As is evident in this figure, the time-averaged amplitudes of the temperature fluctuations, $\langle|\hat{\theta}_n|\rangle$, for both the time-periodic and

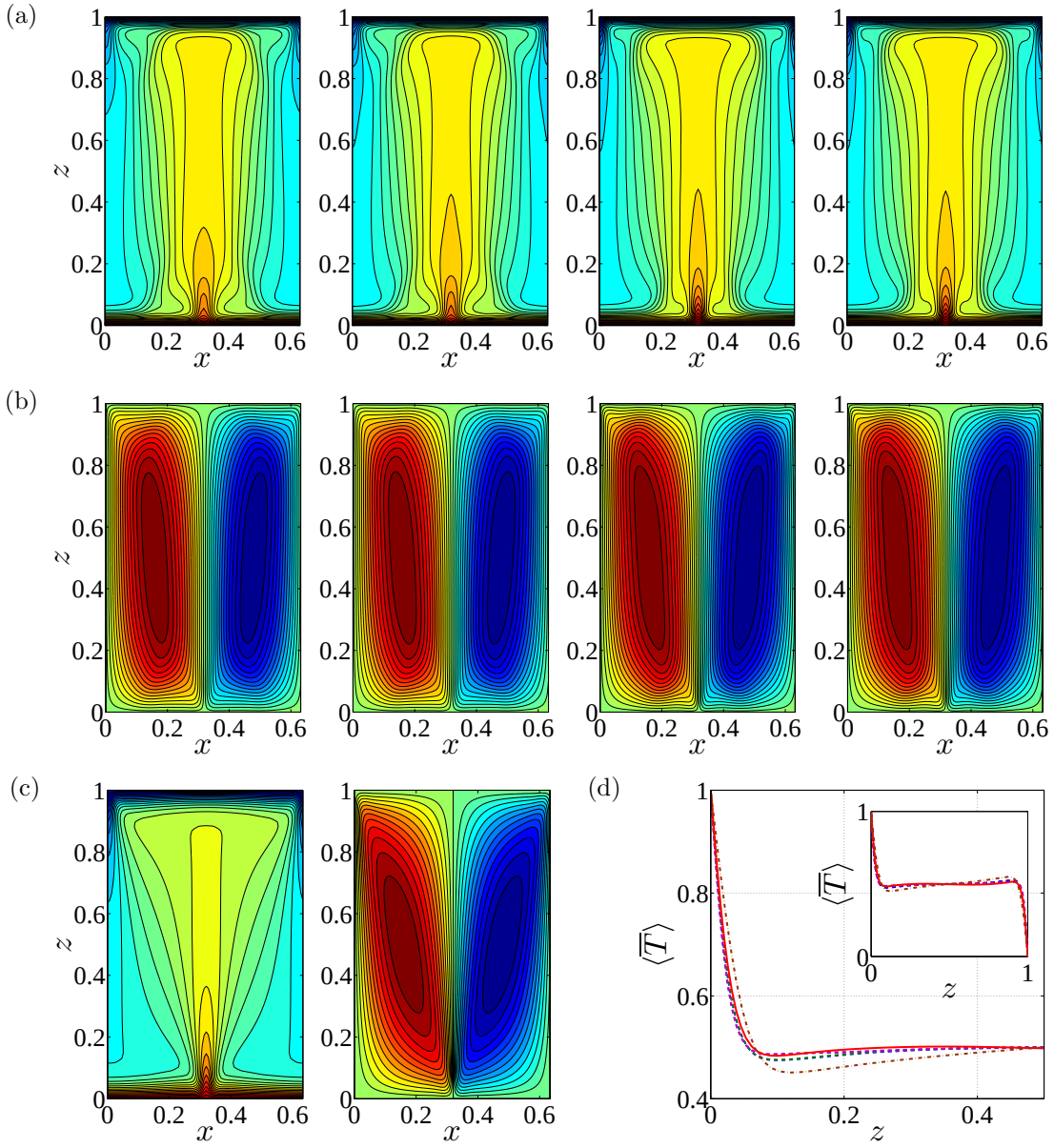

Figure 5-7: Time-averaged temperature (a) and stream function (b) fields of periodic-orbit solutions at $Ra = 1991$ and $L_p = 0.64$. Symmetries of the corresponding solutions in (a) and (b) (from left to right): anticentro-antireflection, centro-antireflection, centro-reflection and anticentro-reflection. For reference, the temperature and stream function fields of the steady convective state at the same parameter values are shown in the left and right plots of (c), respectively. (d): Horizontal and time-averaged temperature profiles for periodic orbits (dashed lines), DNS (solid line) and steady state (dashed-dot line).

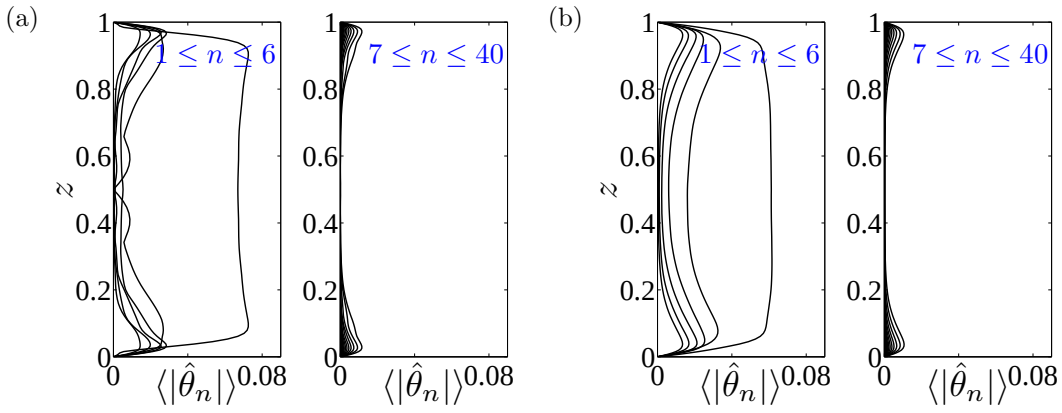

Figure 5-8: Time-averaged Fourier amplitudes of the temperature fluctuations (i.e. deviations from the horizontal mean) at $Ra = 1991$ and $L = 0.64$. (a): Time-periodic solution with centro-reflection symmetry; (b): DNS.

turbulent states reveal that the interior flow is a composite of a few low-wavenumber Fourier modes but is dominated by one mode, consistent with the structure observed at $Ra = 50000$ in Figure 2-6. Furthermore, in the narrow domain ($L = 0.64$), the time-averaged interior flow is well represented by only six Fourier modes, and at high wavenumber, the Fourier amplitudes $\hat{\theta}_n$ are strongly localized near the upper and lower walls, where they superpose to comprise the small rolls and proto-plumes within the thermal and vorticity boundary layers.

Figure 5-9 shows the Reynolds stress divergence of time-periodic solutions with different symmetries at $Ra = 1991$ and $L_p = 0.64$. One obvious observation is that all of the Reynolds stress divergence for different solutions exhibits a centro-reflection symmetry and is strongly localized near the upper and lower walls (see the upper plots in Figure 5-9). Moreover, the horizontal mean of the Reynolds stress divergence $\overline{R}$ (or $-\overline{Q}$) for both periodic orbits and the turbulent state is generally positive near the lower wall and negative near the upper wall (see the lower plot in Figure 5-9), implying that the time-periodic motion and the convective turbulence act like an effective sink that takes the heat out in the bottom boundary layer and

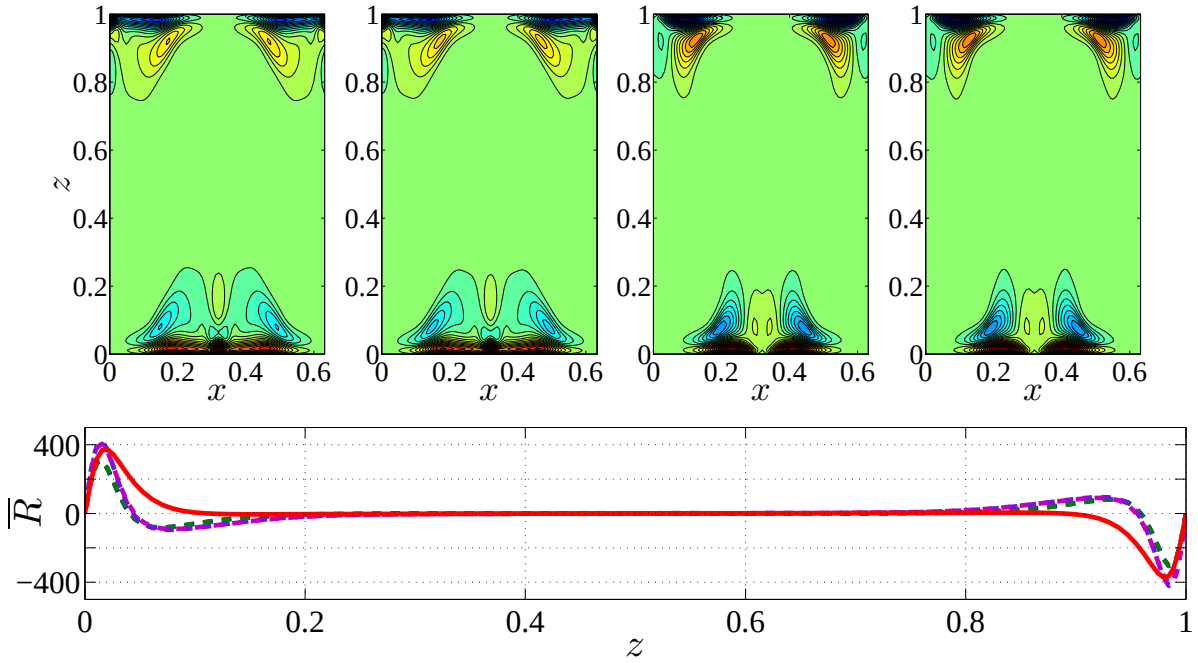

Figure 5-9: Reynolds stress divergence of time-periodic solutions at $Ra = 1991$ and $L_p = 0.64$. Symmetries of the corresponding solutions for the top plots (from left to right): anticentro-antireflection, centro-antireflection, centro-reflection and anticentro-reflection; bottom: horizontal and time-averaged Reynolds stress divergence (DNS: solid line; periodic orbits: dashed lines). It should be noted that the Reynolds stress divergence for both periodic-orbit solutions and the turbulent state is localized near the walls and independent of z in the interior.

re-deposits it as an effective source in the top boundary layer. It should be noted that given a specific 2D Reynolds stress divergence R in Figure 5-9, the corresponding time-averaged temperature field in Figure 5-7(a) is actually a steady solution of (5.7).

As noted in chapter 3, at large Ra, the steady convective flows can be broadly categorized into two distinct forms: for small L_s (close to the linear stability threshold) the flow in the interior can be well predicted using the heat-exchanger model given by Hewitt et al. (2012); for larger L_s, the convective state changes form, exhibiting a stably stratified core. In this section, the aspect-ratio dependence of time-periodic states is investigated at $Ra =$

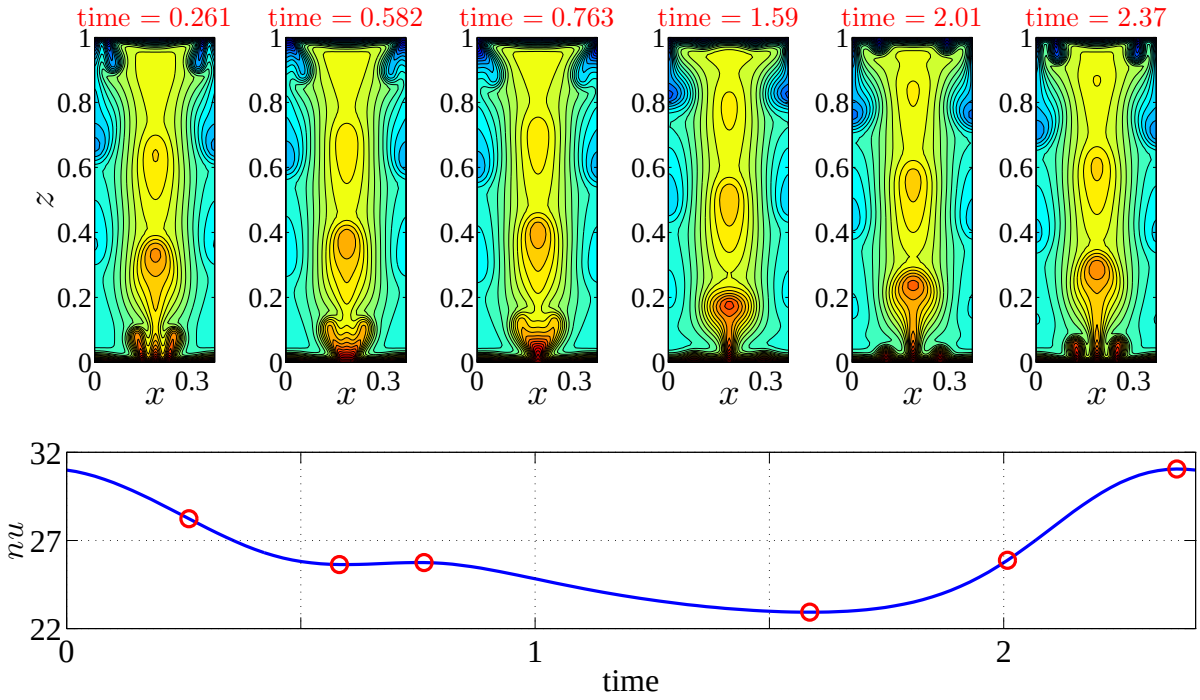

Figure 5-10: Snapshots of the temperature field and time series of the instantaneous Nusselt number for the time-periodic solution with centro-reflection symmetry in one period at $Ra = 3155$ and $L_p = 0.375$. The dots in the bottom plot correspond to the times highlighted in the snapshots. The Nusselt number for this periodic-orbit solution is $Nu = 25.97$ (DNS: $Nu = 24.52$; steady state: $Nu = 17.07$). Note that the mean inter-plume spacing at $Ra = 3155$ is $L_m = 0.54$ measured from DNS with $L = 8$.

3155. Figures 5-10 and 5-11 show snapshots of the temperature field and time series of the instantaneous Nusselt number for the time-periodic solution with centro-reflection symmetry at $L_p = 0.375$ and 1.1. As also observed in Figures 5-3–5-6, the small proto-plumes generated from the upper and lower walls are continually swept into and thus merge with the mega-plumes spanning the height of the porous layer. Meanwhile, the heat taken by these hot (red) proto-plumes from the bottom boundary layer is advected to the upper boundary layer through the vertical channel (mega-plume). One obvious difference between the narrow and wide domain solutions is that the narrow periodic orbit exhibits a vertical columnar structure

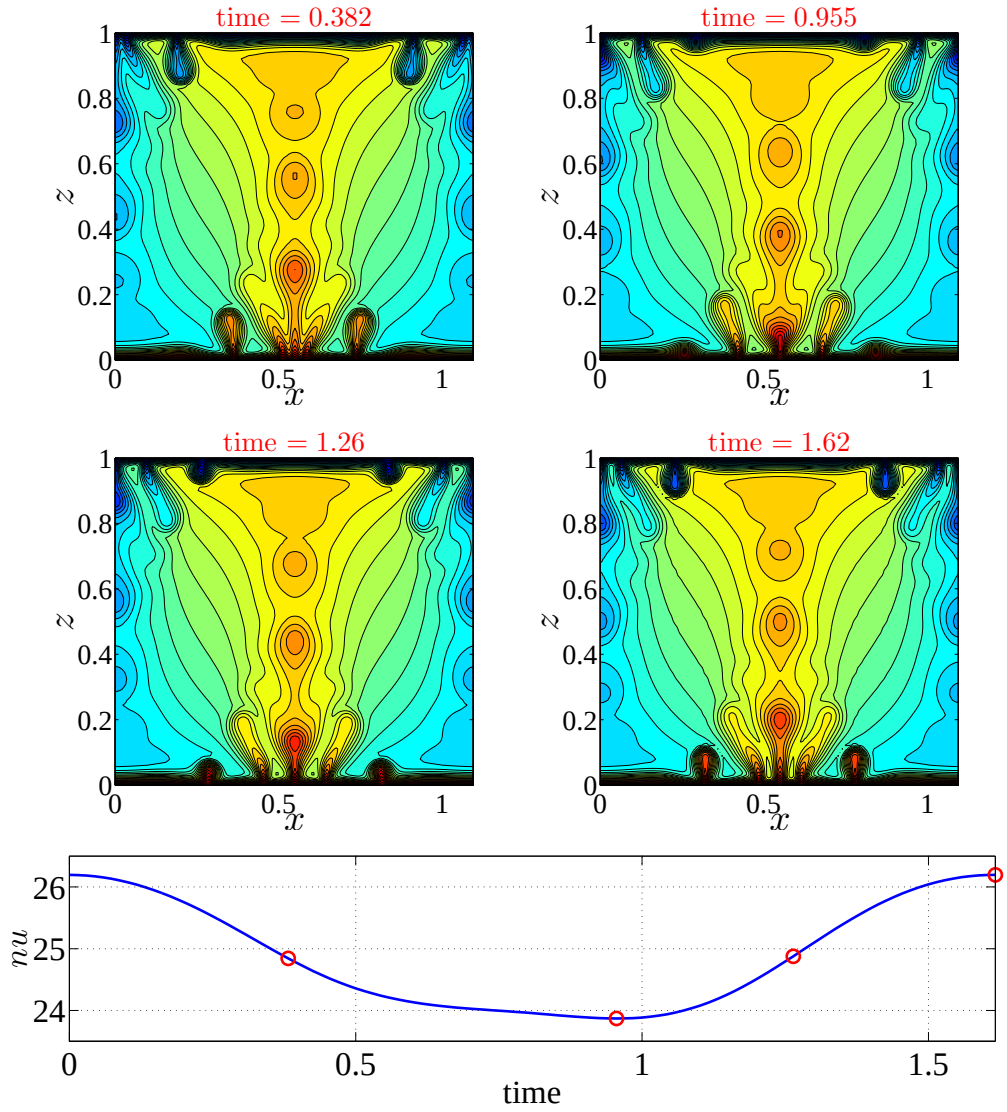

Figure 5-11: Snapshots of the temperature field and time series of the instantaneous Nusselt number for the time-periodic solution with centro-reflection symmetry in one period at $Ra = 3155$ and $L_p = 1.1$. The dots in the bottom plot correspond to the times highlighted in the snapshots. The Nusselt number for this periodic-orbit solution is $Nu = 24.87$ (DNS: $Nu = 24.52$; steady state: $Nu = 11.63$).

in the interior, consistent with the turbulent columnar flow observed in DNS at large Ra, while the wide one exhibits a "V"-type core structure, as found at moderate Ra. Moreover, between the hot and cold channels (i.e. the outer edge of the neighbouring mega-plumes),

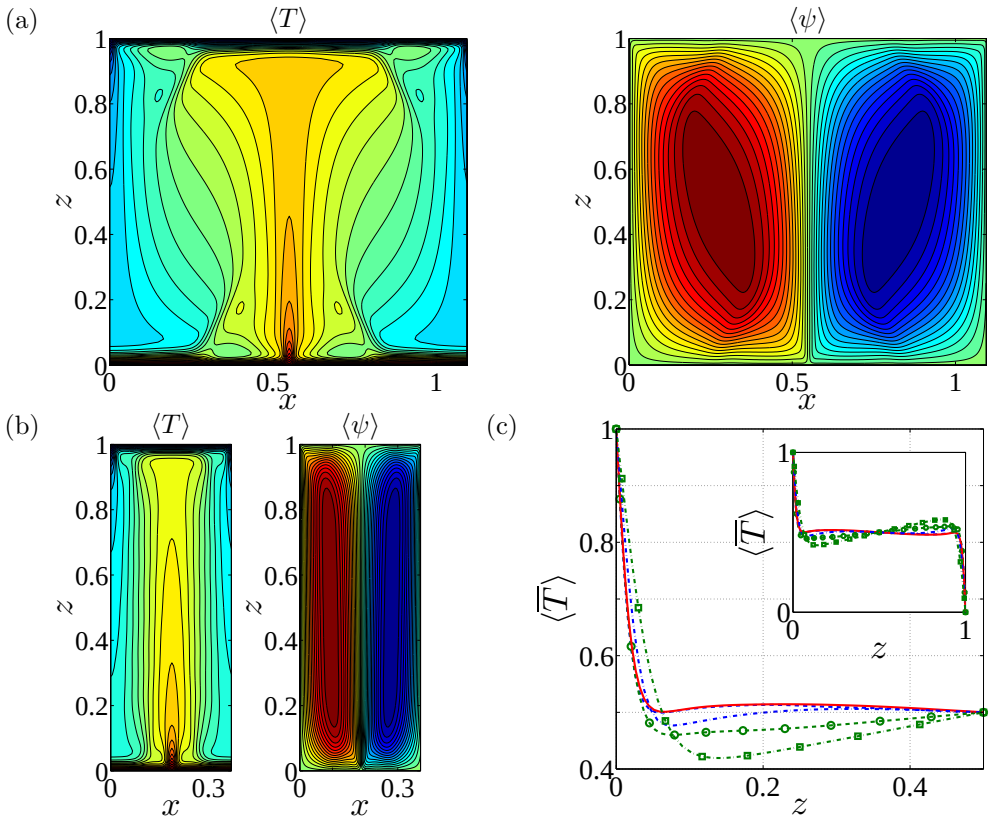

Figure 5-12: Time-averaged temperature and stream function fields of periodic-orbit solutions with centro-reflection symmetry at $Ra = 3155$ in narrow and wide domains: (a): $L_p = 1.1$; (b): $L_p = 0.375$; (c): temporal and horizontal mean temperature profiles of the time-periodic solutions for $L_p = 1.1$ (dashed-circle line) and 0.375 (dashed line), the turbulent state from DNS performed with $L = 8$ (solid line), and the steady states at $L_p = 1.1$ (dashed-square line) and 0.375 (dashed-dot line). The mean temperature gradient at the mid-plane $\partial_z \langle \overline{T} \rangle|_{z=0.5}$ is -0.0348 for $L_p = 0.375$ and 0.109 for $L_p = 1.1$ for the time-periodic solutions reported here, -0.0504 for $L_s = 0.375$ and 0.247 for $L_s = 1.1$ for the steady solutions, and -0.0780 for the turbulent columnar flow from DNS. Note that the mean temperature profile for the smaller L_p (dashed line) agrees very well with that obtained from DNS (solid line).

there exists a zone where the temperature field is almost invariant and the flow becomes stationary even for this unsteady system. Actually, within this region, part of the heat is transported laterally (toward the two sides) by pure diffusion.

Figure 5-12 shows the time-averaged temperature and stream function fields and the mean temperature profiles corresponding to the periodic orbits discussed above. It can be seen from these plots that the time-averaged periodic solutions exhibit different structures as the aspect ratio L_p is changed. For large L_p (see Figure 5-12a), a V-type flow is exhibited in the interior and the flow at the center of the natural/antinatural rolls is nearly at rest; for small L_p (see Figure 5-12b), a vertical columnar flow is exhibited in the interior, as is manifest in DNS. Moreover, Figure 5-12(c) indicates that in both narrow and wide domains, the horizontal- and temporal-mean temperature profiles of the time-periodic flows are closer to that of the real flow obtained from DNS than do those of steady flows. Interestingly, the mean temperature profile of the time-periodic solution at $L_p = 0.375$ almost completely coincides with the corresponding profile obtained from DNS performed in a domain with $L = 8$. Furthermore, as in the steady case, for the time-periodic solution the negative value of $\partial_z \langle \overline{T} \rangle|_{z=0.5}$ at $L_p = 0.375$ reveals that the interior flow is unstably stratified in the narrow domain, while the positive value at $L_p = 1.1$ indicates that the interior flow becomes stably stratified in the wide domain. Figure 5-13 shows that the Reynolds stress divergences of these time-periodic solutions in narrow and wide domains exhibit a very similar structure: both are localized near the upper and lower walls, consistent with those in Figure 5-9.

5.3 Secondary Stability Analysis

5.3.1 Floquet Theory

In previous sections, several time-periodic solutions with different symmetries and in various domain aspect ratios have been presented. The results indicate that these periodic orbits

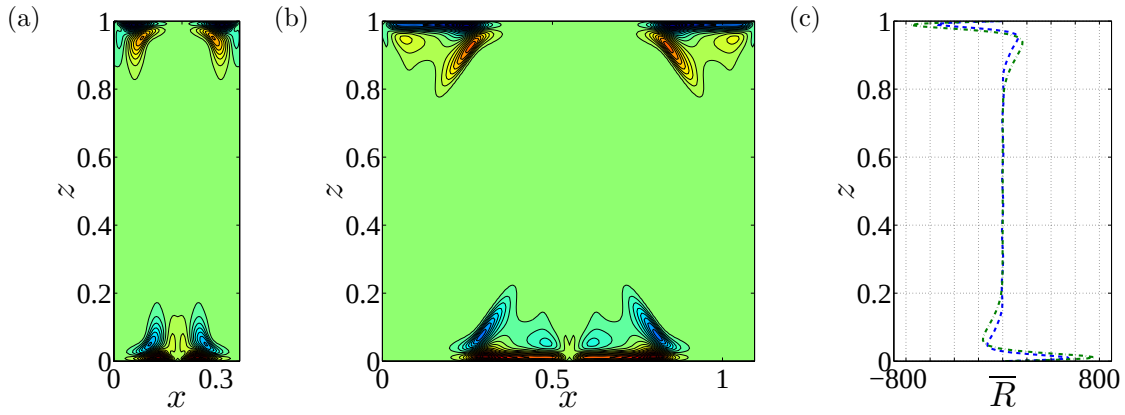

Figure 5-13: Reynolds stress divergence of time-periodic solutions at $Ra = 3115$ for two different aspect ratios: (a) $L_p = 0.375$; (b) $L_p = 1.1$; (c) horizontal-mean profiles with dashed line corresponding to (a) and dashed-dot line corresponding to (b).

contain certain features characterizing the turbulent columnar flows observed in DNS. A natural question concerns the stability of these time-periodic states, e.g. whether the wall and bulk instability modes continue to exist in such unsteady flows and how large the magnitudes of their growth rates are if indeed they do exist. In this section, to address these questions, a secondary stability analysis is performed at large Ra using spatial Floquet theory.

Let $\theta^\star$, $\tau^\star$ be a time-periodic solution satisfying (5.3), namely, $\theta^\star = f^{\tau^\star}(\theta^\star)$. Given a small random perturbation $d\theta$, the unstable state will deviate from the orbit after one period through certain unstable eigenfunctions/directions, while the stable one will be still attracted onto the orbit since all the disturbances will be damped as time evolves. Hence, the linear stability operator $\mathcal{A}$ can be defined as

$$\mathcal{A}d\theta = f^{\tau^\star}(\theta^\star + d\theta) - f^{\tau^\star}(\theta^\star) = f^{\tau^\star}(\theta^\star + d\theta) - \theta^\star, \tag{5.9}$$

where the right-hand side corresponds to the deviation of the flow, due to the initial perturbation, from the orbit after one period (or one time-$\tau^\star$ map). Namely, the right-hand side of (5.9) will grow with time for unstable orbits while it will tend to zero for stable ones.

Rewrite (5.9) as

$$\mathcal{A}\mathbf{V} = \Lambda\mathbf{V}, \tag{5.10}$$

where $\mathbf{V}$ is the eigenvector of operator $\mathcal{A}$ and Λ is the corresponding eigenvalue. For a slightly disturbed time-periodic solution, i.e. $\theta = \theta^\star + \varepsilon\mathbf{V}$ where ε is a small number, the corresponding time-$\tau^\star$ map can be approximated using a Taylor series expansion:

$$f^{\tau^\star}(\theta) = f^{\tau^\star}(\theta^\star + \varepsilon\mathbf{V}) \approx f^{\tau^\star}(\theta^\star) + \partial_\theta f^{\tau^\star}|_{\theta^\star}\varepsilon\mathbf{V} = \theta^\star + \mathcal{A}\varepsilon\mathbf{V} = \theta^\star + \varepsilon\Lambda\mathbf{V}. \tag{5.11}$$

Similarly, the time-$n\tau^\star$ forward map of equation (5.1) can be approximated as

$$f^{n\tau^\star}(\theta) \approx \theta^\star + \varepsilon\Lambda^n\mathbf{V}. \tag{5.12}$$

Therefore, the relative norm of the deviation of the flow (with the small initial perturbation) from the orbit after time-$n\tau^\star$ forward map becomes

$$\frac{||f^{n\tau^\star}(\theta) - \theta^\star||}{||\theta - \theta^\star||} \approx \frac{||\varepsilon\Lambda^n\mathbf{V}||}{||\varepsilon\mathbf{V}||} = |\Lambda|^n. \tag{5.13}$$

Hence, $|\Lambda|$ gives the growth rate of the disturbance after the one-period forward map: for $|\Lambda| < 1$, the perturbed state will converge back to the original orbit as $n \to \infty$, i.e. the time-periodic state is linearly stable; otherwise ($|\Lambda| > 1$), the state is linearly unstable. To make the results compatible with those obtained from the previous stability analysis of

steady convective states, rewrite Λ as

$$\Lambda = e^{\lambda \tau^\star}. \tag{5.14}$$

Then, $\lambda = \ln \Lambda / \tau^\star$. Thus, in convective time units, the growth rate becomes $\sigma = \ln \Lambda / (\tau^\star Ra)$.

5.3.2 Secondary Stability Results

In this study, Arnoldi iteration is utilized to solve the resulting algebraic eigenvalue problem (5.10) to obtain the leading eigenvalues and eigenfunctions. To explore the growth rate of small perturbations with different wavelengths, the stability analysis is performed in domains with different aspect ratios $L = \chi L_p$ with integer $\chi \geq 1$, as shown in Figure 5-14. For $\chi = 1$, the fundamental horizontal wavenumber of the perturbation is same as that of the base state; for $\chi > 1$, the fundamental horizontal wavenumber of the perturbation becomes $1/\chi$ times the wavenumber of the base flow so that some long-wavelength disturbances are introduced.

Figures 5-15 and 5-16 show the eigenspectrum and 2D eigenfunctions corresponding to the periodic orbit shown in Figure 5-14. It can be seen from Figure 5-15 this time-periodic solution is unstable, exhibiting the same fastest growth rate $\mathrm{Re}\{\sigma_m\}$ at $\chi = 1$ and 4. Actually, the results (not reported here) also indicate that $\mathrm{Re}\{\sigma_m\}$ is also unchanged for other χ, implying that the fastest growth rate is essentially independent of χ. However, the imaginary part of the eigenvalue in Figure 5-15, i.e. $\mathrm{Im}\{\sigma\}$, is meaningless, and the flat-boundary structure of the maximum (or minimum) $\mathrm{Im}\{\sigma\}$ is because an arctangent function, whose range is restricted to $(-\pi/2, \pi/2)$ in computations, is used to translate Λ to σ. Figure 5-16(a)

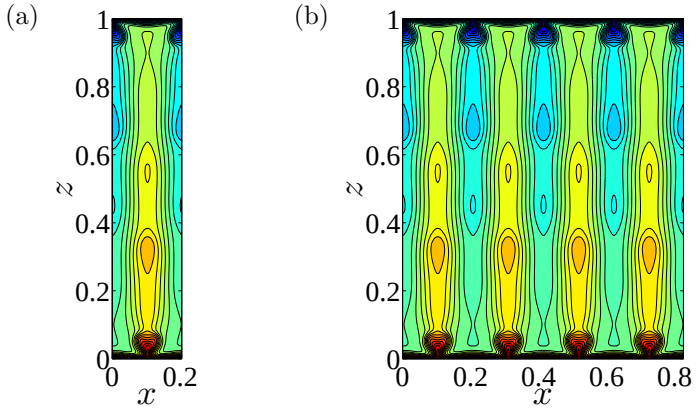

Figure 5-14: Stability analysis of the time-periodic solution at $Ra = 5000$ with centro-reflection symmetry in domains with different aspect ratios $L = \chi L_p$. (a): $L_p = 0.21$, $\chi = 1$, the fundamental horizontal wavenumber of the perturbation is same as that of the base state; (b): $L_p = 0.21$, $\chi = 4$, the fundamental horizontal wavenumber of the perturbation is $1/4$ the wavenumber of the base flow; namely, some long-wavelength disturbances are introduced.

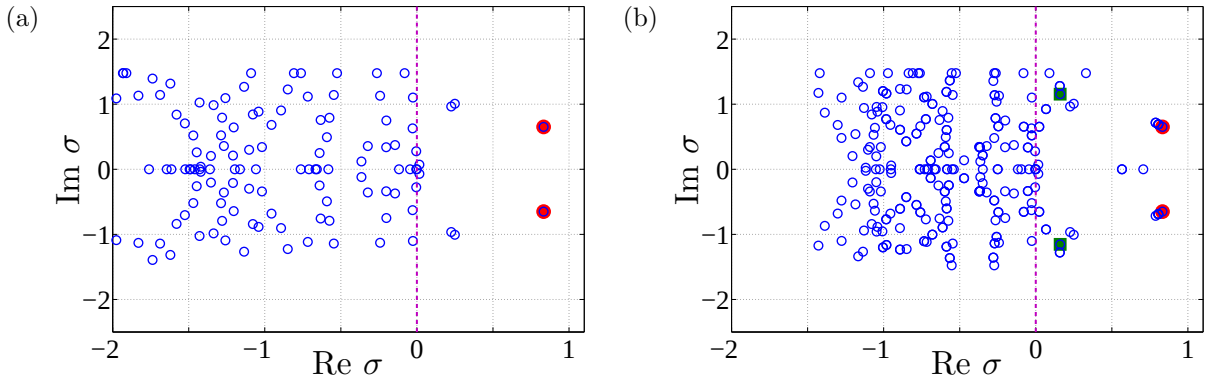

Figure 5-15: The leading eigenvalues from stability analysis of the time-periodic solution with centro-reflection symmetry at $Ra = 5000$: (a) $L_p = 0.21$, $\chi = 1$; (b) $L_p = 0.21$, $\chi = 4$. In each case, the dot denotes the fastest growing (wall) mode and the square marks the bulk mode. It should be noted that the maximum growth rate is essentially independent of χ and the growth rate of the bulk instability is much less than that of the wall instability.

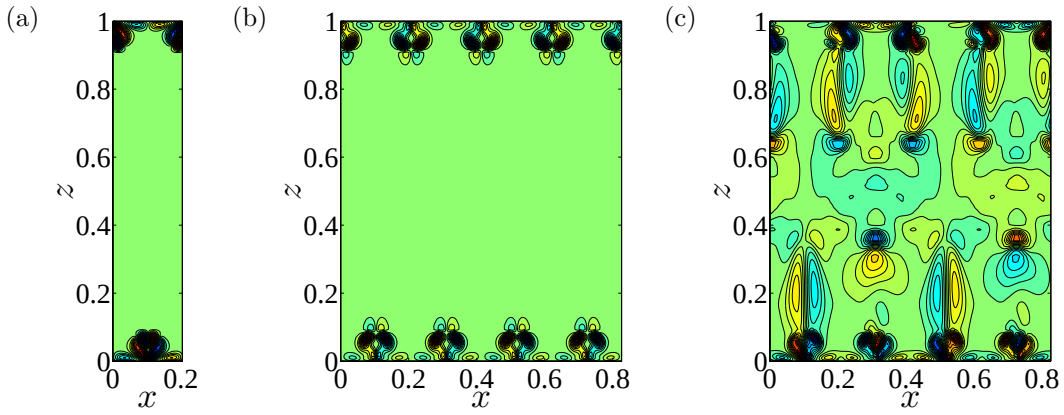

Figure 5-16: The 2D temperature eigenfunctions at $Ra = 5000$ shown in a domain with aspect ratio $L = \chi L_p$ ($L_p = 0.21$): (a) $\chi = 1$, fastest growing mode; (b) $\chi = 4$, fastest growing mode; (c) $\chi = 4$, bulk mode corresponding to the squares in Figure 5-15(b).

and (b) reveal that both of the most unstable perturbations for different χ have a very similar wall-mode structure. Moreover, Figure 5-16(c) indicates that there also exists a bulk instability when $\chi > 1$. This bulk mode always occurs for a long-wavelength disturbance and has a much lower growth rate than the fastest growing wall modes (see the squares in Figure 5-15b). It should be noted that all of these results are consistent with those obtained in the stability analysis of steady convective states: namely, for each L_p or sufficiently large L_s, the fastest growing mode is a wall mode; the bulk mode generally corresponds to long-wavelength perturbations and has a smaller growth rate.

5.4 Summary

In this chapter, the physics of horizontal porous medium convection is explored by investigating the structure and stability of (numerically) exact time-periodic solutions. Four types of periodic-orbit states with different symmetries are obtained through the Hopf bifurcation

– associated with certain wall-mode disturbances – of the steady convective state. These time-periodic states retain the 3-region structure of the turbulent columnar flow, including the proto-plume region, and thereby exhibit very similar heat transport and statistical structure as turbulent flow at large Ra. Comparisons of a series of qualitative and quantitative features of the time-periodic solution and the turbulent state indicate the periodic orbits could be used to elucidate the heat-transport process exhibited in time-dependent turbulent flow. Namely, near the lower/heated wall, the heat is effectively absorbed by a sink, then advected upward through the interior vertical channel (mega-plume), and finally re-deposited by an effective source near the upper/cooled wall. Moreover, the stability analysis of the time-periodic solution at large Ra shows there still exist two types of instability in the time-dependent flow: a bulk instability and a wall instability, although the former, which usually corresponds to long-wavelength disturbances, is generally much weaker than the latter.

CHAPTER 6

HEAT TRANSPORT IN A HORIZONTAL POROUS LAYER AT LARGE RAYLEIGH NUMBER

6.1 Introduction

In previous chapters, the structure and stability of exact coherent states and the dynamics of porous medium convection have been explored using the 2D Darcy–Oberbeck–Boussinesq equations in the infinite Darcy–Prandtl number limit. This mathematical model combines Darcy's law for incompressible flow in a fluid-saturated porous medium and buoyancy forces incorporated through the Boussinesq approximation together with a time-dependent advection-diffusion equation for the temperature field (see chapter 1.4). The sole nonlinearity arises from temperature advection, and consequently this system is considerably simpler than the full Oberbeck–Boussinesq equations.

One crucial phenomenological distinction between Rayleigh–Bénard convection of a pure fluid and that occurring in a fluid-saturated porous layer is the observed mean spacing between adjacent rising and falling thermal plumes, which decreases with increasing Ra in porous

medium but not in classical Rayleigh–Bénard convection (von Hardenberg et al., 2008; Johnston and Doering, 2009; Goluskin and Spiegel, 2012). Indeed, for porous medium convection, linear stability analysis of the purely conducting state reveals that the horizontal wavelength of the high-wavenumber marginal mode scales as $Ra^{-1/2}$ while that of the fastest-growing disturbance decreases as $Ra^{-1/4}$ (see details in chapter 3.2). Remarkably, direct numerical simulations in Hewitt et al. (2012) and chapter 2 of this dissertation not only indicate that the mean inter-plume spacing decreases markedly with Ra, scaling approximately as $Ra^{-2/5}$ for $Ra < 10000$, but also that the flow actually becomes more organized in the interior (i.e. away from the upper and lower thermal boundary layers) as Ra is increased. Moreover, complementary numerical and matched asymptotic investigations of steady cellular solutions in porous medium convection in Corson (2011) and chapter 3 also confirm that those solutions with the highest heat transport decrease in lateral scale – approximately as $Ra^{-1/2}$, just slightly larger than the smallest horizontal scale capable of sustaining convection. Thus, all these investigations confirm the trend toward compression of horizontal scales.

Motivated by these studies, one following crucial question will be addressed in this chapter: *is there a smallest domain aspect ratio $L(Ra)$ above which the Nusselt number Nu, the volume- and time-averaged heat flux normalized by the conduction value, becomes independent of L?* This question is analogous to that of determining the minimal flow unit in wall-bounded shear flow turbulence, the smallest physical domain (with horizontally periodic boundary conditions) in which (low-dimensional) turbulence may sustain itself. Although the above question was addressed empirically *via* highly-resolved DNS utilizing a Fourier–Chebyshev pseudospectral algorithm in Dianati (2013), it is revisited here using upper bound analysis.

A robust theoretical approach for analyzing turbulent thermal convection is to derive using rigorous analysis – without directly simulating the governing equations – bounds on Nu that

all flow solutions (whether steady, unsteady, turbulent, etc.) must satisfy. Lower bounds are easy: $Nu \geq 1$ and this bound is mathematically sharp, being saturated by the stationary (albeit often unstable) no-flow conduction state that exists for all parameter values. The derivation of upper bounds on flow quantities was first given by Howard (originally motivated by the ideas of Malkus (1954)) for Rayleigh–Bénard convection of a pure fluid layer (Howard, 1963) and extended by Busse et al. to various other thermal convection processes as well as to shear flow turbulence (Busse, 1969, 1970; Busse and Joseph, 1972). The Malkus–Howard–Busse (MHB) variational formulation is strictly true for stationary flows but is presumed to be valid in an infinite (rather than finite) horizontal layer owing to the hypothesis of statistical stationarity, i.e. the technical assumption that horizontal averages, and thus also volume averages, are time independent (Doering and Constantin, 1996). Several decades later a background field method was proposed by Doering and Constantin (1992, 1994, 1996, 1998), Constantin and Doering (1995) and Doering and Hyman (1997) to produce rigorous upper bounds on energy dissipation and heat transport in various turbulent flows without any statistical hypotheses, scaling assumptions, or closure approximations. This approach is based on Hopf's method for producing *a priori* estimates for solutions of the Navier–Stokes equations with inhomogeneous boundary conditions (Hopf, 1941), and hereafter is referred to as the Constantin–Doering–Hopf (CHD) variational formalism. The link between the MHB and CDH variational schemes has been discussed in detail by Kerswell (1998, 2001).

In porous medium convection, rigorous analyses of the Darcy–Oberbeck–Boussinesq equations by Doering and Constantin (1998) and Otero et al. (2004) show that $Nu \leq cRa^1$ with different prefactors c. However, since piecewise linear functions were utilized as the background profiles, these upper bounds are not the optimal ones within the CDH variational framework. The aim of this study is to compute the optimal upper bound on Nu as

a function of Ra and L by numerically solving the full background problem using a novel two-step algorithm in which time is introduced into the variational formulation. Generally, numerical continuation is required to solve the "multi-mode" optimization problem arising from the upper bound analysis (Plasting and Kerswell, 2003), but here it will be shown that this two-step algorithm does not require continuation. Moreover, it is also proved that the only steady state to which the numerical method can converge is the true (globally optimal) solution of the variational problem. Using the new two-step algorithm, Nu is bounded and estimated using a combination of upper bound and generalized energy stability theory, thereby providing a systematic exploration of the dependence of Nu on L at large Ra.

The reminder of this chapter is organized as follows. In the next section, the fundamental concepts of upper bound theory and energy (nonlinear) stability theory are reviewed, the Euler–Lagrange equations for the relevant variational optimization problem are derived, the numerical scheme to solve these equations is outlined, and it is proved that the only steady state to which the numerical algorithm can converge is the true solution. The upper bound computations for varying Rayleigh number and aspect ratio are described and analyzed in section 6.3, and a summary is given in section 6.4.

6.2 Computational Methodology

6.2.1 Upper Bound Theory (CDH Formalism)

In the CDH upper bound theory the temperature $T(x, z, t)$ is decomposed into a time-independent background profile $\tau(z)$ carrying the inhomogeneous boundary conditions plus a (arbitrarily large) nonlinear fluctuation $\theta(x, z, t)$ satisfying periodic boundary conditions

in x and homogeneous Dirichlet boundary conditions in z:

$$T(x,z,t) = \tau(z) + \theta(x,z,t), \tag{6.1}$$

where $\tau(0) = 1$, $\tau(1) = 0$, and $\theta(x,0,t) = \theta(x,1,t) = 0$.[1] It should be noted that the background field (or, in the case of Rayleigh–Bénard convection, background temperature profile) is neither a steady solution of the governing equations nor a horizontal/long-time mean. Ensuring that appropriate test background profiles satisfy a certain spectral constraint produces rigorous upper bounds on global transport properties of the flow.

Upper bound analysis in Doering and Constantin (1998) and Otero et al. (2004) shows that for any $\tau(z)$, $a \in (0,1)$ and $Ra \geq 4\pi^2$,

$$Nu \leq 1 + \frac{nu - 1}{4a(1-a)}, \tag{6.2}$$

where $nu = \int_0^1 \tau'(z)^2 dz$, if and only if the spectral constraint

$$0 \leq \min_{\vartheta} \left\{ \frac{1}{L} \int_0^L dx \int_0^1 dz \Big[a\,|\nabla\vartheta|^2 + \tau' W \vartheta \Big] \right\} \tag{6.3}$$

holds for all test functions $\vartheta(x,z)$ satisfying L-periodic boundary conditions in x and homogeneous Dirichlet boundary conditions in z where $W(x,z)$ solves $\nabla^2 W = Ra\partial_x^2\vartheta$ with L-periodic boundary conditions in x and homogeneous boundary conditions in z as well. In section 6.2.2 it will be shown that for $a = 1$ the spectral constraint (6.3) is tantamount to enforcing energy stability about the background profile $\tau(z)$ *as if* it were a steady solution of the Darcy–Oberbeck–Boussinesq equations with suitable sources and sinks.

[1] In chapters 6 and 7, τ denotes the one-dimensional background profile, not the convective time; moreover, it will be shown after (6.2) that nu denotes $\int_0^1 \tau'(z)^2 dz$, not the instantaneous Nusselt number.

In this study, the upper bounds are optimized over the "balance parameter" a. First, this parameter can be scaled out of the problem by defining $ra = Ra/a$ and $\widetilde{\vartheta} = a\,\vartheta$, implying $\nabla^2 W = ra\,\partial_x^2\widetilde{\vartheta}$, so that the spectral constraint (6.3) becomes

$$0 \leq \min_{\substack{\widetilde{\vartheta} \\ \frac{1}{L}\int_0^L\int_0^1 \widetilde{\vartheta}^2 dxdz=1}} \left\{ \frac{1}{L}\int_0^L dx \int_0^1 dz \left[|\nabla\widetilde{\vartheta}|^2 + \tau' W\widetilde{\vartheta} \right] \right\} \tag{6.4}$$

which means the functional

$$\mathcal{H}^\tau = \frac{1}{L}\int_0^L dx \int_0^1 dz \left[|\nabla\widetilde{\vartheta}|^2 + \tau' W\widetilde{\vartheta} \right] = \mathcal{H}^\tau\{\widetilde{\vartheta}(x,z)\} \tag{6.5}$$

is positive semi-definite for all test functions $\widetilde{\vartheta}(x,z)$ satisfying certain boundary conditions. Since W is a linear non-local function of $\widetilde{\vartheta}$, $\mathcal{H}^\tau$ is indeed a quadratic form in terms of $\widetilde{\vartheta}$. The positivity constraint for this quadratic form is equivalent to a spectral constraint for the self-adjoint operator inside $\mathcal{H}^\tau$, namely the non-negativity of the ground state eigenvalue λ^0 of the self-adjoint problem (Otero et al., 2004):

$$-2\nabla^2\widetilde{\vartheta} + \tau' W - \partial_x^2\gamma = \lambda\widetilde{\vartheta}, \tag{6.6}$$

$$\nabla^2 W - ra\partial_x^2\widetilde{\vartheta} = 0, \tag{6.7}$$

$$\nabla^2\gamma + ra\tau'\widetilde{\vartheta} = 0, \tag{6.8}$$

where $\gamma(x,z)$ is the Lagrange-multiplier field enforcing the local constraint (6.7). To obtain the optimal upper bound, nu is minimized subject to this rescaled spectral constraint $\lambda^0 \geq 0$, which is independent of a, for a range of ra. Finally, varying a for each (ra, nu) pair produces a family of curves in the Ra–Nu plane whose lower envelope yields the best bound.

For a given background profile $\tau(z)$, a group of orthogonal eigenfunctions, satisfying homogeneous Dirichlet boundary conditions in z, can be obtained by substituting the following decompositions

$$\widetilde{\vartheta}(x,z) = \sum_{n=-\infty}^{\infty}\sum_{m=0}^{\infty}\Theta_{mn}(z)e^{inkx}, \tag{6.9}$$

$$W(x,z) = \sum_{n=-\infty}^{\infty}\sum_{m=0}^{\infty}W_{mn}(z)e^{inkx}, \tag{6.10}$$

$$\gamma(x,z) = \sum_{n=-\infty}^{\infty}\sum_{m=0}^{\infty}\Gamma_{mn}(z)e^{inkx} \tag{6.11}$$

into (6.6)–(6.8) and solving this self-adjoint eigenvalue problem

$$-2\left[D^2-(nk)^2\right]\Theta_{mn}+\tau' W_{mn}+(nk)^2\Gamma_{mn} = \lambda_{mn}\Theta_{mn}, \tag{6.12}$$

$$\left[D^2-(nk)^2\right]W_{mn}+(nk)^2 ra\Theta_{mn} = 0, \tag{6.13}$$

$$\left[D^2-(nk)^2\right]\Gamma_{mn}+ra\tau'\Theta_{mn} = 0 \tag{6.14}$$

for each horizonal wavenumber nk. It will be shown in chapter 7 that these eigenfunctions, i.e. Θ_{mn}, W_{mn} and Γ_{mn} in (6.12)–(6.14), can be utilized as a basis to build low-dimensional models.

6.2.2 Energy (Nonlinear) Stability Theory

In this section, the CDH formalism discussed above will be interpreted using energy stability theory. Consider a 2D steady solution $T_s(x,z)$, $\mathbf{U}_s(x,z)$ and $P_s(x,z)$ (for temperature,

velocity and pressure fields, respectively) to the system

$$\begin{aligned} \nabla \cdot \mathbf{U}_s &= 0, && (6.15)\\ \mathbf{U}_s + \nabla P_s &= RaT_s\mathbf{e}_z, && (6.16)\\ \mathbf{U}_s \cdot \nabla T_s &= \nabla^2 T_s. && (6.17) \end{aligned}$$

Then the equations governing the evolution of the presumed arbitrary-amplitude disturbances $\tilde{\theta}(x,z,t)$, $\tilde{\mathbf{u}}(x,z,t) = \tilde{u}(x,z,t)\mathbf{e}_x + \tilde{w}(x,z,t)\mathbf{e}_z$ and $\tilde{p}(x,z,t)$ can be expressed as

$$\begin{aligned} \nabla \cdot \tilde{\mathbf{u}} &= 0, && (6.18)\\ \tilde{\mathbf{u}} + \nabla \tilde{p} &= Ra\tilde{\theta}\mathbf{e}_z, && (6.19)\\ \tilde{\theta}_t + \tilde{\mathbf{u}} \cdot \nabla\tilde{\theta} + \mathbf{U}_s \cdot \nabla\tilde{\theta} + \tilde{\mathbf{u}} \cdot \nabla T_s &= \nabla^2\tilde{\theta}. && (6.20) \end{aligned}$$

Multiplying equation (6.20) by $\tilde{\theta}$ and integrating over the domain yields

$$\frac{d}{dt}\left[\frac{1}{L}\int_0^L dx \int_0^1 dz\Big(\frac{1}{2}\tilde{\theta}(x,z,t)^2\Big)\right] = -\frac{1}{L}\int_0^L dx \int_0^1 dz\Big(|\nabla\tilde{\theta}|^2 + \tilde{\theta}\tilde{\mathbf{u}} \cdot \nabla T_s\Big). \qquad (6.21)$$

For any one-dimensional steady solution $T_s = T_s(z)$, (6.21) becomes

$$\begin{aligned} \frac{d}{dt}\left[\frac{1}{L}\int_0^L dx \int_0^1 dz\Big(\frac{1}{2}\tilde{\theta}(x,z,t)^2\Big)\right] &= -\frac{1}{L}\int_0^L dx \int_0^1 dz\Big(|\nabla\tilde{\theta}|^2 + T_s'\tilde{w}\tilde{\theta}\Big)\\ &\equiv -\mathcal{H}^{T_s}\{\tilde{\theta}(x,z,t)\}. && (6.22) \end{aligned}$$

As long as the right-hand side of (6.22) is negative (i.e. $\mathcal{H}^{T_s} \geq 0$), arbitrarily large perturbations of the base state will vanish as $t \to \infty$. Similarly as in section 6.2.1, the positivity

constraint for the quadratic form of $\mathcal{H}^{T_s}$ is equivalent to a spectral constraint for the self-adjoint operator inside $\mathcal{H}^{T_s}$, namely the non-negativity of the ground state eigenvalue $\tilde{\lambda}^0$ of the self-adjoint problem

$$
\begin{aligned}
-2\nabla^2\tilde{\theta} + T_s' W - \partial_x^2\gamma &= \tilde{\lambda}\tilde{\theta}, && (6.23)\\
\nabla^2 W - Ra\partial_x^2\tilde{\theta} &= 0, && (6.24)\\
\nabla^2\gamma + RaT_s'\tilde{\theta} &= 0. && (6.25)
\end{aligned}
$$

Therefore, in the energy stability formulation the spectral constraint $\tilde{\lambda}^0 \geq 0$ means the steady solution T_s is energy stable for any perturbation $\tilde{\theta}(x,z)$ at the given Ra. However, in the upper bound formulation, the spectral constraint $\lambda^0 \geq 0$ indicates for any given $0 < a < 1$, the right-hand side of (6.2) is a rigorous upper bound on Nu at Ra; moreover, from a comparison between (6.6)–(6.8) and (6.23)–(6.25), $\lambda^0 \geq 0$ also implies $\tau(z)$ is *energy stable* at $ra \equiv Ra/a$ *as if* it were a steady, exact solution (which it is not!). Hence, for $a = 1$ ($ra = Ra$), the spectral constraint $\lambda^0 \geq 0$ requires all fluctuations to the background profile $\tau(z)$ to be energy stable at the current Ra as if $\tau(z)$ were a steady solution of the governing equations.

It should be noted that for $a = 1$, the right-hand side of (6.2) is no longer a rigorous bound on Nu. Nevertheless, in following sections, it will be shown that this procedure (i.e. minimizing the functional nu subject to $\lambda^0 \geq 0$ with $a = 1$) can result in a useful prediction of Nu at Ra: the minimum value of nu will be shown to fall below the upper bound and even closer to the true heat flux. Moreover, the background profile $\tau(z)$ specified in this way is much closer to the mean temperature profile $\langle\overline{T}\rangle$ obtained from DNS.

6.2.3 Euler–Lagrange Equations

From the previous upper bound and energy stability analysis, to obtain an upper bound on or a prediction of Nu, nu should be minimized subject to the spectral constraint $\lambda^0 \geq 0$, corresponding to a condition of neutral energy stability. To obtain optimal bounds the background variational problem generally must be solved numerically. Here a novel scheme is proposed to do this accurately and efficiently. Following Plasting and Kerswell (2003), consider the corresponding Euler–Lagrange equations derived by identifying a Lagrange functional for this optimization problem:

$$\begin{aligned}\mathcal{L} = \quad & \int_0^1 \tau'(z)^2 dz - \frac{1}{L}\int_0^L dx \int_0^1 dz[|\nabla\vartheta|^2 + \tau' W\vartheta] \\ & -\frac{1}{L}\int_0^L dx \int_0^1 dz[\gamma(\frac{1}{ra}\nabla^2 W - \partial_x^2\vartheta)],\end{aligned} \tag{6.26}$$

where tildes have been dropped for brevity of notation. The first term in $\mathcal{L}$ is the objective functional to be extremized, the second term enforces the neutral energy stability condition, and the third term relates W to ϑ through the introduction of the Lagrange multiplier field $\gamma(x,z)$ that, like θ, satisfies periodic boundary conditions in x and homogeneous boundary conditions in z. The first variations of this functional with respect to τ, ϑ, W, and γ, respectively, yield the Euler–Lagrange equations

$$\frac{\delta\mathcal{L}}{\delta\tau} = 0 \quad \Rightarrow \quad -\tau_{zz} + \frac{1}{2}\overline{(W\vartheta)}_z = 0, \tag{6.27}$$

$$\frac{\delta\mathcal{L}}{\delta\vartheta} = 0 \quad \Rightarrow \quad -2\nabla^2\vartheta + W\tau_z - \gamma_{xx} = 0, \tag{6.28}$$

$$\frac{\delta\mathcal{L}}{\delta\gamma} = 0 \quad \Rightarrow \quad \nabla^2 W - ra\vartheta_{xx} = 0, \tag{6.29}$$

$$\frac{\delta\mathcal{L}}{\delta W} = 0 \quad \Rightarrow \quad \nabla^2\gamma + ra\tau_z\vartheta = 0, \tag{6.30}$$

where $\overline{(\cdot)} = \frac{1}{L}\int_0^L dx(\cdot)$ and a subscript denotes a partial derivative with respect to the given variable. Solving the Euler–Lagrange equations (6.27)–(6.30) subject to the spectral constraint $\lambda^0 \geq 0$ yields the optimal background profile τ and the prediction nu for Nu at $ra = Ra$. Then, varying a for each (ra, nu) pair produces a family of curves in the Ra–Nu plane whose lower envelope yields the best bound.

Before solving these equations, it is instructive to analyze their structure. First, it can be observed that a subset of the Euler–Lagrange equations (6.28)–(6.30) is identical to the marginally stable eigenvalue system, i.e. (6.6)–(6.8) for $\lambda^0 = 0$. Moreover, the Euler–Lagrange equations derived here have a similar mean-field (or quasi-linear) structure to those in Plasting and Kerswell (2003). In particular, using a Fourier series representation, the solution can be expressed as

$$\begin{bmatrix} \vartheta \\ W \\ \gamma \end{bmatrix} = \sum_{n=1}^{N} \begin{bmatrix} \hat{\vartheta}_n(z) \\ \hat{W}_n(z) \\ \hat{\gamma}_n(z) \end{bmatrix} \cos(nkx), \tag{6.31}$$

where n and $k = 2\pi/L$ are the (integer) horizontal mode number and fundamental wavenumber, respectively, and N is the (generally) *finite* truncation mode number, i.e. the series in (6.31) generally terminates. The true solution, which not only satisfies the Euler–Lagrange equations but also the spectral constraint, is unique and determined solely by the critical modes $n_c k$, i.e. $\hat{\vartheta}_n = \hat{W}_n = \hat{\gamma}_n \equiv 0$ for $n \neq n_c$. In contrast, the solution of the Euler–Lagrange equations is generally *not* unique: the true solution, or global optimal, includes all the critical modes and yields an *admissible* $\tau(z)$ satisfying the spectral constraint, while the spurious solutions, or local optimals, omit certain critical modes and/or include incorrect modes and yield an *inadmissible* $\tau(z)$ for which the ground state eigenvalue becomes

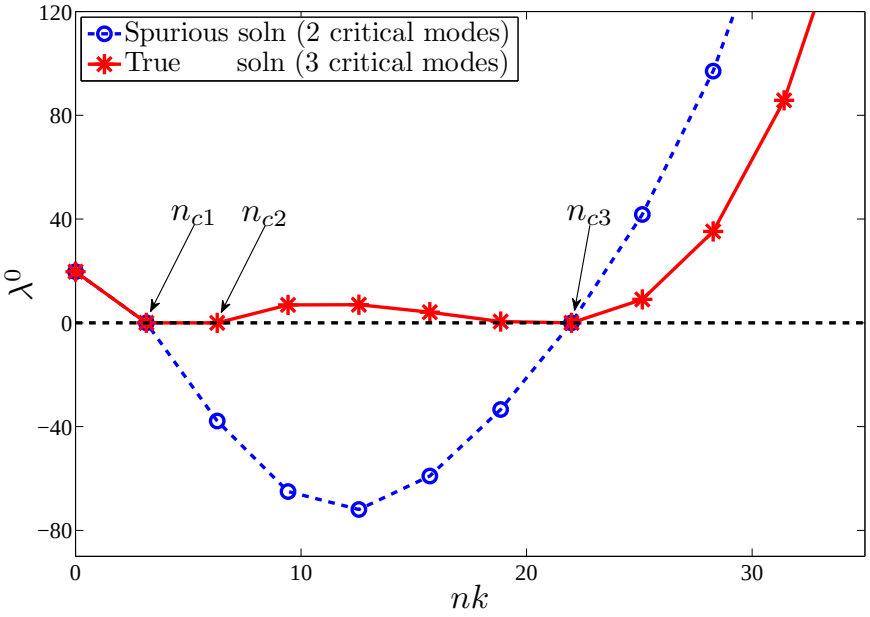

Figure 6-1: Ground state eigenvalue distribution for the true (solid) and spurious (dashed) solutions of the Euler–Lagrange equations at $ra = 998, L = 2$. Both solutions satisfy the Euler–Lagrange equations. However, the true solution, which includes all three critical modes (n_{c1}, n_{c2}, n_{c3}) for this case, also satisfies the spectral constraint $\lambda^0 \geq 0$; in contrast, the spurious solution, which captures only two of the critical modes (n_{c1}, n_{c3}), does not satisfy the spectral constraint, e.g. $\lambda^0 < 0$ at horizontal wavenumber $n_{c2}k$.

negative at some horizontal wavenumber, as shown in Figure 6-1. In the context of Rayleigh–Bénard convection, this sort of eigenstructure was first computed in early numerical work by Doering and Hyman (1997), who used a finite-difference relaxation method to solve the *single*-critical-mode Euler–Lagrange equations; see in particular their Figure 2.

Thus, one of the central challenges in the numerical solution of the Euler–Lagrange equations is the determination of the *a priori* unknown critical modes, which usually requires the use of Newton iteration plus continuation (Plasting and Kerswell, 2003). Here this difficulty is overcome by utilizing a two-step algorithm in which time is introduced into the variational formulation. In the following sections, it will be demonstrated that the two-step algorithm

can indeed be successfully applied to background optimization problems without numerical continuation. Moreover, it is also proved that the only steady state to which this numerical approach can converge is the global optimal.

6.2.4 Two-Step Algorithm

The key idea of the first step is to convert the time-invariant Euler–Lagrange system into a *time-dependent* dynamical system by incorporating certain specific time derivatives into (6.27)–(6.28); *viz.*,

$$\partial_t \tau - \tau_{zz} + \frac{1}{2}\overline{(W\vartheta)}_z = 0, \tag{6.32}$$

$$\partial_t \vartheta - 2\nabla^2 \vartheta + W\tau_z - \gamma_{xx} = 0. \tag{6.33}$$

Then the solutions of the original Euler–Lagrange equations, which correspond exactly to the steady states of the "time-dependent" Euler–Lagrange equations, can be easily obtained by solving the extended equations numerically using a *time-marching* method with non-zero initial data for all horizontal modes $1 \leq n \leq N$. Using the Fourier series representation (6.31), (6.32) can be expressed as

$$\partial_t \tau - D^2 \tau = -\frac{1}{4} D(\sum_{n=1}^{N} \hat{W}_n \hat{\vartheta}_n), \tag{6.34}$$

where: $\overline{(W\vartheta)} = \frac{1}{2}\sum_{n=1}^{N} \hat{W}_n\hat{\vartheta}_n$ and $D \equiv \frac{d}{dz}$. For a given horizontal wavenumber nk, (6.33), (6.29) and (6.30) become

$$\partial_t\hat{\vartheta}_n - 2[D^2 - (nk)^2]\hat{\vartheta}_n = -(D\tau)\hat{W}_n - (nk)^2\hat{\gamma}_n, \tag{6.35}$$

$$\left[D^2 - (nk)^2\right]\hat{W}_n = -ra(nk)^2\hat{\vartheta}_n, \tag{6.36}$$

$$\left[D^2 - (nk)^2\right]\hat{\gamma}_n = -ra(D\tau)\hat{\vartheta}_n. \tag{6.37}$$

In the computations, temporal discretization is achieved using the Crank–Nicolson method for the linear terms and a two-step Adams–Bashforth method for the nonlinear terms, while a Chebyshev spectral collocation method is used for spatial discretization. It is observed that for instantaneously "frozen" $\tau(z,t)$, solutions to (6.35)–(6.37) can be found that are proportional to $\exp(-\lambda_n t)$, where the energy stability eigenvalues λ_n are associated with eigenfunctions with horizontal wavenumber nk. With this identification, it can be seen that the solution to the (steady) Euler–Lagrange equations (6.27)–(6.30) is determined solely by those *critical modes* (denoted with subscript c) in (6.31) for which $\lambda_{n_c} = 0$; thus, $\hat{\vartheta}_n = \hat{W}_n = \hat{\gamma}_n \equiv 0$ for $n \neq n_c$. The strategy for identifying these modes is as follows. First, a non-zero initial condition is given for *all* modes fitting in the L-periodic domain; i.e. for all $1 \leq n \leq N$, where Nk is a pre-determined maximum wavenumber exceeding that of the critical mode with the largest wavenumber. Specifically, $\tau(z,0) = 1 - z$ and $\hat{\vartheta}_n(z,0) = z(1-z)$ for all $1 \leq n \leq N$. As shown in Figure 6-2, as time evolves, the λ_n-spectrum becomes marginally stable (i.e. $\lambda_n \geq 0$ for all n). As the computation proceeds, then, those modes for which λ_n is close to zero, or even negative, are likely candidates for the critical modes. Indeed, it is found that $\hat{\vartheta}_n$, $\hat{W}_n$, and $\hat{\gamma}_n$ for $n = n_c$ converge to the critical mode eigenfunctions associated with the true solution, while $\hat{\vartheta}_n$, $\hat{W}_n$, and $\hat{\gamma}_n$ for $n \neq n_c$ converge to zero. (For example, n_{c1},

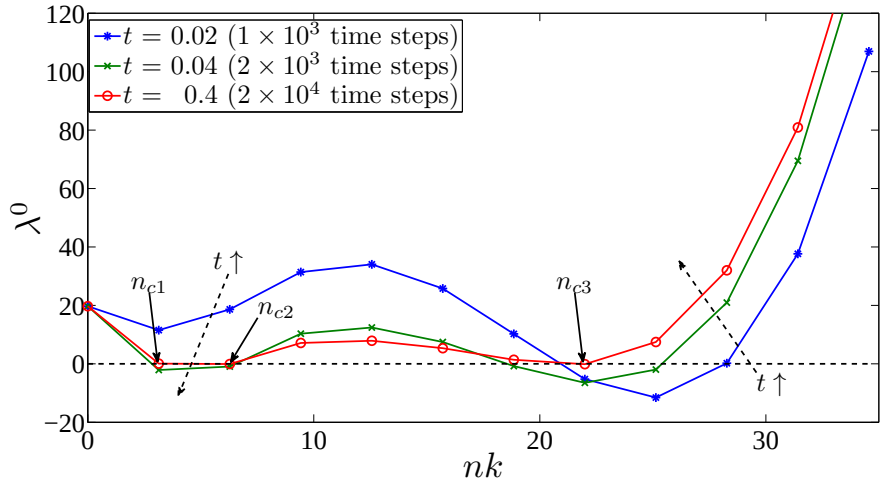

Figure 6-2: Time-evolution, for $ra = 998$ and $L = 2$, of the lowest branch of eigenvalues λ_n as a function of horizontal wavenumber nk for the eigensystem (6.6)–(6.8). As t increases the spectrum becomes marginally stable ($\lambda_n \geq 0$), with the critical modes occurring at those wavenumbers for which $\lambda_n = 0$.

n_{c2} and n_{c3} denote critical modes in Figure 6-2).

The second step of the algorithm is to numerically compute solutions of the Euler–Lagrange equations using only the critical modes. The computational issue is that although the time-marching method is robust (given non-zero initial data for all the modes, it converges to the true solution), for large ra a very small time step must be employed to guarantee numerical stability, which dramatically slows the rate of convergence to the steady state. To overcome this difficulty, it is convenient to employ the time-marching method strictly to locate the critical modes and to provide a suitable initial guess for a Newton–Kantorovich (NK) iterative method (Boyd, 2000), which is then used to compute the true solution. Although quadratically convergent, the NK method is very sensitive to the form of the initial iterate: generally, when the initial guess is not sufficiently close to the desired (true) solution, the algorithm will not converge to that solution, particularly at large values of ra. This difficulty usually is overcome by employing numerical continuation, in which solutions determined at

modest values of ra provide a natural first guess for the solutions at incrementally larger values of this control parameter. One virtue of the new approach used here is that numerical continuation need *not* be employed, since the output from the time-marching scheme is sufficiently close to the true solution to be used as an initial condition for the NK method. More details about the Newton–Kantorovich algorithm for this problem can be found in the appendix. For purposes of *a posteriori* verification, the eigenvalue problem (6.6)–(6.8) is then solved using the $\tau(z)$ computed from the NK routine to confirm that the associated λ_n–spectrum is everywhere non-negative and, hence, that this $\tau(z)$ is, indeed, the unique optimal solution.

6.2.5 The Global Optimal as the only Steady Attractor

In Wen et al. (2015), R. Kerswell (from the University of Bristol) proves that the global attractor is the only steady attractor of the time-augmented variational problem, as shown below. Let $(\tau, \vartheta, W, \gamma)$ satisfy the Euler–Lagrange equations (6.27)–(6.30) and be made up of J x-wavenumbers $n_{cj}k$ so that

$$\tau = \tau(z), \qquad \begin{bmatrix} \vartheta \\ W \\ \gamma \end{bmatrix} = \sum_{j=1}^{J} \begin{bmatrix} \hat{\vartheta}_{n_{cj}}(z) \\ \hat{W}_{n_{cj}}(z) \\ \hat{\gamma}_{n_{cj}}(z) \end{bmatrix} \cos\left(n_{cj}kx\right). \tag{6.38}$$

As discussed previously, there are many such solutions but only one, the true solution or global optimal, satisfies the spectral constraint ($\lambda^0 \geq 0$ from the spectral problem, (6.6)–(6.8)). These solutions – the global, true solution and the local, spurious optimals – are

steady-state solutions of the time-derivative-enhanced equations: (6.29)–(6.30) and (6.32)–(6.33). In this section, it can be demonstrated that all of the spurious (locally optimal) solutions are linearly unstable in the time-dependent system and so can never be attracting endstates of the time-dependent system. It is further shown that the globally optimal solution *is* linearly stable and therefore an attractor. Hence, *if* the time-dependent system converges to a steady state, then this steady state *is* the global optimal. The method of proof is relatively straightforward and, since it exploits the spectral constraint, generalizes easily to other canonical upper bound problems including plane Couette flow (Plasting and Kerswell, 2003) and stress-free Rayleigh–Bénard convection (Wen et al., 2015).

To establish this result, let $(\tilde{\tau}, \tilde{\vartheta}, \tilde{W}, \tilde{\gamma})$ be a small disturbance away from this solution. Then the linearized temporal evolution equations for this disturbance are

$$\partial_t \tilde{\tau} = \tilde{\tau}_{zz} - \tfrac{1}{2}(\overline{\tilde{W}\vartheta + W\tilde{\vartheta}})_z, \tag{6.39}$$

$$\partial_t \tilde{\vartheta} = 2\nabla^2 \tilde{\vartheta} - \tilde{W}\tau_z - W\tilde{\tau}_z + \tilde{\gamma}_{xx}, \tag{6.40}$$

$$0 = \nabla^2 \tilde{W} - ra\,\tilde{\vartheta}_{xx}, \tag{6.41}$$

$$0 = \nabla^2 \tilde{\gamma} + ra\,(\tilde{\tau}_z \vartheta + \tau_z \tilde{\vartheta}). \tag{6.42}$$

where the perturbation fields satisfy L-periodic boundary conditions in x and homogeneous boundary conditions in z (in particular, $\tilde{\tau}(0) = \tilde{\tau}(1) = 0$). Then, the volume integral of $\tilde{\tau} \times (6.39) + \frac{1}{2}\tilde{\vartheta} \times (6.40)$ yields

$$\frac{\partial}{\partial t}\left[\frac{1}{L}\int_0^L dx \int_0^1 dz \left(\tfrac{1}{2}\tilde{\tau}^2 + \tfrac{1}{4}\tilde{\vartheta}^2\right)\right] = \frac{1}{L}\int_0^L dx \int_0^1 dz \Big[-\tilde{\tau}_z^2 - |\nabla\tilde{\vartheta}|^2 + \tfrac{1}{2}\left(\tilde{W}\vartheta\tilde{\tau}_z - \tilde{W}\tilde{\vartheta}\tau_z + \tilde{\vartheta}\tilde{\gamma}_{xx}\right)\Big], \tag{6.43}$$

which can be simplified by noticing that the volume integral of $\tilde{W} \times (6.42) - \tilde{\gamma} \times (6.41)$ together with integration by parts and the homogeneous boundary conditions in z gives

$$\frac{1}{L}\int_0^L dx \int_0^1 dz \left(\tilde{\vartheta}\tilde{\gamma}_{xx}\right) = -\frac{1}{L}\int_0^L dx \int_0^1 dz \left(\tilde{W}\tilde{\vartheta}\tau_z + \vartheta\tilde{W}\tilde{\tau}_z\right). \tag{6.44}$$

Hence the equation (6.43) becomes

$$\left[\frac{1}{L}\int_0^L dx \int_0^1 dz \left(\frac{\tilde{\tau}^2}{2} + \frac{\tilde{\vartheta}^2}{4}\right)\right]_t = \frac{1}{L}\int_0^L dx \int_0^1 dz \Big[- \tilde{\tau}_z^2 - \left(|\nabla\tilde{\vartheta}|^2 + \tilde{W}\tilde{\vartheta}\tau_z\right)\Big], \tag{6.45}$$

where $\tilde{W}$ is related to $\tilde{\vartheta}$ *via* (6.41). Interestingly, the second term on the right-hand side of (6.45) is the spectral constraint on the steady background field τ, which is negative semidefinite if and only if τ satisfies the spectral constraint $\lambda^0 \geq 0$ in (6.6)–(6.8). At this point it is worth noting that eigenfunctions of the linearized evolution operator in (6.39)–(6.42) take one of two distinct forms: either

$$\text{Type I}: \qquad \tilde{\tau} = 0, \qquad \begin{bmatrix} \tilde{\vartheta} \\ \tilde{W} \\ \tilde{\gamma} \end{bmatrix} = \begin{bmatrix} \vartheta^*(z) \\ W^*(z) \\ \gamma^*(z) \end{bmatrix} \cos(nkx), \tag{6.46}$$

where $n \notin \{n_{c1}, n_{c2}, \ldots, n_{cJ}\}$, i.e., the perturbation shares no common wavenumber with the underlying steady state (see (6.38)), or

$$\text{Type II}: \qquad \tilde{\tau} = \tilde{\tau}(z) \neq 0, \qquad \begin{bmatrix} \tilde{\vartheta} \\ \tilde{W} \\ \tilde{\gamma} \end{bmatrix} = \sum_{j=1}^{J} \begin{bmatrix} \vartheta^*_{n_{cj}}(z) \\ W^*_{n_{cj}}(z) \\ \gamma^*_{n_{cj}}(z) \end{bmatrix} \cos(n_{cj}kx). \tag{6.47}$$

The crucial observation is that Type I eigenfunctions are also eigenfunctions of the spectral

constraint operator defined by (6.6)–(6.8). Hence if the spectral constraint is not satisfied as is the case for all spurious (local optimal) solutions, there is a temporally *unstable* Type I eigenfunction: hence the spurious solutions are not attracting states. Moreover, this linear instability persists when the balance parameters are also allowed to vary because Type I eigenfunctions cannot contain balance parameter perturbations (perturbations in the balance parameters are solely carried by Type II eigenfunctions).

In the case of the global optimal, the spectral constraint *is* satisfied and all Type I eigenfunctions are temporally damped (stable) since they have a spectral constraint eigenvalue λ^0 that is strictly positive. For perturbations spanned by Type II eigenfunctions, it is formally possible for the spectral constraint to be marginally satisfied *and* for $\int_0^1 \hat{\tau}_z^2 dz$ to vanish at some instant: i.e. strict monotonic decay of the functional on the left-hand side of (6.45) is not assured. However, if this happens (requiring

$$\begin{bmatrix} \vartheta^*_{n_{cj}}(z) \\ W^*_{n_{cj}}(z) \\ \gamma^*_{n_{cj}}(z) \end{bmatrix} = \alpha_j \begin{bmatrix} \tilde{\vartheta}_{n_{cj}}(z) \\ \tilde{W}_{n_{cj}}(z) \\ \tilde{\gamma}_{n_{cj}}(z) \end{bmatrix} \qquad \forall j \in \{1, \ldots, J\} \tag{6.48}$$

where α_j are some real scalars), (6.39) indicates that $(\int_0^1 \hat{\tau}_z^2 dz)_{tt} > 0$ so this situation cannot persist, i.e. there is no neutral Type II eigenfunction. Thus, all Type II eigenfunctions are also temporally damped and the global optimal is an attractor of the time-dependent problem.

The overall conclusion is that the spurious (local optimal) solutions can never be attractors of the time-dependent system whereas the global optimal is. Put another way, if a steady

solution is reached as the endstate of the time-dependent system it will be the global optimal. This, of course, does not prove that the time-stepping approach will always converge to the global optimal as there may be other attractors (e.g. periodic orbits) but it does retrospectively prove that the steady state reached by the numerical computations reported here must be the desired global optimal.

6.3 Results and Discussion

Computations are performed for a discrete set of $Ra = 50 \cdot 10^{(i-1)/10}$ (for integer i) from $Ra = 50$ to $Ra = 39716$. As Ra is increased the number of Chebyshev modes used in the vertical discretization is increased from 61 to 381. Initially, the aspect ratio $L = 2$ is fixed independently of Ra. In Figure 6-3, the intricate structure of the optimal solution to the background variational problem for porous medium convection at $Ra = 5000$ is evident: from left to right are plotted the optimal background profile $\tau(z)$, the λ_n-spectrum associated with the ground and first two excited states, and a set of eigenfunctions corresponding to the third and sixth critical modes. The optimal background profile is reminiscent of a horizontally- and long-time averaged temperature profile at large Ra observed in DNS, exhibiting a nearly isothermal core and thin boundary layers near the upper and lower walls. The spectra confirm that the pattern first recorded in Chini et al. (2011) for moderate Ra persists at large Ra, with the ground and first excited states being nearly degenerate and a clear spectral gap emerging between these and higher states. For the given L and Ra, there are 7 critical modes. The associated eigenfunction plots are suggestive of a nested boundary layer structure, in accord with snapshots of the dynamical fields taken from DNS; indeed, the highest critical

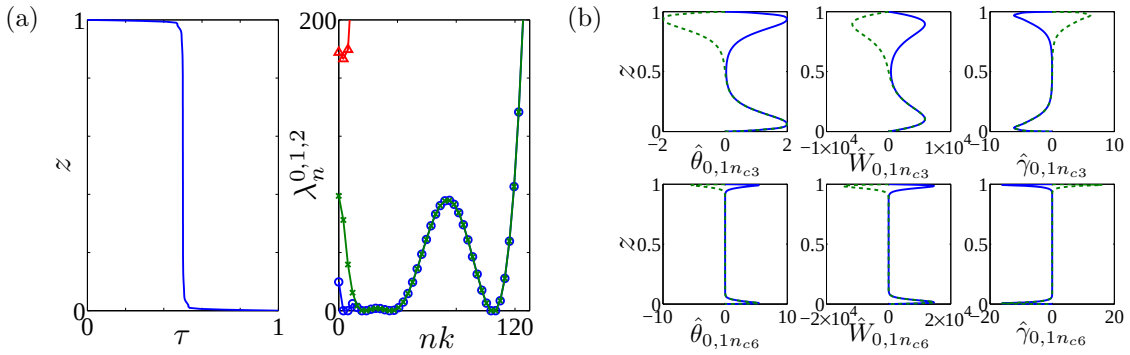

Figure 6-3: Optimal background profile $\tau(z)$ and corresponding eigenvalues and eigenfunctions at $Ra = 5000$ and $L = 2$: (a) optimal background profile and the lowest 3 eigenvalue branches λ_n^0, λ_n^1, and λ_n^2; (b) critical eigenfunctions corresponding to eigenvalues $\lambda_{n_{c3}}^1 \approx \lambda_{n_{c3}}^0 = 0$ and $\lambda_{n_{c6}}^1 \approx \lambda_{n_{c6}}^0 = 0$. The ground state eigenfunctions are even symmetric about $z = 1/2$ (solid curves), while the eigenfunctions corresponding to the first excited state (i.e. to the second lowest branch of eigenvalues) are odd symmetric (dashed curves).

mode corresponds to miniature, nearly isotropic convection cells confined to the $O(Ra^{-1})$ thick thermal boundary layer.

Figure 6-4(a) shows the distribution of the critical modes obtained from the first step of the two-step algorithm. As has been observed in other upper bound analyses of convection (Vitanov and Busse, 1997; Plasting and Kerswell, 2003), the incoming critical modes emerge low in the wavenumber spectrum and exhibit a repeated bifurcation structure as Ra is increased. Figure 6-4(b) compares the optimal upper bound, obtained numerically, with a previously obtained rigorous (i.e. strictly analytical) upper bound and with DNS data of Otero et al. (2004) and Hewitt et al. (2012). Clearly, relative to the DNS data, the new upper bound constitutes a quantitative improvement over the analytical bound, although in pre-factor only; the optimal scaling exponent in the Nu–Ra relationship predicted by both the analytical and the numerical bound is unity, in accord with the latest available DNS results. Moreover, the new bound is computed up to $Ra \approx 26500$, and this order-of-magnitude

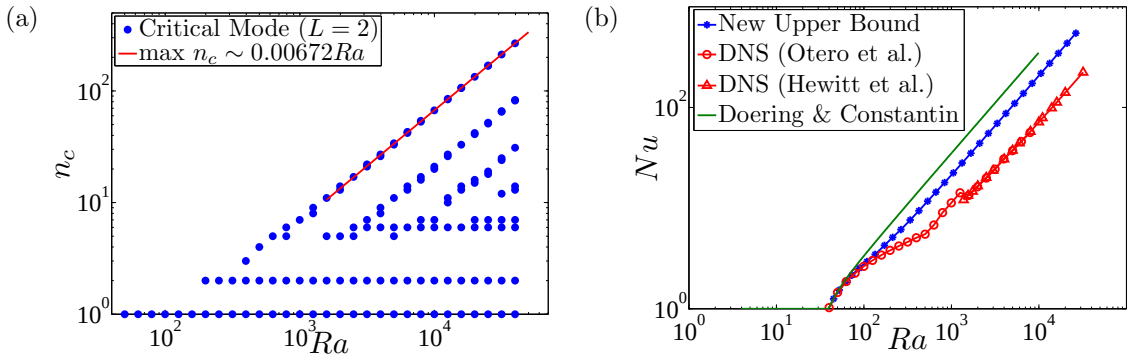

Figure 6-4: Bifurcation diagram showing the number and values of the critical modes and logarithmic Nu–Ra plot as a function of Ra for $L = 2$. In (a), the largest critical mode number $n_c \sim Ra$ at large Ra, same as that of the inverse $O(Ra^{-1})$ thermal boundary-layer thickness in the large-Ra limit. In (b), the new upper bound ($Nu \sim 0.0207Ra$) is compared with the previously obtained analytical bound ($Nu \sim 0.0352Ra$) from Doering and Constantin (1998) and two sets of DNS data from Otero et al. (2004) and Hewitt et al. (2012) ($Nu \sim 0.0068Ra$). It should be noted that both of the DNS are performed in $L = 2$.

increase in Ra for which the background problem can be solved is only made feasible with the new numerical scheme.

As discussed in previous chapters, DNS reveal that the horizontal spacing of the plumes decreases as Ra is increased, suggesting that certain global properties of the convective flow might be quantitatively captured in small domains, at least at sufficiently large Ra. Motivated by this observation, the influence of the domain aspect ratio on the optimal upper bound on Nu is investigated by considering several scenarios in which $L(Ra)$ is decreased as Ra is increased. The specific functional relations between L and Ra are motivated by both linear stability analysis and analysis of DNS data. Specifically, bounds on Nu are computed as a function of Ra with: $L = 2\sqrt{\pi}Ra^{-0.25}$, corresponding to the wavenumber (i.e. $2\pi/L$) of the fastest growing linear mode; $L = 4\pi Ra^{-0.4}$, corresponding to the measured inter-plume scaling in the DNS by Hewitt et al. (2012); and (a) $L = (4\pi/0.15) \cdot (\sqrt{Ra} + \sqrt{Ra - 4\pi^2})^{-1}$,

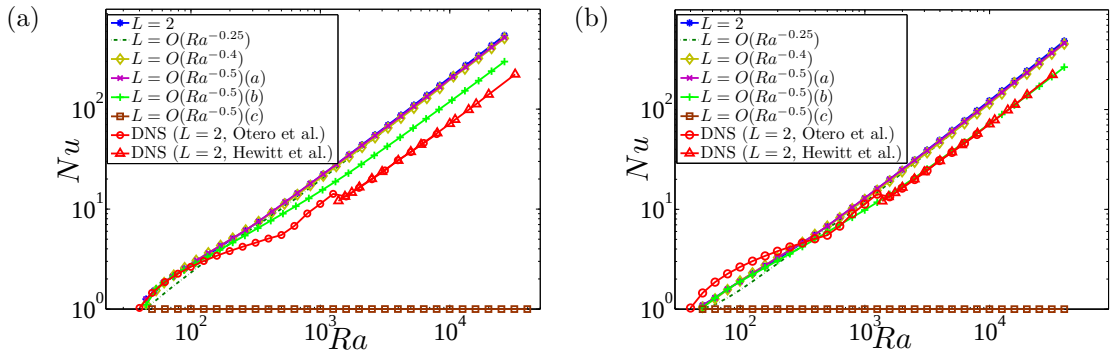

Figure 6-5: The influence of domain aspect ratio L: (a) upper bounds on and (b) predictions of Nu versus Ra for various $L = L(Ra)$ scenarios.

(b) $L = (4\pi/0.45) \cdot (\sqrt{Ra} + \sqrt{Ra - 4\pi^2})^{-1}$, and (c) $L = 4\pi \cdot (\sqrt{Ra} + \sqrt{Ra - 4\pi^2})^{-1}$, corresponding to the *largest wavenumber* at which linear instability is possible. For this last scenario, $L \sim CRa^{-1/2}$ for large Ra, and the effect of the prefactor C on the optimal bound is considered.

Figure 6-5(a) reveals that although the domain aspect ratios for $L = O(Ra^{-0.25})$, $L = O(Ra^{-0.4})$ and $L = O(Ra^{-0.5})$ (a) are less than $L = 2$ (for large Ra), they evidently are still sufficiently large to capture the major transport properties of the flow. Thus, the bounds for these scenarios are nearly identical. For $L = O(Ra^{-0.5})$ (c), the prefactor 2π (for large Ra) is *exactly* that required for marginal *linear* stability. In this case, the aspect ratio is too small for sustained finite-amplitude convection: $\tau(z) = 1 - z$ is marginally stable and the single critical mode is $n_c = 1$. Hence, the bound plummets to $Nu = 1$. Interestingly, for $L = O(Ra^{-0.5})$ (b), the prefactor gives a noticeable improvement in the optimal bound when compared to DNS performed in a *much larger domain* (i.e. $L = 2$).

As noted in section 6.2.2, the solution of the Euler–Lagrange equations (6.27)–(6.30), in which the balance parameter $a = 1$, does not, in fact, produce a bound on Nu (again see (6.2)). For this reason, the raw data pairs (ra, nu) have been further manipulated to obtain

the bounds on Nu as a function of Ra shown in Figure 6-5(a). However, the raw nu data themselves, for $a = 1$, may be interpreted as a *prediction* of Nu obtained by enforcing generalized marginal energy stability about the optimal background profile (as defined in section 6.2.2). For purposes of comparison, the results of these predictions are shown in Figure 6-5(b). Generally, the data seem to be shifted monotonically to larger values of Ra relative to the upper bound curves, bringing the predictions closer to the DNS results at large Ra. In particular, the prefactor for the scenario with $L = O(Ra^{-0.5})$ (b) is *chosen* so that the corresponding prediction of Nu matched the DNS data as closely as possible in the turbulent regime ($Ra > 1300$). What is surprising, perhaps, is that the mean inter-plume spacing measured in the DNS by Hewitt et al. (2012) is much larger than the value $L/2$ used to compute the optimal Nu bound and Nu prediction in this scenario.

To further investigate this issue, Dianati (2013) developed and implemented a DNS solver based on a Fourier–Chebyshev pseudospectral algorithm. The code was thoroughly validated and, indeed, gives Nu values quantitatively matching those of both Otero et al. (2004) and Hewitt et al. (2012) for the fixed aspect ratio case ($L = 2$). In Dianati (2013), DNS were employed to systematically study the influence of aspect ratio on the heat transport in porous medium convection. The results of the numerical investigation are displayed in Figure 6-6(a), a color map of the *re-normalized* Nusselt number as a function of Rayleigh number and inverse domain aspect ratio ($1/L$). Specifically, the colors indicate the value of the Nusselt number normalized by the value obtained for each Ra at $L = 2$. The plot is generated by cubic interpolation between 558 data points on two overlapping lattices of logarithmically-equispaced points in the Ra–L^{-1} plane. One lattice has larger spacing and accounts for low Ra values. The second lattice has a smaller spacing and covers all ranges of Ra, and large $1/L$, including the large-variation area that marks the transition to fully realized convection.

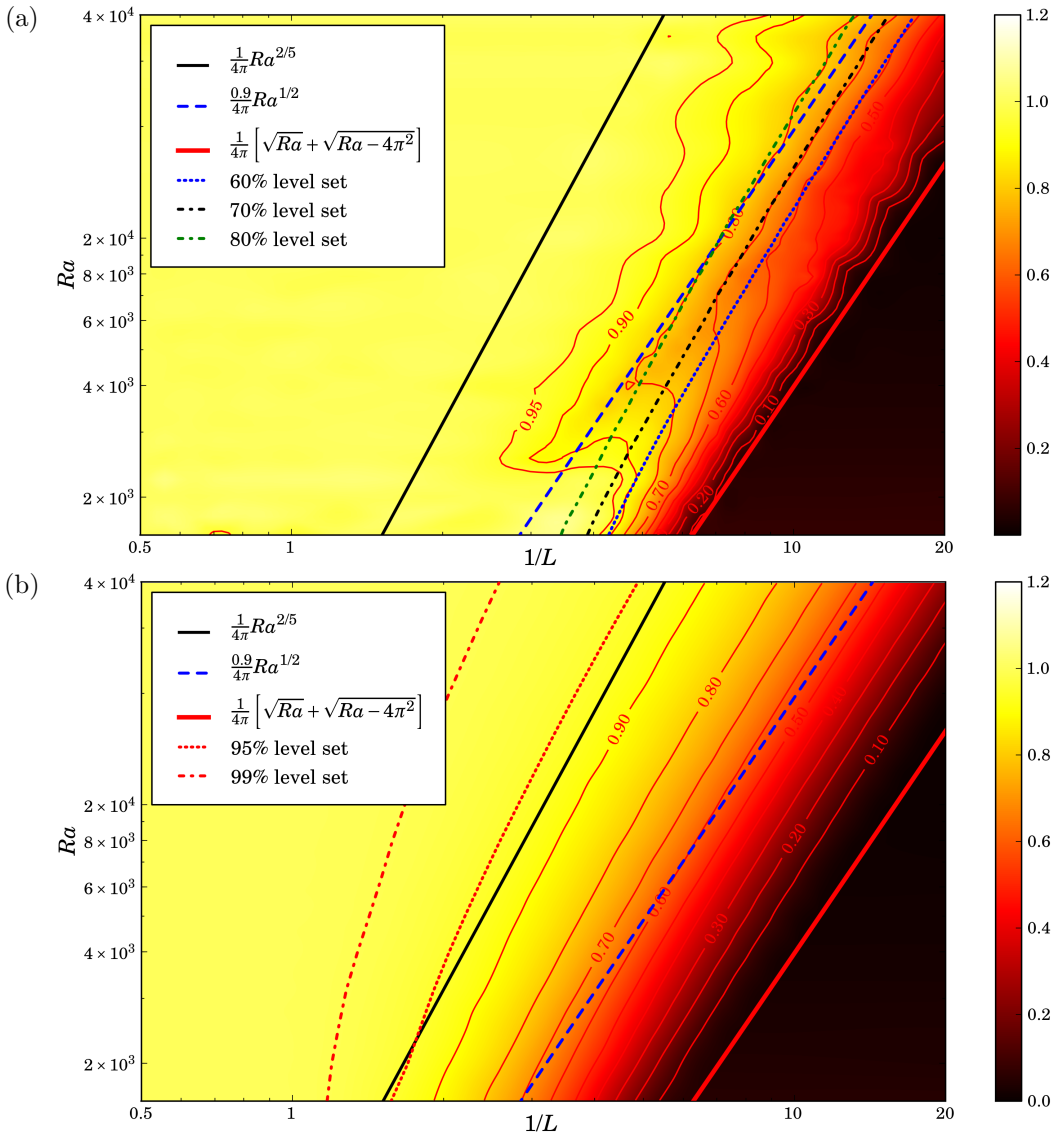

Figure 6-6: A color map of $Nu(Ra, 1/L)/Nu(Ra, 1/2)$ obtained from (a) DNS (Dianati, 2013) and (b) prediction (i.e. for $a = 1$) using the upper bound algorithm. The dark solid line shows the mean inter-plume spacing nonlinearly selected by the intrinsic convection dynamics in the DNS of Hewitt et al. (2012), performed in a domain with $L = 2$; the (blue) dashed line corresponds to the scenario labeled (b) in Figure 6-5; the (red) solid line in the lower right-hand corner indicates the boundary for linear instability of the conduction profile. Relative to the DNS, the renormalized Nusselt contours computed using the upper bound algorithm are uniformly shifted toward larger values of L. The predicted *slopes* of the 0.6, 0.7, and 0.8 contour levels are seen to agree well with the DNS results at large Ra: see the three additional dashed lines in the DNS color map. In the lower plot, the slope of the 0.99 contour line slowly increases to 0.338 at $Ra = 31548$.

(One part of the plot is entirely an extrapolation: $Nu(Ra, 1/L)/Nu(Ra, 1/2)$ in the low $1/L$ and large Ra regime in the upper left portion is assumed to be unity, as the trend strongly indicates.) The relative error in the re-normalized Nusselt number is estimated to be everywhere less than 5%, and much less for most data points.

Clearly, for sufficiently large Ra, the aspect ratio has little impact on the realized Nu until the domain becomes sufficiently small. More precisely, for (Ra, $1/L$) pairs falling to the right of the thick dashed line near the 0.8 contour, Nu decreases markedly until the convection is extinguished (the black triangular region in the lower right-hand corner) for domains smaller than the boundary for linear instability of the conduction profile. As noted on the figure, the thick dashed line corresponds to $L = (4\pi/0.9)Ra^{-1/2}$; i.e. to the scenario labeled (b) in Figure 6-5. For reference, the observed mean *inter-plume* spacing, for a fixed box width $L = 2$, in the DNS of Hewitt et al. (2012) is demarcated by the solid line. Although the 0.90 and 0.95 contours of the re-normalized Nusselt number do not exhibit a clean $1/L$ versus Ra scaling (likely owing to insufficient data points and to the very long integration times required to reliably extract from the DNS an accurate re-normalized Nusselt value close to unity), these contours are not inconsistent with the *conjecture* that the asymptotic (i.e. large Ra) inter-plume spacing nonlinearly selected by the intrinsic dynamics of porous medium convection coincides with the minimum spacing at which the Nusselt number differs negligibly from that realized in larger boxes – the minimal flow unit.

For completeness, in this section the new upper bound algorithm is used to predict (i.e. for $a = 1$) the Nusselt number over a wide swath of (L, Ra) parameter space. The results, shown in Figure 6-6(b), may be compared directly with the corresponding DNS results from Dianati (2013). Specifically, data pairs are computed for 15 logarithmically-equispaced values of Ra and 25 values of L (from $L = 0.01$ to $L = 2$) for each value of Ra. One advantage of this

approach is that long time-averaging is not necessary for estimating the re-normalized Nusselt number. The results are broadly similar to those obtained from the DNS, but there is less variability in the contours and the entire field seems to be shifted leftward; that is, relative to the DNS, the renormalized Nusselt contours computed using the upper bound algorithm are uniformly shifted toward larger values of L. Importantly, there is evident quantitative agreement between the predicted *slopes* of specific contours and the slopes of corresponding contours computed using DNS: see the thin dashed lines in Figure 6-6(a) that align well with the 0.6, 0.7 and 0.8 contours from the DNS. (For fixed L, e.g. for $L = 2$, the predicted slope again agrees with the DNS since both correspond to $Nu \sim cRa$ for some constant c.) This agreement lends confidence to the proposition that the $L(Ra)$ relationship corresponding to a given re-normalized Nusselt value may be reliably obtained from the upper bound algorithm as a surrogate for the corresponding result from the DNS. This correspondence is important since, as noted above, it is difficult to use DNS to compute sufficiently accurate contours of the re-normalized Nusselt number with values close to unity. Adopting this perspective, it should be noted that slope of the 0.99 contour in Figure 6-6(b) has a value of 0.338 at $Ra = 31548$, although it is not clear whether the slope converges to this value for larger Ra.

6.4 Summary

Theoretical considerations and numerical simulations both show that there is a dramatic compression of horizontal scales in porous medium convection at large Ra. In this study the first systematic investigation of the influence of domain aspect ratio (L) on the computed heat transport in "turbulent" porous medium convection was performed using upper bound theory, thereby identifying a lateral scale $L = L(Ra)$ above which the realized heat transport

is effectively independent of L; in this sense, a minimal flow unit for this phenomenon has been identified. The effects of L on the best available upper bounds on and predictions of Nu have been simultaneously explored by developing a novel approach for the computational solution of the background variational problem. Theoretical analysis indicates that the only steady state to which the numerical method can converge is the true (globally optimal) solution of the variational problem in porous medium convection, so that this numerical scheme should be equally useful for other problems to which the background formalism is applicable.

Based on this robust two-step numerical algorithm, the best available bounds on Nu have been computed up to $Ra \approx 26500$ and directly compared with the available DNS results, showing that the bounds lie within a factor of 3 of the DNS data. The optimal bounds are little affected by variations in L until $L = O(Ra^{-1/2})$, the scaling boundary for linear instability. Adjustments in the prefactor of this $L(Ra)$ scaling result in significant variations in the computed bounds on Nu; indeed, for a carefully chosen prefactor, the bounds could be made to lie within a factor of 2 of the results from DNS performed in a domain with fixed $L = 2$. This discrete improvement in the optimal bound is associated with a concomitant *reduction* in the number of critical modes owing to the (carefully prescribed) narrowing of the domain width. It should be noted that although the mean inter-plume spacing is not unique but may itself fall within some small band at very large Ra (see Figure 2-8), the variation of L_m in wide domains almost does not affect the value of Nusselt number Nu (see Figure 2-9). Thus, based on the DNS and upper bound calculations, it can be conjectured that the lower boundary of the band of L_m measured in wide domains in the DNS coincides with the minimal flow unit at sufficiently large Ra.

CHAPTER 7

REDUCED MODELING IN A MINIMAL FLOW UNIT AT LARGE RAYLEIGH NUMBER

7.1 Introduction

As discussed in chapters 1 and 2, DNS reveal that at large Ra porous medium convection exhibits a three-region asymptotic structure: adjacent to the upper and lower walls are extremely thin thermal boundary layers; the interior region is dominated by nearly vertical columnar exchange flow (mega-plumes) spanning the height of the domain; and between these regions, a series of small proto-plumes grow from the boundaries and merge with the interior mega-plumes. As the Rayleigh number is increased, the mean inter-plume spacing L_m shrinks as a power-law scaling of Ra, e.g. $L_m \sim Ra^{-2/5}$ has been proposed by Hewitt et al. (2012). Moreover, the studies described in Dianati (2013) and chapter 6 indicate that at large Ra the mean inter-plume spacing L_m approaches the minimal flow unit, above which the Nusselt number Nu becomes independent of L. In short, all the above investigations imply that the basic physics of high-Ra porous medium convection can be investigated in a narrow domain, where: the flow retains the three-region columnar structure but only consists

of a single rising and descending mega-plume; and the same amount of heat is transported as in wide domains.

The complexity of turbulent flows, even in the simpler case like high-Ra porous medium convection, generally necessitates hundreds of thousands or millions of degrees of freedom to resolve all the spatial and temporal scales. Hence it is desirable to construct models with a reduced number of degrees of freedom, but that still capture the essential nonlinear interactions over different space and time scales. One explicit approach to reducing the number of degrees of freedom in turbulent flows is to study the dynamics in a small domain/box where the turbulence can sustain itself. Of course, the use of small domains eliminates long-wavelength interactions, but in many cases the fundamental features of the turbulent flow are still retained. For instance, as shown in following sections, in a minimal flow unit high-Ra porous medium convection still exhibits the three-region columnar structure and produces the same heat transport as is manifest in wide domains, although the long-wavelength modes are filtered out. Thus, in this chapter, one primary objective is to explore a reduced modeling strategy in which the minimal flow is used for simulations of porous medium convection at large Ra. It should be noted that although very long computing times and very wide domains are required for DNS to firmly establish the nonlinear lateral scale selection, these requirements are no longer necessary for studying the reduced dynamics of high-Ra porous medium convection in narrow domains.

A primary technique known as Proper Orthogonal Decomposition (POD) was developed in recent decades to build low-dimensional models. In this method, an eigenfunction basis whose modes can be ordered in terms of decreasing average energy content is obtained from analysis of either experimental or numerical data. Then, Galerkin projection of the governing partial differential equations (PDEs) onto this POD basis produces a system of ordinary

differential equations (ODEs). Finally, truncations of the infinite set of ODEs yield low-dimensional models. Although POD has been used for model reduction for various turbulent flows (Aubry et al., 1988; Berkooz et al., 1993; Cazemier et al., 1998; Moehlis et al., 2002; Ma and Karniadakis, 2002; Smith et al., 2005; Kalb and Deane, 2007), it is clearly limited: extensive data sets are required from experiments or DNS before the reduced model can be constructed and its dynamics investigated. Moreover, although a small number of POD modes may capture most of the "energy" of the infinite-dimensional dynamics, dynamically important modes having low average energy content may be omitted in the usual ordering employed in the construction of POD models (Chini et al., 2011).

In Chini et al. (2011), *a priori* eigenfunctions drawn from energy stability and upper bound theory were utilized to construct low-dimensional models in low-Ra porous medium convection. Unlike the general Fourier and Chebyshev basis, this upper bound eigenbasis is extracted directly from the governing equations and is thereby naturally adapted to the dynamics at the given parameter values. For instance, as shown in Figure 6-3(b), certain upper bound eigenfunctions at large Ra exhibit boundary-layer structures. In this regard, recall that DNS at large Ra reveal that porous medium convection self-organizes into narrow columnar plumes, with more complex spatiotemporal features being confined to boundary layers near the walls. Moreover, it has also been shown that the interior flow is a composite of a few low-wavenumber Fourier modes but is dominated by one mode, and the Fourier amplitudes of the fluctuation θ at high wavenumber are strongly localized near the upper and lower walls, where they superpose to comprise the small rolls and proto-plumes within the thermal and vorticity boundary layers. Inspired by this specific spectral structure of the columnar flow exhibited at large Ra, two independent strategies will be presented in the following sections to reduce the degrees of freedom in numerical simulations of porous medium

convection. First, a *domain decomposition method* (Boyd, 2000) is used: the domain is split into different regions in which different resolutions are employed for a Fourier–Chebyshev collocation numerical scheme; secondly, a *hybrid reduced model* is built: in horizontal Fourier space, PDEs are solved at low wavenumbers using the regular Fourier–Chebyshev collocation method, while at high wavenumbers ODEs with only wall eigenmodes obtained from upper bound analysis are solved to capture the near wall dynamics within the boundary layers.

The reminder of this chapter is organized as follows. In the next section, two separate strategies for reducing the degrees of freedom in numerical simulations are outlined. In section 7.3, computations using these two approaches are performed at large Rayleigh number in the minimal flow unit, and their results are compared with those from resolved and under-resolved DNS. Finally, a summary is given in section 7.4.

7.2 Reduced Modeling Strategies at Large Ra

7.2.1 Domain Decomposition Method

Figure 7-1 shows a snapshot of the temperature field and its corresponding horizontal mean (i.e. $\overline{T}$) and magnitudes of (complex) Fourier amplitudes of the temperature fluctuations (i.e. $|\hat{\theta}_n|$, the deviations from the horizontal mean) as functions of z from DNS at $Ra = 20000$ in a narrow domain. As is evident in this figure, the flow which consists of a single rising and descending mega-plume has a similar structure as is observed in wide domains. In particular, the interior flow is controlled by only a few low-wavenumber Fourier modes and the Fourier amplitudes $\hat{\theta}_n$ are strongly localized near the walls at high wavenumbers (e.g. $n > 10$). According to this specific structure, the domain can be decomposed into at least

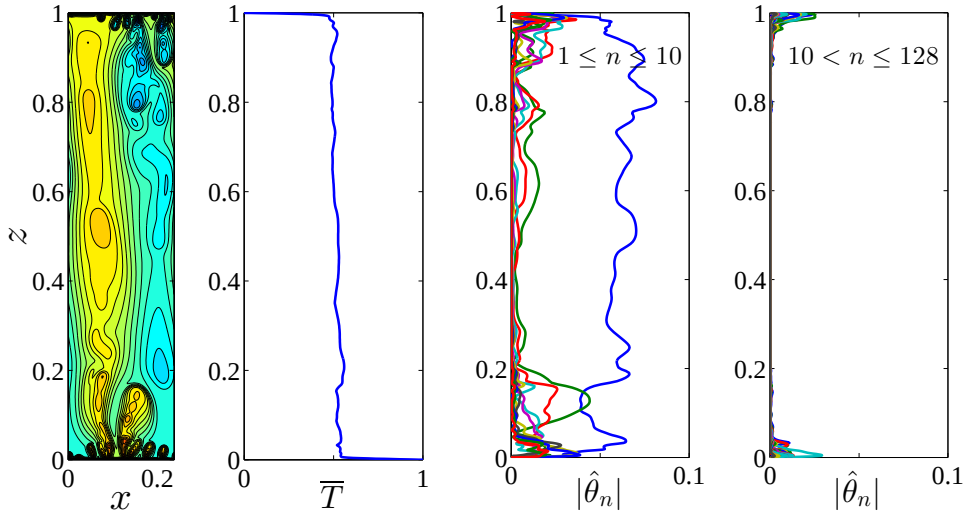

Figure 7-1: A snapshot of the temperature field and the corresponding Fourier amplitudes from DNS at $Ra = 20000$ and $L = 0.24$. The resolution for this case is 256 Fourier modes in x and 321 Chebyshev modes in z.

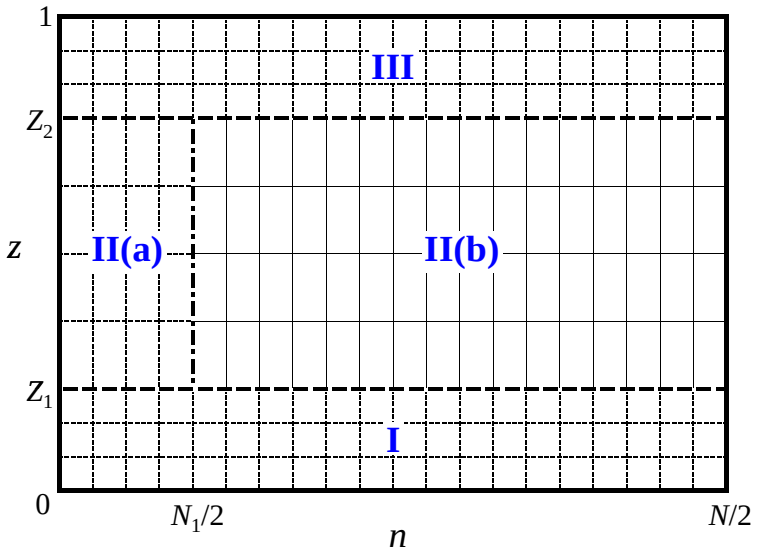

Figure 7-2: Schematic showing decomposition of the domain in Fourier space at large Ra. The plot only shows the positive wavenumber regime ($0 \le n \le N/2$), since the Fourier amplitudes are complex conjugates at negative wavenumbers. Region I: $0 \le z < Z_1$; region II: $Z_1 \le z \le Z_2$ with $Z_2 = 1 - Z_1$; region III: $Z_2 < z \le 1$. In region II, (a) represents the low-wavenumber region with $0 \le n \le N_1/2$, and (b) the high-wavenumber region with $N_1/2 < n \le N/2$.

three subregions at large Ra as schematically shown in Figure 7-2: I and III represent the near-wall regions in which high resolution in both x and z is required to resolve the small-scale motions in the boundary layers; II represents the interior region in which coarse resolution in z can be used to capture the relatively large-scale advective motions. Since the interior flow is controlled by only a few low-wavenumber Fourier modes in region II(a), the high-wavenumebr region can be shut down by setting all the variables in II(b) to zero, as shown below.

The idea underlying the domain decomposition method is simple: at each time step, numerical simulations are preformed separately in each subdomain (I, II, III), and then the solutions in each subdomain are matched using *patching* along their common boundaries ($z = Z_1$ and $z = Z_2$) by requiring that the variable and a finite number of normal derivatives are equal along the interfaces. Below, it is shown how this method is utilized to solve the momentum equation (2.5) in horizontal parous medium convection ($\phi = 0°$).

For a given horizontal wavenumber nk, (2.5) becomes

$$\left[D^2 - (nk)^2\right] \hat{\psi}_n^{[j]} = -ink Ra \hat{\theta}_n^{[j]}, \tag{7.1}$$

where the superscript "$[j]$" denotes to the j-th subdomain, and both $\hat{\psi}_n$ and $\hat{\theta}_n$ satisfy the homogeneous Dirichlet boundary conditions at the heated and cooled walls (i.e. $z = 0$, 1). The general solution in the j-th subdomain, $\hat{\psi}_n^{[j]}(z)$, can always be written as the sum of a particular integral $\hat{\psi}_{n_p}^{[j]}(z)$ plus two homogeneous solutions, namely

$$\hat{\psi}_n^{[j]}(z) = \hat{\psi}_{n_p}^{[j]}(z) + \Psi^{[j-1]} \cdot h_L^{[j]}(z) + \Psi^{[j]} \cdot h_U^{[j]}(z), \tag{7.2}$$

where $\Psi^{[j-1]}$ and $\Psi^{[j]}$ are the undetermined values of $\hat{\psi}_n$ at the boundaries of the j-th subdomain, and the particular integral $\hat{\psi}_{n_p}^{[j]}$ and homogeneous solutions $h_L^{[j]}$ and $h_U^{[j]}$ are defined by

$$\left[D^2-(nk)^2\right]\hat{\psi}_{n_p}^{[j]} = -inkRa\hat{\theta}_n^{[j]}, \qquad \hat{\psi}_{n_p}^{[j]}(d_{j-1})=0, \quad \hat{\psi}_{n_p}^{[j]}(d_j)=0, \tag{7.3}$$

$$\left[D^2-(nk)^2\right]h_L^{[j]} = 0, \qquad h_L^{[j]}(d_{j-1})=1, \quad h_L^{[j]}(d_j)=0, \tag{7.4}$$

$$\left[D^2-(nk)^2\right]h_U^{[j]} = 0, \qquad h_U^{[j]}(d_{j-1})=0, \quad h_U^{[j]}(d_j)=1, \tag{7.5}$$

where d_j denotes the boundary between $(j-1)$-th subdomain and j-th subdomain. It can be seen that one always has the freedom to choose the $\hat{\psi}_{n_p}^{[j]}$ so that it vanishes at both subdomain boundaries, and one may similarly choose $h_L^{[j]}$ so that it is equal to one at the lower boundary and zero at the upper boundary, while $h_U^{[j]}$ is one at the upper boundary but zero at the lower boundary.

One advantage of the decomposition is that the uncoupled equations (7.3)–(7.5) can be solved *independently* for each subdomain. However, to obtain the elemental solution $\hat{\psi}_n^{[j]}(z)$ in (7.2), one needs to compute $(\mathcal{M}+1)$ unknown $\Psi^{[j]}$, the values of $\hat{\psi}_n$ at the subdomain boundaries, where $\mathcal{M}$ denotes the total number of subdomains in the entire domain (e.g. $\mathcal{M}=3$ in Figure 7-2). The two end values of $\Psi^{[j]}$ can be determined by the boundary conditions at the upper and lower walls: $\Psi^{[0]}=\hat{\psi}_n|_{z=0}=0$; $\Psi^{[\mathcal{M}]}=\hat{\psi}_n|_{z=1}=0$. The remaining $(\mathcal{M}-1)$ domain boundary values of $\hat{\psi}_n$ are determined by the requirement of continuity of the first derivative at each of the interior interfaces, which gives

$$h_L^{[j]\prime}\Psi^{[j-1]}+[h_U^{[j]\prime}-h_L^{[j+1]\prime}]\Psi^{[j]}-h_U^{[j+1]\prime}\Psi^{[j+1]}=\hat{\psi}_{n_p}^{[j+1]\prime}-\hat{\psi}_{n_p}^{[j]\prime}, j=1,\cdots,\mathcal{M}-1, \tag{7.6}$$

where the prime denotes the first derivative with respect to z, and all of these derivatives

are computed at the interior interfaces ($z = d_j$) once the particular integral and homogeneous solutions are obtained by solving (7.3)–(7.5). Another advantage of the decomposition method is that the grid can be distributed more reasonably in each subdomain and the condition number is also decreased since the size of the matrix in each subdomain is reduced, compared with the single matrix for the entire domain. Furthermore, according to the specific columnar flow structure at large Ra, the region II(b) can be omitted in the domain decomposition method, with homogeneous Dirichlet boundary conditions enforced directly on its upper and lower interfaces.

7.2.2 Hybrid Reduced Model

In this section, the temperature field is decomposed such that $T(x,z,t) = \tau(z) + \theta(x,z,t)$, as in (6.1). Then from (1.29), the temperature fluctuation $\theta(x,z,t)$ satisfies

$$\frac{\partial \theta}{\partial t} + u\frac{\partial \theta}{\partial x} + w\frac{\partial \theta}{\partial z} = -\tau' w + \nabla^2 \theta + \tau'', \tag{7.7}$$

which is identical to (2.6) *only if* $\tau \equiv 1 - z$. However, here τ is obtained from the upper bound analysis in chapter 6 by minimizing $nu \equiv \int_0^1 \tau'(z)^2 dz$ subject to the spectral constraint (6.4).

The idea behind the hybrid reduced model is somewhat similar to that of domain decomposition. Upper bound analysis in chapter 6 produces a fully *a priori* eigenbasis (i.e. $\Theta_{mn}(z)$, $W_{mn}(z)$ and $\Gamma_{mn}(z)$, see (6.9)–(6.14)) which is naturally adapted to the dynamics of porous medium convection at given parameter values. Then, Galerkin projection of the governing PDEs onto the upper bound eigenfunction basis yields a system of ODEs. As shown

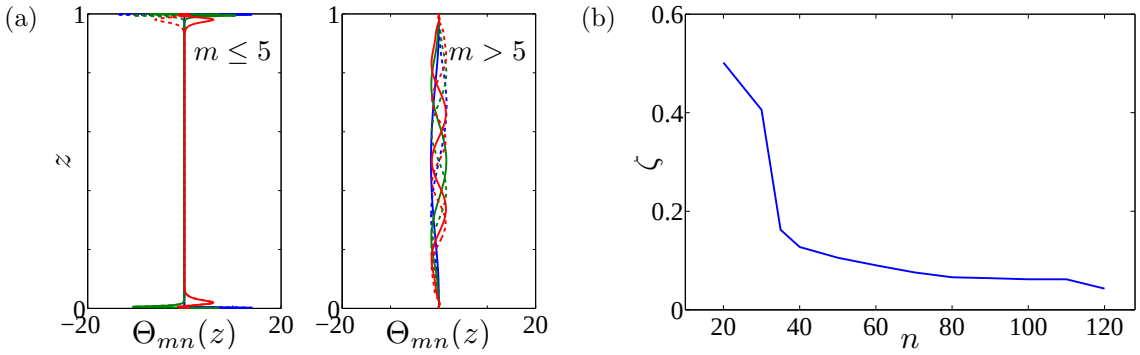

Figure 7-3: (a) Upper bound eigenfunctions for $0 \leq m \leq 11$ at $Ra = 20000$ and $n = 50$. (b) Time-averaged relative error of the projection of $\hat{\theta}_n$ from DNS onto the wall eigenmodes as a function of n at $Ra = 20000$. For both (a) and (b), $L = 0.24$. In (a), at large horizontal mode number n, the eigenfunctions $\Theta_{mn}(z)$ exhibit a near-wall structure for $0 \leq m \leq M_1$ ($M_1 = 5$ in this case), but an interior structure for $m > M_1$; in (b), ζ is defined in (7.9).

in Figure 7-3(a), the upper bound eigenfunctions generally exhibit two types of structures at large Ra: for small vertical mode number m (e.g. $0 \leq m \leq 5$), the eigenfunctions are strongly localized near the upper and lower walls, hereafter referred to as wall eigenmodes/eigenfuntions; for larger m (e.g. $m > 5$), the eigenfunctions have most of their support in the interior, hereafter referred to as interior eigenmodes/eigenfuntions. It should be noted that this mode separation is more obvious at large horizontal wavenumber. Recall that at large Ra, the high x-wavenumber motions always occur near the upper and lower walls (see Figure 7-1). Therefore, one may naturally expect that these upper bound wall eigenmodes might be utilized to effectively capture the small-scale near-wall dynamics. Before pursuing dynamical modeling, the performance of these wall eigenmodes can be evaluated by performing the following projection:

$$\hat{\theta}_n^{\mathrm{P}} = \left(\int_0^1 \hat{\theta}_n^{\mathrm{DNS}} \Theta_{0n} dz \right) \cdot \Theta_{0n} + \left(\int_0^1 \hat{\theta}_n^{\mathrm{DNS}} \Theta_{1n} dz \right) \cdot \Theta_{1n} + \cdots , \tag{7.8}$$

where the DNS data $\hat{\theta}_n^{\mathrm{DNS}}$ are projected only onto the wall eigenmodes at a given horizontal wavenumber nk. If the time-averaged relative error of the projection

$$\zeta = \left\langle \frac{||\hat{\theta}_n^{\mathrm{DNS}} - \hat{\theta}_n^{\mathrm{P}}||}{||\hat{\theta}_n^{\mathrm{DNS}}||} \right\rangle \tag{7.9}$$

is a small value at each n, where $\|\cdot\|$ denotes a 2-norm and $\langle(\cdot)\rangle$ denotes temporal averaging, then these upper bound wall eigenfunctions should be able to concisely capture the dynamics. Figure 7-3(b) shows the variation of ζ with mode number n. Clearly, these wall eigenfunctions have very good performances at large n (high wavenumbers): instead of using 321 Chebyshev modes at each n for $Ra = 20000$ in DNS, 6 wall eigenmodes could accurately represent more than 70% of the fluctuation fields for $n \geq 30$. However, these wall eigenfunctions do not work very well at low and moderate wavenumbers, because: (1) the flow also exhibits some interior structure (mega-plumes) for small n (e.g. $n \leq 6$); (2) the mode-separation feature of the upper bound eigenfunctions is not very obvious for $n < 30$, and thus certain interior eigenmodes which actually exhibit boundary-layer structure near the walls are ignored. Based on these observations, a hybrid model can be constructed as follows: for small and moderate n, PDEs are solved to resolve the low- and moderate-wavenumber dynamics, namely, the motions of interior mega-plumes and near-wall proto-plumes; for large n, ODEs with only the wall eigenmodes are solved to model the small-scale motions within the thermal boundary layers, as schematically shown in Figure 7-4.

As discussed in chapter 6, the self-adjoint operator inside $\mathcal{H}^\tau$ (6.5) associated with the nonlinear stability condition for the background profile $\tau(z)$ produces a complete set of orthogonal eigenfunctions which can be used as a natural basis. In Chini et al. (2011), a 6-mode model was derived (as shown below) using these eigenfunctions in porous medium

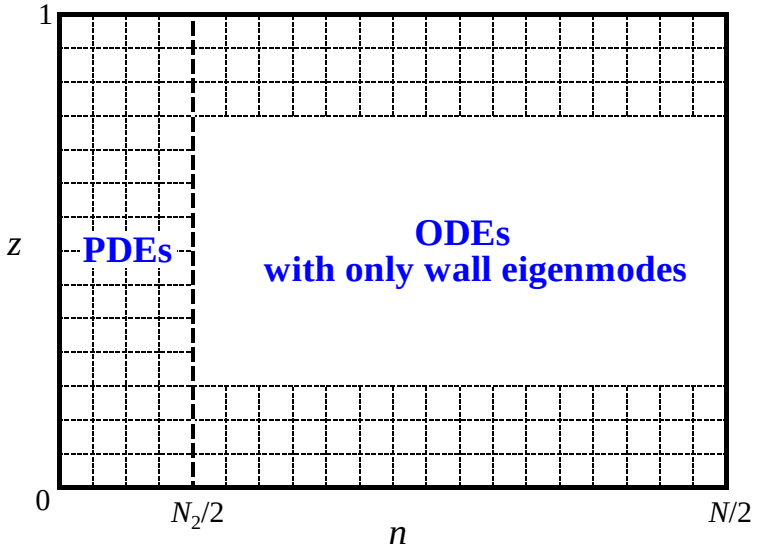

Figure 7-4: Schematic showing hybrid modeling in Fourier space at large Ra. The plot only shows the positive wavenumber regime ($0 \leq n \leq N/2$), since the Fourier amplitudes conjugates complex conjugates at negative wavenumbers. For $0 \leq n \leq N_2/2$, PDEs are solved; for $N_2/2 < n \leq N/2$, ODEs with only the upper bound wall eigenmodes are solved.

convection at $Ra = 100$. First, all the time-dependent fields are decomposed according to

$$\theta(x,z,t) = \sum_{n=-\infty}^{\infty}\sum_{m=0}^{\infty} a_{mn}(t)\Theta_{mn}(z)e^{inkx}, \tag{7.10}$$

$$w(x,z,t) = \sum_{n=-\infty}^{\infty}\sum_{m=0}^{\infty} b_{mn}(t)W_{mn}(z)e^{inkx}, \tag{7.11}$$

$$u(x,z,t) = \sum_{n=-\infty}^{\infty}\sum_{m=0}^{\infty} c_{mn}(t)U_{mn}(z)e^{inkx}, \tag{7.12}$$

where a_{mn}, b_{mn} and c_{mn} are, respectively, the time-dependent coefficients of temperature fluctuation, vertical and horizontal velocities, and the vertical eigenfunctions $\Theta_{mn}(z)$ and $W_{mn}(z)$ satisfy (6.6)–(6.8) subject to the following orthonormalization condition:

$$\int_0^1 \Theta_{mn}(z)\Theta_{pn}(z)dz = \delta_{mp} \tag{7.13}$$

with the delta function $\delta_{mp} = 1$ for $m = p$ and $\delta_{mp} = 0$ for $m \neq p$, and

$$c_{mn}(t)U_{mn}(z) = \frac{-1}{ink} b_{mn}(t) DW_{mn}(z), \tag{7.14}$$

for $n \neq 0$ from the divergence free condition on the velocity field. Moreover, (6.7) and (6.13) also imply that $b_{mn}(t) = a_{mn}(t)$ for $n \neq 0$.

Substituting (7.10)–(7.12) into the temperature fluctuation equation (7.7) and forming the inner product of each term with $\Theta_{pr}(z)\exp(irkx)$ yields a system of ODEs for $n \neq 0$:

$$\dot{a}_{mn} = \mu_{mn} a_{mn} + \sum_{\substack{p=0 \\ (p\neq m)}}^{\infty} \mu^p_{mn} a_{pn} + \sum_{\substack{j=-\infty \\ (j\neq n)}}^{\infty} \sum_{p=0}^{\infty} \sum_{q=0}^{\infty} \Lambda^{jpq}_{mn} a_{qj} a_{p(n-j)}, \tag{7.15}$$

where the linear coefficients are

$$\mu_{mn} = -\lambda_{mn}/2 \leq 0, \quad (\lambda_{mn} \text{ is from (6.12)}) \tag{7.16}$$

$$\mu^p_{mn} = \left(\frac{n^2k^2}{2}\right) \int_0^1 \left[\Theta_{mn}\Gamma_{pn} - \Theta_{pn}\Gamma_{mn}\right] dz, \tag{7.17}$$

and the nonlinear coefficients are

$$\Lambda^{jpq}_{mn} = \int_0^1 \Theta_{mn} \left[\left(\frac{j}{n-j}\right) DW_{p(n-j)}\Theta_{qj} - W_{p(n-j)} D\Theta_{qj} \right] dz. \tag{7.18}$$

For $n = 0$, the eigenfunctions can be obtained analytically from (6.12)–(6.14):

$$\Theta_{m0}(z) = \sqrt{2}\sin\left((m+1)\pi z\right); \quad W_{m0}(z) = U_{m0}(z) = 0. \tag{7.19}$$

Then, Galerkin projection of the horizontally averaged (7.7) onto $\Theta_{p0}(z)$ yields the amplitude equations for $a_{m0}(t)$:

$$\dot{a}_{m0} = \mu_{m0} a_{m0} + \sum_{\substack{j=-\infty \\ (j\neq 0)}}^{\infty} \sum_{p=0}^{\infty} \sum_{q=0}^{\infty} \Lambda_{m0}^{jpq} a_{qj} a_{pj}^{*} + f_m, \tag{7.20}$$

where the asterisk denotes complex conjugation and the coefficients satisfy

$$\mu_{m0} = -(m+1)^2 \pi^2, \tag{7.21}$$

$$\Lambda_{m0}^{jpq} = \sqrt{2}(m+1)\pi \int_0^1 W_{pj} \Theta_{qj} \cos((m+1)\pi z) dz, \tag{7.22}$$

$$f_m = \sqrt{2}(m+1)\pi \left[1 - (m+1)\pi \int_0^1 \tau(z) \sin((m+1)\pi z) dz \right]. \tag{7.23}$$

Finally, the low-dimensional models are obtained by suitably truncating the sums in (7.15) and (7.20).

At large Ra, the PDEs are solved for $0 \leq n \leq N_2/2$ using a Fourier–Chebyshev collocation method, while the ODEs in (7.15) with only wall eigenfunctions are employed for $n > N_2/2$ to model the high-wavenumber near-wall motions. Hence, for $n > N_2/2$, the Fourier components of the temperature field can be approximated as

$$\hat{\theta}_n(z,t) \approx \sum_{m=0}^{M_1} a_{mn}(t) \Theta_{mn}(z), \tag{7.24}$$

where all the eigenfunctions $\Theta_{mn}(z)$ for $0 \leq m \leq M_1$ exhibit a near-wall structure (see Figure 7-3*a*). However, the computations will be extremely *inefficient* if the ODEs are solved by directly integrating (7.15), since in this way the nonlinear terms need to be determined by computing the convolution of the modes included in the relevant sums. Actually, these

nonlinear terms in the ODE governing the evolution of mode a_{mn} are obtained by projecting the nonlinear terms in the governing PDEs onto the upper bound eigenfunctions Θ_{mn}, *viz.*

$$\mathcal{N}_{mn}^{\mathrm{ODE}} = \sum_{\substack{j=-\infty \\ (j\neq n)}}^{\infty} \sum_{p=0}^{\infty} \sum_{q=0}^{\infty} \Lambda_{mn}^{jpq} a_{qj} a_{p(n-j)} = \int_0^1 \widehat{\mathcal{N}}_n^{\mathrm{PDE}} \Theta_{mn} dz, \tag{7.25}$$

where $\widehat{\mathcal{N}}_n^{\mathrm{PDE}}$ denotes the Fourier components of the nonlinear terms $(-u\partial_x\theta - w\partial_z\theta)$ for a given horizontal wavenumber nk. Since the Fast Fourier Transform (FFT) algorithm can be used to efficiently compute $\widehat{\mathcal{N}}_n^{\mathrm{PDE}}$, the nonlinear terms $\mathcal{N}_{mn}^{\mathrm{ODE}}$ are determined here according to the following steps. Suppose the coefficients of the ODE modes a_{mn} and b_{mn} are given initially. First, the Fourier components of the temperature fluctuation and velocity fields are computed, respectively, through (7.24) and

$$\hat{u}_n = \left(\frac{-1}{ink}\right) \sum_{m=0}^{M1} b_{mn} DW_{mn}, \tag{7.26}$$

$$\hat{w}_n = \sum_{m=0}^{M1} b_{mn} W_{mn}. \tag{7.27}$$

Then, $\widehat{\mathcal{N}}_n^{\mathrm{PDE}}$ is computed using the standard pseudo-spectral method for solving PDEs. Finally, $\mathcal{N}_{mn}^{\mathrm{ODE}}$ is obtained by projecting $\widehat{\mathcal{N}}_n^{\mathrm{PDE}}$ onto Θ_{mn} using (7.25). Compared with the pseudospectral numerical solution of the governing PDEs, there exist two obvious advantages in solving ODEs: first, it is not necessary to solve the momentum equation (2.5) in each time step once the eigenfunctions are obtained; secondly, since only 4 or 6 wall eigenfunctions are retained for each horizontal mode n, the number of modes is significantly reduced. Although the projection step (7.25) leads to some extra calculations, the total operation count is still decreased since the number of ODE modes used for each n is so small.

For a given horizontal mode n, these ODEs can be written in matrix form

$$\begin{bmatrix} \dot{a}_{0n} \\ \dot{a}_{1n} \\ \dot{a}_{2n} \\ \dot{a}_{3n} \\ \vdots \end{bmatrix} = \begin{bmatrix} \mu_{0n} & \mu^1_{0n} & \mu^2_{0n} & \mu^3_{0n} & \cdots \\ \mu^0_{1n} & \mu_{1n} & \mu^2_{1n} & \mu^3_{1n} & \cdots \\ \mu^0_{2n} & \mu^1_{2n} & \mu_{2n} & \mu^3_{2n} & \cdots \\ \mu^0_{3n} & \mu^1_{3n} & \mu^2_{3n} & \mu_{3n} & \cdots \\ \vdots & \vdots & & \ddots & \end{bmatrix} \begin{bmatrix} a_{0n} \\ a_{1n} \\ a_{2n} \\ a_{3n} \\ \vdots \end{bmatrix} + \begin{bmatrix} \mathcal{N}_{0n} \\ \mathcal{N}_{1n} \\ \mathcal{N}_{2n} \\ \mathcal{N}_{3n} \\ \vdots \end{bmatrix}^{\text{ODE}}, \tag{7.28}$$

or in vector form

$$\dot{\vec{a}}_n = \mathcal{A}_n \vec{a}_n + \vec{\mathcal{N}}_n^{\text{ODE}}, \tag{7.29}$$

where $\mathcal{A}_n$ is matrix of linear coefficients and $\vec{\mathcal{N}}_n$ is vector of nonlinear terms. In computations, for both the PDEs and ODEs, the temporal discretization is achieved using the Crank–Nicolson method for the linear terms and a two-step Adams–Bashforth method for the nonlinear terms, yielding second-order accuracy in time. Moreover, in the computations employing the domain decomposition method, the domain is split into three regions with $Z_1 = 0.1$ and $Z_2 = 0.9$, and the the interior high-wavenumber region II(2) is completely omitted.

7.3 Results and Discussion

In this chapter, $L = 4\pi Ra^{-0.4}$ is utilized as approximate width of the minimal flow unit, although it has been shown in previous chapters that the appropriate scaling exponent is still unclear at very large Ra. Figure 7-5 shows the snapshots of the temperature fields obtained

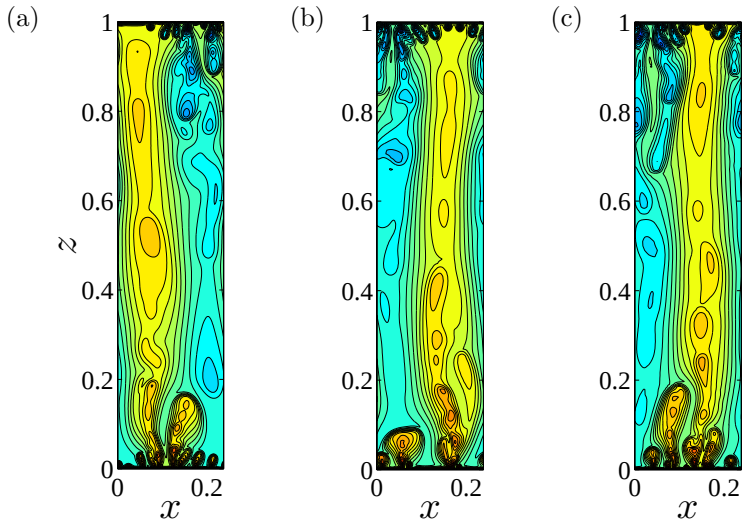

Figure 7-5: Snapshots of the temperature fields from (a) DNS, (b) domain decomposition method and (c) hybrid model at $Ra = 20000$ and $L = 0.24$. These three cases correspond to the "resolved DNS", "domain decomposition" and "hybrid model 1", respectively, in Table 7-1.

from DNS, the domain decomposition method and the hybrid model in the minimal flow unit at $Ra = 20000$. It can be seen that both the domain decomposition method and hybrid model capture the main features of the turbulent columnar flow, with well organized megaplumes in the interior and more complex spatiotemporal features near the heated and cooled walls. The corresponding resolution and Nusselt number for these three cases are shown in Table 7-1. Remarkably, compared with the DNS, the domain decomposition method yields nearly the exact value of the Nusselt number (with a relative error less than 1%), confirming that the interior high-wavenumber region (II(b) in Figure 7-2) can generally be ignored in high-Ra porous medium convection.

As discussed in previous sections, at large horizontal mode number (e.g. $n > 40$ at $Ra = 20000$ and $L = 0.24$), the Fourier amplitudes of the temperature fluctuations are strongly localized near the upper and lower walls, where they superpose to comprise the small rolls

Method	$N_1/2$ or $N_2/2$	$N/2$	M	# Modes	Nu	Error
Resolved DNS	128	128	320	82176	139.7	0
Unresolved DNS	40	40	320	25680	213.1	52.5%
DD region I	10	128	64	16640		
DD region II(a)	10	10	128	2580	138.9	0.57%
DD region III	10	128	64	16640		
Hybrid model 1	40	128	PDE:320; ODE:5	26736	168.6	20.7%
Hybrid model 2	6	128	PDE:320; ODE:5	5316	185.7	32.9%

Table 7-1: Resolution and Nusselt number for different computational schemes at $Ra = 20000$ and $L = 0.24$. For reference, an unresolved (i.e. under-resolved) DNS with high wavenumbers removed is shown in the third row, and "DD" in the fourth row denotes the domain decomposition method. The resolved DNS is treated as the "truth" for computing the error in the Nusselt number obtained with the other methods. Note that the "hybrid model 2" in which only less than one-tenth of the number of modes used in the DNS is retained still produces an estimate of the Nusselt number with a relative error of only about 30%.

within the thermal boundary layers. To investigate the effects of the small-scale motions on heat transport, an "unresolved DNS" with only low and moderate wavenumbers retained (e.g. $n \leq 40$) is also shown in Table 7-1. Evidently, the heat flux Nu is increased by nearly 50% due to the exclusion of the small-scale motions within the thermal boundary layers. However, for the "hybrid model 1" in which a very small number of upper bound wall eigenfunctions (ODEs) are utilized to model the thermal-boundary-layer dynamics, this error is reduced to about 20%; even for the hybrid model 2 in which only 7 PDEs (including the horizontal-mean equation) are used to resolve the very low-wavenumber large-scale motions, the error is still reduced to 30%. Figure 7-6 shows the variation of Nu as a function of

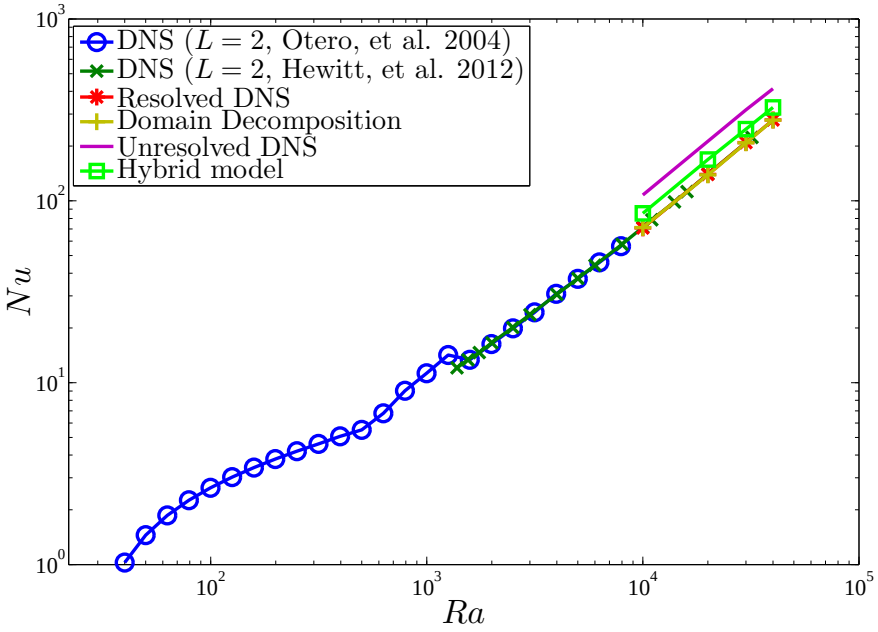

Figure 7-6: *Nu vs. Ra* for different computing strategies at large values of Rayleigh number. All the simulations in this plot are performed in the minimal flow unit $L = 4\pi Ra^{-0.4}$ except the studies of Otero et al. (2004) and Hewitt et al. (2012). In domain decomposition, the high-wavenumber interior region II(b) ($n > 10$) is shut down for each Ra; in hybrid mode, 6 ODEs for each horizontal mode number n are employed to capture the small-scale dynamics within the thermal boundary layers.

Ra for the various approaches. This figure confirms that convection in a minimal flow unit produces the same amount of heat transport as that in wide domains. Moreover, the domain decomposition method with the interior high-wavenumber region omitted is seen to be able to nevertheless adequately resolve the dynamics. Furthermore, the upper bound wall eigenmodes can efficiently represent the small-scale motions within the thermal boundary layers, which indeed play a significant role in heat transport in high-Ra porous medium convection.

Although computations utilizing either of these two approaches (i.e. the domain decomposition method or the hybrid model) are generally 2–3 times faster than the DNS, they (the

former) will increase the programming complexity, and in the hybrid model, many preprocessing steps (e.g. computing the background profile τ, solving the corresponding eigenvalue problems to obtain the eigenbasis, and computing the coefficients for the ODEs) are required at given parameter values before simulations can be performed. However, the results for these two strategies reported above are still meaningful since they indeed reveal that the flow should be treated differently in each subdomain according to its specific characteristics in that subdomain. And the physics revealed by these results should provide at least partial insight into the construction of more efficient reduced models in the future.

7.4 Summary

In this chapter, two different strategies have been presented to reduce the degrees of freedom in numerical simulations of high-Ra porous medium convection: a domain decomposition method and a hybrid model using an upper bound eigenbasis. In the first strategy, the entire domain is decomposed into three subdomains according to the specific structure of the flow at large Ra. Although only a few low wavenumbers are kept in the interior by shutting down the high-wavenumber region II(b), the dynamics can still be well resolved. In the second strategy, a set of *a priori* eigenfunctions obtained from upper bound analysis of the system is used to model the small-scale-roll motions within the upper and lower thermal boundary layers. Since these eigenfunctions are directly extracted from the governing equations, they inherently contain certain characteristics of the system at the given parameter values. The results indicate that the upper bound wall eigenmodes can efficiently represent the small-scale motions of rolls near the upper and lower walls. However, compared with DNS, the computational efficiency of these two approaches is not remarkably improved. To achieve

a significantly high computational efficiency, there is a pressing need for building a multi-scale asymptotically-reduced model which successfully couples the large-scale (slow) interior dynamics with the small-scale (fast) near-wall dynamics in the asymptotic limit of large Rayleigh number.

CHAPTER 8

CONCLUSIONS

Buoyancy-driven convection in fluid-saturated porous media is a key environmental and technological process, with numerous geoscientific and engineering applications ranging from carbon dioxide storage in terrestrial aquifers to the design of compact heat exchangers. Moreover, as a paradigm for forced-dissipative infinite-dimensional nonlinear dynamical systems, porous medium convection also displays much (though not all) of the rich dynamics of Rayleigh–Bénard convection in a pure fluid layer, including a hierarchy of instabilities and bifurcations, pattern formation, and spatiotemporally chaotic dynamics (if not "true" fluid dynamical turbulence). To thoroughly understand the underlying flow and transport mechanisms governing this spatiotemporally-chaotic system, this dissertation characterizes the coherent structure, transport properties and reduced dynamics of turbulent convective states at large Ra using a complement of DNS, secondary stability and dynamical system theory, and variational analysis.

Previous DNS by Otero et al. (2004) and Hewitt et al. (2012) show that 2D convection in a horizontal porous layer self-organizes into narrow columnar plumes at sufficiently large values of the Rayleigh number, with more complex spatiotemporal features being confined

to boundary layers near the heated and cooled walls. In particular, Hewitt et al. (2012) also point out that as Ra is increased, the interior columnar exchange flow becomes increasingly well organized, and the time-mean inter-plume spacing L_m shrinks in proportion to $Ra^{-0.4}$. However, the relevance of this scaling remains an open question as $Ra \to \infty$, since these DNS were generally conducted up to $Ra = 4 \times 10^4$ and in domains with $L \simeq 2$. In chapter 2, new DNS of horizontal porous medium convection are performed up to $Ra \simeq 10^5$ using long averaging times and in wide domains to characterize the statistical structure of spatiotemporally-chaotic convective states. The new DNS confirm the remarkable tendency for the interior flow to self-organize into narrow columnar plumes at sufficiently large Ra; however, the results show that the scaling $L_m \sim Ra^{-0.4}$ is only valid for $Ra \leq 10^4$, and for $Ra \geq 39716$ the final inter-plume spacing is not unique but may itself fall within some small band. In addition to the horizontal case, the first systematic high-resolution DNS have been carried out for porous medium convection in an inclined layer at large Ra up to $Ra \simeq 10^5$. When the layer is inclined, theoretical analysis indicates that the inclination will induce a background mean flow which becomes more vigorous as the angle of inclination ϕ is increased. The DNS results here reveal that this basic state strengthens the natural-roll motions while weakening the antinatural-roll motions, thereby modifying the flow patterns at different ϕ. For $0^\circ < \phi < 25^\circ$, the convective flow still exhibits the narrow columnar structure but with a larger mean inter-plume spacing compared with $\phi = 0^\circ$. However, as the angle is increased, the antinatural rolls becomes too weak to remain attached to the upper and lower walls. Finally, when $\phi \gtrsim \phi_t = 31.30^\circ$ above which the basic state becomes linearly stable, the antinatural rolls are completely detached from the walls and the flow then transitions to large-scale traveling-wave motions.

To gain insight into the mechanisms of pattern formation in high-Ra horizontal and inclined

porous medium convection, the structure, stability and transport properties of exact coherent states are characterized using Newton iteration and (Floquet) secondary stability theory in chapter 3 to chapter 5. First, a systematic investigation of unstable steady-state solutions of the Darcy–Oberbeck–Boussinesq equations is performed for $\phi = 0^\circ$ in domains of varying aspect ratio L in chapter 3. The steady convective states are shown to transport less heat than the statistically steady turbulent flow realized at the same parameter values: the Nusselt number $Nu \sim Ra$ for turbulent porous medium convection, while $Nu \sim Ra^{0.6}$ for the maximum heat-transporting steady solutions. A key finding is that the lateral scale of the heat-flux-maximizing solutions shrinks roughly as $L \sim Ra^{-0.5}$, reminiscent of the decrease of the mean inter-plume spacing observed in turbulent porous medium convection as the thermal forcing is increased. A spatial Floquet analysis is performed to investigate the linear stability of the fully nonlinear steady convective states, extending a recent study by Hewitt et al. (2013) by treating a base convective state – and secondary stability modes – that satisfy appropriate boundary conditions along plane parallel walls. As in that study, a bulk instability mode is found for sufficiently small aspect-ratio base states. However, the growth rate of this bulk mode is shown to be significantly reduced by the presence of the walls. Beyond a certain critical Ra-dependent aspect-ratio, the base state is most strongly unstable to a secondary mode that is localized near the heated and cooled walls. Direct numerical simulations, strategically initialized to investigate the fully nonlinear evolution of the most dangerous secondary instability modes, suggest that the (long time) mean inter-plume spacing in statistically-steady porous medium convection results from an interplay between the competing effects of these two types of instability.

In chapter 4, the structure and stability of steady convective states in an inclined porous layer are explored. Unlike the horizontal case, the inclination of the layer destroys the

reflection symmetry of the natural and antinatural rolls. At moderate Ra, the background basic state enhances the strength of the large-scale natural rolls and causes them to become more tightly attached to the upper and lower walls; however, the large-scale antinatural-roll motions are greatly suppressed and become detached from the walls at large ϕ. Consistent with this observation, the stability analysis also indicates that the inclination will stabilize the natural rolls but destabilize the antinatural rolls. At large Ra, the steady convective flow exhibits two distinct forms for different aspect ratios L_s: for small L_s, the narrow plumes are distorted in the same direction as the background base flow; however, as L_s is increased, the plumes are distorted oppositely to the basic flow. It should be noted that for large L_s, the steady flow at large Ra exhibits a similar structure as observed at moderate Ra: the natural rolls become more vigorous and then more tightly attach to the walls, and the antinatural rolls become much weaker and thereby start to detach from the walls. Secondary stability analysis of these steady convective states at large Ra reveals that the inclination of the layer will intensify the bulk instability, thereby making it difficult for the narrowly spaced plumes to survive.

Although these steady convective states share certain attributes of the columnar flows seen in the DNS, e.g. thermal boundary layers and mega-plumes, they do not capture the proto-plumes. Precisely due to their failure to represent this structure, the steady unicellular solutions only achieve $Nu \sim Ra^{0.6}$, less than $Nu \sim Ra$ obtained from DNS. To capture the time-dependent, small-scale motions within the thermal and vorticity boundary layers, unstable periodic-orbit solutions are computed at large Ra in the horizontal porous layer using a Newton-hookstep searching algorithm in chapter 5. By classifying the eigenfunctions emerging from the stability analysis of the steady convective states, four types of time-periodic states with different symmetries are obtained through the Hopf bifurcation from the

fixed-point solution. These solutions retain the three-region structure of turbulent columnar flow, including the proto-plume region, thereby exhibiting very similar instantaneous and statistical structure as the real turbulent flow and accomplishing heat transport close to that observed in the DNS. Moreover, the motions of the time-periodic solutions ideally reveal the heat-transport processing of the turbulent state: the heat is effectively absorbed by a sink near the lower/heated wall, then advected upward through the interior vertical channel (mega-plume), and finally re-deposited by an effective source near the upper/cooled wall. Stability analysis of the unsteady exact coherent states shows that two types of instabilities are (again) found: the bulk instability always corresponds to long-wavelength disturbances and is generally much weaker than the wall instability. In short, all the results in chapter 3 to chapter 5 confirm that studies of exact coherent states does, indeed, shed light on the development of spatiotemporally chaotic convection.

As discussed above, DNS show that the instantaneous flow self-organizes into recurring quasi-coherent structures, suggesting that basic physics of high-Ra porous medium convection can be understood in terms of these building blocks and the patterns they form. An important natural question concerns the existence of the minimal flow unit in which the turbulence can sustain itself and above which domain size the Nusselt number becomes independent of the aspect ratio L. This question is addressed by computing upper bounds on and predictions of Nu as a function of Ra and L in chapter 6. To solve the optimization problem arising from the energy stability and upper bound analysis, an accurate and efficient two-step algorithm in which time is introduced into the variational formulation is developed, so that the computations can proceed up to $Ra \sim O(10^4)$ and then the results are directly compared with the DNS results from Dianati (2013). It has been theoretically demonstrated

that in porous medium convection (and other upper bound problems including plane Couette flow and stree-free Rayleigh–Bénard convection, see the proofs in Wen et al. (2015)), the only steady state to which the numerical method can converge is the true solution of the variational problem. Hence, this computational approach should be widely applicable to other systems to which the background formalism can be applied. The results reveal that the upper bound algorithm produces a reliable $L(Ra)$ relationship corresponding to a given re-normalized Nusselt value, relative to the corresponding results from DNS. Moreover, the mean inter-plume spacing measured in the DNS by Hewitt et al. (2012) appears to approach the minimal flow unit at sufficiently large Ra.

In chapter 7, two strategies are presented to reduce the degrees of freedom in numerical simulations of porous medium convection in the minimal flow unit by exploiting the specific, well-organized structure of the high-Ra columnar flow. Both approaches utilize the idea of decomposition since the flow exhibits different dynamics in different regions of the domain. For instance, the small-scale-roll motions are generally localized within the thermal and vorticity boundary layers near the upper and lower walls, and in the interior, the flow always exhibits large-scale structures and only a few low-wavenumber Fourier modes are active. Hence, in the first strategy, the domain is decomposed directly into three regions: two near-wall regions (I and III) and one interior region (II). The results show that shutting down the interior high-wavenumber region (IIb) will not change the essential flow features and transport properties. In the second strategy, a hybrid reduced mode is constructed by using the fully *a priori* eigenfunctions drawn from energy stability and upper bound theory, thereby extending the previous model reduction strategy developed by Chini et al. (2011) to large Ra. The results indicate that the wall upper bound eigenmodes can efficiently represent the small-scale rolls within the thin thermal boundary layers.

In short, one important extension of this work is to quantitatively characterize the dynamics and heat transport in horizontal and inclined porous medium convection at large values of the Rayleigh number by using DNS, secondary stability and dynamical systems theory, and variational analysis. As mentioned at the beginning of this dissertation, efficient and reliable reduced dynamical models are pressingly needed for high-Ra porous medium convection. Nevertheless, the computational cost of the reduced modeling strategies investigated in this dissertation suggests that to achieve significantly increased efficiency, a multi-scale *asymptotically-reduced* model, which successfully couples the large-scale interior flow with the small-scale near-wall dynamics in the asymptotic limit $Ra \to \infty$, may be a promising and necessary direction for future research. It is hoped that the physics elucidated here for high-Ra porous medium convection will provide at least partial guidance into the construction of such a multi-scale reduced model.

BIBLIOGRAPHY

Aidun, C. K. and Steen, P. H. (1987). Transition to oscillatory convective heat transfer in a fluid-saturated porous medium. *J. Thermophys. H. T.*, 1:268–273.

Alex, S. M. and Patil, P. R. (2000). Thermal instability in an inclined isotropic porous medium. *J. Porous Media*, 3:207–216.

Aubry, N., Holmes, P., Lumley, J. L., and Stone, E. (1988). The dynamics of coherent structures in the wall region of a turbulent boundary layer. *J. Fluid Mech.*, 192:115–173.

Barletta, A. and Storesletten, L. (2011). Thermoconvective instabilities in an inclined porous channel heated from below. *Int. J. Heat Mass Transfer*, 54:2724–2733.

Bejan, A. (2013). *Convection Heat Transfer*. Wiley, Hoboken, New Jersey, 4th edn edition.

Berkooz, G., Holmes, P., and Lumley, J. L. (1993). On the relation between low-dimensional models and the dynamics of coherent structures in the turbulent wall layer. *Theor. Comput. Fluid Dyn.*, 4:255–269.

Blunt, M. (2010). Carbon dioxide storage. *Grantham Institute for Climate Change Briefing paper No 4*.

Bories, S. A. and Combarnous, M. A. (1973). Natural convection in a sloping porous layer. *J. Fluid Mech.*, 57:63–79.

Bories, S. A., Combarnous, M. A., and Jaffrenou, J. (1972). Observations des différentes formes d'écoulements thermoconvectifs dans une couche poreuse inclinée. *C. R. Acad. Sci.*, Paris A 275:857–860.

Bories, S. A. and Monferran, L. (1972). Condition de stabilité et échange thermique par convection naturelle dans une couche poreuse inclinée de grande extension. *C. R. Acad. Sci.*, Paris B 274:4–7.

Boyd, J. P. (2000). *Chebyshev and Fourier Spectral Methods*. Dover, New York, 2nd edn edition.

Brand, E. and Gibson, J. F. (2014). A doubly-localized equilibrium solution of plane Couette flow. *J. Fluid Mech. Rapids*, 750 R3:1–12.

Busse, F. (1969). On Howard's upper bound for heat transport by turbulent convection. *J. Fluid Mech.*, 37:457–477.

Busse, F. (1970). Bounds for turbulent shear flow. *J. Fluid Mech.*, 41:219–240.

Busse, F. and Joseph, D. (1972). Bounds for heat transport in a porous layer. *J. Fluid Mech.*, 54:521–543.

Busse, F. H. (1967). The stability of finite amplitude cellular convection and its relation to an extremum principle. *J. Fluid Mech.*, 30:625–649.

Busse, F. H. (1972). The oscillatory instability of convection rolls in a low Prandtl number fluid. *J. Fluid Mech.*, 52:97–112.

Caltagirone, J. P. and Bories, S. (1985). Solutions and stability criteria of natural convective flow in an inclined porous layer. *J. Fluid Mech.*, 155:267–287.

Caltagirone, J. P., Cloupeau, M., and Combarnous, M. (1971). Convection naturelle fluctuante dans une couche poreuse horizontale. *C. R. Acad. Sci.*, Paris B 273:833.

Cazemier, W., Verstappen, R. W. C. P., and Veldman, A. E. P. (1998). Proper orthogonal decomposition and low-dimensional models for driven cavity flows. *Phys. Fluids*, 10:1685.

Chini, G. P., Dianati, N., Zhang, Z., and Doering, C. R. (2011). Low dimensional models from upper bound theory. *Physica D*, 240:241–248.

Chini, G. P., Julien, K., and Knobloch, E. (2009). An asymptotically reduced model of turbulent Langmuir circulation. *Geophysical and Astrophysical Fluid Dynamics*, 103:179–197.

Clever, R. M. and Busse, F. H. (1974). The oscillatory instability of convection rolls in a low Prandtl number fluid. *J. Fluid Mech.*, 65:625–645.

Clever, R. M. and Busse, F. H. (1992). Three-dimensional convection in a horizontal layer subjected to constant shear. *J. Fluid Mech.*, 234:511–527.

Constantin, P. and Doering, C. R. (1995). Variational bounds on energy dissipation in incompressible flows. II. Channel flow. *Phys. Rev. E*, 51:3192–3198.

Corson, L. T. (2011). Maximizing the heat flux in steady unicellular porous media convection. In *Geophysical Fluid Dynamics Program report.* Woods Hole Oceanographic Institution.

Cvitanović, P. and Gibson, J. F. (2010). Geometry of turbulence in wall-bounded shear flows: periodic orbits. *Physica Scripta*, 142:014007.

Dianati, N. (2013). *Reduced-Dimensional Models of Porous-Medium Convection*. Ph.D. thesis, University of Michigan.

Doering, C. R. and Constantin, P. (1992). Energy dissipation in shear driven turbulence. *Phys. Rev. Lett.*, 69:1648–1651.

Doering, C. R. and Constantin, P. (1994). Variational bounds on energy dissipation in incompressible flows: Shear flow. *Phys. Rev. E*, 49:4087–4099.

Doering, C. R. and Constantin, P. (1996). Variational bounds on energy dissipation in incompressible flows. III. Convection. *Phys. Rev. E*, 53:5957–5981.

Doering, C. R. and Constantin, P. (1998). Bounds for heat transport in a porous layer. *J. Fluid Mech.*, 376:263–296.

Doering, C. R. and Hyman, J. M. (1997). Energy stability bounds on convective heat transport: Numerical study. *Phys. Rev. E*, 55:7775–7778.

Elder, J. W. (1967). Steady free convection in a porous medium heated from below. *J. Fluid Mech.*, 27:29–48.

Faisst, H. and Eckhardt, B. (2003). Traveling waves in pipe flow. *Phys. Rev. Lett.*, 91:224502.

Gibson, J. F. and Brand, E. (2014). Spanwise localized solutions of planar shear flows. *J. Fluid Mech.*, 745:25–61.

Gibson, J. F., Halcrow, J., and Cvitanović, P. (2008). Visualizing the geometry of state space in plane Couette flow. *J. Fluid Mech.*, 611:107–130.

Gibson, J. F., Halcrow, J., and Cvitanović, P. (2009). Equilibrium and traveling-wave solutions of plane Couette flow. *J. Fluid Mech.*, 638:243–266.

Goluskin, D. and Spiegel, E. A. (2012). Convection driven by internal heating. *Phys. Lett. A*, 377:82–92.

Graham, M. D. and Steen, P. H. (1992). Strongly interacting traveling waves and quasiperiodic dynamics in porous medium convection. *Physica D*, 54:331–350.

Graham, M. D. and Steen, P. H. (1994). Plume formation and resonant bifurcations in porous-media convection. *J. Fluid Mech.*, 272:67–90.

Herbert, T. (1983). Secondary instability of plane channel flow to subharmonic three-dimensional disturbances. *Phys. Fluids*, 26:871–874.

Herbert, T. (1988). Secondary instability of boundary layers. *Ann. Rev. Fluid Mech.*, 20:487–526.

Hewitt, D. R. (2014). *High Rayleigh Number Convection in a Porous Medium*. Ph.D. thesis, University of Cambridge.

Hewitt, D. R., Neufeld, J. A., and Lister, J. R. (2012). Ultimate regime of high Rayleigh number convection in a porous medium. *Physical Review Letters*, 108:224503.

Hewitt, D. R., Neufeld, J. A., and Lister, J. R. (2013). Stability of columnar convection in a porous medium. *J. Fluid Mech.*, 737:205–231.

Hewitt, D. R., Neufeld, J. A., and Lister, J. R. (2014). High Rayleigh number convection in a three-dimensional porous medium. *J. Fluid Mech.*, 748:879–895.

Hopf, E. (1941). Ein allgemeiner endlichkeitssatz der hydrodynamik. *Mathematische Annalen*, 117:764–775.

Horne, R. N. and OSullivan, M. J. (1974). Oscillatory convection in a porous medium heated from below. *J. Fluid Mech.*, 66:339–352.

Horton, C. W. and Rogers, F. T. (1945). Convection currents in a porous medium. *J. Appl. Phys.*, 16:367–370.

Howard, L. N. (1963). Heat transport by turbulent convection. *J. Fluid Mech.*, 17:405–432.

Itano, T. and Toh, S. (2001). The dynamics of bursting process in wall turbulence. *J. Phys. Soc. Japan*, 70:703–716.

Johnston, H. and Doering, C. R. (2009). Comparison of turbulent thermal convection between conditions of constant temperature and constant flux. *Phys. Rev. Lett.*, 102:064501.

Kalb, V. L. and Deane, A. E. (2007). An intrinsic stabilization scheme for proper orthogonal decomposition based low-dimensional models. *Phys. Fluids*, 19:054106.

Kaneko, T. (1972). *An Experimental Investigation of Natural Convection in Porous Media*. M.Sc. Thesis, University of Calgary.

Kaneko, T., Mohtadi, M. F., and Aziz, K. (1974). An experimental study of natural convection in inclined porous media. *Int. J. Heat Mass Transfer*, 17:485–496.

Kawahara, G. and Kida, S. (2001). Periodic motion embedded in plane Couette turbulence: regeneration cycle and burst. *J. Fluid Mech.*, 449:291–300.

Kelly, R. E. (1967). On the stability of an inviscid shear layer which is periodic in space and time. *J. Fluid Mech.*, 27:657–689.

Kerswell, R. R. (1998). Unification of variational principles for turbulent shear flows: the background method of Doering–Constantin and the mean-fluctuation formulation of Howard–Busse. *Physica D*, 121:175–192.

Kerswell, R. R. (2001). New results in the variational approach to turbulent Boussinesq convection. *Phys. Fluids*, 13:192–209.

Kerswell, R. R. and Tutty, O. (2007). Recurrence of travelling wave solutions in transitional pipe flow. *J. Fluid Mech.*, 584:69–102.

Kimura, S., Schubert, G., and Straus, J. M. (1986). Route to chaos in porous-medium thermal convection. *J. Fluid Mech.*, 166:305–324.

Kimura, S., Schubert, G., and Straus, J. M. (1987). Instabilities of steady, periodic, and quasi-periodic modes of convection in porous media. *J. Heat Transfer*, 109:350–355.

Lapwood, E. R. (1948). Convection of a fluid in a porous medium. *Proc. Camb. Phil. Soc.*, 44:508–521.

Ma, X. and Karniadakis, G. E. (2002). A low-dimensional model for simulating three-dimensional cylinder flow. *J. Fluid Mech.*, 458:181–190.

Malkus, W. V. R. (1954). The heat transport and spectrum of thermal turbulence. *Proc. R. Soc. Lond.*, A225:196–212.

Metz, B., Davidson, O., de Coninck, H., Loos, M., and Meyer, L. (2005). *IPCC Special Report on Carbon Dioxide Capture and Storage*. Cambridge University Press, New York.

Moehlis, J., Smith, T. R., Holmes, P., and Faisst, H. (2002). Models for turbulent plane Couette flow using the proper orthogonal decomposition. *Phys. Fluids*, 14:2493.

Moya, S. L., Ramos, E., and Sen, M. (1987). Numerical study of natural convection in a tilted rectangular porous material. *Int. J. Heat Mass Transfer*, 30:741–756.

Nagata, M. (1990). Three-dimensional finite-amplitude solutions in plane Couette flow: bifurcation from infinity. *J. Fluid Mech.*, 217:519–527.

Nagata, M. (1997). Three-dimensional traveling-wave solutions in plane Couette flow. *Phys. Rev. E*, 55:2023–2025.

Neufeld, J. A., Vella, D., Huppert, H. E., and Lister, J. R. (2011). Leakage from gravity currents in a porous medium. Part I. A localized sink. *J. Fluid Mech.*, 666:391–413.

Nield, D. A. (2011). A note on convection patterns in an inclined porous layer. *Transp. Porous Media*, 86:23–25.

Nield, D. A. and Bejan, A. (2006). *Convection in Porous Media*. Springer, New York, 3rd edn edition.

Nikitin, N. (2006). Third-order-accurate semi-implicit Runge–Kutta scheme for incompressible Navier–Stokes equations. *Int. J. Numer. Meth. Fluids*, 51:221–233.

Ormond, A. and Genthon, P. (1993). 3-D thermoconvection in an anisotropic inclined sedimentary layer. *Geophys. J. Int.*, 112:257–263.

Orszag, S. A. and Patera, A. T. (1983). Secondary instability of wall-bounded shear flows. *J. Fluid Mech.*, 128:347–385.

Otero, J., Dontcheva, L. A., Johnston, H., Worthing, R. A., Kurganov, A., Petrova, G., and Doering, C. R. (2004). High-Rayleigh-number convection in a fluid-saturated porous layer. *J. Fluid Mech.*, 500:263–281.

Palm, E., Weber, J. E., and Kvernvold, O. (1972). On steady convection in a porous medium. *J. Fluid Mech.*, 54:153–1633.

Park, J., Chung, T., Choi, C., and Kim, M. (2006). The onset of mixed convection in a porous layer heated with a constant heat flux. *AIChE Journal*, 52:2677–2683.

Pau, G., Bell, J., Pruess, K., Almgren, A. S., Lijewski, M. J., and Zhang, K. (2010). High-resolution simulation and characterization of density-driven flow in CO_2 storage in saline aquifers. *Advances in Water Resources*, 33:443–455.

Peyret, R. (2002). *Spectral Methods for Incompressible Viscous Flow*. Springer, New York.

Phillips, O. M. (1991). *Flow and Reactions in Permeable Rocks*. Cambridge University Press.

Phillips, O. M. (2009). *Geological Fluid Dynamics: Sub-surface Flow and Reactions*. Cambridge University Press.

Plasting, S. C. and Kerswell, R. R. (2003). Improved upper bound on the energy dissipation rate in plane Couette flow: the full solution to Busse's problem and the Constantin–Doering–Hopf problem with one-dimensional background field. *J. Fluid Mech.*, 477:363–379.

Press, W. H., Teukolsky, S. A., Vetterling, W. T., and Flannery, B. P. (2001). *Numerical recipes 3rd edition: the art of scientific computing*. Cambridge University Press, New York.

Rees, D. and Barletta, A. (2011). Linear instability of the isoflux Darcy–Bénard problem in an inclined porous layer. *Transp. Porous Media*, 87:665–678.

Rees, D. and Bassom, A. (2000). The onset of Darcy–Bénard convection in an inclined layer heated from below. *Acta Mech.*, 144:103–118.

Rees, D. and Postelnicu, A. (2001). The onset of convection in an inclined anisotropic porous layer. *Int. J. Heat Mass Transfer*, 44:4127–4138.

Rees, D., Storesletten, L., and Postelnicu, A. (2006). The onset of convection in an inclined anisotropic porous layer with oblique principle axes. *Transp. Porous Media*, 62:139–156.

Riaz, A., Hesse, M., Tchelepi, H. A., and Orr, F. M. (2006). Onset of convection in a gravitationally unstable diffusive boundary layer in porous media. *J. Fluid Mech.*, 548:87–111.

Riley, D. S. and Winters, K. H. (1990). A numerical bifurcation study of natural convection in a tilted two-dimensional porous cavity. *J. Fluid Mech.*, 215:309–329.

Riley, D. S. and Winters, K. H. (1991). Time-periodic convection in porous media : the evolution of Hopf bifurcations with aspect ratio. *J. Fluid Mech.*, 223:457–474.

Schubert, G. and Straus, J. M. (1982). Transitions in time-dependent thermal convection in fluid-saturated porous media. *J. Fluid Mech.*, 121:301–313.

Sen, M., Vasseur, P., and Robillard, L. (1987). Multiple steady states for unicellular natural convection in an inclined porous layer. *Int. J. Heat Mass Transfer*, 30:2097–2113.

Smith, T. R., Moehlis, J., and Holmes, P. (2005). Low-dimensional models for turbulent plane Couette flow in a minimal flow unit. *J. Fluid Mech.*, 538:71–110.

Steen, P. H. and Aidun, C. K. (1988). Time-periodic convection in porous media: transition mechanism. *J. Fluid Mech.*, 196:263–290.

Storesletten, L. and Tveitereid, M. (1999). Onset of convection in an inclined porous layer with anisotropic permeability. *Applied Mechanics and Engineering*, 4:575–587.

Tandon, A. and Leibovich, S. (1995). Secondary instabilities in langmuir circulations. *J. Phys. Oceanogr.*, 25:1206–1217.

Trefethen, L. N. and Bau, III, D. (1997). *Numerical Linear Algebra*. Society for Industrial and Applied Mathematics (SIAM), Philadelphia.

Trew, M. and McKibbin, R. (1994). Convection in anisotropic inclined porous layers. *Transp. Porous Media*, 17:271–283.

Viswanath, D. (2007). Recurrent motions within plane Couette turbulence. *J. Fluid Mech.*, 580:339–358.

Vitanov, N. K. and Busse, F. H. (1997). Bounds on the heat transport in a horizontal layer with stress-free boundaries. *Z. Angew. Math. Phys.*, 48:310–324.

von Hardenberg, J., Parodi, A., Passoni, G., Provenzale, A., and Spiegel, E. A. (2008). Large-scale patterns in Rayleigh–Bénard convection. *Phys. Lett. A*, 372:2223–2229.

Voss, C. I., Simmons, C. T., and Robinson, N. I. (2010). Three-dimensional benchmark for variable-density flow and transport simulation: matching semi-analytic stability modes for steady unstable convection in an inclined porous box. *Hydrogeol. J.*, 18:5–23.

Walch, J. and Dulieu, B. (1982). Convection de Rayleigh–Béenard dans une cavité poreuse faiblement inclinée. *J. Phys. Lett.*, 43:103–107.

Waleffe, F. (1998). Three-dimensional coherent states in plane shear flows. *Phys. Rev. Lett.*, 81:4140–4143.

Waleffe, F. (2001). Exact coherent structures in channel flow. *J. Fluid Mech.*, 435:93–102.

Waleffe, F. (2003). Homotopy of exact coherent structures in plane shear flows. *Phys. Fluids.*, 15:1517–1543.

Weber, J. (1975). Thermal convection in a tilted porous layer. *Int. J. Heat Mass Transfer*, 18:474–475.

Wedin, H. and Kerswell, R. R. (2004). Exact coherent structures in pipe flow: traveling wave solutions. *J. Fluid Mech.*, 508:333–371.

Wen, B., Chini, G. P., Kerswell, R. R., and Doering, C. (2015). A new computational approach for solving upper bound problems: application to two-dimentional Rayleigh–Bénard convection. *Submitted to Phys. Rev. E.*

APPENDIX A

NUMERICAL ALGORITHMS FOR SOLVING THE DARCY–OBERBECK–BOUSSINESQ EQUATIONS

In a horizontal porous layer, the non-dimensional Darcy–Oberbeck–Boussinesq equations in the infinite Darcy–Prandtl number limit are

$$\nabla^2\psi = -Ra\theta_x, \tag{A.1}$$

$$\partial_t\theta = -\partial_z\psi\partial_x\theta + \partial_x\psi\partial_z\theta - \partial_x\psi + \nabla^2\theta, \tag{A.2}$$

where the solution can be expressed as

$$\begin{bmatrix} \theta \\ \psi \end{bmatrix} = \sum_{n=-N/2}^{N/2} \begin{bmatrix} \hat{\theta}_n(z,t) \\ \hat{\psi}_n(z,t) \end{bmatrix} e^{inkx} = \sum_{n=-N/2}^{N/2} \sum_{m=0}^{M} \begin{bmatrix} a_{mn}(t) \\ b_{mn}(t) \end{bmatrix} \mathrm{T}_m(\tilde{z})\, e^{inkx}, \tag{A.3}$$

where $\mathrm{T}_m(\tilde{z})$ is the standard m-th Chebyshev polynomial with $\tilde{z} \in$ [-1, 1], $a_{mn}(t)$ and $b_{mn}(t)$ are the corresponding m-th Chebyshev coefficients for $\hat{\theta}_n(z,t)$ and $\hat{\psi}_n(z,t)$, respectively, and $z = (\tilde{z}+1)/2$ is projection of the *Chebyshev–Lobatto points* $\tilde{z}$ in [-1, 1] onto [0, 1]. Since

$D \equiv \frac{d}{dz} = 2\frac{d}{d\tilde{z}} \equiv 2\widetilde{D}$, for a given horizontal wavenumber nk, (A.1) and (A.2) become

$$\left[4\widetilde{D}^2 - (nk)^2\right]\hat{\psi}_n = -inkRa\hat{\theta}_n, \tag{A.4}$$

$$\partial_t\hat{\theta}_n = \widehat{\mathcal{N}}_n + \left[4\widetilde{D}^2 - (nk)^2\right]\hat{\theta}_n, \tag{A.5}$$

where $\widehat{\mathcal{N}}_n$ is the Fourier coefficient of the nonlinear term $(-\partial_z\psi\partial_x\theta + \partial_x\psi\partial_z\theta - \partial_x\psi)$. Next, Chebyshev-tau method and different temporal discretizations (Peyret, 2002) will be utilized to numerically solve (A.4) and (A.5).

A.1 Chebyshev-tau Method

In this section, (A.4) is solved as an example using Chebyshev-tau method; then, (A.5) can be solved following the same strategy. In Fourier and Chebyshev spectral space and for each mode (m, n), (A.1) becomes

$$4b_{mn}^{(2)} - (nk)^2 b_{mn} = -inkRaa_{mn}, \tag{A.6}$$

where $b_{mn}^{(2)}$ is the m-th Chebyshev coefficient of the second-order derivative of $\hat{\psi}_n(\tilde{z}, t)$ with respect to $\tilde{z}$, namely,

$$\frac{\partial^2\hat{\theta}_n(\tilde{z}, t)}{\partial\tilde{z}^2} = \sum_{m=0}^{M} b_{mn}^{(2)}(t)\mathrm{T}_m(\tilde{z}). \tag{A.7}$$

For each n, the expansion coefficients satisfy the following recurrence relation

$$P_m b_{m-2}^{(2)} + Q_m b_m^{(2)} + R_m b_{m+2}^{(2)} = b_m, \quad 2 \le m \le M \tag{A.8}$$

with

$$P_m = \frac{c_{m-2}}{4m(m-1)}, \quad Q_m = \frac{-e_{m+2}}{2(m^2-1)}, \quad R_m = \frac{e_{m+4}}{4m(m+1)}, \tag{A.9}$$

where

$$e_m = \begin{cases} 1 & \text{if} \quad m \leq M \\ 0 & \text{if} \quad m > M \end{cases}, \quad c_m = \begin{cases} 2 & \text{if} \quad m = 0 \\ 1 & \text{if} \quad m \geq 1 \end{cases}. \tag{A.10}$$

Hence, (A.6) can be rewritten as

$$\begin{aligned} P_m \left(4b^{(2)}_{m-2} - (nk)^2 b_{m-2}\right) + Q_m \left(4b^{(2)}_{m} - (nk)^2 b_{m}\right) + R_m \left(4b^{(2)}_{m+2} - (nk)^2 b_{m+2}\right) = \\ -inkRa \left(P_m a_{m-2} + Q_m a_m + R_m a_{m+2}\right). \end{aligned} \tag{A.11}$$

Therefore, (A.8) and (A.11) yield

$$\begin{aligned} &(nk)^2 P_m b_{m-2} + \left[(nk)^2 Q_m - 4\right] b_m + (nk)^2 R_m b_{m+2} = \\ &inkRa \left[P_m a_{m-2} + Q_m a_m + R_m a_{m+2}\right], \quad 2 \leq m \leq M. \end{aligned} \tag{A.12}$$

Let $\widetilde{P}_m = (nk)^2 P_m$, $\widetilde{Q}_m = (nk)^2 Q_m - 4$ and $\widetilde{R}_m = (nk)^2 R_m$, then the matrix form of (A.12) can be expressed as

$$\mathbf{A}\vec{\mathbf{b}} = \vec{\mathbf{y}}, \tag{A.13}$$

where the $(M+1) \times 1$ vector $\vec{\mathbf{b}} = (b_0, b_1, \cdots, b_{M-1}, b_M)^{\mathrm{T}}$, the $(M-1) \times 1$ vector $\vec{\mathbf{y}} = inkRa(P_2 a_0 + Q_2 a_2 + R_2 a_4, \cdots, P_m a_{m-2} + Q_m a_m + R_m a_{m+2}, \cdots, P_M a_{M-2} + Q_M a_M)^{\mathrm{T}}$, and

the $(M-1)\times(M+1)$ matrix

$$\mathbf{A}=\begin{bmatrix}
\widetilde{P}_2 & 0 & \widetilde{Q}_2 & 0 & \widetilde{R}_2 & 0 & 0 & \cdots & 0\\
0 & \widetilde{P}_3 & 0 & \widetilde{Q}_3 & 0 & \widetilde{R}_3 & 0 & \cdots & 0\\
0 & 0 & \widetilde{P}_4 & 0 & \widetilde{Q}_4 & 0 & \widetilde{R}_4 & \cdots & 0\\
0 & 0 & 0 & \ddots & 0 & \ddots & 0 & \ddots & 0\\
0 & 0 & 0 & 0 & \widetilde{P}_{M-2} & 0 & \widetilde{Q}_{M-2} & 0 & \widetilde{R}_{M-2}\\
0 & 0 & 0 & 0 & 0 & \widetilde{P}_{M-1} & 0 & \widetilde{Q}_{M-1} & 0\\
0 & 0 & 0 & 0 & 0 & 0 & \widetilde{P}_{M-1} & 0 & \widetilde{Q}_{M-1}
\end{bmatrix}. \tag{A.14}$$

To take the Dirichlet boundary conditions into account, the coefficients must satisfy

$$\sum_{m=0}^{M}(-1)^m b_m=0,\quad \sum_{m=0}^{M} b_m=0. \tag{A.15}$$

These two constraints in (A.15) can be added as two rows into the matrix $\mathbf{A}$, so that the new matrix becomes

$$\begin{bmatrix}
1 & -1 & 1 & -1 & 1 & -1 & 1 & \cdots & (-1)^M\\
1 & 1 & 1 & 1 & 1 & 1 & 1 & \cdots & 1\\
\widetilde{P}_2 & 0 & \widetilde{Q}_2 & 0 & \widetilde{R}_2 & 0 & 0 & \cdots & 0\\
0 & \widetilde{P}_3 & 0 & \widetilde{Q}_3 & 0 & \widetilde{R}_3 & 0 & \cdots & 0\\
0 & 0 & \widetilde{P}_4 & 0 & \widetilde{Q}_4 & 0 & \widetilde{R}_4 & \cdots & 0\\
0 & 0 & 0 & \ddots & 0 & \ddots & 0 & \ddots & 0\\
0 & 0 & 0 & 0 & \widetilde{P}_{M-2} & 0 & \widetilde{Q}_{M-2} & 0 & \widetilde{R}_{M-2}\\
0 & 0 & 0 & 0 & 0 & \widetilde{P}_{M-1} & 0 & \widetilde{Q}_{M-1} & 0\\
0 & 0 & 0 & 0 & 0 & 0 & \widetilde{P}_{M-1} & 0 & \widetilde{Q}_{M-1}
\end{bmatrix}^{(M+1)\times(M+1)} \tag{A.16}$$

and the vector $\vec{\mathbf{y}}$ becomes $inkRa(0, 0, P_2a_0+Q_2a_2+R_2a_4, \cdots, P_ma_{m-2}+Q_ma_m+R_ma_{m+2}, \cdots, P_Ma_{M-2} + Q_Ma_M)^{\mathrm{T}}$. Finally, due to the quasi-tridiagonal form of matrix (A.16), the linear equation (A.13) can be solved in $O(M)$ steps by employing the Thomas algorithm (Press et al., 2001), in contrast to $O(M^3)$ steps to solve a (dense) matrix equation arising in a Chebyshev collocation formulation. It should be noted that even accounting for the cost of the FFTs/IFFTs associated with Chebyshev spectral transformations, the Chebyshev-tau algorithm described here requires only $O(M \log M)$ computing steps.

A.2 Temporal Discretization

In this dissertation, various temporal discretizations are utilized to perform DNS and compute periodic-orbit solutions.

A.2.1 Semi-Implicit 2nd-Order Adams–Bashforth/Crank–Nicolson (AB/CN) Scheme

The two-step AB/CN scheme for the time-discretization of (A.5) is

$$\frac{\hat{\theta}_n^{s+1} - \hat{\theta}_n^s}{\triangle t} = \frac{1}{2}\left(3\widehat{\mathcal{N}}_n^s - \widehat{\mathcal{N}}_n^{s-1}\right) + \frac{1}{2}\left[4\widetilde{D}^2 - (nk)^2\right]\left(\hat{\theta}_n^{s+1} + \hat{\theta}_n^s\right), \tag{A.17}$$

where the superscript s refers to the step number, i.e. $t^{s+1} = t^s + \triangle t$, the Crank–Nicolson method is used for the linear terms (i.e. terms linear in the variable being advanced), and the two-step Adams–Bashforth method for the nonlinear (i.e. remaining) terms. Generally, the AB/CN scheme yields second-order accuracy in time.

A.2.2 Adams–Bashforth/Backward–Differentiation Semi-Implicit 4th-Order (AB/BDI4) Scheme

For a time-dependent partial differential equation

$$\partial_t u = \mathbf{N}(u) + \mathbf{L}(u), \tag{A.18}$$

where $\mathbf{N}(u)$ is a nonlinear first-order term and $\mathbf{L}(u)$ is a linear second-order term, the general high-order AB/BDIk (k-th order) scheme is of the form

$$\frac{1}{\triangle t}\sum_{j=0}^{\mathrm{k}} c_j u^{s+1-j} = \sum_{j=0}^{\mathrm{k}-1} d_j \mathbf{N}(u^{s-j}) + \mathbf{L}(u^{s+1}) \tag{A.19}$$

with specific coefficients c_j and d_j.

The fourth-order AB/BDI scheme for the time-discretization of (A.5) is

$$\sum_{j=0}^{4} c_j \hat{\theta}_n^{s+1-j} = \triangle t \sum_{j=0}^{3} d_j \widehat{\mathcal{N}}_n^{s-j} + \triangle t \left[4\widetilde{D}^2 - (nk)^2\right] \hat{\theta}_n^{s+1} \tag{A.20}$$

with coefficients

$$\begin{aligned} c_0 = \frac{25}{12}, \quad c_1 = -4, \quad c_2 = 3, \quad c_3 = -\frac{4}{3}, \quad c_4 = \frac{1}{4}; \\ d_0 = 4, \quad d_1 = -6, \quad d_2 = 4, \quad d_3 = -1. \end{aligned} \tag{A.21}$$

Finally, (A.20) can be solved numerically using the Chebyshev-tau method described in section A.1.

A.2.3 Semi-Implicit Four-Stage 3rd-Order Runge–Kutta (RK3) Scheme

One common feature for the AB/CN and AB/BDI4 schemes is that both of them belong to the multistep method, so that for each step information of the previous few steps is required. In DNS, some low-order accurate, one-step schemes (e.g. Euler method) can be employed to compute the first one or three steps to provide initial conditions for the mutistep schemes, and the temporary reduction of time accuracy generally will not affect the final statistical results. However, in seeking periodic-orbit solutions, high-order time-discretization scheme is needed for each step to accurately compute the time period. Therefore, in order to maintain the high accuracy in time, for the first few steps it is very necessary to utilize some high-order one-step schemes. In this section, a four-stage (one-step) third-order-accurate semi-implicit Runge–Kutta scheme, developed by Nikitin (2006), is used in numerical simulations of porous medium convection.

Let $\widehat{\mathcal{H}}_n$ denote the right-hand side of (A.5), namely

$$\partial_t \hat{\theta}_n = \widehat{\mathcal{H}}_n = \widehat{\mathcal{N}}_n + \left[4\widetilde{D}^2 - (nk)^2\right] \hat{\theta}_n. \tag{A.22}$$

Then, the first stage of the semi-implicit Runge–Kutta scheme is

$$\frac{\hat{\theta}_n^{s1} - \hat{\theta}_n^s}{\triangle t} = \frac{2}{3}\widehat{\mathcal{H}}_n^s + \chi\widehat{\mathcal{L}}_n\left(\hat{\theta}_n^{s1} - \hat{\theta}_n^s\right), \tag{A.23}$$

where χ is an arbitrary positive number and $\widehat{\mathcal{L}}_n$ is the Fourier component of a linear operator $\mathcal{L}$ at the n-th mode; the second stage is

$$\frac{\hat{\theta}_n^{s2}-\hat{\theta}_n^{s}}{\triangle t}=\frac{1}{3}\widehat{\mathcal{H}}_n^{s}+\frac{1}{3}\widehat{\mathcal{H}}_n^{s1}+\chi\widehat{\mathcal{L}}_n\left(\hat{\theta}_n^{s2}-\hat{\theta}_n^{s1}\right); \tag{A.24}$$

the third stage is

$$\frac{\hat{\theta}_n^{s3}-\hat{\theta}_n^{s}}{\triangle t}=\frac{1}{4}\widehat{\mathcal{H}}_n^{s}+\frac{3}{4}\widehat{\mathcal{H}}_n^{s1}+\chi\widehat{\mathcal{L}}_n\left(\hat{\theta}_n^{s3}-\tilde{\hat{\theta}}_n\right), \tag{A.25}$$

where

$$\tilde{\hat{\theta}}_n=\frac{3}{2}\left[\xi\hat{\theta}_n^{s1}+(1-\xi)\,\hat{\theta}_n^{s2}\right]-\frac{1}{2}\hat{\theta}_n^{s}; \tag{A.26}$$

the fourth stage is

$$\frac{\hat{\theta}_n^{s+1}-\hat{\theta}_n^{s}}{\triangle t}=\frac{1}{4}\widehat{\mathcal{H}}_n^{s}+\frac{3}{4}\widehat{\mathcal{H}}_n^{s2}+\chi\widehat{\mathcal{L}}_n\left(\hat{\theta}_n^{s+1}-\hat{\theta}_n^{s3}\right). \tag{A.27}$$

In these four stages, three evaluations of $\widehat{\mathcal{H}}_n$, i.e. $\widehat{\mathcal{H}}_n^{s}$, $\widehat{\mathcal{H}}_n^{s1}$ and $\widehat{\mathcal{H}}_n^{s2}$ are conducted, and the whole scheme (A.23)–(A.27) possesses a third-order accuracy irrespective of the values of χ and ξ, and of the operator $\mathcal{L}$. It should be noted that $\chi=1/3$, $\xi=3/2$ and $\mathcal{L}=\nabla^2$ are chosen here for the computations of porous medium convection. Moreover, in DNS of inclined porous medium convection and studies of periodic-orbit solutions, this third-order-accurate Runge–Kutta scheme is only employed for computations of the first three steps; then the AB/BDI4 scheme is utilized for the remaining steps. Hence, generally the fourth-order accuracy in time is still retained.

APPENDIX B

NEWTON–KANTOROVICH ALGORITHM FOR SOLVING THE EULER–LAGRANGE EQUATIONS

The Euler–Lagrange equations (6.27)–(6.30) can be rewritten as

$$\begin{aligned} \tau_{zz} &= F^{\tau}(\vartheta, W, \vartheta_z, W_z), && \text{(B.1)} \\ 2\nabla^2\vartheta + \gamma_{xx} &= F^{\vartheta}(W, \tau_z), && \text{(B.2)} \\ \nabla^2 W - ra\cdot\vartheta_{xx} &= F^{W} = 0, && \text{(B.3)} \\ \nabla^2\gamma &= F^{\gamma}(\vartheta, \tau_z). && \text{(B.4)} \end{aligned}$$

Suppose the iterates $\tau^i(z)$, $\vartheta^i(x,z)$, $W^i(x,z)$, and $\gamma^i(x,z)$ are good approximations to the true solution $\tau(z)$, $\vartheta(x,z)$, $W(x,z)$, and $\gamma(x,z)$. Taylor expanding the functionals F^{τ}, F^{ϑ}, F^{W} and F^{γ} in (B.1)–(B.4) about the i^{th} iterate yields

$$\begin{aligned} \tau_{zz} &= (F^{\tau})^i + (F^{\tau}_{\vartheta})^i[\vartheta - \vartheta^i] + (F^{\tau}_{W})^i[W - W^i] + (F^{\tau}_{\vartheta_z})^i[\vartheta_z - \vartheta^i_z] + (F^{\tau}_{W_z})^i[W_z \\ &\quad - W^i_z] + O([\vartheta - \vartheta^i]^2, [W - W^i]^2, [\vartheta_z - \vartheta^i_z]^2, [W_z - W^i_z]^2), \qquad \text{(B.5)} \end{aligned}$$

$$
\begin{aligned}
2\nabla^2\vartheta + \gamma_{xx} &= (F^{\vartheta})^i + (F^{\vartheta}_{W})^i[W - W^i] + (F^{\vartheta}_{\tau_z})^i[\tau_z - \tau_z^i] \qquad \text{(B.6)}\\
&\quad + O([W - W^i]^2[\tau_z - \tau_z^i]^2),\\
\nabla^2 W - ra\vartheta_{xx} &= 0, \qquad \text{(B.7)}\\
\nabla^2\gamma &= (F^{\gamma})^i + (F^{\gamma}_{\vartheta})^i[\vartheta - \vartheta^i] + (F^{\gamma}_{\tau_z})^i[\tau_z - \tau_z^i] \qquad \text{(B.8)}\\
&\quad + O([\vartheta - \vartheta^i]^2, [\tau_z - \tau_z^i]^2),
\end{aligned}
$$

where, for example, F^{τ}_{ϑ} denotes the Frechet derivative of the function $F^{\tau}(\vartheta, W, \vartheta_z, W_z)$ with respect to ϑ. By defining correction terms

$$
\triangle^{\tau} = \tau^{i+1} - \tau^i, \;\; \triangle^{\vartheta} = \vartheta^{i+1} - \vartheta^i, \;\; \triangle^{W} = W^{i+1} - W^i, \;\; \triangle^{\gamma} = \gamma^{i+1} - \gamma^i, \qquad \text{(B.9)}
$$

and computing the Frechet derivatives, the linear differential equations for the corrections can be expressed as

$$
\begin{aligned}
\triangle^{\tau}_{zz} - (F^{\tau}_{\vartheta})^i\triangle^{\vartheta} - (F^{\tau}_{\vartheta_z})^i\triangle^{\vartheta}_z - (F^{\tau}_{W})^i\triangle^{W} - (F^{\tau}_{W_z})^i\triangle^{W}_z &= (F^{\tau})^i - \tau^i_{zz}, \qquad \text{(B.10)}\\
-(F^{\vartheta}_{\tau_z})^i\triangle^{\tau}_z + 2\nabla^2\triangle^{\vartheta} - (F^{\vartheta}_{W})^i\triangle^{W} + \triangle^{\gamma}_{xx} &= (F^{\vartheta})^i - 2\nabla^2\vartheta^i \qquad \text{(B.11)}\\
&\quad - \gamma^i_{xx},\\
-ra\triangle^{\vartheta}_{xx} + \nabla^2\triangle^{W} &= ra\vartheta^i_{xx} - \nabla^2 W^i, \qquad \text{(B.12)}\\
-(F^{\gamma}_{\tau_z})^i\triangle^{\tau}_z - (F^{\gamma}_{\vartheta})^i\triangle^{\vartheta} + \nabla^2\triangle^{\gamma} &= (F^{\gamma})^i - \nabla^2\gamma^i. \qquad \text{(B.13)}
\end{aligned}
$$

Let

$$
\hat{\triangle}^{\vartheta} = \hat{\vartheta}^{i+1} - \hat{\vartheta}^i, \;\; \hat{\triangle}^{W} = \hat{W}^{i+1} - \hat{W}^i, \;\; \hat{\triangle}^{\gamma} = \hat{\gamma}^{i+1} - \hat{\gamma}^i; \qquad \text{(B.14)}
$$

then (B.10) becomes

$$D^2\triangle^\tau - \frac{1}{4}\sum_{n=1}^{N}[(D\hat{W}_n^i + \hat{W}_n^i D)\hat{\triangle}_n^\vartheta] - \frac{1}{4}\sum_{n=1}^{N}[(D\hat{\vartheta}_n^i + \hat{\vartheta}_n^i D)\hat{\triangle}_n^W] = -D^2\tau^i + \frac{1}{4}D[\sum_{n=1}^{N}(\hat{W}_n^i\hat{\vartheta}_n^i)]. \tag{B.15}$$

For a given nk, (B.11), (B.12) and (B.13) become

$$\begin{aligned} -\hat{W}_n^i D\triangle^\tau + 2[D^2-(nk)^2]\hat{\triangle}_n^\vartheta - D\tau^i\hat{\triangle}_n^W - (nk)^2\hat{\triangle}_n^\gamma &= -2[D^2-(nk)^2]\hat{\vartheta}_n^i \quad \text{(B.16)} \\ &\quad + D\tau^i\hat{W}_n^i + (nk)^2\hat{\gamma}_n^i, \\ ra(nk)^2\hat{\triangle}_n^\vartheta + [D^2-(nk)^2]\hat{\triangle}_n^W &= -ra(nk)^2\hat{\vartheta}_n^i \quad \text{(B.17)} \\ &\quad - [D^2-(nk)^2]\hat{W}_n^i, \\ raD\tau^i\hat{\triangle}_n^\vartheta + ra\hat{\vartheta}_n^i D\triangle^\tau &= -raD\tau^i\hat{\vartheta}_n^i \quad \text{(B.18)} \\ &\quad - [D^2-(nk)^2]\hat{\gamma}_n^i. \end{aligned}$$

Although the Newton-Kantorovich method is only locally convergent, the basin of attraction can be expanded (in the space of initial iterates) by updating the variables for each iterate using

$$\begin{bmatrix} \tau \\ \hat{\vartheta}_n \\ \hat{W}_n \\ \hat{\gamma}_n \end{bmatrix}^{i+1} = \begin{bmatrix} \tau \\ \hat{\vartheta}_n \\ \hat{W}_n \\ \hat{\gamma}_n \end{bmatrix}^{i} + a \begin{bmatrix} \triangle^\tau \\ \hat{\triangle}_n^\vartheta \\ \hat{\triangle}_n^W \\ \hat{\triangle}_n^\gamma \end{bmatrix}, \tag{B.19}$$

where $0 \le a \le 1$. The step length is reduced whenever $F_{res}^{i+1} > bF_{res}^i$, where F_{res}^i is the norm of the residual of the Euler–Lagrange equations at the i^{th} iterate, and $b \approx 1$ is an adjustable parameter.

APPENDIX C

TABLE OF ACRONYMS

2D – two-dimensional

3D – three-dimensional

AB/BDI4 – 4th-order-accurate semi-implicit Adams–Bashforth/Backward–Differentiation

AB/CN – Adams–Bashforth/Crank–Nicolson

CHD – Constantin–Doering–Hopf

CO_2 – carbon dioxide

DNS – direct numerical simulations

GMRES – generalized minimal residual

MHB – Malkus–Howard–Busse

NK – Newton–Kantorovich

ODE – ordinary differential equation

PDE – partial differential equation

POD – Proper Orthogonal Decomposition

r.e.v. – representative elementary volume

RK3 – 3rd-order-accurate Runge–Kutta